NANYANG TECHNOLOGICAL UNIVERSITY

NUMERICAL MODELING OF MULTIPHASE FLOWS IN MICROCHANNELS

YAP YIT FATT

SCHOOL OF MECHANICAL & AEROSPACE ENGINEERING

2007

Numerical Modeling of Multiphase Flows in Microchannels

Yap Yit Fatt

School of Mechanical & Aerospace Engineering

A thesis submitted to the Nanyang Technological University
in fulfillment of the requirement for the degree of
Doctor of Philosophy

2007

ABSTRACT

Numerical modeling plays an important role in understanding the physics in micro-scale multiphase flow given the small length and time scales involved. The difficulty of modeling such type of flows is caused by the existence of unknown moving interfaces. These interfaces can be only determined as a part of the solution. The present work devises and implements numerical procedures to simulate multiphase flows where precise prediction of these interfaces is essential.

In this study, a three-phase flow model with two fluids and a solid phase involving two moving interfaces, i.e. fluid-fluid (F-F) and fluid-solid (F-S) interfaces, is proposed. Two limiting cases of the model are two-fluid flow and fluid-solid flow.

The F-F interface is captured using a level-set method. Two mass conservation schemes, i.e. Global (GMC) and Local (LMC) Mass Correction Schemes, are presented to ensure mass conservation for the level-set method. While GMC is for general two-fluid flow problems, LMC is developed for stratified two-fluid flows. These schemes are extended to the situation where a solid phase is present. Artificial viscosity is introduced in selected region away from the F-F interface during the advection of the level-set function and shown to improve numerical stability.

A new fixed-grid F-S interface tracking technique is proposed. Solids, represented by local distance functions, are tracked explicitly. The procedure can handle flows with multiple complex shaped solids. The F-F interface tracking procedure is extended to the case where there is a slip velocity at the solid surfaces as encountered in the modeling of electrophoresis of particles.

A set of combined conservation equations is employed for the physical domain consists of the three phases. Surface tension effects at the F-F interface, both curvature and Marangoni driven, are incorporated using the Continuum Surface Force model. Solution of the governing equations together with the F-F interface capturing and F-S interface tracking procedures are implemented in a finite volume method.

Validation of the present model is made against available results in two-fluid and fluid-solid flows. The applications of the present model in a large variety of multiphase flow problems are demonstrated.

ACKNOWLEDGEMENT

This project was blessed with advice, helpful guidance and constructive criticism from my supervisor, Assoc Prof John Chai Chee Kiong and co-supervisor, Dr. Zhang Hengyun. I wish to thank them for their willingness to spare their precious time to guide and supervise the project. It has been most rewarding for me to work with Assoc Prof John Chai. His expertise and experiences in numerical modeling of complex physical problems never stop to amaze me.

The opportunity to interact and work with Assoc Prof Wong Teck Neng, Assoc Prof Toh Kok Chuan and Assoc Prof Nguyen Nam-Trung proves to be extremely fruitful and phenomenally inspiring. I was passionately motivated by their enthusiasm on the quest for truth in science. For Prof Amer Nordin Darus, my former guru, the environment and training that he created for me during my master program have been most useful. To all of them, I express my sincere thanks.

I would like to express a deep sense of gratitude and appreciation to my parents, both have done hack of a great job on me over the years, my eldest sis, Anne, in fact the greatest sister I have, being most supportive in every imaginable way, my elder sis, Feng, whom I am deeply impressed and admired for her strength of will against all odds, my younger brother Choy, whom I am enchanted by his unusual resilience and determination for success and to achieve a better life, and my 4th uncle and his wife, who have always been very concern about my well being. I treasure their love, trust and support.

I am grateful for having the opportunity to interact with people with very diverse backgrounds and cultures in the host country, Singapore. Along the way in the completion of the project, challenges were met and overcome with the most generous helps, advices and encouragements from the most interesting characters I met and interacted with. I learnt tremendously, well beyond the realm of scientific research, from them. This acknowledgement is incomplete and seriously flawed without mentioning them in a bit more detailed. Therefore, I feel compelled but pleasured to say a word or two about them. They are, listed in the alphabetical order,

Chui Ling, a wonderful internet friend, although never met, I just cannot help but keep on teasing her in every possible way. The good thing is we all have great laughter over it, at least this is what I think. ☺ She seems to have an "Irish" boyfriend of which she denies in a not at all graceful way, only to further convince me otherwise.

Kai, the very best friend and bro one could only imagine, shared with me his most hard earned experiences and the most useful advice I needed in the early stage of the project.

Kian Leong, who motivated me to start the current project and helped me through all the tedious works involved in the application process with his superb organizational and management skills.

Ling Eng, from whom I have learned a great deal on the meaning of life in a very Buddhistic philosophical context, normally over coffee sessions (when we "snake"). Ling Eng and I share an important similarity, we are all products of the same corporation, i.e. JC CHAI Private Limited Inc.

Marcos, my personal advisor on food and beverages with astoundingly gifted talent and Einsteinian instinct in appreciating the real meaning of food and beverages tested to the very limits, from whom I think I unconsciously picked up most of the Singlish terms which I treasure, e.g. ending sentences with “one”, “hor”, “lor”, etc, and interesting stuffs like “kan-jiong spider” and “blurred sotong”, wakaka. This guy did interesting but highly mathematical research on electro-osmostic flows using Green’s functions and published a book on it which I was “sabo-ed” (cajoled) into buying. However, the highly “Marcosian” stuffs presented, although seemed to worth the price, are beyond the comprehension and grasp of any ordinary man. It is therefore not unexpected that the book ended up permanently fossilized in my bookshelf (relieved!! ☺).

Meng Yun, a pretty and extremely sweet girl, of course second only to my wife (future, mentioned for the sake of my ears or else she is going to tear them off!), that I met and missed. It is most unfortunate for me as she has been going steadily with another lucky guy. ☹ With the two little MAS wings on her back, she just could not help to keep her feet on the ground but fly around the world all the time. I am deeply influenced by her enthusiasms to life.

Murshed, to whom I shared and discussed (venting out my frustrations) occasionally my views of the prevailing international political environment terminally infested with the most selfish and greedy sharks lurking for an endless thirst and desire for power, dominance and above all interest in every facets. We mocked these cynically in the process and perhaps derived immense pleasure from it. I think life would be dull without his extraordinary mottoes: “ponggol” (also “half-ponggol”), “mehun”, “out-of-box” and “suck some dutt”. For the first one, Ling Eng and I had a hand in coining it together.

Prasenjit, although with warm and very approachable personality, possesses fascinatingly strong dedication to research. I was fortunate enough to share the same office with him for the past three years, learning from him, apart from research, a great deal about India.

Richard Kang, another superb friend and bro, enlightened me with his extraordinary courage, endeavors and perseverance in pursuing the dreamt career, switching from a well-trained civil engineer to a successful stock analyst. We share amazingly similar values and worldviews.

Yong Liang, a perfectionist who impressed me with his most formidable sense of discipline only the extreme elite force in the armies could ever muster, whom I emulate and remind myself of. In spite of that, he can be very funny and stunningly creative, enthralling us all occasionally with ideas of extreme originality like “Pilots roam the skies, Astronauts roam the space, but Mathematicians roam the universe” and the more thrilling “做人没意思，that’s why must 做爱” .

Last but not least, special thanks to enterprising Kheng Hoo, techno-informed Liwen, friendly Nutt, cheerful Shu Lan, industrious Teck Hui and persistent Yong Ping. They have all been very helpful in the course of the project and enriched my life with laughter and passion.

CONTENTS

ABSTRACT I

ACKNOWLEDGEMENT III

CONTENTS VII

NOMENCLATURE XI

LIST OF FIGURES XVIII

LIST OF TABLES XXV

1 INTRODUCTION 1

1.1 Introduction 1

1.2 Literature Reviews 5

1.2.1 Fluid-fluid (F-F) Interface Prediction 5

1.2.1.1 Moving-Grid Methods 7

1.2.1.2 Front-Tracking Method 8

1.2.1.3 Boundary-Integral Method 11

1.2.1.4 Marker-and-Cell (MAC) Method 12

1.2.1.5 Volume of Fluid (VOF) Method 13

1.2.1.6 Phase-Field Method 15

1.2.1.7 Level-Set Method 16

1.2.2 Fluid-Solid (F-S) Interface Prediction 19

1.2.2.1 Moving-Grid Method 21

1.2.2.2 Fixed-Grid Methods 22

1.2.2.2.1 Fictitious Domain Method 22

1.2.2.2.2 Fictitious Boundary Method 23

1.2.2.2.3 Immersed Boundary Method 24

1.2.2.2.4 Level-Set Method 25
1.2.3 Combined F-F and F-S Interface Prediction 25
1.3 Remarks on Existing Works 27
1.4 Objective and Scope 30
1.5 Contributions 32
1.6 Outline of the Thesis 33
2 MATHEMATICAL FORMULATION 42
2.1 Problem Description 42
2.2 F-F Interface Capturing – The Level-Set Method 43
2.2.1 Artificial Viscosity 44
2.2.2 Redistancing 45
2.2.3 Mass Correction 46
2.2.3.1 Global Mass Correction (GMC) Scheme 46
2.2.3.1.1 Remarks on GMC Scheme 49
2.2.3.2 Local Mass Correction (LMC) Scheme 51
2.2.4 Algorithm for F-F Interface Capturing 53
2.3 F-S Interface Tracking 54
2.3.1 The Local and Global Distance Functions 54
2.3.2 Construction of the Local and Global Distance Functions 55
2.3.3 Calculation of Resultant Surface Force and Torque on a Solid 57
2.3.4 The Motion of Solids 58
2.3.5 Algorithm for F-S Interface Tracking 59
2.3.6 Remarks on F-S Interface Tracking 59
2.4 Combined Conservation Equations 62
2.4.1 The Navier-Stokes Equations 63
2.4.2 The Energy Equation 65

2.4.3 Electrokinetic Effects 65
2.4.4 Boundary Conditions 66
2.4.5 Overall Solution Algorithm 67
2.5 Concluding Remarks 68
3 NUMERICAL SOLUTION PROCEDURE 74
3.1 Governing Equations in 2-Dimensions 74
3.2 The Finite Volume Discretization 76
3.2.1 Numerical Solution for the Combined Conservation Equations 77
3.2.1.1 Combined Conservation Equations with Scalar Dependent Variable 77
3.2.1.2 Implementation of Boundary Conditions 80
3.2.1.3 Solution of the Discretization Equation 81
3.2.2 SIMPLER for Velocity-Pressure Coupling 82
3.2.2.1 Implementation of Velocity Boundary conditions 85
3.2.2.2 SIMPLER Algorithm 85
3.3 Numerical Solution for F-F Interface Capturing 86
3.4 Numerical Solution for F-S Interface Tracking 87
3.5 Convergence Criterion 88
3.6 Concluding Remarks 88
4 CASE STUDIES 91
4.1 Rigid Body Rotation of Discs 93
4.2 Droplet Flow in a Straight Channel 94
4.3 Droplet Flow in a Double Bend 95
4.4 Droplet Flow in a Constricted Channel 98
4.5 Two-fluid Flow with Variable Surface Tension (Marangoni Effect) 100
4.5.1 Marangoni Force Driven Stratified Two-fluid Flow 100

4.5.2 Droplet Flow in a Micro T-junction with Thermocapillary Effect..... 103

4.5.2.1 Importance of Artificial Viscosity..... 106

4.6 Pressure Driven Stratified Two-fluid Flow in a Straight Channel 109

4.6.1 Fluids of Identical Properties..... 109

4.6.2 Fluids of Different Properties 113

4.7 Pressure Driven Stratified Two-fluid Flow in a Double-Bend..... 117

4.8 Flow around Stationary, Forced and Freely Rotating Cylinders..... 120

4.9 Sedimentation of a Circular Cylinder between Parallel Plates 123

4.10 Flow of Particles in a Microchannel System 123

4.11 Electrophoresis of Circular and Elliptical Particles 126

4.12 Flow of Particle-Encapsulated Droplet through a Constricted Microchannel 130

4.13 Flow of Particle-Encapsulated Droplets in a Microchannel System 133

4.14 Concluding Remarks..... 135

5 CONCLUSIONS..... 207

5.1 Summary and Conclusions 207

5.2 Suggestions for Future Work 209

REFERENCES 212

APPENDIX: Flow of Two Stratified Fluids Driven by Marangoni Force..... 227

NOMENCLATURE

a	major axis of an ellipse [m]
a_E	coefficient in the discretized general transport equation
a_W	coefficient in the discretized general transport equation
a_N	coefficient in the discretized general transport equation
a_S	coefficient in the discretized general transport equation
a_P	coefficient in the discretized general transport equation
A	area [m^2]
b	minor axis of an ellipse [m] or coefficient in the discretized transport equation
c_p	specific heat capacity [$Jkg^{-1}{}^{\circ}C^{-1}$]
C_D	drag coefficient [-]
C_L	lift coefficient [-]
Ca	Capillary number [-]
d	diameter [m]
D	Dirac delta function [1/m] or diffusion rate [m^3s^{-1}]
e	eccentricity [-]
E	applied electric field intensity [V/m]
$\vec{E}$	electric field intensity [V/m]
Eo	Eötvös number [-]
$\vec{f}_B$	body force per unit volume [Nm^{-3}]
$\vec{f}_F$	interfacial force at the F-F interface per unit volume [Nm^{-3}]
F	flow rate [m^3s^{-1}]
F_D	drag force [N]

$\vec{F}_i$	resultant surface force on the *i*-th solid [N]
F_L	lift force [N]
g	gravitational acceleration [m/s^2]
$\vec{G}_i$	resultant body force on the *i*-th solid [N]
H	smoothed heaviside function
$\overline{\overline{I}}_i$	inertia tensor of the *i*-th solid [kgm^2]
k	thermal conductivity [Wm^{-1}K^{-1}]
K	artificial viscosity [m^{2}s^{-1}]
l	maximum distance between two nodes in the physical domain [m]
l_d	length of a slug-liked droplet [m]
L	length [m]
$\dot{m}$	mass flowrate [kg/s]
m_i	mass of the *i*-th solid [kg]
$\dot{M}$	mass flowrate [kg/s]
M_c	the most current mass of the reference fluid [kg]
$\dot{M}_c$	the most current mass flowrate of the reference fluid [kgs^{-1}]
M_{cor}	mass correction factor GMC [-]
$\dot{M}_{cor}$	mass correction factor for LMC [-]
M_d	the desired mass of the reference phase [kg]
$\dot{M}_d$	the desired mass flowrate of the reference phase [kgs^{-1}]
$\dot{M}_{\text{in}}$	mass flowrate at the inlet [kgs^{-1}]
M_{err}	mass error for GMC [-]
$\dot{M}_{err}$	mass error for LMC [-]

Ma	Marngoni number [-]
n	a factor used in implementing artificial viscosity
N	number of solids in the domain
$\hat{N}_F$	unit normal at the F-F interface (pointing into fluid 2)
$\hat{N}_S$	unit normal at the F-S interface (pointing into the fluid)
$\hat{N}_W$	unit normal at the channel wall (pointing into the fluid)
p	pressure [Nm^{-2}]
p'	correction for pressure [Nm^{-2}]
p^*	guessed pressure [Nm^{-2}]
Pe	Peclet number [-]
Pr	Prandtl number [-]
q	heat flux [W/m^2]
Re	Reynolds number [-]
S	source term in the general transport equation
S_C	source term in the discretized general transport equation
$S_{C,extra}$	additional source term due to given flux boundary condition
S_{extra}	additional source term due to given flux boundary condition
S_P	coefficient for the linearized source term
$S_{P,extra}$	coefficient for additional source term due to given flux boundary condition
S_T	energy source or sink [Wm^{-3}]
t	time [s]
$t*$	dimensionless time [-]
$t', \bar{t}$	pseudo-time [-]
T	temperature [°C]

T^*	dimensionless temperature [-]
$\vec{T}_i$	resultant torque on the i-th solid [Nm]
u	velocity component in the x-direction [kgs^{-1}]
u^*	guessed velocity component in the x-direction [ms^{-1}]
u'	correction for velocity component in the x-direction [ms^{-1}]
$\vec{u}$	velocity vector [ms^{-1}]
u_s	streamwise velocity component [ms^{-1}]
U_e	electrophoretic velocity of particle [m/s]
$\vec{U}_i$	translational velocity of the i-th solid [ms^{-1}]
v	velocity component in the y-direction [kgs^{-1}]
v'	correction for velocity component in the y-direction [ms^{-1}]
v^*	guessed velocity component in the y-direction [ms^{-1}]
$\dot{V}$	volumetric flowrate [m^3/s]
W	width [m]
x	coordinate axis
x'	coordinate axis
$\vec{x}$	position vector [m]
$\vec{x}_{c,i}$	position vector of the center of mass for the i-th solid [m]
$\vec{x}_F$	position vector of the F-F interface [m]
y	coordinate axis
y'	coordinate axis

Greek symbols

α	thermal diffusivity [m^2/s]
β	dimensionless angular velocity [-]
δ	F-F interface location in stratified two-fluid flow [m]
δx	horizontal distance between two neighbouring nodes [m]
δy	vertical distance between two neighbouring nodes [m]
ε	half of the F-F interface thickness (a factor of the control volume size) [m]
ε_e	electrical permittivity [Fm^{-1}]
ϕ	global signed distance function for F-S interface [m]
ϕ_i	local signed distance function of the *i*-th solid [m]
γ	property of fluid or solid
φ	electrical potential [V]
λ	factor for artificial viscosity
μ	viscosity [Pa.s]
θ_i	orientation of the *i*-th solid [rad]
ρ	density [kgm^{-3}]
σ	surface tension coefficient [N/m]
$\overline{\overline{\sigma}}$	stress tensor [Nm^{-2}]
τ	stress [N/m^2]
ω	relaxation factor
ξ, ψ, ψ'	level-set functions [m]
ζ	zeta potential [V]
ζ_W	zeta potential of the charged channel wall [V]
ζ_S	zeta potential of the charged solid body [V]

Δ	the smallest length of a control volume [m]

ΔA	surface area of a control volume [m^2]
ΔV	elemental volume or volume of a control volume [m^3]
Δx	width of a control volume [m]
Δy	height of a control volume [m]
Φ	general dependent variable of interest [varies]
Γ	diffusion coefficient [m^2s^{-1}]
Γ_F	F-F interface
Γ_S	F-S interface
Ω_1	fluid 1 region
Ω_2	fluid 2 region
Ω_F	fluid region
$\vec{\Omega}_i$	angular velocity vector of the i-th solid body [$rads^{-1}$]
Ω_S	solid region

Subscripts

1	fluid 1
2	fluid 2
A	inlet A
B	inlet B or boundary
c	centroid of a solid
d	droplet
e	east surface of P control volume
E	fully-developed or node on the east of P control volume
i	the *i*-th solid
in	inlet
m	mean

n	north surface of P control volume
N	node on the north of P control volume
P	P control volume
ref	reference value or reference fluid
s	south surface of P control volume
S	solid or node on the south of P control volume
w	west surface of P control volume
W	wall or node on the west of P control volume
x	component in the *x*-direction
y	component in the *y*-direction

Superscripts

o	variable evaluated at time t
n	*n*-th iteration

LIST OF FIGURES

Figure 1-1: Air-water two-phase flow with air forming droplets or the inner core in a 100μm tube (Serizawa et al, 2002). 35

Figure 1-2: Droplet generation and flow in microchannel..... 36

Figure 1-3: Droplet formation suing “flow focusing” in a cross-junction (Anna et al., 2003) 36

Figure 1-4: Enhanced mixing within droplet via serpentine microchannels (Shestopalov et al., 2004, with the Reaction 1 section shortened). 37

Figure 1-5: Splitting of droplets using T-junction (Link et al., 2004)..... 37

Figure 1-6: Merging of droplets (Tan et al., 2004). 38

Figure 1-7: Particle separation under applied electric field (Kang et al., 2006). 38

Figure 1-8: Cell encapsulated in a droplet (Fisher and Lee, 2004). 39

Figure 1-9: A deforming curvilinear coordinate system (Magnaudet et al., 1995). 39

Figure 1-10: A freely deformed mesh in the moving-mesh approach (McHyman, 1984). 40

Figure 1-11: Markers seeded at the interface (Scardovelli and Zaleski, 1999). 40

Figure 1-12: Volume fraction function for computational cells (Scardovelli and Zaleski, 1999). 40

Figure 1-13: Contours of constant level-set function. 41

Figure 1-14. A typical chimera grid (Petersson, 1999). 41

Figure 2-1: Schematic of a three-phase flow problem. 69

Figure 2-2: The F-F interface. 69

Figure 2-3: F-F interface requires: (a) mass addition and (b) mass removal for GMC. 70

Figure 2-4: Schematic of a stratified flow. 70

Figure 2-5: F-F interface requires: (a) mass addition and (b) mass removal for LMC. 71

Figure 2-6: A local distance function for a particular solid. 71

Figure 2-7: Description of the *i*-th elliptical solid with two different coordinate systems. 72

Figure 2-8: Distribution of Dirac delta function across the F-S interface. 72

Figure 2-9: Representation of circular solids using Heaviside step functions (Duchanoy and Jongen, 2003). 72

Figure 2-10: Undetected and over-predicted displacements of the F-S interface in the approach of Duchanoy and Jongen (2003). 73

Figure 3-1 A staggered grid arrangement for the P control volume. 89

Figure 3-2: A control volume for scalar variables. 89

Figure 3-3: Given flux at the boundary. 89

Figure 3-4: CVs for momentum equations. 90

Figure 3-5: Velocity components at an outflow boundary. 90

Figure 4-1: Rigid body rotation of discs. 137

Figure 4-2: Droplet flow in a straight channel. 138

Figure 4-3a: Grid independent study. 138

Figure 4-3b: Effect of surface tension. 139

Figure 4-4: Droplet flow in a double-bend. 139

Figure 4-5: Evolution of a droplet in a double-bend without surface tension. 140

Figure 4-6: Velocity profiles for the flow in a double-bend channel at t = 110. 142

Figure 4-7: Evolution of a droplet flowing in a double-bend channel with surface tension effect. 143

Figure 4-8: Evolution of a droplet flowing in a double-bend channel with surface tension effect $\sigma = 0.01$ computed with and without GMC. 144

Figure 4-9: Droplet flow through a constricted channel. 145

Figure 4-10a: Grid independent study for a droplet squeezed through a constricted channel. 146

Figure 4-10b: Droplet interface and velocity vectors at $t = 25$ for a droplet squeezed through a constricted channel. 147

Figure 4-10c: Mass errors for a droplet squeezed through a constricted channel computed with and without GMC..... 147

Figure 4-11a: Present and VOF comparisons for the evolution of a droplet squeezed through a constricted channel for $\sigma = 0$ 148

Figure 4-11b: Present and VOF comparisons for the evolution of a droplet squeezed through a constricted channel for $\sigma = 0.05$. 149

Figure 4-12: Flow of two stratified fluid layers driven by Marangoni force..... 150

Figure 4-13: Velocity profile for viscosity combination of $\mu_1 = 1$ and $\mu_2 = 10$ 151

Figure 4-14: Velocity profile for viscosity combination of $\mu_1 = 10$ and $\mu_2 = 10$ ... 152

Figure 4-15: Velocity profile for viscosity combination of $\mu_1 = 1$ and $\mu_2 = 10$ with different F-F interface locations..... 153

Figure 4-16: Schematic of a droplet in a micro T-junction. 153

Figure 4-17: Evolution of a droplet in a T-junction for $Ma = 0$ 154

Figure 4-18a: Dimensionless temperature field in a T-junction for $Ma = 40$. 155

Figure 4-18b: Unequal splitting of a droplet in a T-junction for $Ma = 40$. 156

Figure 4-19: Switching of a droplet into a desired branch at a T-junction for $Ma = 80$. 157

Figure 4-20: Velocity field around a droplet entering branch A. 158

Figure 4-21: Computational domain for a micro T-junction..... 161

Figure 4-22: F-F interface evolution with and without artificial viscosity. 162

Figure 4-23: Schematic of a stratified two-fluid flow in a straight channel. 172

Figure 4-24: Grid independent study for the F-F interface location for two fluids of identical properties. 173

Figure 4-25. Mass errors for fluid 1 and fluid 2. 174

Figure 4-26: Control volumes at a given x 174

Figure 4-27a: The F-F interface location and velocity profiles for two fluids of identical properties with a uniform inlet velocity. 175

Figure 4-27b: The F-F interface location and velocity profiles for two fluids of identical properties with a non-uniform inlet velocity. 175

Figure 4-28: Grid independent study for the F-F interface location for two fluids of identical properties with $\mathrm{Re} = 0.01$ and $Ca = 0.1$ 176

Figure 4-29: The F-F interface location and velocity profiles for two fluids of identical properties with $\mathrm{Re} = 0.01$ and $Ca = 0.1$ 176

Figure 4-30: The F-F interface location for two fluids of identical properties with various Ca 177

Figure 4-31a: The F-F interface location for two different fluids with various inlet F-F interface locations. 177

Figure 4-31b: Mass error with LMC. 178

Figure 4-32: The F-F interface location and velocity profiles for two different fluids with different inlet F-F interface locations 179

Figure 4-33: Fully-developed interface location (δ_E / W) versus volumetric flow ratio ($\dot{V}_1 / \dot{V}_2$). 180

Figure 4-34: Effect of Eo on the F-F interface profile for $\mathrm{Re} = 0.01$ and $Ca = 0.1$. 180

Figure 4-35: The F-F interface location and velocity profiles for two different fluids with $\delta_{in} / W = 0.3$ and $Ca = 0.1$ 181

Figure 4-36: The F-F interface location and pressure distribution for two different fluids with $\delta_{in}/W = 0.3$ and $Ca = 0.1$. 181

Figure 4-37: The F-F interface location for two different fluids with various Ca 182

Figure 4-38: The F-F interface location for two different fluids with various inlet F-F interface locations. 182

Figure 4-39: Stratified two-fluid flow in a double-bend. 183

Figure 4-40: F-F interface profile in a double-bend with $Ca = 0.1$ obtained using 40×20, 80×40 and 160×80 CVs. 183

Figure 4-41: The F-F interface and velocity profiles in a double-bend with and without LMC. 184

Figure 4-42: Mass error for with and without LMC. 184

Figure 4-43: Velocity field in a double-bend with $Ca = 0.1$. 185

Figure 4-44: The F-F interface and velocity profiles in a double-bend with $Ca = 0.1$. 185

Figure 4-45: Pressure distribution in a double-bend with $Ca = 0.1$. 186

Figure 4-46: The F-F interface and velocity profiles in a double-bend with and without surface tension. 186

Figure 4-47: Flow around a circular cylinder in a two-dimensional channel. 187

Figure 4-48: Sedimentation of a circular cylinder between parallel plates 187

Figure 4-49: Settling trajectories of a circular cylinder under gravity for $\mathrm{Re} = 0.522$. 188

Figure 4-50: Schematic for flow of a particle in a microchannel system. 188

Figure 4-51: Grid independent study. 189

Figure 4-52: Effect of particle size on its trajectory. 189

Figure 4-53: Effect of particle density on its trajectory. 190

Figure 4-54a: Trajectories of three particles in a microchannel system. 190

Figure 4-54b: Trajectories of two complex shaped particles in a microchannel system. 191

Figure 4-55: Schematic of the electrophoresis of a charged particle in a microchannel. 191

Figure 4-56a: Steady-state translational velocity of the charged circular particle..... 192

Figure 4-56b: Steady-state angular velocity of the charged circular particle. 192

Figure 4-57: Electrokinetic effects on the wall and the particle. 192

Figure 4-58: The instantaneous location of particles with different zeta potentials. .. 193

Figure 4-59: Flow field around a positively charged particle. 194

Figure 4-60: Flow field around a positively charged particle. 195

Figure 4-61: Flow field around a negatively charged particle. 196

Figure 4-62: Electrophoresis of multiple particles..... 197

Figure 4-63: Flow of a particle-encapsulated droplet carried by an immiscible carrier fluid in a constricted microchannel. 198

Figure 4-64a: Evolution of a particle-encapsulated droplet through a constricted microchannel. 199

Figure 4-64b: Mass error of the reference fluid (fluid 1)..... 199

Figure 4-65: Effect of carrier fluid viscosity. 200

Figure 4-66: Effect of surface tension..... 201

Figure 4-67: Effect of particle density on u of the particle. 201

Figure 4-68: Effect of particle density. 202

Figure 4-69: Schematic for flow of a particle in a microchannel system. 202

Figure 4-70a: Evolution of a particle-encapsulation droplet in a microchannel system. 203

Figure 4-70b: Evolution of the particle-encapsulated droplet with and without GMC. 203

Figure 4-70c: Mass error of the reference fluid (fluid 1). 204

Figure 4-71: Evolution of two particle-encapsulation droplets in a microchannel system. 205

LIST OF TABLES

Table 4-1: C_D for flow around a stationary cylinder. 122

Table 4-2: C_L and C_D for flow around a forced rotating cylinder. 122

Table 4-3: C_L and C_D for flow around a freely rotating cylinder. 122

CHAPTER 1

INTRODUCTION

1.1 Introduction

Multiphase flows refer to flows involving any combination of gas, liquid and solid phases simultaneously. These flows are encountered in a wide range of engineering applications. For examples, liquid-gas flow with gas bubbles in air-lift pumps or scrubbers; liquid-gas flow with liquid droplets in atomizers and combustors; liquid-liquid flow in pipeline transportation of heavy/viscous crude oil as water continuous emulsion; gas-solid particle flow in fluidized beds and cyclone separators and liquid-solid flow in slurry transport or hydrotransport in mineral processing. Only two different phases are involved in these examples. For more general multiphase flows, more than two phases can present. In the above mentioned macro-scale multiphase flows, the flow is highly turbulent with phases interacting and affecting each other significantly.

Much attention is given to micro-scale multiphase flows recently. Micro-scale multiphase flows become increasingly important due to recent development of microfluidics. Microfluidics refers to devices and methods for controlling and manipulating fluid flows with length scale less than a millimeter (Squires and Quake, 2005). The behaviour of multiphase flows is dictated by a competition between various driving mechanisms. While the effects of inertia and gravity dominate macro-scale multiphase transports, their influences diminish when the system size reduces. In microfluidic systems, inertia no longer plays an important role in determining the fluid

flow behaviour. Instead, micro-scale multiphase flows are affected profoundly by surface tension, because of a large increase in surface to volume ratio, and viscosity.

Multiphase flows in microfluidics includes but are not limited to liquid-gas (or vapour) flows, liquid-liquid droplet flows in digital microfluidics, liquid-solid particle flows and particle-encapsulated droplet flows.

A large variety of flow patterns occurs in liquid-gas flow (Fig. 1-1). The flow pattern for a given liquid-gas flow depends strongly on the relative flowrates of the liquid and the gas. Among these flow patterns, annular flow is of particular interest as it is shown to be the dominant flow pattern in two-phase convective boiling microchannel heat sink for cooling purposes in high performance electronics (Jiang et al., 2001, Yen et al., 2003, Qu and Mudawar, 2003a and Pettersen, 2004). An annular flow, characterized by a vapour/gas core and liquid film flowing attached to the channel wall, can be considered as a special case of a stratified flow with the liquid layer stratified on the channel wall. Most of the available models for annular flow are of the mechanistic type with strong dependence on empirical correlations (Qu and Mudawar, 2003a and b).

The generation, transport and manipulation (merging and splitting) of liquid droplets are important processes in droplet-based microfluidics. Chemical or biological agents are contained inside the droplets. Given the small size of the droplets, only a tiny volume of regent is required. Generation of these droplets can be achieved by shearing a stream of liquid at a T-junction by another immiscible liquid (Fig. 1-2) and via a “flow-focusing” channel geometry (Fig. 1-3). The droplet size and the generation frequency can be controlled by adjusting the relative flowrates of the two liquids. These droplets form micro reaction chambers and can be transported downstream. The transport of the

droplet results in a circulatory flow within the droplet (Wang et al., 2006) and therefore enhances mixing. Alternatively, serpentine microchannels can be introduced to enhance mixing within droplets (Figs. 1-2b and 1-4). A T-junction can be employed to split a droplet in two daughter droplet of smaller size (Fig. 1.5a). The droplets are split unequal given the difference in the length of the branches. A longer branch creates larger resistance to flow and therefore creating smaller daughter droplet. A series of T-junctions can be connected to further split the daughter droplets into even smaller droplets of desirable size (Fig. 1-5b). This type of branched configuration is called trees matched canopy-to-canopy (Kim et. al, 2006). Merging of droplets can be achieved via specially designed channel configuration (Fig. 1-6).

In many microsystems, the transports of micro sized solids, micro capsules, biological cells, cellular organelles and etc are encountered. For ease of discussion, these are referred collectively as particles in the present study given their microscopic sizes. Very often, the size of the particles is comparable to the size of the microchannels. The particle motion and flow field (possible with energy and electric field) are closely coupled. Particle transports in microchannels due to an applied external pressure is encountered when a syringe is used to push particle-laden solution. Electrophoresis is the motion of a charged particle relative to the surrounding liquid due to an imposed external electric field (Ghosal, 2006). It applications include but are not limited to characterization and manipulation of organic (cells for instance, Voldman, 2006) and inorganic particles (Fig. 1-7). In particular electrophoresis has been applied to a variety of separation problems involving nucleic acids, proteins and drugs.

One of the applications of droplets is to transport cargo on microfluidic platforms, Atencia and Beebe (2005). These cargoes include but are not limited to cells and cellular

organelles. Fisher and Lee (2004) demonstrated cell encapsulation in a novel microfluidic device (Fig. 1-8). He et al. (2005) performed encapsulation of single cell and subcellular organelles into even smaller droplets separately on two different designs, i.e. a micro T-junction and a constricted microchannel. These droplets are termed particle-encapsulated droplets. The particles are transported in the form of encapsulation in the droplets carried by an immiscible carrier fluid in microchannels. The droplet provide the encapsulated particle both physical and chemical isolation. This is potentially useful for single cell or single organelle study in a controlled manner. Chemical analysis can be initiated on the encapsulated particle by fusing the droplet which contains the encapsulated particle with another droplet containing appropriate reagents in the transportation process.

Given the small size of these systems, numerical modeling plays a significant role in understanding the fundamental issues important to microscale multiphase flows. For the purpose of numerical modeling, the above mentioned micro-scale multiphase flows can be categorized according to the type of interface involved. For liquid-gas and liquid-liquid flows, both consist of two immiscible fluids separated by a moving and deformable fluid-fluid (F-F) interface. Liquid-solid particle flow contains a fluid and a rigid solid phase with a moving but non-deformable fluid-solid (F-S) interface. For particle-encapsulated droplet flow, a total of three phases (two fluids and a solid phase) are present with both F-F and F-S interfaces coexist together. Technically, this is a combination of the two. Both F-F and F-S interfaces play a major role in determining the flow behavior. Therefore, an accurate prediction of these interfaces is essential.

The essential fluid physics of a system is dictated by a competition between various driving mechanisms. Macro-scale and micro-scale transports have different dominant

driving mechanisms. While macro-scale transport is dominated by inertia and gravity, micro-scale transport is strongly affected by viscosity and surface tension. However, as long as continuum mechanics applies, micro-scale and macro-scale (laminar flow with low Reynolds number) multiphase flows are essentially governed by the same transport equations, although other driving mechanisms like electric field may be important in micro-scale. With this, the same interface prediction method is applicable for both macro-scale and micro-scale transports. The available numerical prediction methods for F-F and F-S interfaces are presented next. A detailed review of the history and development of each method is beyond the scope of this review. The next section gives an overview of these methods including their respective strengths and weaknesses and some recent results representative of the state of the art of the methods.

1.2 Literature Reviews

1.2.1 Fluid-fluid (F-F) Interface Prediction

The prediction of F-F interface can best be illustrated via two-fluid flow problems. In two-fluid flow problems, there are two sets of conservation equations governing the motion of each fluid. The two fluids are separated by an F-F interface. This interface evolves under the flow field driving both fluids. It may be geometrically complex and may change topology with time. Generally, the movement of the interface is not known in advance. Given the unknown F-F interface, the exact domain where each set of conservation equation applies is unknown. The solution of these two set of governing equations are coupled through relationships or jump conditions at the interface. As such, a precise representation of the interface is required for an accurate implementation of these interfacial relationships. The F-F interface, and thus each fluid domain, must be determined as part of the solution.

Several numerical techniques have been proposed for F-F interface prediction. Each of these techniques has the following basic ingredients: (1) a scheme to describe the interface geometry and location, (2) an algorithm to evolve the interface with time and (3) a means to implement the jump conditions at the interface. F-F interface prediction techniques can be classified according to the way the interface is handled. These are interface-tracking methods and interface-capturing methods.

In the interface-tracking methods, the interface is explicitly tracked either with a moving-grid or massless markers seeded at the interface. Either a moving-grid or a moving-grid-coupled fixed grid can be employed. The interface is maintained sharp with its exact location determined throughout the calculation. However, these methods require special treatment when the interface is subject to large deformation or stretching. Interface-tracking methods include moving-grid methods, front-tracking method and boundary integral method.

In the interface-capturing methods, an indicator function is employed, usually on a fixed-grid, to describe the interface. The indicator function is defined for the whole domain. The exact interface location is not known. The interface geometry and its location are inferred and can be reconstructed from the indicator function. Interface-capturing techniques include Marker and Cell (MAC) method, volume of fluid (VOF) method, phase field method and the level-set method.

1.2.1.1 Moving-Grid Methods

In moving-grid methods, as the name implied, solution procedure is carried out on a moving-grid/mesh. There are basically two approaches, classified based on the grid employed: grid with deforming boundary-fitted curvilinear coordinate system and freely deforming grid.

In the first approach, boundary-fitted curvilinear coordinate systems are introduced. The interface is defined by setting one of the coordinate variables to a constant. An example is shown in Fig. 1-9 with the coordinate system shown for fluid 2. One of the coordinates conforms to the interface. Since these coordinate systems evolve with the flow field, the interface is tracked automatically. With the knowledge of the interface exact location, interfacial jump conditions can be enforced precisely at the interface. Either one coordinate system for the whole domain or two coordinate systems with one for each fluid domain can be employed depending on convenience. The conservation equations for each fluid are recast in to the newly defined coordinate systems. These equations are solved independently and then matched the interfacial boundary conditions at the interface. Such a procedure usually requires an iterative algorithm. Given the variety of interface geometries, the versatility of this approach is limited. It is not always possible to devise such boundary-fitted curvilinear coordinate systems to represent the precise interface geometry. Extension to the situation with topological change in the interface remains elusive. This approach was employed successfully by Son and Dhir (1997) in the investigation of film boiling on a horizontal surface.

For the freely deforming grid approach, the grid/mesh, on which the discretizated conservation equations are solved, is permitted to deform freely with the flow. The

deforming grid/mesh conforms to the interface. Figure 1-10 shows an example of a deforming mesh with the mesh deformed to force the boundaries of the computational cell, e.g. control volumes for the finite volume discretization and elements for the finite element discretization, to coincide with the interface. Such an approach offers a higher versatility given the flexibility in which grid/mesh can be generated for a given interface geometry. However, severe distortion of the grid/mesh leads to the deterioration of the solution accuracy and eventually termination of the simulation. Therefore, re-gridding or remeshing is required for each time step. Information on the old grid/mesh has to be transferred to the new grid/mesh for the subsequent computation. A substantial portion of the total computational time is spent on these. Due to complex grid/mesh handling, it is limited to problems without significant topological changes of the interface. With a deforming mesh, Welch (1995) investigated phase change of a two-dimensional micro bubble. Investigation on the axisymmetric droplet deformation has been carried out by Bozzi et al. (1997). Currently, such method has been demonstrated impressively by Dai and Schmidt (2005) for three-dimensional free surface flow involving deforming liquid ligaments, periodic jets, and colliding of micro droplets and Quan and Schmidt (2006) in three-dimensional two-phase flow with topological changes in micro ligament end-pinching in a gaseous flow and modulated jet pinching.

1.2.1.2 Front-Tracking Method

In the front-tracking method, two set of grids, a fixed and a moving, are used. The conservation equations governing the motion of both fluids are solved on the fixed grid. The two set of conservation equations can be combined to circumvent the complication of dealing directly with two separate sets of conservation equations.

Massless markers are seeded at the interface (Fig. 1-11). These markers are linked together to form the moving-grid representing discretely the interface. The motions of the markers, dictated by the flow of the two fluids, are tracked explicitly. The moving-grid moves through the fixed-grid giving the precise location and geometry of the interface. The interface is therefore remains sharp. With more markers employed, subgrid resolution of the interface is achievable. Interfacial jump condition or source term such as surface tension is then transferred to the fixed-grid via a discrete delta function. It is distributed to a few grid points nearest to the interface.

The marker distribution has to be as regular as possible (equally spaced) for interface quantities like curvature and normal to be calculated accurately. As the interface moves and deforms, the markers may drift along the interface following the tangential velocity. This results in a change in the marker distribution. Markers may distribute sparsely in certain portion of the interface but cluster in another. A sparse distribution of markers may result from the stretched of the interface by the flow. The interface is not well resolved with a sparse distribution of markers. Therefore, markers are added, deleted or even redistributed if necessary for the sake of regularity.

There is an inherited weakness of the front-tracking method in handling a change in topology of the interface. Topological changes do not result from localized interface physics models, instead resulting from algorithm intervention via decision such as whether or not to “cut” a front into pieces or to join two fronts into one.

Given the complication in the bookkeeping of markers connectivity, the requirement on the regularity of the marker distribution and its weakness in handling topological change, the extension of the front-tracking method to three-dimensional problem is rather

involved in the implementations.

Front-tracking methods have been used extensively by the Glimm's group and the Tryggvason's group. Despite the difficulties involved in the front-tracking method, both groups performed three-dimensional calculations of two-phase flow. Glimm et al. (1998) and Glimm et al. (2001) performed three-dimensional front-tracking procedure on Rayleigh-Talyar instability problems. Unverdi and Tryggvason (1992) investigated the rising of one and two bubbles. This is followed by a paper with more three-dimensional problems investigated by Tryggvason et al. (2001). They considered the rising of multiple bubbles in an initially quiescent fluid and under the influence of thermocapillary force. Agresar et al. (1998) simulated a pressure driven cell modeled as a micro Newtonian droplet with constant surface tension into a micropipette. Problems with topological changes involving breakup of drops and jet were also investigated. Esmaeeli and Tryggvason (2003) and Esmaeeli and Tryggvason (2004) extended the approach to the cases with phase change.

Recently, Shin and Juric (2002) and Shin et al. (2005) proposed the use of a level contour reconstruction technique in a front-tracking method to model automatically the merging and breakup of interfaces in three-dimensional flows. This technique obviates bookkeeping for the connectivity of the markers, an inherited complication of the front-tracking method. The idea is to reconstruct the interface from a smoothed Heaviside function once in a prescribed number of time steps. However, any subgrid information of the interface is lost once reconstruction of the interface is carried out. The potential of the technique with the preservation of these information remains to be explored. With the level contour reconstruction technique, Shin and Juric (2002) investigated the flow of a micro bubble rising in a quiescent fluid. Shin and Juric (2002)

demonstrated successfully the computations of three-dimensional flow with bubble rising and merging, drops collision and film boiling.

1.2.1.3 Boundary-Integral Method

In the boundary-integral method, the interface is explicitly tracked. The flow solution in the entire domain is deduced sole from the information of the discrete points along the interface. Therefore, the flow problem is reduced by one dimension with only quantities at the interface involved. The boundary-integral method is suitable for flows with regular interfaces. It has difficulty in dealing with topological changes. Local "surgical" procedure of the interface is required in the event of topological changes. For boundary-integral method, numerical solution is susceptible to numerical instability given its near singular nature. This puts higher requirements on the numerical procedure used. Extension to three dimensions is not straight forward for the boundary-integral method and remains to be further explored. The method is overall mathematically very involved.

Recent reviews on the application of boundary-integral method are given by Pozrikidis (2001) and Hou (2001). Coulliette and Pozrikidis (1998) investigated pressure-driven transient motion of liquid drops through a cylindrical tube at vanishing Reynolds number, representative of micro-scale transports. Despite the difficulties in extension to three-dimensional flow, Cristini et al. (2001) performed impressive simulations with the boundary integral method on three-dimensional breakup of an initially spherical drop in shear flow, evolution of two drops in shear flow and near-contact motion of drops.

1.2.1.4 Marker-and-Cell (MAC) Method

Marker-and-Cell (MAC) method was introduced by Harlow and Welch (1965) for free surface flow. It was extended to two-fluid flow by Daly (1967). In MAC, a fixed-grid can be employed to solve the conservation equations for both fluids. One of the fluids is selected as the reference fluid and will be marked by massless markers. Massless markers are scattered initially in region containing the reference fluid. Their presence in a computational cell indicates the presence of the marked reference fluid. These markers are passively advected by the flow field. The motions of the markers are tracked explicitly with interpolated velocities. The markers do not track interface directly, but instead track infinitesimal reference fluid volumes. Therefore, topological changes of the interface are handled implicitly. For a given time, the interface can be reconstructed based on the density of the markers in the computational cells. A large number of markers per computational cell are required to obtain a well defined interface.

To better resolve the interface, markers are seeded denser around the interface. However, the total number of markers is still large for resolving the interface accurately. For three-dimensional flow, the number of markers increases substantially. Tracking the motions of these markers is computationally expansive.

The popularity of the original MAC is decreasing given the available of other more robust interface tracking/capturing procedures. However, its modified variants are still employed. Recently, De Sousa et al. (2004) employed a variant of MAC method and demonstrated impressively the simulations of splashing of a drop falling into a free surface of a heavier and more viscous fluid, bubbles rising and bubbles coalescence in a continuous phase. These problems involve a total of three different fluids.

1.2.1.5 Volume of Fluid (VOF) Method

The VOF method was pioneered by DeBar (1974) and Nichols and Hirt (1975). It was presented in details by Hirt and Nichols (1981). A recent review is given by Scardovelli and Zaleski (1999). In the VOF method, a fixed-grid is employed. The domain is discretized into computational cells. An indicator function, i.e. the volume fraction function, is introduced and defined for every computational cell throughout the whole domain. The volume fraction function is defined as the fraction of volume of the computational cell filled with the reference fluid. Either fluid can be used as the reference fluid. It has a value between 0 and 1. Figure 1-12 shows a typical distribution of the volume fraction function with the fluid represented by the hatched region as the reference fluid. For a volume fraction function of unity, the computational cell is completely filled with the reference fluid. Any computational cell with volume fraction function less than unity implies that it is partially filled with the reference fluid. There is no reference fluid in a computational cell with a volume fraction function of 0. Such a computational cell is completely filled with the remaining fluid. Therefore, the interface lies in computational cell with a volume fraction function of in between 0 and 1. The interface information is discarded in favour of the discrete volume fraction function data.

The interface evolution is captured by evolving the volume fraction function in time with a standard convection equation. Accurate algorithm is required for advecting the volume fraction function to preserve the conservation of mass. Interface reconstruction from the volume fraction function is required to determine the weighted density and viscosity for the computational cells and compute the volume flux necessary for the convective terms in the evolution equation. Early interface reconstruction algorithm is

based on the Simple Line Interface Construction (SLIC) by Noh and Woodward (1976). In SLIC, only vertical or horizontal lines are used to reconstruct the interface. Over the years, more sophisticated interface reconstruction algorithms have been proposed. These include Piecewise Linear Interface Construction (PLIC) employing straight oblique lines (Rider et al., 1995, Rider and Kothe, 1998, Lopez et al., 2005) and more advanced Parabolic Reconstruction of Surface Tension (PROST) employing piecewise parabolic-curves (Renardy and Renardy, 2002).

For VOF method, only a fixed grid is required. The volume and thus mass of each fluid is well conserved. Since the interface is captured implicitly in the evolution of the volume fraction function, topological change in the interface is handled automatically. However, reconstructing the interface from the volume fraction function is rather involved especially in three dimensions. Flotsam and jetsam, i.e. small droplets unphysically disconnecting from the interface, may occur unless care is exercised in the selections of both the schemes for volume fraction function advection and for interface reconstruction. Interfacial geometrical quantities, e.g. unit normal and curvature, are calculated from the volume fraction function which is nearly discontinuously distributed. It is not straight forward to calculate these quantities accurately. The modeling of interfacial phenomena that require an accurate calculation of these quantities, including surface tension and phase change, is compromised.

Three-dimensional flows have been computed with the VOF method. Lorstad and Fuchs (2004) investigated three-dimensional bubble rising in a quiescent fluid. The rising of two bubbles with an eventual merging of the bubbles was studied by Annaland et al. (2005). Taha and Cui (2006a) and Taha and Cui (2006b) investigated single bubble rising in tube where the bubble is of size much larger than the tube. Recently, Wu et al.

(2004) simulated using the VOF method the formation, ejection, and impact of a micro liquid droplet in a squeeze-type piezoelectric micro-inkjet printing device. Hardt et al. (2001) simulated the formation of micro droplets in micromixers. Zeng and Korsmeyer (2004) investigated electrically driven micro droplets generation and fusion.

1.2.1.6 Phase-Field Method

Phase-field method, also known as diffuse-interface method, shares many similarities with the level-set method. A recent review is given by Anderson et al. (1998). The phase-field function is defined as the relative mass concentration of the reference fluid in a given computational cell. Fluid properties at a given location can be expressed as a function of the phase-field function. In this case, the interface is defined as location where the phase-field function is 0.5. The phase-field function varies rapid but smoothly across the interface. Therefore, a fine grid is required around the interface.

The evolution of the phase-field function is governed by the Cahn-Hilliard equation (Cahn and Hilliard, 1959), a fourth order nonlinear parabolic diffusion equation. Numerical solution of the Cahn-Hilliard equation is difficult given its inherited non-linearity. Although improvement has been made (Kim et al., 2004), this needs to be further explored. Adaptive grid refinement is normally required to resolve the steep variation of the phase-field function across the interface.

The phase-field method offers the ease in computing geometrical quantities. Topological changes of the interface are handled automatically. It can be extended to multi-component fluid system and three dimensions with ease.

Simulations on three-dimensional Rayleigh-Taylor instability (Jacqmin, 1999), multiple pinch-offs of a long cylindrical thread at small Reynolds number (Kim, 2005a) and deformation of a spherical drop in a shear flow (Kim, 2005b) have been demonstrated.

1.2.1.7 Level-Set Method

The level-set method was proposed in a landmark paper by Osher and Sethian (1988) for curvature driven motions. It is well documented in books by Sethian (1999) and Osher and Fedkiw (2003). Reviews of the level-set method are given by Osher and Fedkiw (2001), Sethian (2001) and Lossasso et al. (2006). Application of the works in incompressible multiphase flows is extended by Sussman et al. (1994) and Chang et al. (1996). In the level-set method, the domain is normally discretized into a fixed-grid system. An indicator function, the level-set function, is introduced over the whole domain. The level-set function is defined as the signed shortest normal distance from the interface. Therefore, the interface is implicitly represented by the zero level-set. To distinguish between the two-fluids, a positive signed is attached to one fluid but a negative sign is associated to the other. Figure 1-13 shows the contours of constant level-set function. Each of these curves is of constant distance from the interface. Fluid properties can be calculated from the level-set function through a smoothed heaviside function.

The level-set function, with information of the interface embedded, is advected by the flow field. The evolution of the level-set function is governed by a standard advection equation, i.e the level-set equation. The discretization of the level-set equation can lead to significant numerical dissipation. This causes a loss of mass (or volume) in areas of high curvature or other under-resolved regions. As such, normally, the level-set function

is evolved numerically via higher order advection schemes. In the evolution of the level-set function, it generally drifts away from the distance function property. This again causes mass conservation problem. To alleviate such problem, redistancing procedure introduced by Sussman et al. (1994) is performed. The detailed redistancing procedure is given by Sussman and Fatemi (1999). It although improves mass conservation significantly, this however does not solve the mass imbalance problem of the level-set method.

Additional techniques are introduced for mass conservation. Four of the approaches are briefly discussed here. These are the particle-level-set method (Enright et al., 2002), the coupled level-set/VOF approach (Bourlioux, 1995 and Sussman and Puckett, 2000), mass/area preserving re-initialization (Chang et al., 1996) and global volume/area correction technique (Lakehal et al., 2001).

Enright et al. (2002) devised the particle-level-set method. Massless particles are seeded around the interface. The motions of these particles are tracked. As the particles move with the same velocity as the level-set function, they should not cross the zero level-set unless numerical inaccuracies arise. With such an additional constraint accounted for in the evolution of the level-set function, very good mass conservation is achieved. Additional computations need to be performed for tracking of the particles. Substantial computational time may be required if large amount of particles are used for more accurate prediction.

The level-set method is coupled with the VOF method to tap the strength of the VOF method in conserving mass (Bourlioux, 1995 and Sussman and Puckett, 2000). In the coupled level-set/VOF approach, while the volume fraction function is used for mass

conservation and level-set function is used for better approximation of geometrical quantities. The volume fraction function is used to reconstruct a piecewise linear interface. The level-set function is subsequently reconstructed from this piecewise linear interface. Such a reconstruction procedure is rather involved and limits its application to complicated geometries.

Mass/area preserving re-initialization has been proposed by Chang et al. (1996) to preserve mass during the evolution of the level-set function. The idea is to conserve the total mass (both fluid 1 and 2) in the domain by solving a perturbed Hamilton-Jacobi equation to a steady-state. Although the total mass in the domain is well preserved, the mass conservation of each individual fluid is not clear.

Global volume/area correction technique (Lakehal et al., 2001 and Lakehal et al., 2002) has been proposed to for mass conservation. Mass conservation is deduced with the volume/area of the reference fluid conserved. A correction is added to the level-set function so that volume/area of the reference fluid represented by the new corrected level-set function is equal to its initial area/volume. This is achieved through an iterative procedure. Volume/area is conserved in a global sense. No preference is given to the local property of the level-set function at the interface in the correction procedure.

In the level-set method, the interface is implicitly represented by the zero level-set. Topological change of the interface is handled automatically. Since the level-set function is smooth even across the interface, interfacial geometrical properties, e.g. curvature and normal, can be calculated accurately. With this, interfacial physics, e.g. surface tension and phase change, can be modeled with higher confidence. Given the simplicity in its implementation, the level-set method can be generalized to three

dimensions easily.

The level-set method has been applied in three-dimensional simulation of two-fluid flow. For flow of unchanged topology, rising of an inviscid air bubble in water (Sussman et al., 2000) and implosion and rebound of micro air bubble in water (Nagrath et al., 2006) have been simulated. Computations of more complicated flows involving topological changes have been demonstrated. These include non-axisymmetric merging of two viscous gas bubbles in a quiescent fluid (Sussman et al., 2000), breakup of an extended drop under surface tension driven Stokes flow (Zheng et al., 2005) and head on collision and off-center collision of micro droplets (Tanguy and Berlemont, 2005). Other than the flow of drops and bubbles, simulations on dam breaking with a cylindrical obstacle (Marchandise and Remacle, 2006) and liquid film formation in a horizontal annular flow (Fukano and Inatomi, 2003) were carried out using the level-set method.

1.2.2 Fluid-Solid (F-S) Interface Prediction

F-S interface prediction is discussed via fluid-solid flow problems where two phases are involved: a fluid and a rigid solid. There may be multiple solids of different densities, sizes and shapes. The solids' surfaces separate the solid phase from the fluid. These surfaces are collectively termed F-S interface. As the solid moves, the F-S interface evolves and therefore it is time dependent.

The motions of the fluid and the solids are governed by two separate set of conservation equations. For the fluid, it is the Navier-Stokes equations (for a Newtonian fluid, possibly coupled with other conservation equations, e.g. the energy equation or a Poisson equation for electrical potential). The motion of the solid can be either (1)

prescribed via a given velocity (both translational and rotational) or dynamically coupled with the flowing fluid. The position and orientation of the solid can be obtained kinematically for (1). Only in the case where the motions of all solids are prescribed can the F-S interface be known in advanced. Otherwise, the F-S interface remains unknown and has to be determined as part of the solution. For (2), the motions of the solids and the fluid are interrelated with the solids interacting with each other via the fluid. The flowing fluid exerts additional components of hydrodynamic force and torque on the solids. Both the hydrodynamic force and torque arise from the motion of the fluid is not known in advance. The dynamics of the solid is given by the Newton-Euler equations (conservation of linear and angular momentum). The fluid's Navier-Stokes equations and the solids' Newton-Euler equations are coupled via the slip or no-slip boundary condition at the unknown time dependent F-S interface. Due to the number of solids involved, the transient fluid region demarcated by the time dependent F-S interface can be very irregular.

Similar to two-fluid problems, the existence of the unknown time dependent F-S interface, although without topological changes, complicates the analysis. In the present study, modeling of both F-F and F-S interfaces coexist together is of interest. Once the grid system is chosen for the F-F interface procedure, it is more convenient for the same grid system to be adopted for the F-S interface prediction. Therefore, it is natural to classify the F-S interface prediction methods according to the grid system employed. These are the moving-grid and the fixed-grid methods. Fixed-grid methods include but are not limited to fictitious domain method, fictitious boundary method and immersed boundary method.

1.2.2.1 Moving-Grid Method

In the moving-gird method, the F-S interface is sharply described by a boundary-conforming grid. The computational cell boundary is made to coincide with the F-S interface. Appropriate F-S interfacial conditions can be applied directly at the exact location. This provides good accuracy for the implementation of F-S interfacial conditions. The gird must follow the motion of the interface in order to capture the F-S interface properly for all time. As the solid moves, a new boundary-conforming grid is generated to capture the new F-S interface. Information is then transferred to the new grid system on which further computations are made. Both remeshing and remapping the information from the old grid onto the new grid are computational expensive.

This approach was implemented within the framework of the finite element method on an unstructured grid by Hu et al. (1992) in their landmark paper as the arbitrary Lagrangian-Eulerian moving mesh method. In two follow up papers of the same group, Feng et al. (1994a) and Feng et al. (1994b) investigated the motion and interaction of circular and elliptical particles during sedimentation, in Couette and Poiseuille flows. Despite large computation required for three-dimensional flows, Hu et al. (2001) performed three-dimensional simulation on the migration of a buoyant sphere in a Poiseuille flow and sedimentation of single and two spheres in a channel. Recently, Sharma and Patankar (2005) considered the sedimentation of 10 spheres in a channel. Sedimentations of a disc and a plate were also simulated. Three-dimensional electrophoretic motion of a micro non-conducting sphere in a micro T-junction was simulated by Ye and Li (2004).

In another type of moving-grid method, the chimera grid method, two overlapping grids are employed. These are a fixed-grid and a boundary-fitted moving-grid. An example of chimera grid with a fixed Cartesian grid and two boundary-fitted grids for each circular solid is show in Fig. 1-14. The fixed-grid is employed for the fluid calculation. The boundary-fitted grid, employed to represent the boundary of the solid, overlaps the fixed-grid. The number of boundary-fitted grid is identical to the number of solid in the domain. Flow information is communicated between the two grid systems. Such an information transferring procedure becomes very complicated when the boundary-fitted grid moves as a result of the solid motion. Simulation of a two-dimensional flow around an ellipse with prescribed rotational motion using a chimera grid method has been demonstrated by Maruoka (2003).

1.2.2.2 Fixed-Grid Methods

1.2.2.2.1 Fictitious Domain Method

In the fictitious domain approach, the entire domain, including the space occupied by the solids, is assumed to be a fluid. The solid regions are constraint to move with rigid body motion. Both the fluid and the solid equations of motion are combined in a weak formulation within the framework of a finite-element method. In this combined formulation, the hydrodynamic force and torque on the solids are treated implicitly. The no-slip boundary condition on the particle boundaries is enforced as a constraint using a distributed Lagrange multiplier. The distributed Lagrange multiplier represents the additional body force per unit volume required to create a rigid body motion inside each solid. Such a solution procedure can be implemented on a fixed-grid, either structured or unstructured.

In the fictitious domain method, the fluid and solid momentum equations are coupled implicitly. Such a coupling, although avoid the complication of computing the forces and torque on every solid, requires the solution of a larger system of the linear and nonlinear algebraic equations for the coupled variables of fluid and solids. This slows down the solution procedure (Wan and Turek, 2006).

Two-dimensional sedimentations of 504 (Glowinski et al., 1999), 1008 (Glowinski et al., 2000) and 6400 (Glowinski et al., 2001) circular particles have been demonstrated. For three-dimensional flows, sedimentation of two (Glowinski et al., 1999) and 128 (Glowinski et al., 2000) were demonstrated. Glowinski et al. (2001) performed simulation of the fluidization of 1204 spheres. The sedimenting flow of two ellipsoids was investigated by Pan et al. (2005). Besides gravitational driven solid motion, the motion of five spheres in a three-dimensional pressure driven Poiseuille flow was investigated by Pan and Glowinski (2005). Recently, Aubry and Singh (2006) investigated the influence of particle-particle interactions and particles rotational motion in dielectrophoresis. A simulation with a total of 105 micro spheres was demonstrated.

1.2.2.2.2 Fictitious Boundary Method

Fictitious boundary method bears many similarities to the fictitious domain method. It assumed the solid regions were filled with fluid. The solids are constraint to move with rigid body motion. A fixed-grid is adopted allowing the solid to move freely through the computational grid. However, unlike fictitious domain method, the flow fluid equations and solid equations are solved separately. The hydrodynamic force and torque on each solid is calculated explicitly. This is done efficiently via converting the surface integration of the stress into volume integration. With this, the approximation of the

traction exactly at the solid surface is not required. The calculated hydrodynamic force and torque are used to update the solid locations explicitly.

Fictitious boundary method has been implemented within the framework of the finite element method by Wan and Turek (2005) and Wan and Turek (2006) for two-dimensional flows. In these studies, sedimentation of 790 circular particles of different sizes, sedimentation of 10000 circular particles and plunging of three big circular particles plunging into 2000 smaller particles in a cavity were demonstrated. Similar approach is implemented in a finite volume context by Duchanoy and Jongen (2003) for two-dimensional flows.

1.2.2.2.3 Immersed Boundary Method

The immersed boundary method was introduced by Peskin (1972). A recent review is given by Peskin (2002). In the immersed boundary method, the solid region is assumed to be filled with fluid. The surface of the solid is represented by a set of Lagrangian markers. To represent the effect of the solid, an additional force, determined by the configuration of the Lagrangian marker and a prescribed constitutive law for the solid, is added into the fluid momentum equations. Two grid systems are employed. These are: (1) a fixed-grid (normally Cartesian) for fluid calculations and (2) a Lagrangian grid for the set of Lagrangian markers representing a solid. These grid systems communicate with each other via a discrete Dirac delta function. The fluid velocity is interpolated from the fixed-grid to the Lagrangian grid to calculate the stress on the solid. When the solid moves or deforms, it generates a force on the fluid and this is spread from the Lagrangian grid to the fixed-grid for the subsequent fluid calculations. There is a tendency for the solid (a close immersed boundary) to slowly lose volume as if the fluid

were leaking out.

The immersed boundary method was originally created to study the fluid dynamics of cardiovascular flows (Peskin, 1972, Peskin, 1977, Peskin and McQueen, 1989 and McQueen and Peskin, 1989). Recently, it has been implemented for flow around moving body. Kim and Choi (2006) simulated the flow around arbitrarily moving solid in an infinite domain including three-dimensional simulations on freely falling sphere and cube.

1.2.2.2.4 Level-Set Method

The level-set method was employed in a fluid-solid flow problem by Marella and Krishnan (2005). The level-set function is advected via the standard advection equation. Such an approach inherits the weakness of the level-set method, (1) the solid loses volume over time and (2) numerical diffusion in advection of the level-set function deforms the rigid solid. They demonstrated flow around a two-dimensional cylinder and three-dimensional sphere with prescribed oscillation. In their simulations, the displacement of the solids is small.

1.2.3 Combined F-F and F-S Interface Prediction

Numerical simulation on the flow involving two fluids and a solid phase has not received much attention given the difficulties of dealing with two moving interfaces. These interfaces are handled by combining a F-F and a F-S interface prediction procedures.

Son (2005) investigated gas-liquid flow in a domain with an immersed solid. The solid is stationary, thus can be considered as an internal stationary boundary. A fixed-grid is adopted. Both the gas-liquid and fluid-solid interfaces are represented using level-set function. No-slip condition is implemented on the fluid-solid interface. The gas-liquid level-set function is extended into the solid to enforce the contact angle condition at the gas-liquid-solid interline. Since the solid is stationary, no complication arises in the capturing of the fluid-solid interface. The motion of a bubble adhered to a cylindrical solid is simulated.

Yokoi (2002) demonstrated the motion of a rectangular rigid body falling into a liquid. A total of three phases, i.e. gas, liquid and solid, are involved. Both gas-liquid and fluid-solid interfaces are captured using level-set functions. A technique is devised to prevent error accumulation during the redistancing of the level-set function. With the technique employed, the shape of the rigid rectangular solid is shown to be well maintained. It is most unfortunate that the details of the advection of the level-set function for the fluid-solid interface are not presented.

Singh and Joseph (2005) simulated three-dimensional motion of solids floating in a fluid-fluid interface. They employed a level-set method for the fluid-fluid interface and a fictitious domain approach for the fluid-solid interface. Solution procedure is implemented with a finite element method. The problem of three-phase contact angle is also addressed. Simulations were impressively demonstrated for multiple spheres and cylinders.

Free surface problems involved two fluids in which the effect of one fluid on the fluid-fluid interface is negligible. Therefore, the conservation equations for the fluid of

negligible effect are not solved. Free surface problems with solid bodies immersed and interacting have been investigated recently. In these problems, two moving interfaces, i.e. free surface and the solid surface, need to be considered.

Van Sint Annaland et al. (2006) combined an immersed boundary method and a VOF method in their simulation of a falling spherical liquid droplet on a stationary solid sphere of the same diameter. The solid remains stationary throughout the simulation. The free surface is captured by the VOF method and the solid sphere is represented via the immersed boundary method.

Wei (2005a,b) investigated problems involving a free surface interacting with a solid. A VOF method is employed to track the free surface. Area and volume fraction are calculated for the computational mesh to describe the location and motion of the solids based on a technique introduced by Hirt and Sicilian (1985). The motion of the solids is calculated explicitly. Entry of a sphere into water (Wei, 2005a) and impact of a sphere (less dense) on a water surface (Wei, 2005b) have been demonstrated.

1.3 Remarks on Existing Works

Two types of procedures are available to handle the F-F interface, i.e. interface-tracking and interface-capturing. Interface-tracking methods include moving-grid methods, front-tracking method and boundary integral method. Interface-capturing techniques include Marker and Cell (MAC) method, volume of fluid (VOF) method, phase field method and the level-set method. For a F-F interface prediction procedure, the following qualities are essential:

(1) The procedure can be implemented on a fixed-grid, and preferably a structured

grid/mesh. The troubles associated with the moving-grid methods which include remeshing and transferring of information between the old and new grid systems are circumvented.

(2) Only one single grid system is required. The complication in transferring information between two grid systems is avoided.

(3) The solution procedure for the F-F interface evolution can be easily implemented.

(4) No reconstruction for the interface is required. Interface reconstruction required extra computational efforts and is complicated in three dimensions.

(5) The interfacial geometrical quantities can be calculated accurately with ease. This facilitates a better modeling of interfacial phenomena.

(6) Topological changes of the F-F interface are handled automatically.

(7) Extension to three dimensions is straight forward

(8) Conservation of mass of both fluids is essential.

The level-set method possesses all the above qualities except (8). In the implementation of the level-set method, only one single fixed-grid is required. The level-set equation governing the evolution of the interface is a hyperbolic equation. Numerical schemes for hyperbolic conservation laws are abundant (e.g. Leveque, 2002) and applicable. No explicit reconstruction of the interface is required during the solution process. The level-set function can be used to calculate interfacial geometrical quantities, e.g. curvature, accurately and elegantly. The evolution of the interface is captured implicitly, therefore, no additional work is required in the event of topological changes. Extension of the level-set method from two to three dimensions is straight forward with no additional new numerical formulation involved. As mentioned earlier, the level-set method does not conserve mass of the fluids well. Various mass conservation schemes have been proposed to overcome it and achieve considerable success. As the level-set

method meets almost all the above preferences, it is the preferred F-F interface prediction procedure in the present study.

F-S interface can be predicted using two methods classified according to the grid employed. These are the moving-grid and the fixed-grid methods. Fixed-grid methods include but are not limited to fictitious domain method, fictitious boundary method and immersed boundary method. For the present study, a desired F-S interface prediction procedure should have the following qualities:

(1) The F-S interface prediction procedure is easy to be coupled with a selected F-F interface prediction procedure.

(2) The procedure is implemented on a fixed-grid, and preferably a structured grid/mesh.

(3) Only one single grid system is required.

(4) Rigidity of the solids needs to be well enforced.

(5) The ability to handle multiple solids even of complicated geometries.

(6) Both slip and no-slip boundary conditions are enforceable at the solids surface.

(7) Extension to three dimensions is straight forward

In the moving-grid method, both remeshing and remapping the information from the old grid onto the new grid are computational expensive. Two grid systems are employed in immersed boundary method. Transfer of information between the two grid systems to couple the fluid motion to that of the solid is required. Besides, the volume of the solid is not well conserved. For the level-set method, the solid loses mass over time and the F-S interface is subjected to unphysical deformation due to numerical diffusion.

In the fictitious domain method, the implicit coupling of the fluid and solid momentum equations requires the solution of a larger system of the linear and nonlinear algebraic

equations for the coupled variables of fluid and solids. Since the F-S interface prediction procedure is to be coupled eventually with the F-F interface prediction procedure in this study, employing a fictitious domain approach would increase the computational requirement significantly.

Unlike fictitious domain method, the coupling of the fluid and solid momentum equations is explicit in the fictitious boundary method. The hydrodynamic force and torque are calculated to explicitly track the solid motion. This avoids solving a large system of algebraic equations. Most of the works were implemented in the context of finite element method except that of Duchanoy and Jongen (2003). The work of Duchanoy and Jongen (2003) is attractive as it is implemented with a finite volume method. It however suffers from a few drawbacks. These will be discussed in details in Chapter 2. A new F-S interface tracking procedure meeting the above preferences for a F-S interface prediction procedure and with the drawbacks of Duchanoy and Jongen (2003) overcome is preferred in the present study.

The available numerical works on flows with combined F-F and F-S interfaces are limited. This type of flow involves two moving interfaces, and is therefore more difficult to solve.

1.4 Objective and Scope

Given the small length and time scales involved in micro-scale multiphase flows, numerical modeling plays an important role in the understanding of the physics in these processes. The present study does not aim to delve deeply into the rich physics involved in these processes but rather to provide a means to facilitate the investigation of such

phenomena. The objective of the present work is to devise and implement numerical procedures for the prediction of micro-scale multiphase flows. With this, it is hope that the prediction procedures developed in the present study will be used to investigate further the understanding of these multiphase transport processes.

The scope of the thesis includes:

(1) Implement a F-F interface capturing procedure based on the level-set method within the framework of the finite volume method. Surface tension effects, both curvature and Marangoni driven, has to be incorporated. New mass conservation schemes to improve the mass conservation of the F-F interface capturing procedure are targeted. As higher order scheme is employed for the evolution of the level-set function, a method is required to stabilize the evolution of the level-set function in the event of numerical instability for flow in complex geometries.

(2) Devise a new fixed-grid F-S tracking procedure implementable within the framework of the finite volume method. An accurate representation of the F-S interface with the rigidity of the solids strictly enforced is targeted. The procedure should be able to handle multiple solids, even of non-regular geometries, with ease. Both the implementations of slip and no-slip boundary conditions on the F-F interface are required.

(3) Develop a three-phase flow model by combining both F-F interface capturing and F-S interface tracking procedures. The three phases are two fluids and a solid phase. Two-fluid and fluid-solid flows are two limiting cases of the three-phase flow model with either of the interface prediction procedure switched off.

(4) Validate and demonstrate the applications of the above interface handling procedures for two-dimensional multiphase flows.

1.5 Contributions

The F-F interface capturing procedure is based on the level-set method. A weakness of the level-set method is its weak mass conservation. To overcome this, two mass conservation schemes are proposed:

(1) A global mass correction (GMC) scheme (Yap et al., 2006c) is presented for general two-fluid flow problems. With GMC, good mass conservation is demonstrated for droplet flows in various channels. GMC is extended to the situation where a third solid phase is present.

(2) A local mass correction (LMC) scheme (Yap et al., 2005) is developed for stratified two-fluid flows to ensure mass conservation. LMC has been employed successfully for stratified two-fluid flow with surface tension (Yap et al., 2006b) or phase-change (Yap et al., 2005) and annular flow in both circular channel (Yap et al., 2004) and three-dimensional square channel (Yap et al., 2006a).

For flow in complex geometries, artificial viscosity is introduced in the level-set advection equation. Artificial viscosity is either added to region beyond the interface or specific regions deemed susceptible to numerical disturbances. It is demonstrated that the added artificial viscosity damps away any numerical disturbance and improves the numerical stability tremendously.

A new F-S interface tracking procedure has been proposed (Yap et al., 2006d). It is a fixed-grid approach. The procedure is demonstrated for flows of multiple complex

shaped solids. The F-F interface tracking procedure is extended to the case where there is a slip velocity at the solid surfaces as in the modeling of electrophoresis of particles. The F-S interface tracking procedure has been employed in tracking the movement of cell with negligible deformation in a microchannel (Yap et al., 2006e).

The F-S interface tracking procedure is compatible with the level-set based F-F interface capturing procedure. A new three-phase flow model is developed by combining the F-F interface capturing and the F-S interface tracking procedures. It is employed in modeling the motions of particle-encapsulated droplets in different microchannels. Although the F-F interface capturing and the F-S interface tracking procedures are demonstrated for two-dimensional situations, extension of these procedures to three-dimensional is straight forward.

With the present model, new numerical results are obtained for droplet flow in a micro T-junction with thermocapillary effect, stratified two-fluid flows in straight channel and in a double bend, electrophoretic flow of particles and particle-encapsulated droplets flow in different microchannels. An analytical solution for Marangoni force driven stratified two-fluid flow is derived.

1.6 Outline of the Thesis

There are five chapters in this thesis. In Chapter 1, a brief review of micro-scale multiphase flows is presented. This is followed by a review of the existing numerical techniques in handling F-F interface and F-S interface. The review includes the situations where these techniques are combined when both interfaces coexist together. The mathematical formulation for a three phase flow problem is given in Chapter 2. The

F-F interface capturing and a new F-S interface tracking procedures are presented. This is followed by the conservation equations together with the relevant boundary conditions. This chapter ends with an outline of the solution algorithm. Numerical solution procedure of the governing equations within the framework of the finite volume method is presented in Chapter 3. In Chapter 4, the interface prediction procedures are validated. Various applications of the interface prediction procedures are demonstrated. Finally, the present work is concluded in Chapter 5 with future research direction suggested.

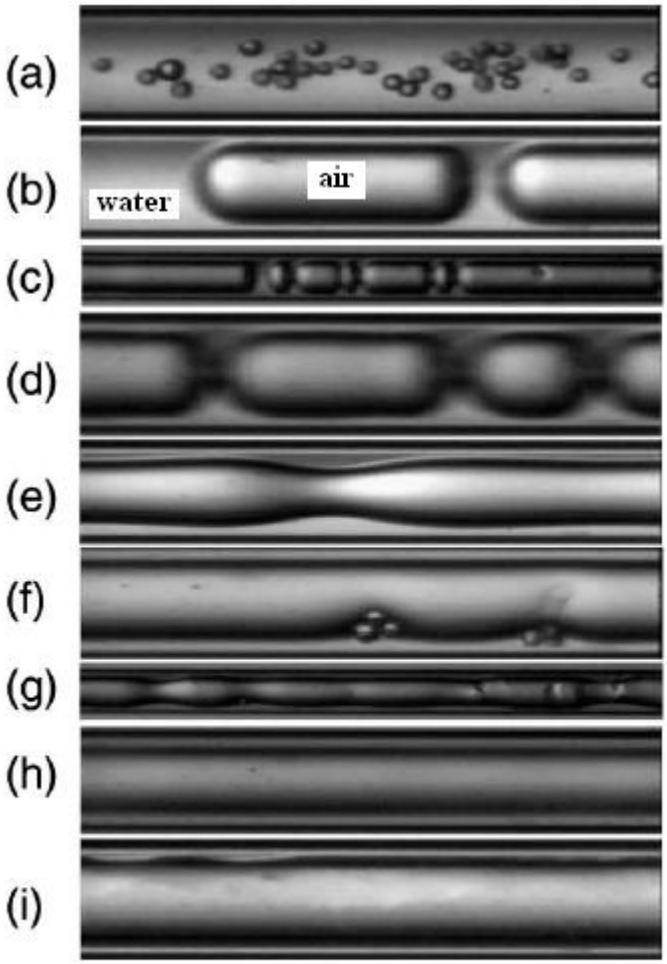

(a) Bubbly Flow (b) Slug Flow
(c) Transition (d) Skewed Flow (Yakitori Flow)
(e) Liquid Ring Flow (f) Frothy Annular Flow
(g) Transition (h) Annular Flow
(i) Rivulet Flow

Figure 1-1: Air-water two-phase flow with air forming droplets or the inner core in a 100μm tube (Serizawa et al, 2002).

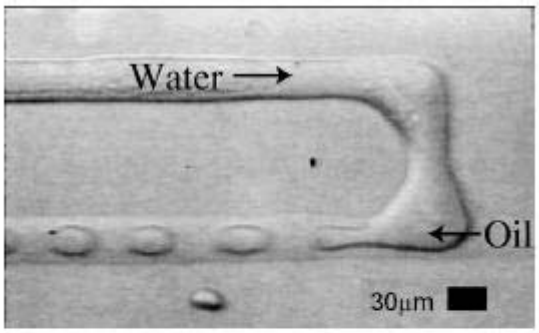

(a) Thorsen et al. (2001)

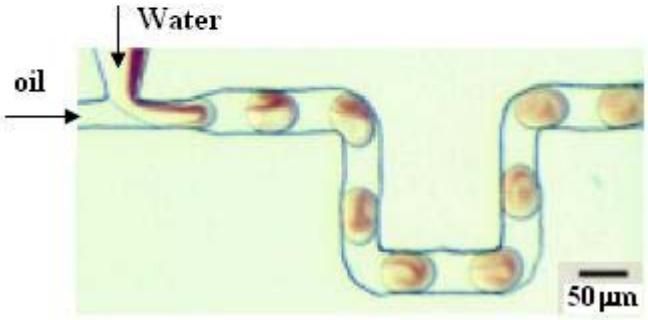

(b) Song et al. (2003)

Figure 1-2: Droplet generation and flow in microchannel.

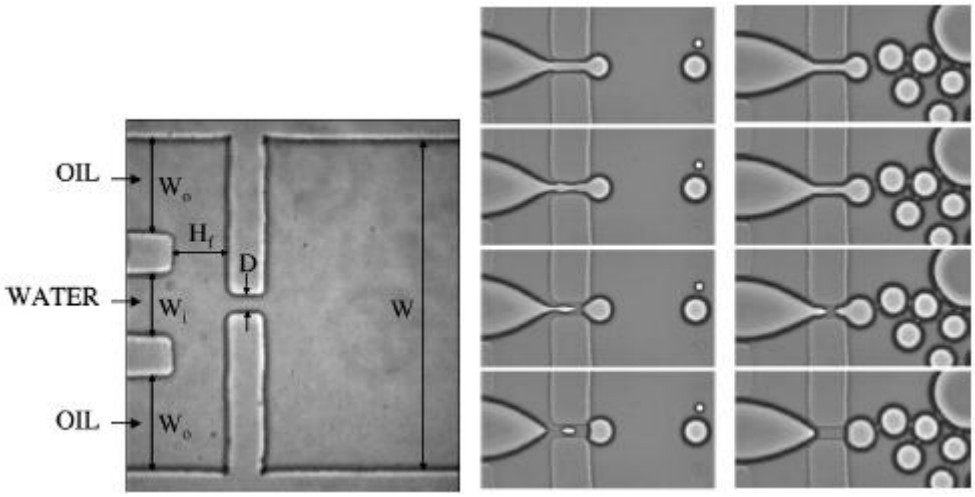

Figure 1-3: Droplet formation suing “flow focusing” in a cross-junction (Anna et al., 2003)

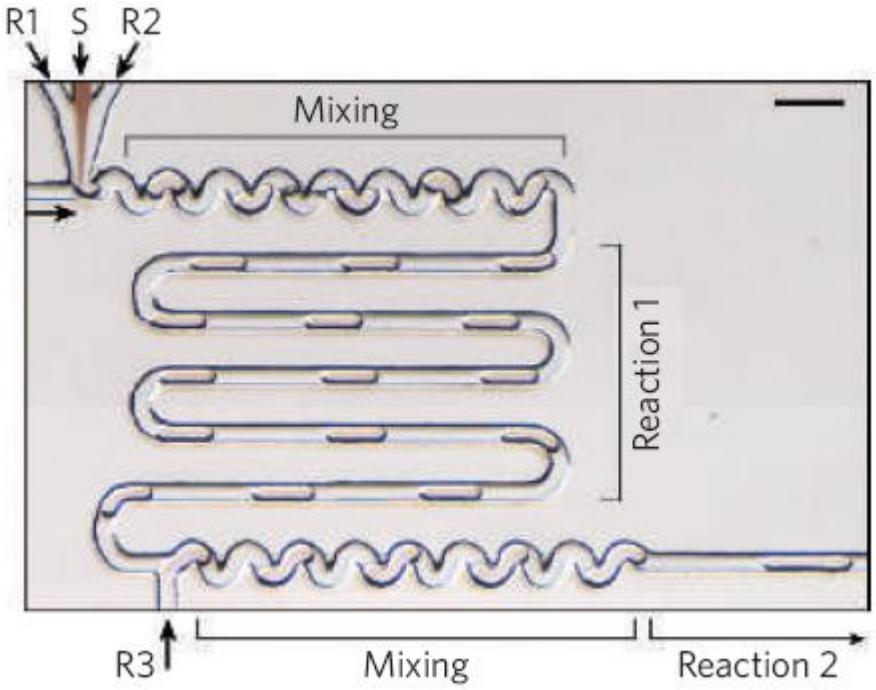

Figure 1-4: Enhanced mixing within droplet via serpentine microchannels (Shestopalov et al., 2004, with the Reaction 1 section shortened).

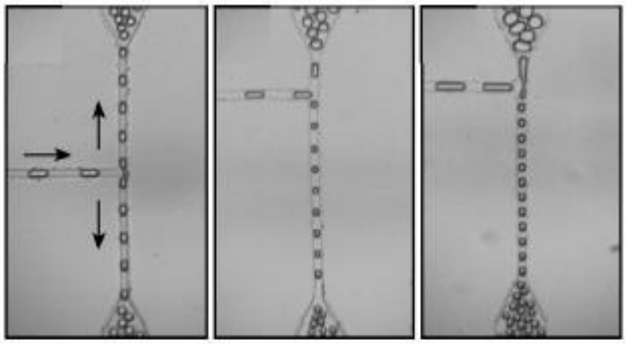

(a) Droplet splitting in different T-junction.

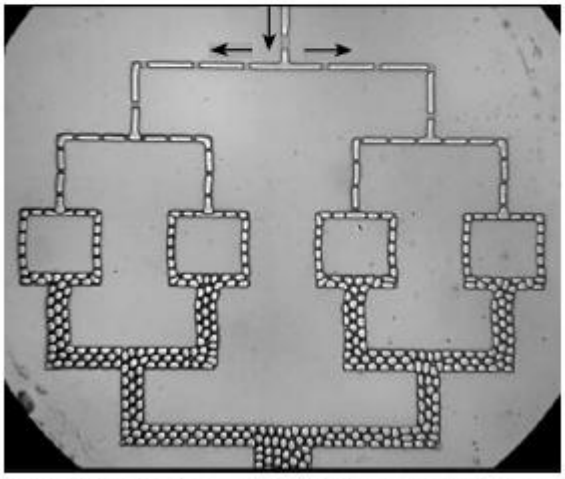

(b) Droplet splitting in a series of T-junctions.

Figure 1-5: Splitting of droplets using T-junction (Link et al., 2004).

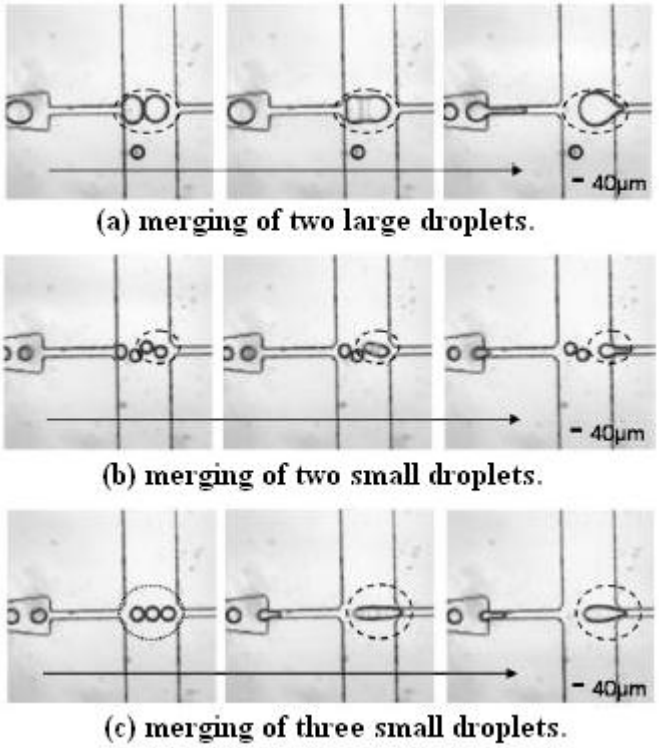

Figure 1-6: Merging of droplets (Tan et al., 2004).

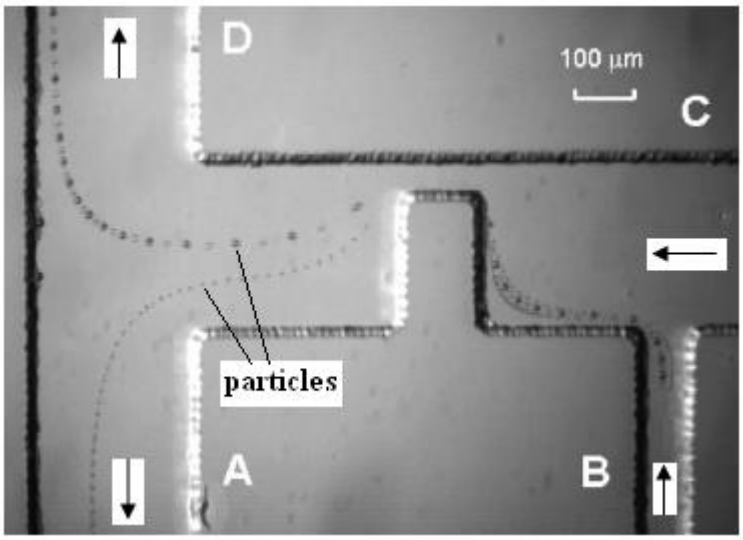

Figure 1-7: Particle separation under applied electric field (Kang et al., 2006).

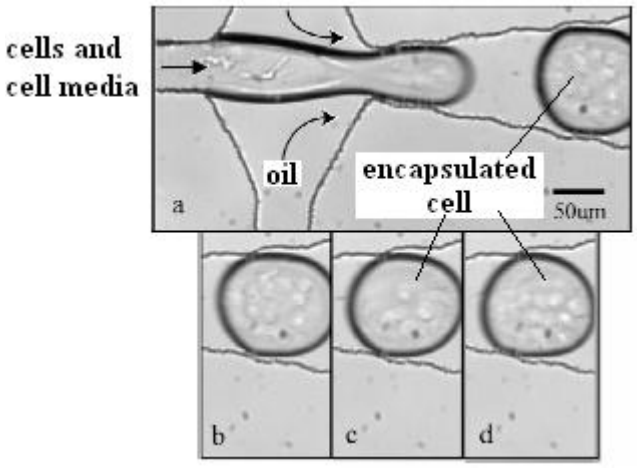

Figure 1-8: Cell encapsulated in a droplet (Fisher and Lee, 2004).

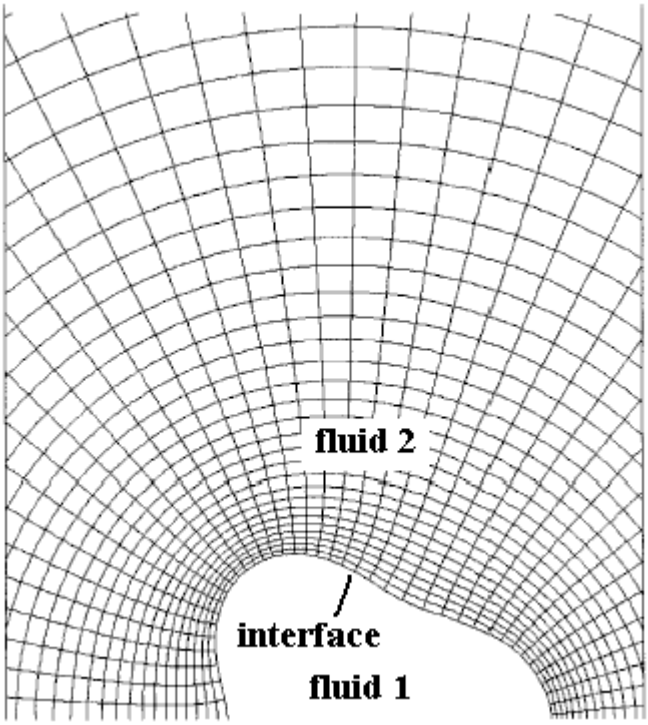

Figure 1-9: A deforming curvilinear coordinate system (Magnaudet et al., 1995).

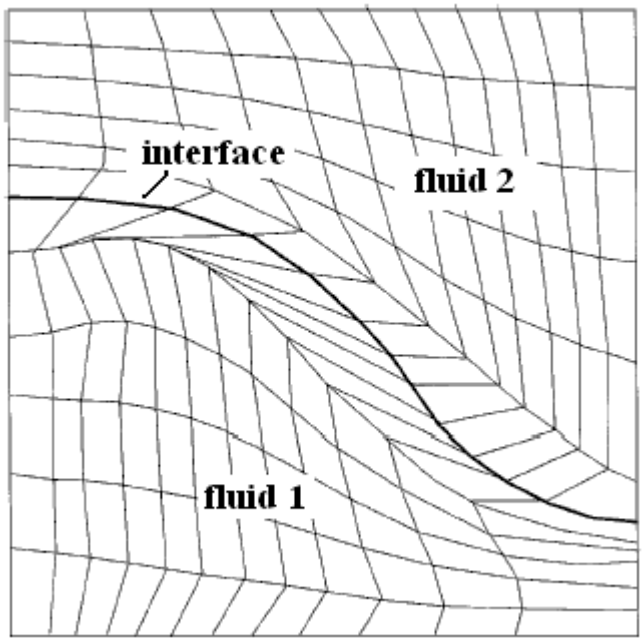

Figure 1-10: A freely deformed mesh in the moving-mesh approach (McHyman, 1984).

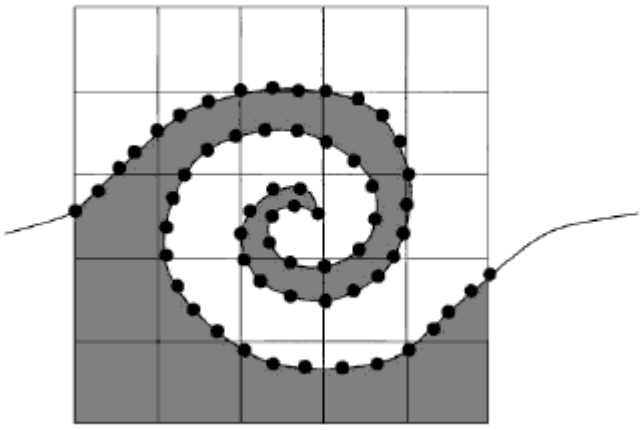

Figure 1-11: Markers seeded at the interface (Scardovelli and Zaleski, 1999).

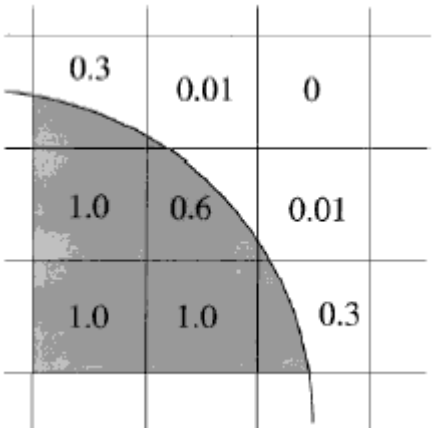

Figure 1-12: Volume fraction function for computational cells (Scardovelli and Zaleski, 1999).

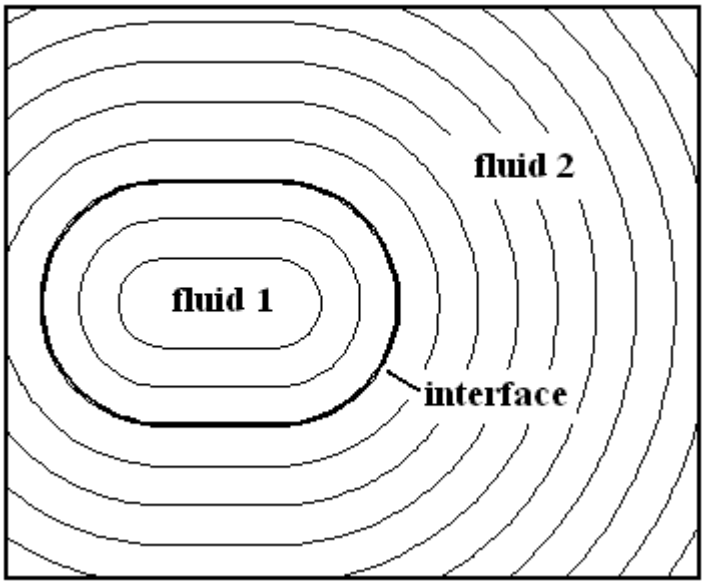

Figure 1-13: Contours of constant level-set function.

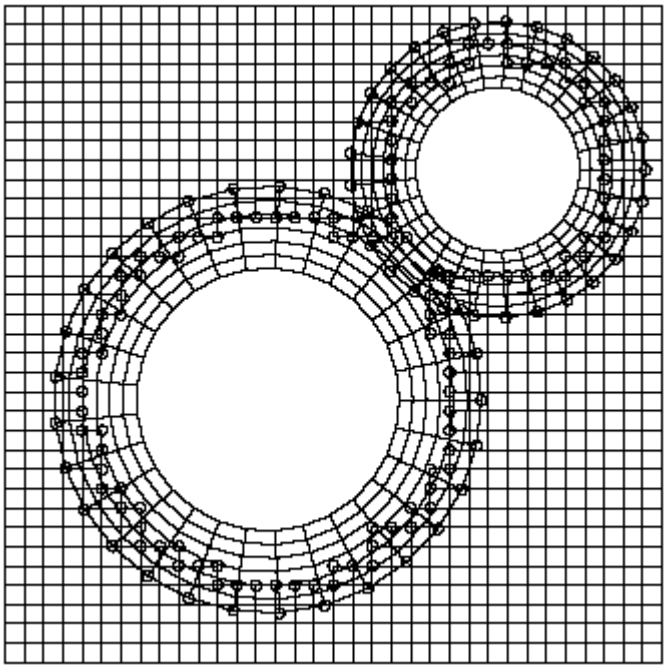

Figure 1-14. A typical chimera grid (Petersson, 1999).

CHAPTER 2

MATHEMATICAL FORMULATION

In this chapter, the mathematical formulation for a three phase flow problem is presented. The chapter begins with a description of the three phase flow problem involving 2 fluids and a solid phase. Essential to the physics of the flow are two interfaces, i.e. fluid-fluid and fluid-solid interfaces. The capturing of the fluid-fluid interface and the tracking of the fluid-solid interface are discussed next. With these interfaces capturing or tracking procedures, a set of combined conservation equations can then be written for the physical domain consists of the three phases. The formulation ends with the details of the overall solution algorithm. Finally, a few concluding remarks are given.

2.1 Problem Description

Figure 2-1 shows a physical domain with three different phases. The word "phase" is used for either fluid or solid. There are two fluids: fluid 1 and fluid 2 occupying regions Ω_1 and Ω_2 respectively. $\Omega_F = \Omega_1 \cup \Omega_2$ is the fluid region. Both fluids are immiscible in each other. Γ_F is the interface between the two fluids. This interface will henceforth be referred to as the fluid-fluid (F-F) interface. The hatched regions (Ω_S) within fluid 1 represent solids, i.e. the third phase. The case where these solids are fully immersed in fluid 1 is of interest in the present study. Therefore, there is no physical contact between the solids and fluid 2. Under such condition, the interface between fluid 1 and the solids, Γ_S, can be safely referred to as the fluid-solid (F-S) interface without any ambiguity.

When driven by pressure difference, gravitational force, electrical force or a combination of them, all the phases are set in motion. To fluid 2, the F-F interface is the only moving boundary. However, to fluid 1, both the F-F and the F-S interfaces are moving boundaries. The motions of fluid 1 and the solids generate entirely new F-F and F-S boundaries for the flow field. Consequently, the flow field changes. This in turn affects the motions of fluid 1, fluid 2 and the solids. Therefore, this is a complex transient process with the motion of the three phases strongly coupled together.

To capture the motion of all phases involved, the F-F and F-S interfaces have to be tracked precisely for all time. These are presented in the following sections.

2.2 F-F Interface Capturing – The Level-Set Method

The level-set method of Osher and Sethian (1988) is employed to capture the F-F interface. The F-F interface, i.e. the solid curved in Fig. 2-2, separates fluid 2 from the remaining phases (fluid 1 and the solids). The level-set function ξ is defined as the signed distance function from the F-F interface. Obviously, the value of ξ at the F-F interface is zero, i.e. $\Gamma_F = \{\vec{x} \mid \xi(\vec{x}) = 0\}$. The dashed curves are curves of constant ξ. Any convenient sign for ξ can be assigned to fluid 2 as long as the remaining phases (fluid 1 and the solids) have the opposite sign. In the present study, the value of ξ for fluid 2 is assigned positive. ξ can be expressed mathematically as

$$\xi(\vec{x},t) = \begin{cases} < 0, & \vec{x} \in \text{fluid 1 or solids} \\ = 0, & \vec{x} \in \text{F - F interface} \\ > 0, & \vec{x} \in \text{fluid 2} \end{cases} \tag{2-1}$$

The evolution of the level-set function ξ is governed by

$$\frac{\partial \xi}{\partial t} + \vec{u} \bullet \nabla \xi = 0 \tag{2-2}$$

2.2.1 Artificial Viscosity

Solid blockages in the solution domain can be modeled using the "blocked-off-region" approach of Patankar (1980). This approach offers great versatility in creating different flow geometries of interest. In the evolution of the F-F interface via Eq. (2-2), the solution is susceptible to numerical fluctuations in region near or in the solid blockages. These fluctuations grow and eventually lead to the blow-up of the solution.

Adding artificial viscosity helps to mitigate numerical fluctuations. However, any artificial viscosity added near or at the F-F interface inevitably modifies the evolution of the F-F interface. This is highly undesirable. Rather than adding artificial viscosity throughout the whole domain, artificial viscosity is added to Eq. (2-2) away from the F-F interface. To achieve this, Eq. (2-2) is modified as

$$\frac{\partial \xi}{\partial t} + \vec{u} \bullet \nabla \xi = K \tag{2-3a}$$

where

$$K = \begin{cases} 0 \quad , & |\xi| < n\varepsilon \\ \lambda \nabla^2 \xi , & |\xi| \geq n\varepsilon \end{cases} \tag{2-3b}$$

n and ε are a factor and a factor of the control volume size respectively. Notice that K only acts in the region of $|\xi| > n\varepsilon$. Any fluctuation arises in the region of $|\xi| > n\varepsilon$ during the solution of Eq. (2-2) will be damped and therefore improve numerical stability. Artificial viscosity is normally turned off unless specified otherwise.

2.2.2 Redistancing

Since the level-set function is a distance function, it satisfies

$$|\nabla \xi| = 1 \tag{2-4}$$

Preserving this property is essential for precise interface tracking (improvement in mass/volume conservation), good estimation of geometric quantities (e.g. unit normal vector and curvature), accurate calculation of interfacial effects (e.g. phase change or surface tension effects) and above all enhanced numerical stability. At $t = 0$, ξ can be initialized properly as a distance function with the knowledge of the initial F-F interface. However, Eq. (2-3) does not ensure ξ to remain as a distance function, i.e. $|\nabla \xi| \neq 1$, for all time. As iteration proceeds for the consequent time steps, ξ will generally drift away from the initialized value of signed distance. To overcome this, another function, $\psi(\vec{x}, \bar{t})$, which is a distance function and possesses the same interface as ξ is solved for. This new distance function ψ is the "steady-state" solution of Eq. (2-5) (Sussman et. al., 1994).

$$\frac{\partial \psi}{\partial \bar{t}} = \overline{sign}(\xi)(1 - |\nabla \psi|) \tag{2-5a}$$

where $\bar{t}$ is a pseudo time for ψ. In Eq. (2-5a), $\overline{sign}(\xi)$ is a modified sign function given by (Peng et. al., 1999)

$$\overline{sign}(\xi) = \frac{\xi}{\sqrt{\xi^2 + |\nabla \xi|^2 (\Delta^2)}} \tag{2-5b}$$

where Δ is the smallest control volume size. Equation (2-5) is subjected to the following initial condition.

$$\psi(\vec{x}, 0) = \xi(\vec{x}) \tag{2-5c}$$

Obviously, the "steady-state" solution of Eq. (2-5) has the property of $|\nabla \psi| = 1$, that is a distance function. The initial condition of Eq. (2-5c) ensures ψ is zero at the same

spatial location, and thus, possesses the same interface. The level-set function $\xi(\vec{x})$ can then be replaced by the "steady-state" of ψ.

2.2.3 Mass Correction

While Eq. (2-5) reinitializes ξ as a distance function, it does not ensure mass conservation for either fluids. This drawback can be overcome by introducing mass correction schemes. A mass correction scheme selects one of the fluids as the reference fluid and conserves mass for the reference fluid. This in turns conserves mass for the other fluid automatically. Two different mass correction schemes are presented: (1) Global Mass Correction (GMC) Scheme (Yap et. al., 2006c) and (2) Local Mass Correction (LMC) Scheme (Yap et. al., 2005). While GMC is suitable for most general applications, LMC is specifically tailored for stratified flow.

2.2.3.1 Global Mass Correction (GMC) Scheme

For a general type of flow, Global Mass Correction (GMC) Scheme is employed. If there is no physical process that alters the mass of the fluids, e.g. phase change, injection and removal of fluids, the mass of either fluid remains constant. The presence of solids presents no additional complication. The volume occupied by the solids is fixed. In GMC, this volume is assumed to be filled with fluid 1.

Figure 2-3 shows the two possible situations where global mass correction is needed. The dashed lines represent the current F-F interface (with mass imbalance). The solid lines are the correct F-F interface where mass of the reference fluid is conserved. Figure 2-3a shows a situation where there is mass loss during the solution process. Mass must

be added to ensure conservation of mass for the reference fluid. The reverse is shown in Fig. 2-3b. Mass must be removed to ensure that the mass of the reference fluid is conserved. In both cases, the mass correction term must shift the F-F interface from the dotted line to the solid line.

Either fluid can be chosen as the reference fluid. For the purpose of discussion and without loss of generality, fluid 1 is taken to be the reference fluid. In Fig. 2-3a, due to the addition of mass of the reference fluid, the values of the distance function (for the whole solution domain) are smaller after mass correction. The values of the distance function (again for the whole solution domain) increase when mass is removed to ensure the conservation of the mass for the reference fluid (Fig. 2-3b.)

To achieve this, the "steady-state" solution to a third distance function ψ' is obtained from Eq. (2-6).

$$\frac{\partial \psi'}{\partial t'} = M_{cor} \tag{2-6a}$$

where t' and M_{cor} are a pseudo-time which can be different from $\bar{t}$ and a dimensionless mass correction factor respectively. The "steady-state" values of the second distance function ψ are used as the "initial" condition for Eq. (2-6). The dimensionless mass correction factor is given by

$$M_{cor} = sign\left(\xi_{ref}\right)\frac{M_d - M_c}{M_d} \tag{2-6b}$$

where M_d and M_c are the desired mass and the most current mass of the reference fluid respectively. In this case the desired mass is the original mass of the reference fluid. It increases when there is injection of reference fluid but decreases when there is removal of the reference fluid. When mass of the reference fluid is conserved, $M_c = M_d$ and thus $M_{cor} = 0$. Since the reference fluid is a matter of choice, if fluid 2

is chosen instead, the sign of the reference fluid is positive. The sign function $sign(\xi_{ref})$ gives an appropriate sign for M_{cor} in this situation. The level-set function $\xi(\vec{x})$ can then be replaced by the "steady-state" ψ'.

A smoothed heaviside function is introduced to facilitate the calculation of the fluid properties (density in this case). It is given by (Chang et al.,1996)

$$H(\xi)=\begin{cases}0, & \xi<-\varepsilon \\ \dfrac{\xi+\varepsilon}{2\varepsilon}+\dfrac{1}{2\pi}\sin\left(\dfrac{\pi\xi}{\varepsilon}\right), & |\xi|\le\varepsilon \\ 1, & \xi>\varepsilon\end{cases} \tag{2-7}$$

The Heaviside function is smoothed over a finite thickness of 2ε. The parameter ε is related to the grid size and is usually taken as a factor of the grid spacing. In this study ε is set to one and a half control volume thickness. With $H(\xi)$ defined, the mass of the reference fluid can be calculated using

$$M=\begin{cases}\sum \rho_{ref}(1-H)\Delta V & \text{if fluid 1 is the reference fluid} \\ \sum \rho_{ref} H\Delta V & \text{if fluid 2 is the reference fluid}\end{cases} \tag{2-8}$$

The summation is performed over the whole solution domain. The original mass of the reference fluid is calculated using the initial condition. The presented mass correction given by Eq. (2-6), (1) reduces M_{cor} to zero once mass is conserved, (2) modifies the distance functions (by a constant) for the whole domain and (3) can be applied to situations where the densities of the two fluids are different. For condition (2), the present procedure corrects the distance function by adding a uniform correction factor globally as the name implied.

2.2.3.1.1 Remarks on GMC Scheme

In GMC, any mass loss/gain within a given time step Δt is corrected by distributing this amount of mass imbalance (loss/gain) uniformly over the F-F interface. For the subsequent time step, the F-F interface deforms forming a new F-F interface. GMC is again implemented with mass imbalance added uniformly to the new F-F interface. Even though the F-F interface is corrected uniformly within each time step, the total correction on the F-F interface is not uniform over the two consecutive time steps. This is due to the fact that the correction is performed on the F-F interface of two different shapes. Therefore, GMC corrects the F-F interface uniformly within each time step but non-uniformly over time.

Mass/area preserving re-initialization has been proposed by Chang et al. (1996) to preserve mass during the evolution of the level-set function. Chang et al. (1996) chooses to conserve the total mass for both fluids. The level-set function is corrected by a normal motion proportional to its local curvature and the total mass imbalance. The correction procedure had to be stabilized by adding a certain constant. The mass for each independent fluid is not guaranteed conserved. In a number of two-fluid flows, one of the fluids is of more interest than the other. For example, the droplet fluid in the flow of a droplet carrier by another immiscible carrier fluid in channels. Thus, the conservation for the mass of the droplet is more critical. In such a situation, the present global mass correction procedure chooses the droplet fluid as the reference fluid and has its mass conserved.

In the implementation of the correction procedure of Chang et al. (1996), the mass of the reference fluid, the magnitude of the gradient of the level-set function and curvature are

computed. However, only the mass of the reference fluid is required for the present global mass correction procedure.

Unlike the global volume/area correction technique of Lakehal et al. (2001) which ensures global volume/area conservation, the present global mass correction procedure chooses mass as the conserved variable rather than volume/area. The present global mass correction procedure offers the below advantages:

(1) GMC can be applied to the situation where the density of the reference fluid is not uniform as it is not volume/area conservation but mass conservation that is ensured.

(2) For flow with large density ratio, a slight imbalance in volume may suggest a large imbalance in mass. Therefore, it is better to conserve mass directly instead of volume/area.

In the implementation of the global volume/area correction technique of Lakehal et al. (2001), the volume/area of the reference fluid and the F-F interface surface/length are required. For the F-F interface length in two-dimensional flow, they resort to calculating computational cells in the interface region. The calculation of the surface area of the F-F interface in three-dimensional flows, although not mentioned by Lakehal et al. (2001), would require more computational efforts. No calculation of the F-F interface surface/length is required for the present global mass correction procedure.

The global volume/area correction technique is implemented through an iterative algorithm. However, in the present study, the correction procedure is performed via a pseudo-time marching technique. The same numerical procedure used in the redistancing of the level-set function can be used. Mass is well conserved in around 10 pseudo-time steps. No new numerical procedure is required.

Sussman and Fatemi (1999) added a constraint in the redistancing equation of the level-set function. Such constraint prevents any volume loss/gain of the domain bounded by the zero-level set *during* the redistancing procedure. It *does not* correct the mass loss/gain during the advection of the level-set function via the level-set equation. In the present study, such a constraint is not added in the redistancing procedure as even if there is mass loss/gain of the reference fluid during redistancing, it is corrected in the subsequent global mass correction procedure.

2.2.3.2 Local Mass Correction (LMC) Scheme

Local Mass Correction (LMC) Scheme is specifically designed for stratified flow. Figure 2.4 shows a schematic of a stratified flow in a channel. There are two stratified layers of fluid. The lower layer is fluid 2. Fluid 1 and the solids constitute the upper layer. In LMC, the volume occupied by the solids is again assumed to be filled with fluid 1. Rather than based on the mass of the reference fluid as in GMC, LMC uses the mass flowrate of the reference fluid in achieving mass conservation. The underlying idea of LMC is that the mass flowrate of either layer at every streamwise location remains constant.

In the case where solid is absent, either fluids can be selected as the reference fluid. However if solids are present, since the velocity field in the solids is set to zero (this will be presented and discussed in a Section 2.4.4), fluid 2 is chosen to be the reference fluid. This avoids complication in calculating the mass flowrate of a reference fluid with immersed solids. Without the lost of generality, fluid 2 is chosen as the reference fluid in the following discussion.

To illustrate the idea of LMC, a section of the channel with a small length of Δ (contained within the dashed rectangle) is selected. An enlarged schematic of it is depicted in Fig. 2-5. The reference fluid flows in at the section inlet and leaving at the section outlet. The dashed line is the most current F-F interface. It gives a mass flowrate of the reference fluid at the section outlet of $\dot{M}_c$ which generally different from the mass flowrate of the reference fluid into the section. There exists an imbalance of mass for the reference fluid. The correct mass flowrate of the reference fluid at the section outlet should be $\dot{M}_d$. In Fig. 2-5a, $\dot{M}_c$ is smaller than $\dot{M}_d$. Therefore, the F-F interface at the outlet should be adjusted upward to increase the mass flowrate of the reference fluid at the section outlet. Figure 2-5b shows the reverse. $\dot{M}_c$ is larger than $\dot{M}_d$ so that the F-F interface needs to be adjusted downward. In both cases, the current F-F interface (dashed lines) needs to be adjusted to the correct F-F interface (solid lines) so that mass flowrate of the reference fluid is conserved. If there is no injection, removal or phase change of the reference fluid along the channel, the desired mass flowrate $\dot{M}_d$ is the mass flowrate of the reference fluid $\dot{M}_{in}$ at the channel inlet (Fig.2-4).

To perform LMC, the "steady-state" solution to a third distance function ψ' is obtained from Eq. (2-9).

$$\frac{\partial \psi'}{\partial t'} = \dot{M}_{cor} \tag{2-9a}$$

where $\dot{M}_{cor}$ is the dimensionless mass correction factor given by

$$\dot{M}_{cor} = sign\left(\xi_{ref}\right)\frac{\dot{M}_d - \dot{M}_c}{\dot{M}_d} \tag{2-9b}$$

Since the reference fluid is a matter of choice, if fluid 1 is chosen instead, the sign of the

reference fluid is negative. The sign function $sign(\xi_{ref})$ gives an appropriate sign for $\dot{M}_{cor}$ in this situation. $\dot{M}_c$ varies with the streamwise location, so does $\dot{M}_{cor}$. The "steady-state" values of the second distance function ψ are used as the "initial" condition for Eq. (2-9). The level-set function $\xi(\vec{x})$ can then be replaced by the "steady-state" ψ'.

The mass flowrate of the reference fluid can be conveniently calculated using

$$\dot{M} = \begin{cases} \sum \rho_{ref}(1-H)u_s \Delta A & \text{if fluid 1 is the reference phase} \\ \sum \rho_{ref} H u_s \Delta A & \text{if fluid 2 is the reference phase} \end{cases} \quad (2\text{-}10)$$

where u_s and ΔA are the streamwise velocity component and the elemental cross-sectional area of the channel (perpendicular to the streamwise direction) respectively.

2.2.4 Algorithm for F-F Interface Capturing

The algorithm to evolve the F-F interface from $\xi(t)$ to $\xi(t+\Delta t)$ for a known velocity field $\vec{u}(t+\Delta t)$ can be summarized as:

1. Solve for $\xi(t+\Delta t)$ (Eq. 2-3) using the available $\vec{u}(t+\Delta t)$.
2. Solve for the "steady-state" ψ (Eq. 2-5) using the values of $\xi(t+\Delta t)$ from Step 1 as the initial values.
3. Solve for the "steady-state" ψ' (Eq. 2-6 for GMC or Eq. 2-9 for LMC) using the values of ψ from Step 5 as the "initial" values.
4. Set $\xi(\vec{x}, t+\Delta t) = \psi'(\vec{x})$.

At the end of the first "steady-state" solution (Step 2), ψ is a distance function.

However, mass might not be conserved. The "steady-state" solution at the end of Step 3 ensures that ψ' is a distance function and also conserves mass.

2.3 F-S Interface Tracking

In Fig. 2-1, there are N solids interact with fluids 1 and 2 in the domain. The solids are assumed rigid and sufficiently large that momentum is exchanged between the solids and the flowing fluid. As a result, the solids affects the fluid motion significantly and vice-versa. The solids undergo different translational and rotational motions under the influence of the flow field.

2.3.1 The Local and Global Distance Functions

The motions of the solids are tracked separately. Therefore, each solid needs to be identified. For this purpose, a local signed distance function ϕ_i is introduced to identify the F-S interface for the *i*-th solid. It is defined as the shortest signed normal distance from the F-S interface of that particular solid. Curves of constant ϕ_i around the *i*-th solid are shown as dashed lines in Fig. 2-6. The solid line represents the F-S interface $\Gamma_{Si} = \{\vec{x} \mid \phi_i(\vec{x}) = 0\}$ for that particular solid.

In order to differentiate the *i*-th solid region Ω_{Si} from the rest of the domain (constituted by fluid 1 and 2 and other solids), ϕ_i of the *i*-th solid region can either be assigned a positive or a negative sign as long as ϕ_i of the rest of the domain has an opposite sign. For the ease of discussion and without the lost of generality, ϕ_i of the *i*-th solid region is assigned a negative sign. Therefore,

$$\phi_i(\vec{x},t)=\begin{cases}<0, & \text{if } \vec{x}\in \text{the i - th solid}\\ =0, & \text{if } \vec{x}\in\Gamma_{Si}\\ >0, & \text{if } \vec{x}\in \text{fluid 1 or 2 or other solids}\end{cases} \tag{2-11}$$

where $\vec{x}$ and t are the position vector and time respectively. This sign convention is adopted in the construction of local distance function for all other solids. With this choice of sign convention, the unit outward normal to the F-S interface for the *i*-th solid can be expressed as

$$\hat{N}_{Si}=\nabla\phi_i \tag{2-12}$$

Since ϕ_i is a distance function, it satisfies $|\nabla\phi_i|=1$.

A global signed distance function ϕ can then be constructed by combining all the local distance functions to represents the F-S interfaces for all solid bodies. Again, ϕ for the solid region given by $\Omega_S=\bigcup_{i=1}^{N}(\Omega_{Si})$ is assigned negative. With this,

$$\phi(\vec{x},t)=\begin{cases}<0, & \text{if } \vec{x}\in \text{solids}\\ =0, & \text{if } \vec{x}\in\Gamma_S\\ >0, & \text{if } \vec{x}\in \text{fluid 1 or 2}\end{cases} \tag{2-13}$$

The construction of both local and global signed distance functions will be detailed next.

2.3.2 Construction of the Local and Global Distance Functions

The construction of ϕ_i for the two-dimensional situations is demonstrated. Extension to three-dimensional is straight forward. Figure 2-7 shows an inclined elliptical solid with its center of mass located at $\vec{x}_{c,i}$. It has a major axis of $2a$ and a minor axis of $2b$. The elliptical solid is inclined at an angle θ_i to the x-axis. Surfaces of constant ϕ_i are shown as dashed ellipses. Each of these constant ϕ_i ellipse is of equal distance

from the interface Γ_{Si}. To calculate ϕ_i, a new Cartesian coordinate $Ox'y'$ is introduced. This coordinate is related to the original coordinate Oxy via

$$\begin{pmatrix} x' \\ y' \end{pmatrix} = \begin{pmatrix} \cos\theta_i & \sin\theta_i \\ -\sin\theta_i & \cos\theta_i \end{pmatrix} \begin{pmatrix} x \\ y \end{pmatrix} \tag{2-14}$$

The constant ϕ_i ellipses are given by

$$\frac{(x'-x'_c)^2}{(a+\phi_i)^2} + \frac{(y'-y'_c)^2}{(b+\phi_i)^2} = 1 \tag{2-15}$$

where $\vec{x}'_{c,i} \equiv (x', y')$ is the center of mass of the solid (mass is uniformly distributed) with respect to the $Ox'y'$ coordinate system. ϕ_i at a given spatial location can be calculated by solving Eq. (2-15). Circular objects can be modeled by setting $a = b$.

The global distance function ϕ is constructed once all the local distance functions are obtained. The procedure for the construction of the global ϕ is:

1. Set the solid index i to 1.

2. Calculate $\vec{x}'_{c,i}$ (with respect to $Ox'y'$) using Eq. (2-14).

3. For a given point P of interest (node of a control volume), calculate $\vec{x}'_{P,i}$ (with respect to $Ox'y'$) corresponding to $\vec{x}_{P,i}$ using Eq. (2-14).

4. Solve Eq. (2-15) for ϕ_i (for the selected control volume P).

5. Repeat steps (3) and (4) for all points.

6. If $i = 1$, set $\phi = \phi_i$.

7. Set $\phi = \text{MIN}[\phi, \phi_i]$.

8. Repeat steps (2) to (7) for all N solids.

2.3.3 Calculation of Resultant Surface Force and Torque on a Solid

The resultant surface force $\vec{F}_i$ acting at the center of mass of the *i*-th solid is given by

$$\vec{F}_i = \int_{\Gamma_{Si}} \overline{\overline{\sigma}} \bullet \hat{N}_{Si}\, dA \tag{2-16}$$

where dA and $\overline{\overline{\sigma}}$ are the infinitesimal interfacial area and the stress tensor respectively. For the ease of implementation, the surface integral is transformed into a volume integral around Γ_{Si}.

To achieve this, a Dirac delta function $D(\phi_i - \varepsilon)$ is defined.

$$D(\phi_i - \varepsilon) = \begin{cases} \left(1 + \cos\left[\pi(\phi_i - \varepsilon)/\varepsilon\right]\right)/(2\varepsilon), & 0 \le \phi_i \le 2\varepsilon \\ 0 \quad , & \text{otherwise} \end{cases} \tag{2-17}$$

where ε is a parameter proportional to the mesh size. It is taken to be the smallest length of the control volumes. The distribution of $D(\phi_i - \varepsilon)$ is shown in Fig. 2-8. $D(\phi_i - \varepsilon)$ has the following property

$$\int_{\phi_i^-}^{\phi_i^+} D(\phi_i - \varepsilon)\, d\phi_i = \begin{cases} 1, & \phi_i^- \le 0 \text{ and } \phi_i^+ \ge 2\varepsilon \\ 0, & \phi_i^- < \phi_i^+ \le 0 \text{ or } 2\varepsilon \le \phi_i^- < \phi_i^+ \end{cases} \tag{2-18}$$

Making use of Eq. (2-18), Eq. (2-16) can be rewritten as

$$\vec{F}_i = \int_{\Delta V} D(\phi_i - \varepsilon) \overline{\overline{\sigma}} \bullet \hat{N}_{Si}\, dV \tag{2-19}$$

where ΔV is the volume sandwiched between the constant $\phi_i = 0$ and $\phi_i = 2\varepsilon$ surfaces (Fig. 2-8). With this, the resultant surface force $\vec{F}_i$ (Eq. 2-16) is reformulated into an equivalent body force (Eq. 2-19). It now acts within a volume defined by $0 \le \phi_i \le 2\varepsilon$, rather than concentrating at the interface Γ_{Si}. The integration is performed over the fluid side of the interface because the force on the *i*-th solid is exerted by the fluid flowing next to the solid.

Similarly, the torque $\vec{T}_i$ acting on the solid is given by

$$\vec{T}_i = \int_{\Delta V} D(\phi_i - \varepsilon)(\vec{x} - \vec{x}_{c,i}) \times \overline{\overline{\sigma}} \bullet \hat{N}_{Si}\, dV \tag{2-20}$$

2.3.4 The Motion of Solids

The translational and rotational motions of the solids are governed respectively by the conservations of linear and angular momentum applied to each solid. These are the Newton-Euler equations.

The translational motion of the *i*-th solid is governed by

$$m_i \frac{d\vec{U}_i}{dt} = \vec{F}_i + \vec{G}_i \tag{2-21a}$$

where $\vec{U}_i$ is the translational velocity vector (of the center of mass) of the *i*-th solid given by

$$\vec{U}_i = \frac{d\vec{x}_{c,i}}{dt} \tag{2-21b}$$

Equation (2-21a) is subjected to the initial condition of

$$\vec{x}_{c,i}(t=0) = \vec{x}_{c,io} \tag{2-21c}$$

In Eq. (2-21), m_i, $\vec{F}_i$ and $\vec{G}_i$ are the mass, the resultant surface and the body forces on the *i*-th solid respectively.

The conservation of angular momentum for the *i*-th solid can be expressed as

$$\overline{\overline{I}}_i \frac{d\vec{\Omega}_i}{dt} + \vec{\Omega}_i \times \overline{\overline{I}}_i \vec{\Omega}_i = \vec{T}_i \tag{2-22}$$

where $\overline{\overline{I}}_i$ and $\vec{\Omega}_i$ represent the inertia tensor and the angular velocity of the *i*-th solid respectively. The torque induced by the surface force is denoted as $\vec{T}_i$. For a

two-dimensional situation, only one component of $\vec{\Omega}_i$ is non-zero. Thus, Eq. (2-22) reduces to only one equation, i.e.

$$I_i \frac{d\Omega_i}{dt} = T_i \tag{2-23a}$$

Ω_i is related to the orientation of the *i*-th solid via

$$\Omega_i = \frac{d\theta_i}{dt} \tag{2-23b}$$

with the initial condition of

$$\theta_i(t=0) = \theta_{io} \tag{2-23c}$$

2.3.5 Algorithm for F-S Interface Tracking

The algorithm to evolve the F-S interface from $\phi(t)$ to $\phi(t+\Delta t)$ for a known velocity $\vec{u}(t+\Delta t)$ and pressure $p(t+\Delta t)$ fields can be summarized as:

1. Calculate $\vec{F}_i(t+\Delta t)$ and $\vec{T}_i(t+\Delta t)$ for $i = 1,...,N$ using Eqs. (2-19) and (2-20).
2. Calculate $\vec{x}_{c,i}(t+\Delta t)$ and $\theta_i(t+\Delta t)$ for $i = 1,...,N$ using Eqs. (2-21) and (2-23).
3. Construct the local distance function $\phi_i(t+\Delta t)$ for $i = 1,...,N$ from Eq. (2-15).
4. Construct the global distance function $\phi(t+\Delta t)$.

2.3.6 Remarks on F-S Interface Tracking

A few remarks on the F-F interface tracking procedure are given before proceeding further. The present F-S interface tracking procedure is compared to those employed by Marella et al. (2005) and Duchanoy and Jongen (2003). The differences and strengths of the present procedure with those adopted in these works, in particular Duchanoy and Jongen (2003), are given and discussed in details.

For fluid-solid flow problems, Marella et al. (2005) employed a level-set method to handle the F-S interface. The solid is represented using a level-set function, i.e. a distance function. The distance function is evolved via the level-set equation, capturing the F-S interface implicitly. As a result, the F-S interface is subjected to numerical diffusion leading to unphysical distortion of the rigid solid. In the present study, a distance function is chosen to represent the F-S interface. However, the distance function is reconstructed from the location and orientation of the solid tracked explicitly at every time step. There is no numerical diffusion and therefore the rigidity of the solid is perfectly maintained. This avoids the unphysical deformation of the solid encountered in Marella et al. (2005). Besides, the implementation of a slip velocity on the solid surface has not been explored by Marella et al. (2005). The present F-S interface procedure bears no similarity in the handling of the F-S interface with the work of Marella et al. (2005) apart from using the distance function to represent the F-S interface.

Duchanoy and Jongen (2003) employed a Heaviside step function as the indicator function to represent the solid. The Heaviside step function changes sharply from 0 (fluid region) to 1 (solid region). For every computational cell, the value of the indicator function can either be 1 or 0 only. The F-S interface is therefore not smooth as shown in Fig. 2-9. The unit outward normal vector required for the calculation of hydrodynamic force and torque on each solid is calculated from the Heaviside step function. With the employed Heaviside step function, the unit outward normal vector of the solid surface can only point in the direction of a multiple of 45° as shown. This works fine for circular solids given its symmetry. However, this does not represent other non-circular solids adequately. The calculation of the force and torque on these non-circular solids is not

accurate and therefore their motions could not be tracked with confidence. In the present F-S interface tracking procedure, a solid of more complicated geometry can be created easily by merging the distance functions of a few smaller simple shaped solid. With a distance function representation, the unit outward normal vector can be calculated accurately even for solids of complicated geometry. Representation of solid with a distance function offers more versatility on the type of solid geometry than that of a Heaviside function as in Duchanoy and Jongen (2003).

With different indicator function to represent the F-S interface, the implementation of the hydrodynamic force and torque calculation differs. Duchanoy and Jongen (2003) employed volume integration over all the first control volume *inside* the solid in calculating both force and torque one the solid. However, instead of performing the integration over the solid side of the F-S interface, the volume integration is performed over the fluid side of the F-S interface because the force on the solid is exerted by the fluid flowing adjacent but outside of the solid.

With the Heaviside step function representation of the solid by Duchanoy and Jongen (2003), a displacement of the solid less than one CV cannot be tracked properly. Figure 2-10 shows two situations where the displacement of the F-S interface is undetected or over-predicted. The figures on the left and right present the actual movement of the interface and the tracked movement of the F-F interface. If the F-F interface moves between two nodes, no displacement of the interface is detected. However, if the interface moves across the CV nodes, no matter how small the displacement is, it is tracked as a displacement of one CV. In both situations, the accuracy in the calculation of the hydrodynamic force and torque on the solid is compromised. This does not occur in the present F-S interface tracking procedure for any small displacement is tracked and

reflected in the reconstructed distance function.

In the approach adopted by Duchanoy and Jongen (2003), the velocity of a rigid body motion is implemented in the entire solid region of that particular solid. The implementation of a slip velocity on the solid surface has not been explored. Unlike the approach of Duchanoy and Jongen (2003), the present study enforces the rigid body motion of the solid only in an interior volume layer (of the solid, will be discussed in the next section) adjacent to the F-S interface. With such an implementation, slip boundary condition at the solid surface can be implemented.

2.4 Combined Conservation Equations

Figure 2-1 shows a physical domain constituted by three different phases. These are two fluids (fluid 1 and fluid 2) and a solid phase. The F-F and F-S interfaces are identified by the level-set function $\xi(\vec{x},t)$ and a global distance function $\phi(\vec{x},t)$ given by

$$\xi(\vec{x},t)=\begin{cases}<0, & \vec{x}\in \text{fluid 1 or solids}\\ =0, & \vec{x}\in \text{F - F interface}\\ >0, & \vec{x}\in \text{fluid 2}\end{cases} \tag{2-24a}$$

and

$$\phi(\vec{x},t)=\begin{cases}<0, & \text{if } \vec{x}\in \text{solids}\\ =0, & \text{if } \vec{x}\in \Gamma_S\\ >0, & \text{if } \vec{x}\in \text{fluid 1 or 2}\end{cases} \tag{2-24b}$$

With ξ and ϕ defined, any property γ of interest (e.g. ρ, μ, k and c_p) at any spatial location in the domain for a given time t can be expressed as

$$\gamma(\phi,\xi)=\begin{cases}\gamma_S, & \phi<0\\ (1-H)\gamma_1+H\gamma_2, & \phi>0\end{cases} \tag{2-25a}$$

where

$$H = \begin{cases} 0 & \xi < -\varepsilon \\ \dfrac{\xi + \varepsilon}{2\varepsilon} + \dfrac{1}{2\pi}\sin\left(\dfrac{\pi\xi}{\varepsilon}\right) & |\xi| \le \varepsilon \\ 1 & \xi > \varepsilon \end{cases} \tag{2-25b}$$

In Eqs. (2-25) the subscripts 1, 2 and S indicate fluid 1, fluid 2 and the solids respectively.

The solids are modeled as highly viscous fluids. The "fluids" in the solids behave as rigid bodies and are therefore constrained to move with rigid body motions. With the solids modeled as such, a combined formulation (for the three phases) where a single set of conservation equations written for the entire domain can be employed.

2.4.1 The Navier-Stokes Equations

The motions of the phases are governed by the unsteady incompressible Navier-Stokes equations. The continuity and the momentum equations can be written for the entire domain as

$$\frac{\partial \rho}{\partial t} + \nabla \bullet \left(\rho \vec{u}\right) = 0 \tag{2-26}$$

$$\frac{\partial \left(\rho \vec{u}\right)}{\partial t} + \nabla \bullet \left(\rho \vec{u}\vec{u}\right) = -\nabla p + \nabla \bullet \left[\mu\left(\nabla \vec{u} + \nabla \vec{u}^{\,T}\right)\right] + \vec{f}_B + \vec{f}_F \tag{2-27}$$

where $\vec{u}$, p, ρ and μ are the velocity vector, pressure, density and viscosity respectively. ρ and μ represent the density and viscosity appropriate for the phase occupying the particular spatial location at a given instant of time can be evaluated using Eq. (2-25).

In Eq. (2-27), $\vec{f}_B$ and $\vec{f}_F$ represent body force and interfacial force at the F-F

interface per unit volume respectively. If gravity is considered $\vec{f}_B$ can be expressed as

$$\vec{f}_B = \rho\vec{g} \tag{2-28}$$

The interfacial force $\vec{f}_F$ is modeled using the Continuum Surface Force model of Brackbill et al. (1992). Rather than acting at the F-F interface, it is reformulated as an equivalent body force acting within a band of 2ε at the interface. This is achieved using a Dirac delta function $D(\vec{x}-\vec{x}_F)$. Surface tension force is considered in the present study. The interfacial force can be expressed as

$$\vec{f}_F = -\kappa\sigma\hat{N}_F D(\vec{x}-\vec{x}_F) + (\hat{N}_F \times \nabla\sigma) \times \hat{N}_F D(\vec{x}-\vec{x}_F) \tag{2-29a}$$

where $D(\vec{x}-\vec{x}_F)$, $\hat{N}_F$ and κ are defined respectively as

$$D(\vec{x}-\vec{x}_F) = D(\xi) = \begin{cases} \dfrac{1+\cos(\pi\xi/\varepsilon)}{2\varepsilon} & |\xi| < \varepsilon \\ 0 & \text{otherwise} \end{cases} \tag{2-29b}$$

$$\hat{N}_F = \frac{\nabla\xi}{|\nabla\xi|} \tag{2-29c}$$

$$\kappa = \nabla \bullet \hat{N}_F \tag{2-29d}$$

The first and the second terms on the RHS in Eq. (2-29a) represent capillary and Marangoni effects respectively. The capillary force is proportional to local curvature of the interface. The Marangoni force is induced by a surface tension gradient. The surface tension gradient is inducible either by surfactant concentration gradient (salutocapillary), temperature (thermocapillary) or electrical (electrocapillary) fields. While the capillary force acts perpendicular to the interface, the Marangoni force acts tangentially along the F-F interface.

2.4.2 The Energy Equation

In the cases where temperature field is important, the energy equation is required. It is given by

$$\frac{\partial(\rho c_p T)}{\partial t} + \nabla \bullet (\rho c_p \vec{u} T) = \nabla \bullet (k \nabla T) + S_T \tag{2-30}$$

where T, c_p, k and S_T are temperature, specific heat, thermal conductivity and energy source or sink. c_p and k can be calculated using Eq. (2-25). Viscous dissipation is neglected in the energy equation.

2.4.3 Electrokinetic Effects

If the fluids 1 and 2 are both aqueous solutions, with an applied electric field, both electroosmotic of the solution and electrophoresis of the solids occur. It is assumed that both the channel walls and the solid body are non-conducting. For a thin EDL (electric double-layer) with the electric field develops instantly, the electrical potential φ is governed by the Gauss's Law

$$\nabla \bullet (\varepsilon_e \nabla \varphi) = 0 \tag{2-31}$$

where ε_e is the electrical permittivity calculated from Eq. (2-25). For the non-conducting solids, $\varepsilon_e = 0$. In Eq. (2-31), the ionic concentration is uniform and therefore the local volume charge density is zero.

Now since the charged solids are in an electric field, electrostatic force acts on it. There is an additional hydrodynamic force acts within the EDL. These forces have the same value but operate in the opposite direction canceling each other (Ye and Li, 2004). Therefore, no additional treatment of the force and torque acting on the solids is required.

2.4.4 Boundary Conditions

No slip condition is applied at the bounding walls. When there is an EDL layer at the walls, the Helmholtz-Smoluchowski slip velocity is imposed.

$$\vec{u} = \frac{\varepsilon_e \zeta_W}{\mu}\left(\bar{\bar{I}} - \hat{N}_W \hat{N}_W\right) \bullet \nabla\varphi \tag{2-32}$$

where ζ_W and $\hat{N}_W$ are the zeta potential and unit normal of the charged walls.

The interface Γ_{S_i} of every solid serves as the moving boundaries for fluid 1. The condition at the moving boundary Γ_{S_i} is imposed in the following manner. An inner layer of the *i*-th solid, defined as $-\varepsilon \le \phi_i \le 0$ (the shaded region in Fig. 2-8), is set to be in rigid body motion. The velocities in this region are specified as

$$\vec{u} = \vec{U}_i + \Omega_i \hat{k} \times \left(\vec{x} - \vec{x}_{c,i}\right) + \frac{\varepsilon_e \zeta_S}{\mu}\left(\bar{\bar{I}} - \hat{N}_S \hat{N}_S\right) \bullet \nabla\varphi \tag{2-33}$$

where the first and the second terms on the right represent the translational and the rotational motions respectively. The third term represents the Helmholtz-Smoluchowski slip velocity due to the presence of EDL around the solid. ζ_S is the zeta potential of the charged solid body. This term is zero when no electrical field is applied. The velocity in the remaining region of the solid body defined by $\phi_i < -\varepsilon$ is forced to be zero. The setting of the velocity in these two regions of the solid body is achieved using the internal control volume approach of Patankar (1980). This somewhat clumsy implementation of the particle motion using a two-region solid is employed as the slip velocities (with EDL effect) can be implemented easily.

At any outlet, the outflow boundary condition is employed whereby the velocity of fluid is calculated so that mass is conserved.

For the energy equation, either the temperature or heat flux is specified at the domain boundary. For the electrical field governed by Eq. (2-31), the electrical potential is specified at the boundary. The walls of the channel are both thermally and electrically insulated unless specified otherwise.

2.4.5 Overall Solution Algorithm

The level set function $\xi(t=0)$ is constructed from the known initial F-F interface. The location and orientation of each solid are prescribed at time $t=0$. These are used to construct the local distance function $\phi_i(t=0)$ for all solids. Then, the global distance function $\phi(t=0)$ is obtained by combining all the local distance functions. This completes the setup for the solution procedure. The remaining task is to evolve the F-F interface and track the F-S interface simultaneously as time progresses.

A time marching procedure, evolving the known solution at time t to the new solution at time $t+\Delta t$, is employed. The time marching procedure can be summarized as:

1. Set $\xi(t+\Delta t)=\xi(t)$ and $\phi(t+\Delta t)=\phi(t)$.
2. Calculate ρ and μ (Eq. 2-25) and solve Eqs. (2-26) and (2-27) for $\vec{u}(t+\Delta t)$ and $p(t+\Delta t)$.
3. If temperature field is important, solve Eq. 2-30 for $T(t+\Delta t)$.
4. If electrokinetic effect is considered, solve Eq. 2-31 for φ.
5. Evolve the new F-F interface $\xi(t+\Delta t)$.
6. Track the new F-S interface $\phi(t+\Delta t)$.
7. Repeat Steps 2 to 6 until convergence is attained for time $t+\Delta t$.

Repeat the procedure for the remaining time steps.

If a small time step Δt is used, the F-S interface needs no be tracked in every iteration given the small displacement of the solids. The F-S interface (Step 6) can then be tracked after Step 7 where the converged velocity and pressure fields for $t + \Delta t$ are obtained.

2.5 Concluding Remarks

In this chapter, the mathematical formulation for three phase flow problems is presented. The simultaneous flow of two fluids and a solid phase is considered. Two-phase flows involving fluid-fluid or fluid-solid flows are two limiting cases of the generalized three phase flow model. The former is attained when there is not solid in the physical domain and thus the F-S interface tracking procedure is switched off. For the later, fluid 1 and fluid 2 are identical and no interfacial force acts at the F-F interface. Therefore, the F-F interface is not important. The F-F interface evolution procedure is thus turned off.

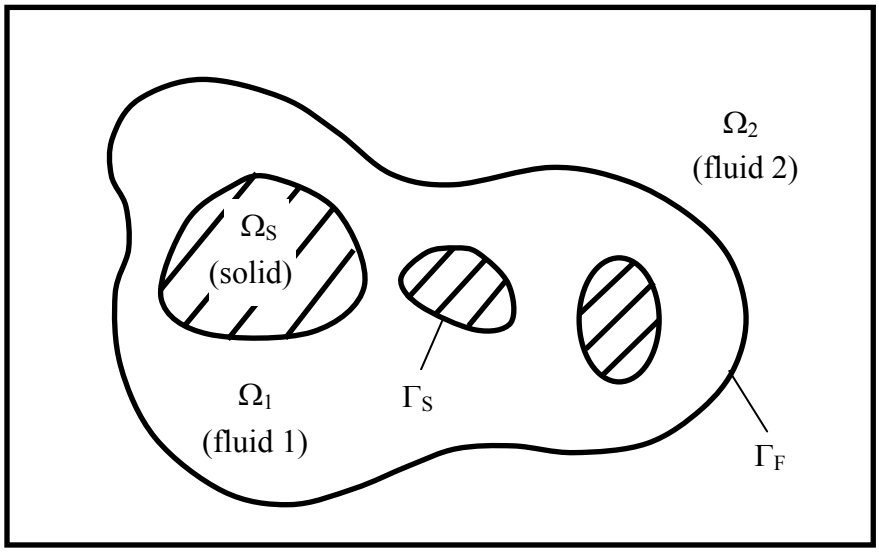

Figure 2-1: Schematic of a three-phase flow problem.

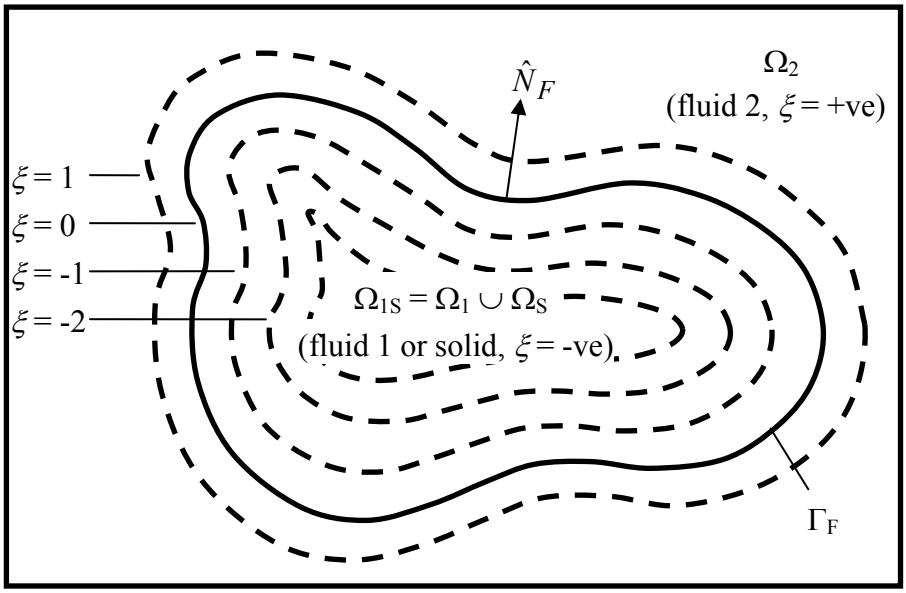

Figure 2-2: The F-F interface.

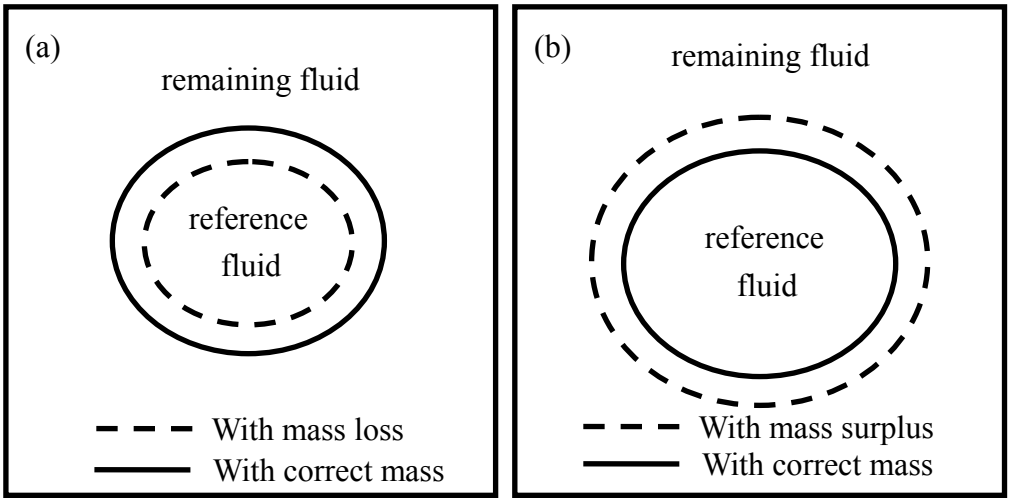

Figure 2-3: F-F interface requires: (a) mass addition and (b) mass removal for GMC.

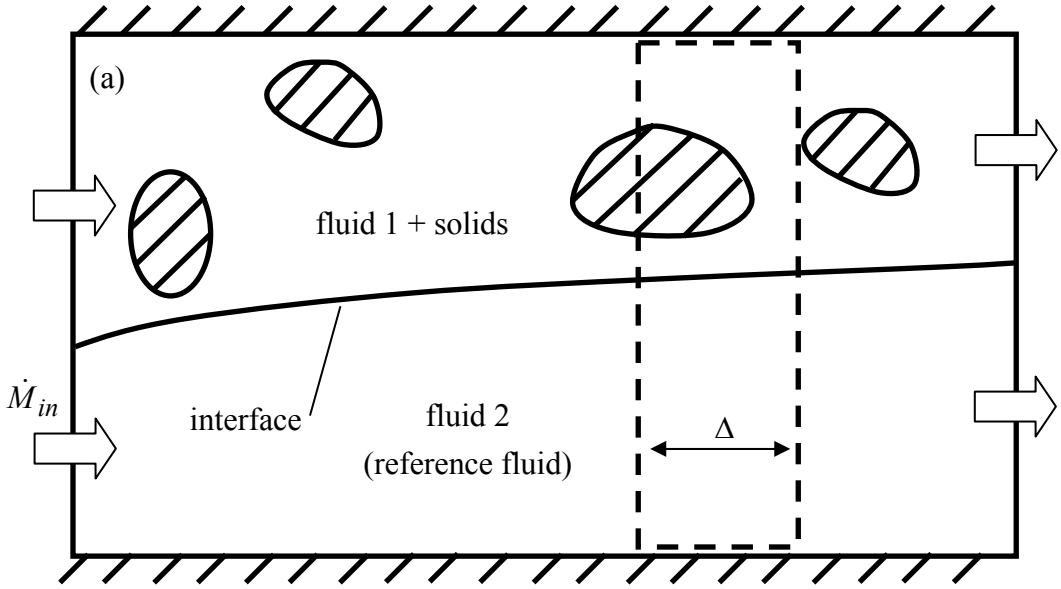

Figure 2-4: Schematic of a stratified flow.

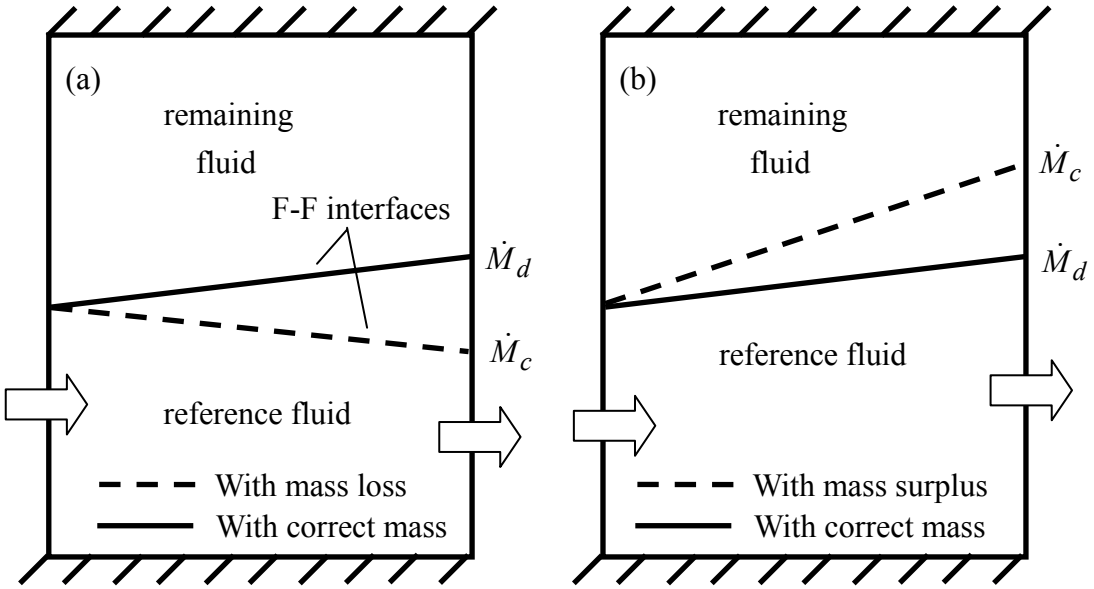

Figure 2-5: F-F interface requires: (a) mass addition and (b) mass removal for LMC.

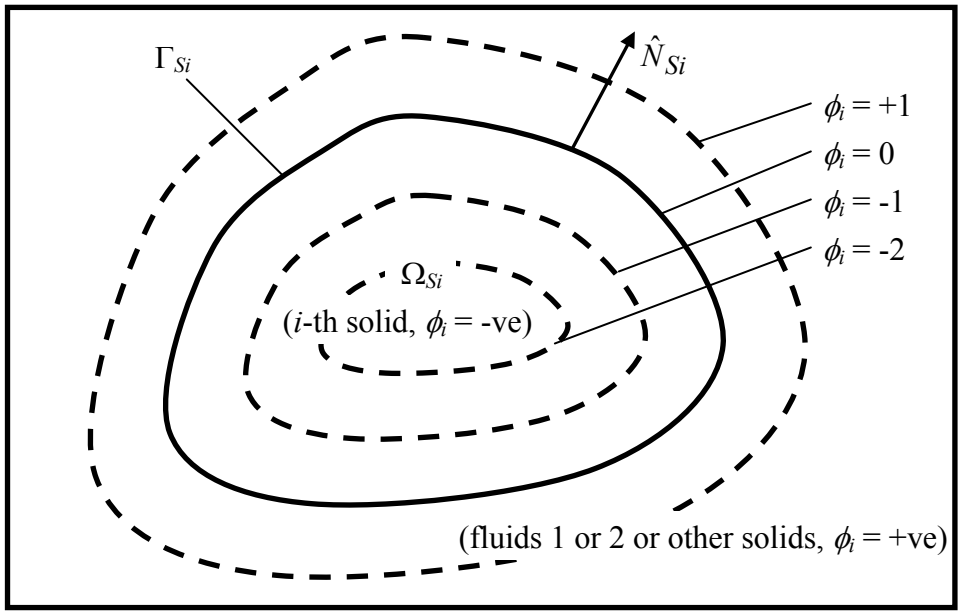

Figure 2-6: A local distance function for a particular solid.

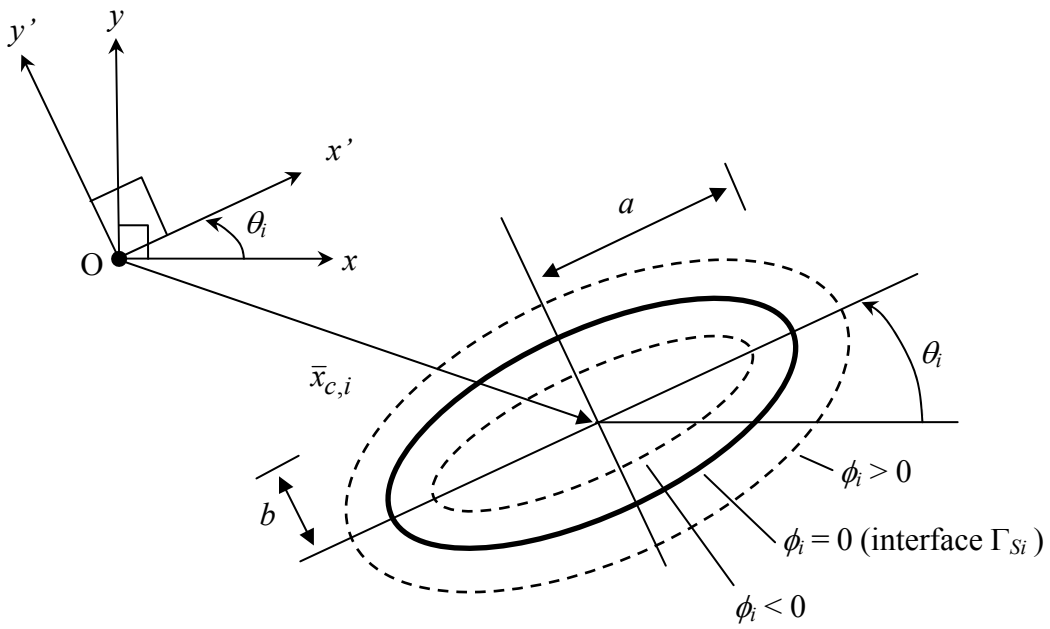

Figure 2-7: Description of the *i*-th elliptical solid with two different coordinate systems.

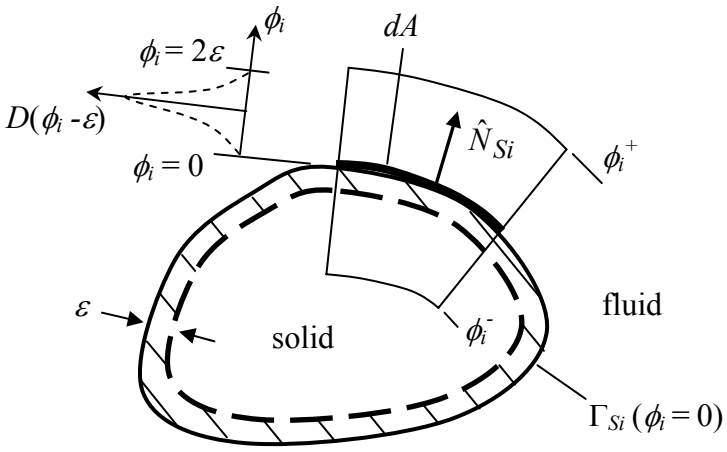

Figure 2-8: Distribution of Dirac delta function across the F-S interface.

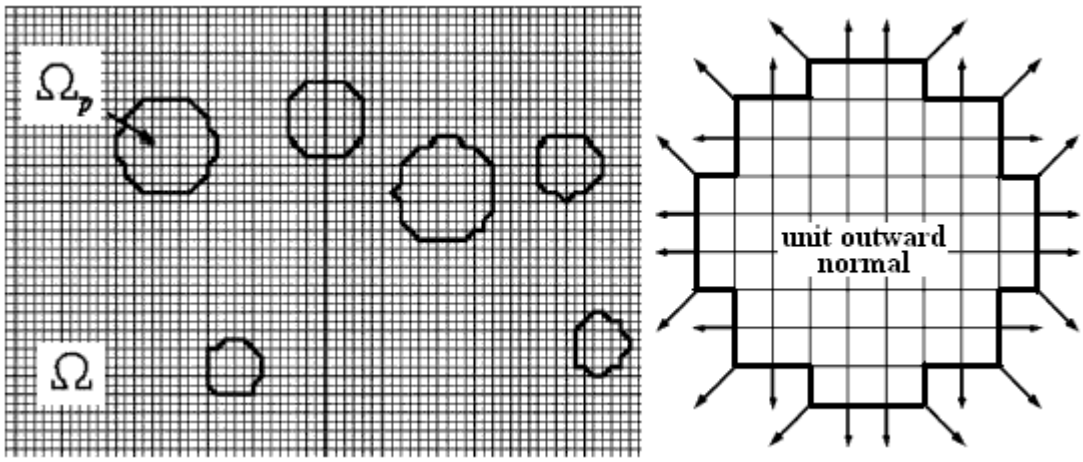

Figure 2-9: Representation of circular solids using Heaviside step functions (Duchanoy and Jongen, 2003).

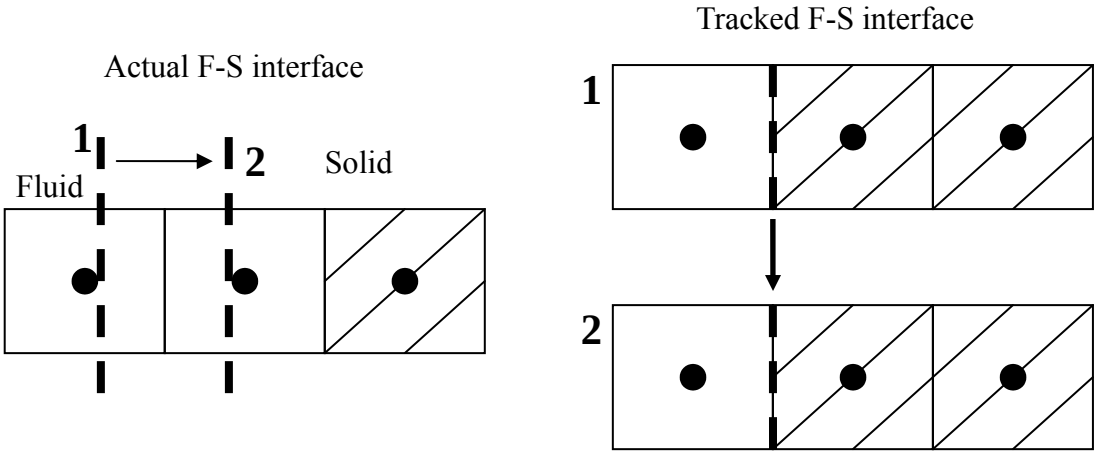

(a) An undetected large displacement of the F-F interface between the two nodes.

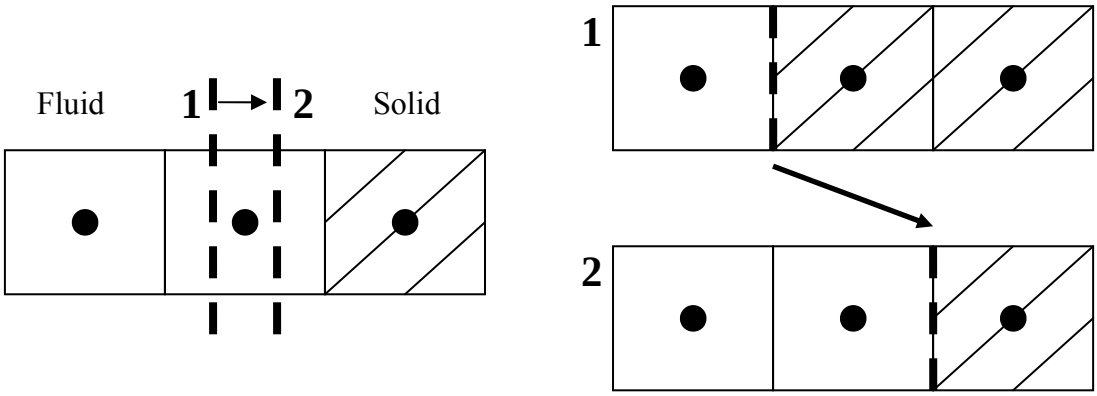

(b) An over-predicted small displacement of F-F interface across a node.

Figure 2-10: Undetected and over-predicted displacements of the F-S interface in the approach of Duchanoy and Jongen (2003).

CHAPTER 3

NUMERICAL SOLUTION PROCEDURE

This chapter presents the numerical solution of the governing equations for the three-phase flow model. The governing equations for a two-dimensional situation are presented. The chapter proceeds with the discretization of these equations and then the associated numerical solution procedures. Finally, a few concluding remarks are given.

3.1 Governing Equations in 2-Dimensions

The two-dimensional governing equations for the three phase flow model are (refer to Section 2.4):

Combined Conservation Equations

Continuity Equation

$$\frac{\partial \rho}{\partial t}+\frac{\partial(\rho u)}{\partial x}+\frac{\partial(\rho v)}{\partial y}=0 \tag{3-1}$$

x-Momentum Equation

$$\frac{\partial(\rho u)}{\partial t}+\frac{\partial(\rho u u)}{\partial x}+\frac{\partial(\rho v u)}{\partial y}=-\frac{\partial p}{\partial x}+\frac{\partial}{\partial x}\left(\mu\frac{\partial u}{\partial x}\right)+\frac{\partial}{\partial y}\left(\mu\frac{\partial u}{\partial y}\right)+\frac{\partial \mu}{\partial x}\frac{\partial u}{\partial x}+\frac{\partial \mu}{\partial y}\frac{\partial v}{\partial x}+f_{Bx}+f_{Fx} \tag{3-2a}$$

y-Momentum Equation

$$\frac{\partial(\rho v)}{\partial t}+\frac{\partial(\rho u v)}{\partial x}+\frac{\partial(\rho v v)}{\partial y}=-\frac{\partial p}{\partial y}+\frac{\partial}{\partial x}\left(\mu\frac{\partial v}{\partial x}\right)+\frac{\partial}{\partial y}\left(\mu\frac{\partial v}{\partial y}\right)+\frac{\partial \mu}{\partial x}\frac{\partial u}{\partial y}+\frac{\partial \mu}{\partial y}\frac{\partial v}{\partial y}+f_{By}+f_{Fy} \tag{3-2b}$$

Energy Equations

$$\frac{\partial(\rho c_p T)}{\partial t}+\frac{\partial(\rho c_p u T)}{\partial x}+\frac{\partial(\rho c_p v T)}{\partial y}=\frac{\partial}{\partial x}\left(k\frac{\partial T}{\partial x}\right)+\frac{\partial}{\partial y}\left(k\frac{\partial T}{\partial y}\right)+S_T \tag{3-3}$$

Gauss's Law

$$0 = \frac{\partial}{\partial x}\left(\varepsilon_e \frac{\partial \varphi}{\partial x}\right) + \frac{\partial}{\partial y}\left(\varepsilon_e \frac{\partial \varphi}{\partial y}\right) \tag{3-4}$$

F-F Interface Capturing

Level-set Equation

$$\frac{\partial \xi}{\partial t} + u\frac{\partial \xi}{\partial x} + v\frac{\partial \xi}{\partial y} = K \tag{3-5}$$

Redistancing

$$\frac{\partial \psi}{\partial \bar{t}} = \overline{sign}(\xi)\left(1 - |\nabla \psi|\right) \tag{3-6}$$

Global Mass Correction

$$\frac{\partial \psi'}{\partial t'} = M_{cor} \tag{3-7}$$

Local Mass Correction

$$\frac{\partial \psi'}{\partial t'} = \dot{M}_{cor} \tag{3-8}$$

F-S Interface Tracking

Local Distance Function

$$\frac{(x' - x'_c)^2}{(a + \phi_i)^2} + \frac{(y' - y'_c)^2}{(b + \phi_i)^2} = 1 \tag{3-9}$$

Conservation of x-Linear Momentum

$$m_i \frac{dU_i}{dt} = F_{ix} + G_{ix} \tag{3-10a}$$

$$U_i = \frac{dx_{c,i}}{dt} \tag{3-10b}$$

Conservation of y-Linear Momentum

$$m_i \frac{dV_i}{dt} = F_{iy} + G_{iy} \tag{3-11a}$$

$$V_i = \frac{dy_{c,i}}{dt} \tag{3-11b}$$

Conservation of Angular Momentum

$$I_i \frac{d\Omega_i}{dt} = T_i \tag{3-12a}$$

$$\Omega_i = \frac{d\theta_i}{dt} \tag{3-12b}$$

3.2 The Finite Volume Discretization

The Finite Volume Method of Patankar (1980) is used to solve the governing equations for the present model. In the Finite Volume Method, the physical domain is divided into a number of control volumes (CVs). The conservation principles are applied to these CVs. Integration of the governing equations is performed over every CV to derive discretized governing equations relating the dependent variable of that CV to those of the neighbouring CVs. The discretized governing equations express the conservation principle for the CV.

A typical control volume is shown in Fig. 3-1. A node (grid point) labeled P is located at the centre of the CV. The neighbouring nodes are denoted as W, E, N and S. This CV has four boundaries, denoted by e, w, n and s (with area of A_e, A_w, A_n and A_s respectively). Δx and Δy are the length and height of the CV. δx and δy are the distances between grid points. The scalar variable, such as pressure, temperature, electrical potential and etc, are stored at the node P. Velocity components are stored at the CV boundaries. While u is staggered half a CV to the left, v is staggered half a CV downward. A staggered grid is adopted to avoid the check-board distribution of the pressure field.

3.2.1 Numerical Solution for the Combined Conservation Equations

Equations (3-1) – (3-4) can be recast into a general transport equation of the form

$$\underbrace{\frac{\partial(\rho\Phi)}{\partial t}}_{Transient} + \underbrace{\frac{\partial}{\partial x}(\rho u\Phi)+\frac{\partial}{\partial y}(\rho v\Phi)}_{Convection} = \underbrace{\frac{\partial}{\partial x}\left(\Gamma\frac{\partial\Phi}{\partial x}\right)+\frac{\partial}{\partial y}\left(\Gamma\frac{\partial\Phi}{\partial y}\right)}_{Diffusion} + \underbrace{S}_{Source} \tag{3-13}$$

where Φ, Γ and S are the dependent variable, the diffusion coefficient and the source term respectively. The source term contains all other terms that cannot be fitted neatly into the convection or diffusion terms.

3.2.1.1 Combined Conservation Equations with Scalar Dependent Variable

For any scalar dependent variable Φ (e.g. T in Eq. 3-3 and φ in Eq. 3-4), the following discretization procedure is employed. Equation (3-13) is rewritten as

$$\frac{\partial(\rho\Phi)}{\partial t}+\frac{\partial}{\partial x}\left(\rho u\Phi-\Gamma\frac{\partial\Phi}{\partial x}\right)+\frac{\partial}{\partial y}\left(\rho v\Phi-\Gamma\frac{\partial\Phi}{\partial y}\right)=S \tag{3-14}$$

This equation is then integrated over the CV in Fig. 3-2 to give

$$\frac{\partial}{\partial t}\int_{\Delta V}(\rho\Phi)dVdt+\int_{\Delta V}\frac{\partial}{\partial x}\left(\rho u\Phi-\Gamma\frac{\partial\Phi}{\partial x}\right)dV+\int_{\Delta V}\frac{\partial}{\partial y}\left(\rho v\Phi-\Gamma\frac{\partial\Phi}{\partial y}\right)dV=\int_{\Delta V}SdV \tag{3-15a}$$

The volume integration of the second and third terms in Eq. (3-15a) is converted into surface integration via the divergence theorem. This gives

$$\frac{\partial}{\partial t}\int_{\Delta V}(\rho\Phi)dVdt+\int_{\Delta A}\left(\rho u\Phi-\Gamma\frac{\partial\Phi}{\partial x}\right)dA+\int_{\Delta A}\left(\rho v\Phi-\Gamma\frac{\partial\Phi}{\partial y}\right)dA=\int_{\Delta V}SdV \tag{3-15b}$$

Perform the integration in Eq. (3-15b) gives

$$\frac{\left(\rho_P\Phi_P-\rho_P^o\Phi_P^o\right)\Delta x\Delta y}{\Delta t}+J_e-J_w+J_n-J_s=\left(S_C+S_P\Phi_P\right)\Delta x\Delta y \tag{3-16a}$$

where

$$J_e = A_e\left(\rho u\Phi - \Gamma\frac{\partial\Phi}{\partial x}\right)_e \tag{3-16b}$$

$$J_w = A_w\left(\rho u\Phi - \Gamma\frac{\partial\Phi}{\partial x}\right)_w \tag{3-16c}$$

$$J_n = A_n\left(\rho v\Phi - \Gamma\frac{\partial\Phi}{\partial y}\right)_n \tag{3-16d}$$

$$J_s = A_s\left(\rho v\Phi - \Gamma\frac{\partial\Phi}{\partial y}\right)_s \tag{3-16e}$$

$$A_e = A_w = \Delta y \tag{3-16f}$$

$$A_n = A_s = \Delta x \tag{3-16g}$$

In Eq. (3-16a), ρ_P, Φ_P and S are assumed to prevail over the CV. All terms are evaluated at $t+\Delta t$ except ρ_P^o and Φ_P^o. ρ_P^o and Φ_P^o are evaluated at t.

The J terms in Eq. (3-16) are evaluated at the CV surfaces. These J terms need to be related to Φ at the neighbouring nodes. For this purpose, the power-law scheme is employed. For the CV interface e, it is defined as

$$J_{\mathrm{e}} = \begin{cases} F_{\mathrm{e}}\Phi_{\mathrm{E}} & Pe < -10 \\ F_{\mathrm{e}}\left[\Phi_{\mathrm{E}} - \beta_{\mathrm{e}}(\Phi_{\mathrm{E}} - \Phi_{\mathrm{P}})\right] & -10 \le Pe < 0 \\ F_{\mathrm{e}}\left[\Phi_{\mathrm{P}} - \beta_{\mathrm{e}}(\Phi_{\mathrm{E}} - \Phi_{\mathrm{P}}\right] & 0 \le Pe \le 10 \\ F_{\mathrm{e}}\Phi_{\mathrm{P}} & Pe > 10 \end{cases} \tag{3-17a}$$

where β_{e} and Pe_{e} (the Peclet number at interface e) are

$$\beta_{\mathrm{e}} = \frac{\left(1 - 0.1|Pe_{\mathrm{e}}|\right)^5}{Pe_{\mathrm{e}}} \tag{3-17b}$$

$$Pe_{\mathrm{e}} = \frac{F_{\mathrm{e}}}{D_{\mathrm{e}}} \tag{3-17c}$$

J_w, J_n and J_s are defined similarly. In the calculation of the Peclet number for the J terms, the flow rates and diffusive rates at e, w, n and s are given as

$$F_{\mathrm{e}} = (\rho u)_{\mathrm{e}} A_{\mathrm{e}}, \qquad D_{\mathrm{e}} = \frac{\Gamma_{\mathrm{e}} A_{\mathrm{e}}}{\delta x_{\mathrm{e}}} \tag{3-18b}$$

$$F_{\mathrm{w}} = (\rho u)_{\mathrm{w}} A_{\mathrm{w}}, \qquad D_{\mathrm{w}} = \frac{\Gamma_{\mathrm{w}} A_{\mathrm{w}}}{\delta x_{\mathrm{w}}} \tag{3-18c}$$

$$F_{\mathrm{n}} = (\rho v)_{\mathrm{n}} A_{\mathrm{n}}, \qquad D_{\mathrm{n}} = \frac{\Gamma_{\mathrm{n}} A_{\mathrm{n}}}{\delta y_{\mathrm{n}}} \tag{3-18d}$$

$$F_{\mathrm{s}} = (\rho v)_{\mathrm{s}} A_{\mathrm{s}}, \qquad D_{\mathrm{s}} = \frac{\Gamma_{\mathrm{s}} A_{\mathrm{s}}}{\delta y_{\mathrm{s}}} \tag{3-18e}$$

In the evaluation of the diffusive rates, Γ is the harmonic mean of two grid points.

The source term S in Eq. (3-15b) has be linearized as

$$S = S_C + S_P \Phi_P \tag{3-19}$$

where S_C and S_P are the related coefficients.

To have better enforcement of continuity, the continuity equation has to be considered in the discretization of the general transport equation. For this purpose, the continuity equation (Eq. 3-1) is similarly integrated over the CV to give

$$\frac{\left(\rho_P - \rho_P^o\right)\Delta x \Delta y}{\Delta t} + F_{\mathrm{e}} - F_{\mathrm{w}} + F_{\mathrm{n}} - F_{\mathrm{s}} = 0 \tag{3-20}$$

Eq. (3-20) is then multiplied by Φ_P and the resulted equation is subtracted from Eq. (3-16a). This gives the final discretized equation for the general transport equation as

$$\frac{\left(\Phi_P - \Phi_P^o\right)\rho_P^o \Delta x \Delta y}{\Delta t} + \left(J_e - F_{\mathrm{e}}\Phi_P\right) - \left(J_w - F_{\mathrm{w}}\Phi_P\right) + \left(J_n - F_{\mathrm{n}}\Phi_P\right) - \left(J_s - F_{\mathrm{s}}\Phi_P\right) = \left(S_C + S_P \Phi_P\right)\Delta x \Delta y \tag{3-21}$$

For numerical implementation, Eq. (3-21) can be written in a compact form as

$$a_{\mathrm{P}}\Phi_{\mathrm{P}} = a_{\mathrm{E}}\Phi_{\mathrm{E}} + a_{\mathrm{W}}\Phi_{\mathrm{W}} + a_{\mathrm{N}}\Phi_{\mathrm{N}} + a_{\mathrm{S}}\Phi_{\mathrm{S}} + b \tag{3-22a}$$

where

$$a_{\mathrm{E}} = D_{\mathrm{e}} A\left(\left|Pe_{\mathrm{e}}\right|\right) + \left\| -F_{\mathrm{e}}, 0 \right\| \tag{3-22b}$$

$$a_{\mathrm{W}} = D_{\mathrm{w}} A\left(\left|Pe_{\mathrm{w}}\right|\right) + \left\|F_{\mathrm{w}}, 0\right\| \tag{3-22c}$$

$$a_{\mathrm{N}} = D_{\mathrm{n}} A\left(\left|Pe_{\mathrm{n}}\right|\right) + \left\|-F_{\mathrm{n}}, 0\right\| \tag{3-22d}$$

$$a_{\mathrm{S}} = D_{\mathrm{s}} A\left(\left|Pe_{\mathrm{s}}\right|\right) + \left\|F_{\mathrm{s}}, 0\right\| \tag{3-22e}$$

$$a_P^o = \frac{\rho_P^o \Delta x \Delta y}{\Delta t} \tag{3-22f}$$

$$a_{\mathrm{P}} = a_{\mathrm{E}} + a_{\mathrm{W}} + a_{\mathrm{N}} + a_{\mathrm{S}} + a_P^o - S_{\mathrm{P}} \Delta x \Delta y \tag{3-22g}$$

$$b = S_{\mathrm{C}} \Delta x \Delta y + a_P^o \Phi_P^o \tag{3-22h}$$

In Eqs. (3-22b) to (3-22e), the power law has been written compactly as

$$A\left(\left|Pe\right|\right) = \left\|0, \left(1 - 0.1\left|Pe\right|\right)^5\right\| \tag{3-22i}$$

where $\left\|A, B\right\|$ is defined as the greater of A and B.

3.2.1.2 Implementation of Boundary Conditions

The discretized equation (Eq. 3-22) relates the variable Φ at the center of a CV to that of the neighbouring CVs. The number of equations and unknowns are equal to the number of CVs only if the boundary conditions are known. Then, the discretized equation has a unique solution. Numerical enforcement of three different boundary conditions is considered:

1) Boundary values are given.

2) Boundary fluxes are given.

3) Zero gradient condition ($\frac{\partial \Phi}{\partial n} = 0$).

No additional work is required if the boundary values are given. For the case of given boundary fluxes, the boundary conditions can be accounted for by suppressing the link of the discretized equations to boundary side and then modifying the source terms. The

appropriate coefficient of the discretized equation is set to zero and the boundary side flux is introduced through source term S_C and S_P. For instance, if the heat flux for the energy equation is given at the boundary as shown in Fig. 3-3,

$$S_{\text{extra}} = \frac{J_B(area)}{volume},\ S_{C,\text{extra}} = S_{\text{extra}},\ S_{P,\text{extra}} = 0,\ a_B = 0 \tag{3-23a}$$

The zero gradient condition is enforced via

$$\Phi_P = \Phi_B \tag{3-23b}$$

3.2.1.3 Solution of the Discretization Equation

The discretized equation (Eq. 3-22) is non-linear. The coefficients of the equation may depend on the variable Φ. An iterative method is used to solve the equation. First, the coefficients are computed using the guess values of Φ. The value available Φ^o at the previous time step is a good guess. With these coefficients, the equation is linearized. The linearized discretized equation is solved for the updated value of Φ. Then, the coefficients are recalculated using the new values of Φ and again the equation is solved. This process is repeated until the convergence of Φ is achieved.

Under-relaxation is employed for the sake of stability. The discretized equation for general variable Φ_P in the *n*-th iteration can be expressed as

$$a_P \Phi_P^n = \sum a_{nb} \Phi_{nb}^n + b \tag{3-24a}$$

$$\Phi_P^n = \frac{\sum a_{nb} \Phi_{nb}^n + b}{a_P} \tag{3-24b}$$

In Eq. (3-24a), a_{nb} stands for coefficients at the neighbouring nodes namely W, E, S and N. For underrelaxation, a relaxation factor ω is introduced. Equation (3-24b) is written as

$$\Phi_P^n = \Phi_P^{n-1} + \omega(\Phi_P^n - \Phi_P^{n-1}) \tag{3-24c}$$

where

$$0 \le \omega \le 1 \tag{3-24d}$$

Substituting Eq. (3-24b) into Eq. (3-24c) gives

$$\frac{a_P}{\omega}\Phi_P^n = \sum a_{nb}\Phi_{nb}^n + b + (1-\omega)\frac{a_P}{\omega}\Phi_P^{n-1} \tag{3-24e}$$

Optimum underrelaxation factor ω is problem dependent.

3.2.2 SIMPLER for Velocity-Pressure Coupling

The pressure field is coupled with the velocity in the momentum equations. This coupling is achieved via the SIMPLER algorithm.

Different CVs are used when discretizing *x*-momentum and *y*-momentum equations. These CVs are shown in Fig. 3-4. However, the discretized momentum equations have exactly the same form as Eq. (3-22). For example, the discretized *x*-momentum equation can be written as

$$a_w u_w = \sum a_{nb} u_{nb} + b + (p_W - p_P)A_w \tag{3-25}$$

For convenience, Eq. (3-25) can be written as:

$$u_w = \hat{u}_w + (p_W - p_P)d_w \tag{3-26a}$$

where

$$\hat{u}_w = \frac{\sum a_{nb} u_{nb} + b}{a_w} \tag{3-26b}$$

$$d_w = \frac{A_w}{a_w} \tag{3-26c}$$

The velocities u at the boundary e and v at the boundaries s and n can be expressed in a similar form.

For a known pressure field (either guessed or estimated), the velocity fields can be solved using an iterative procedure from the discretized momentum equations. The continuity equation can be made use of in calculating the required pressure field. Substituting all the velocities in the form of Eqs. (3-26) into the discretized continuity equation (Eq. 3-20) gives

$$a_P p_P = a_E p_E + a_W p_W + a_N p_N + a_S p_S + b \tag{3-27a}$$

where

$$a_E = \rho_e d_e A_e \tag{3-27b}$$

$$a_W = \rho_w d_w A_w \tag{3-27c}$$

$$a_S = \rho_s d_s A_s \tag{3-27d}$$

$$a_N = \rho_n d_n A_n \tag{3-27e}$$

$$a_P = a_E + a_W + a_N + a_S \tag{3-27f}$$

$$b = -\frac{\left(\rho_P - \rho_P^o\right)\Delta x \Delta y}{\Delta t} + \rho_w \hat{u}_w A_w - \rho_e \hat{u}_e A_e + \rho_s \hat{u}_s A_s - \rho_n \hat{u}_n A_n \tag{3-27g}$$

The pressure field obtained from Eq. (3-27) satisfies the continuity equation. However, the velocities used do not normally satisfy the continuity equation. This is due to the fact that these velocities are obtained from the momentum equation with only a guessed or estimated pressure field. To overcome this, the velocity correction method is employed to give a better prediction of the velocities. It is described below.

In the iterative process, the velocities (from the momentum equations) and the pressure are taken as temporal values. A small correction must be added to the velocities and the pressure.

$$u = u^* + u' \tag{2-28a}$$

$$v = v^* + v' \tag{2-28b}$$

$$p = p^* + p' \tag{3-28c}$$

u^*, v^* and p^* are guessed values. u', v' and p' are corrections to be added to the guessed values. u, v and p are the correct velocity and pressure fields.

Substituting Eqs. (3-28) into the discretized momentum equations in the form Eq. (3-25) gives

$$u'_{\mathrm{w}} = \hat{u}'_{\mathrm{w}} + (p'_{\mathrm{W}} - p'_{\mathrm{P}})d_{\mathrm{w}} \tag{3-29a}$$

$$v'_{\mathrm{s}} = \hat{v}'_{\mathrm{s}} + (p'_{\mathrm{S}} - p'_{\mathrm{P}})d_{\mathrm{s}} \tag{3-29b}$$

At this point, u' and v' are unknown. In the SIMPLER algorithm, $\hat{u}'$ and $\hat{v}'$ are neglected. Therefore,

$$u'_{\mathrm{w}} = (p'_{\mathrm{W}} - p'_{\mathrm{P}})d_{\mathrm{w}} \tag{3-30a}$$

$$v'_{\mathrm{s}} = (p'_{\mathrm{S}} - p'_{\mathrm{P}})d_{\mathrm{s}} \tag{3-30b}$$

The correction formulae for u_{w} and v_s can be obtained by substituting Eqs. (3-30) into Eqs. (3-28a) and (3-28b)

$$u_{\mathrm{w}} = u^*_{\mathrm{w}} + (p'_{\mathrm{W}} - p'_{\mathrm{P}})d_{\mathrm{w}} \tag{3-31a}$$

$$v_{\mathrm{s}} = v^*_{\mathrm{s}} + (p'_{\mathrm{S}} - p'_{\mathrm{P}})d_{\mathrm{s}} \tag{3-31b}$$

Finally, these correction formulas are substituted into the continuity equation (Eq. 3-20) again to give an equation for the pressure correction p'.

$$a_{\mathrm{P}} p'_{\mathrm{P}} = a_{\mathrm{E}} p'_{\mathrm{E}} + a_{\mathrm{W}} p'_{\mathrm{W}} + a_{\mathrm{N}} p'_{\mathrm{N}} + a_{\mathrm{S}} p'_{\mathrm{S}} + b \tag{3-32a}$$

where

$$a_{\mathrm{E}} = \rho_{\mathrm{e}} d_{\mathrm{e}} A_{\mathrm{e}} \tag{3-32b}$$

$$a_{\mathrm{W}} = \rho_{\mathrm{w}} d_{\mathrm{w}} A_{\mathrm{w}} \tag{3-32c}$$

$$a_S = \rho_s d_s A_s \tag{3-32d}$$

$$a_N = \rho_n d_n A_n \tag{3-32e}$$

$$a_P = a_E + a_W + a_N + a_S \tag{3-32f}$$

$$b = -\frac{\left(\rho_P - \rho_P^o\right)\Delta x \Delta y}{\Delta t} + \rho_w u_w^* A_w - \rho_e u_e^* A_e + \rho_s u_s^* A_s - \rho_n u_n^* A_n \tag{3-32g}$$

3.2.2.1 Implementation of Velocity Boundary conditions

When the velocities are known at the boundary, no special treatment is required. If there is an outflow, and assume that the flow is in the x-direction at the outlet (Fig. 3-5), the outlet velocity u is calculated to satisfy mass conservation. It is proposed that

$$u_{B+1} = u_B + C \tag{3-33a}$$

Equate the inlet mass flow rate to the outlet mass flow rate gives

$$C = \frac{\dot{M}_{in} - \rho u_B A_B}{\rho A_B} \tag{3-33b}$$

where $\dot{M}_{in}$ is inlet mass flow rate.

For v at the outlet, zero gradient is prescribed as

$$v_B = v_{B-1} \tag{3-33c}$$

For pressure equation (Eq. 3-27) and pressure correction equation (Eq. 3-32), all boundary values are set known, so the corresponding coefficients are set to zero.

3.2.2.2 SIMPLER Algorithm

The SIMPLER algorithm, used to evolve the known velocity and pressure fields at time t to those of $t + \Delta t$, can be summarized as

1. Set $u(t + \Delta t) = u(t)$ and $v(t + \Delta t) = v(t)$ for the guessed velocity field.
2. Calculate the coefficients of Eq. (3-27).

3. Solve for $p(t+\Delta t)$ from Eq. (3-27) and set $p^* = p$.

4. Solve the discretized momentum equations (e.g. Eq. 3-25) and set the velocity field obtained to u^* and v^*.

5. Solve Eq. (3-32) for the pressure correction p'.

6. Calculate $u(t+\Delta t)$ and $v(t+\Delta t)$ from Eqs. (3-31).

The SIMPLER algorithm forms Step 2 (i.e. to solve the continuity and momentum equations for $\vec{u}(t+\Delta t)$ and $p(t+\Delta t)$) in the solution algorithm of the three phase flow model outline in Chapter 2. The above procedure is performed in Step 2 to couple the velocity and the pressure field.

3.3 Numerical Solution for F-F Interface Capturing

Equations (3-5) to (3-8) can be written in the form of the general transport (Eq. 3-13). Therefore, these equations are solved in the FVM spirit. However, for the level-set equation of Eq. (3-5), higher order scheme is required in the discretization of the convective terms in order to capture the F-F interface properly. Therefore, an implicit time stepping with CLAM scheme (Van Leer, 974) for the convective terms is employed. The artificial viscosity K, if turned on, is treated as a linearized source term evaluated using the available values from the previous iteration.

For Eqs. (3-6) to (3-8), t is replaced by a pseudo time (t' or $\bar{t}$). The discretized form of these equations can be written in a compact form as

$$a_P \Phi_P = a_E \Phi_E + a_W \Phi_W + a_N \Phi_N + a_S \Phi_S + b \qquad (3\text{-}34a)$$

where

$$a_{\mathrm{E}} = a_{\mathrm{W}} = a_{\mathrm{N}} = a_{\mathrm{S}} = 0 \tag{3-34b}$$

and b is the associated source term.

3.4 Numerical Solution for F-S Interface Tracking

To obtain the local distance function, equation (3-9) is rearranged as

$$(a+\phi_i)^2(b+\phi_i)^2 - (x'-x'_c)^2(b+\phi_i)^2 - (y'-y'_c)^2(a+\phi_i)^2 = 0 \tag{3-35}$$

The local distance function ϕ_i at each node is the root of Eq. (3-23). A bisection method is employed to extract the root. ϕ_i lies in $-l \le \phi_i \le l$ where l is the largest distance between two nodes in the domain. For example, for a rectangular domain, l is the diagonal. Therefore, $\phi_i = -l$ and $\phi_i = l$ are used to start the bisection method. Although bisection method is not the most efficient root-finding algorithm, convergence can be achieved within 25 iterations.

The Euler Equations (Eqs. 3-10 to 3-12) can be expressed in a general form of

$$\frac{d\Phi}{dt} = S \tag{3-36}$$

with Φ known at time t. To march the solution at t to $t+\Delta t$, implicit Euler method is employed for the time discretization. The term S is evaluated using the available values from the previous iteration.

3.5 Convergence Criterion

In the iterative procedure for time $t+\Delta t$, the solution is considered converged if the maximum change of Φ for two successive iterations is less than a prescribed value η, i.e.

$$\left|\frac{\Phi^{n}-\Phi^{n-1}}{\Phi^{n}}\right|_{max} \leq \eta \qquad (3\text{-}37)$$

The above criterion applies to all dependent variables of interest.

3.6 Concluding Remarks

The finite volume discretization of the governing equations in 2-dimensions is presented in this chapter. The governing equations are discretized on a staggered grid. The discretized governing equations march a known solution at time t to $t+\Delta t$. The SIMPLER algorithm is employed for velocity pressure coupling. Implementation of both F-F interface capturing and F-S interface tracking within the FVM framework is straightforward and requires no special treatment.

This completes the numerical model of the three phase flow system. Various case studies of the model are presented in the next chapter.

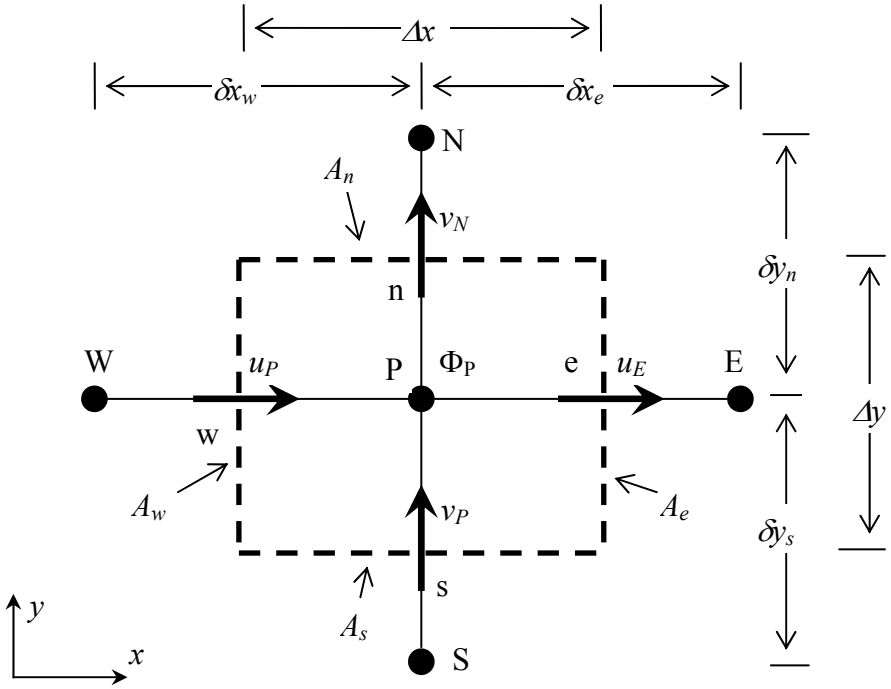

Figure 3-1 A staggered grid arrangement for the P control volume.

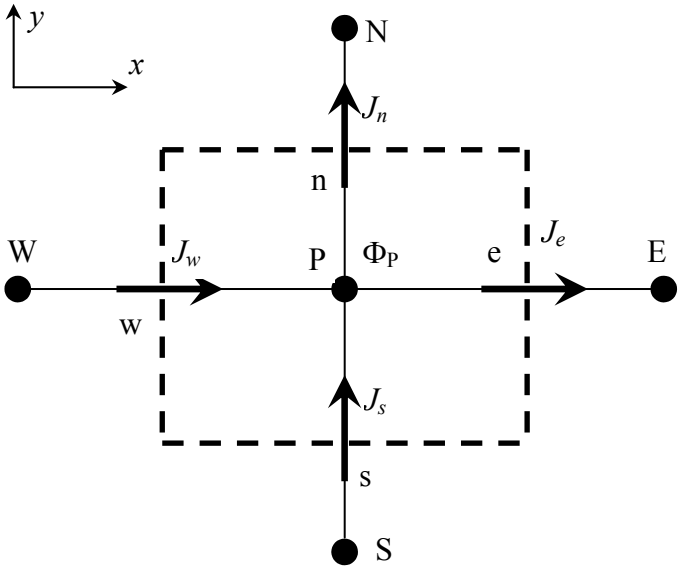

Figure 3-2: A control volume for scalar variables.

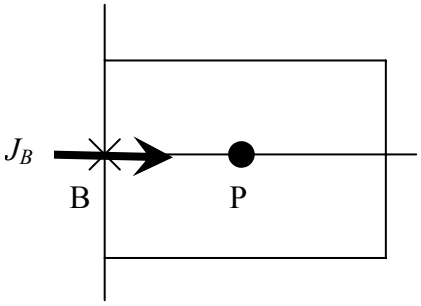

Figure 3-3: Given flux at the boundary.

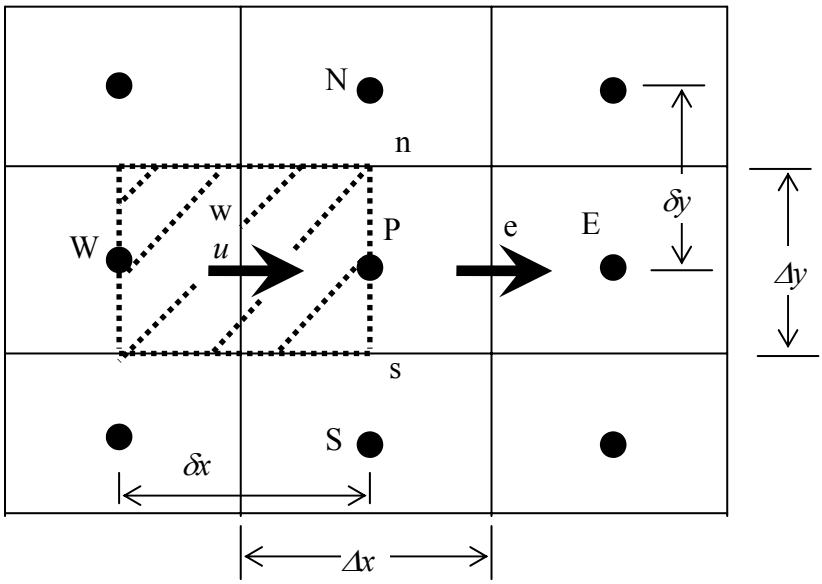

(a) CV for *x*-momentum equation.

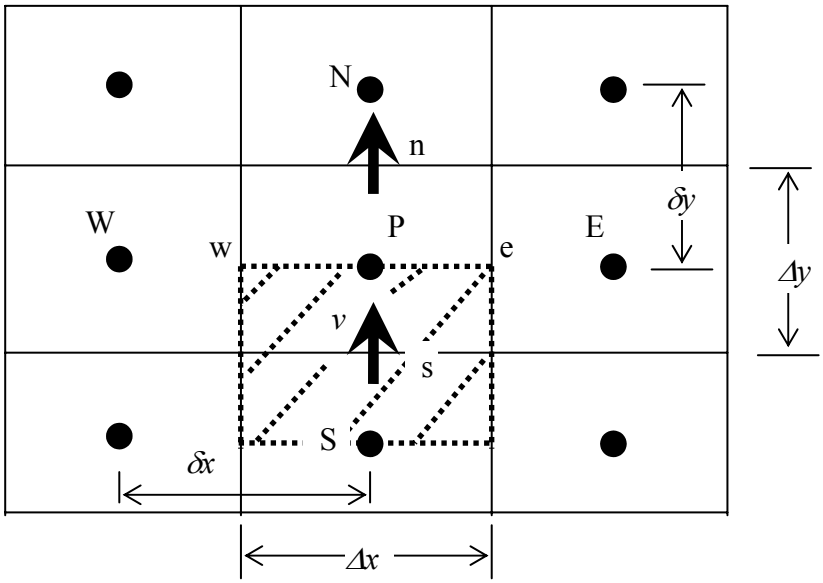

(b) CV for *y*-momentum equation.

Figure 3-4: CVs for momentum equations.

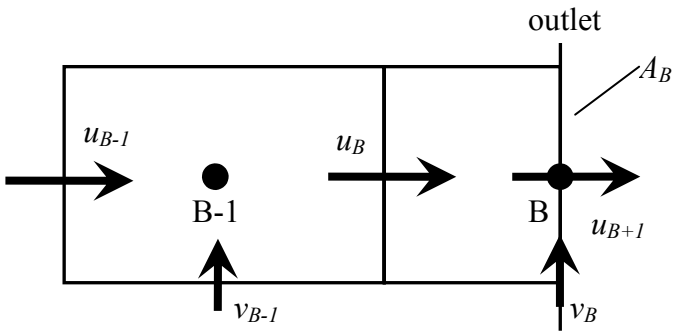

Figure 3-5: Velocity components at an outflow boundary.

CHAPTER 4

CASE STUDIES

The mathematical formulation and the associated solution procedure of a three-phase flow model are presented in the previous chapters. In this chapter, the model is tested and validated against available analytical solutions and existing numerical results. This demonstrates simultaneously the variety of multiphase flow problems to which the current model can be applied. The selected case studies are:

Fluid-fluid flow

1. Rigid body rotation of discs
2. Droplet flow in a straight channel
3. Droplet flow in a double bend
4. Droplet flow in a constricted channel
5. Two-fluid flow with variable surface tension (Marangoni effect)
    (a) Marangoni Force Driven Stratified Two-fluid Flow
    (b) Droplet Flow in a Micro T-junction with Thermocapillary Effect
6. Pressure driven stratified two-fluid flow in a channel
    (a) Fluids of identical properties
    (b) Fluids of different properties
7. Pressure driven stratified two-fluid flow in a double bend

Fluid-solid flow

8. Flow around stationary, forced and freely rotating cylinders
9. Sedimentation of a cylinder between parallel plates under gravity

10. Flow of particles in microchannel system

11. Electrophoresis of circular and elliptical particles

Fluid-fluid-solid flow

12. Flow of particle-encapsulated droplet through a constricted microchannel

13. Flow of particle-encapsulated droplets in a microchannel system

For fluid-fluid flow, only the F-F interface capturing procedure is activated. In case study 1, the diffusion error arises in the F-F interface capturing procedure is investigated. Case studies 2-4 validate F-F interface capturing procedure and demonstrate the capability of GMC in ensuring mass conservation. A strong emphasis of mass conservation is given for these fluid-fluid flow problems. With GMC, flows driven by surface tension gradient (Marangoni force) are investigated in case study 5. The formulation for interfacial force tangential to the interface is validated via comparison with an analytical solution in case study 5a. Besides investigation on the Marangoni effect, case study 5b demonstrates the importance of artificial viscosity in improving numerical stability. The capability of LMC in conserving mass for stratified two-fluid flows is demonstrated in case studies 6 and 7.

In fluid-solid flow problems, the F-S interface tracking procedure is employed. The procedure is validated in case studies 8 and 9. The validation is performed progressively from the calculation of forces and torques on the solids to the dynamics of the solids. A demonstration of the F-S interface tracking procedure is given in case study 10. Case study 11 shows an example of electrophoresis of particles. The capability of the F-S interface tracking procedure in handling velocity slip boundary conditions at the solid surface is demonstrated in this example.

Finally in case studies 12 and 13, the F-F interface capturing and F-S interface tracking procedure are activated for three phase flow problems involving two fluids and a solid phase.

4.1 Rigid Body Rotation of Discs

Rigid body rotations of discs in a constant flow field are suitable test cases to identify the diffusion errors of the F-F interface capturing method. The CLAM scheme advection of the interface represented by the level-set function is tested using two examples, i.e. rotation of an elliptical disc and a slotted circular disc. While the former has a smooth interface, the later has a few sharp corners. In the first example, an elliptical disc initially located at $(50,70)$ in a 100×100 domain is rotated around $(50,50)$ with an angular velocity of $\frac{\pi}{314}$ rad/s. This gives a velocity field of $(u,v)=\frac{\pi}{314}(50-y,x-50)$. The semi-major and semi-minor axes of the elliptical disc are 15 and 7.5 respectively. A uniform mesh of 100×100 CVs with a time step of $\Delta t = 0.125$ s is employed. The disc returns to its initial position after 5024 time steps. Figure 4-1a shows the disc at the beginning and after one revolution. The shape of the disc is well maintained. This shows that the presented method captures smooth interface properly.

The rotation of a slotted circular disc is also more commonly known as the Zalesak's problem (Zalesak, 1979). It tests the ability of the numerical scheme employed in handling sharp corners. The elliptical disc is now replaced by a slotted circular disc of radius 15 placed at $(50,75)$. The length and width of the slot are 20 and 6 respectively. The disc is rotated at the same angular velocity. A uniform mesh of 200×200 CVs with a time step of $\Delta t = 0.125$ s is employed. Figure 4-1b shows the disc at the beginning and

after one revolution. Although the shape of the disc is maintained, the corners are somewhat rounded due to numerical diffusion. These two examples show that the CLAM scheme is sufficient accurate for the evolution of the level-set function.

4.2 Droplet Flow in a Straight Channel

Figure 4-2 shows a droplet of fluid 1 suspended in a channel filled with fluid 2. The channel is of length $L = 2$ and height $W = 1$. The droplet has a diameter of $d_d = 0.30$ and is initially located at $(x_d, y_d) = (0.4, 0.5)$. The densities and viscosities for fluid 1 are 2 and 2, and for fluid 2 are 1 and 1 respectively. Initially, both fluids are at rest. A stream of fluid 2 then flows into the channel with a uniform velocity of $u_{in} = 0.01$ at the inlet. As fluid 2 flows, it carries the droplet with it. The droplet evolves gradually under the action of both the hydrodynamic and surface tension forces.

In Fig. 4-3a, the effect of both spatial grids and time step sizes on the droplet evolution along the channel is shown. GMC is turned on for this computation. Surface tension σ is set to zero. Gravity is in the *z*-direction and therefore not considered. A mesh of 100×50 control volumes (CVs) with a time step size of $\Delta t = 0.1$ is sufficient to achieve both spatial and temporal independent solution. This mesh and time step size is used for the subsequent computations for this problem.

Figure 4-3b shows the evolution of a droplet in a channel with different surface tensions namely, $\sigma = 0$, 0.01 and 0.10. When the coefficient of surface tension is set to zero, there is no surface tension force acting at the interface. Thus, the hydrodynamic force is the only force acting on the droplet. It distorts the droplet into a "bullet-like" shape. Generally, a "bullet-like" shape possesses a smaller drag force. Therefore, the

hydrodynamic force acts to reduce the drag force on the droplet by deforming it. The surface tension force acts to minimize the interfacial area. In this case, it strives to retain the droplet in its original circular shape. Thus, the hydrodynamic and surface tension forces have opposite effects. When the droplet is deformed (for example by hydrodynamic force), surface tension force acts to restore the droplet to its original circular shape. As σ increases, smaller deformation is observed. There is no noticeable deformation for the case of $\sigma = 0.10$.

Figure 4-3b also shows comparisons between the present solutions with that of VOF. Geo-reconstruction scheme coupled with SIMPLEC for pressure-velocity coupling is employed in the VOF model. Although not shown here, the VOF solutions are grid independent. The present solutions ($\sigma = 0$ and 0.1) are in good agreements with that of VOF.

4.3 Droplet Flow in a Double Bend

Figure 4-4 shows a droplet of fluid 1 suspended in a double-bend channel filled with fluid 2. The detailed geometry of the double-bend channel is given in the figure. The droplet has a diameter of $d_d = 0.30$ and is initially suspended at $(x_d, y_d) = (0.3, 0.8)$. The densities and viscosities for fluid 1 are 2 and 2, and for fluid 2 are 1 and 1 respectively. Initially, both fluids are at rest. A stream of fluid 2 then flows into the channel with a uniform velocity of $u_{in} = 0.01$ at the inlet. The droplet is carried by the fluid 2 stream through the double-bend channel. Large deformation of the droplet is expected as the droplet negotiates the bends.

The effect of the spatial grids and time step sizes on the droplet evolution is shown in Fig.

4-5a. Solutions obtained using 360×200 CVs with $\Delta t = 0.10$ and 540×300 CVs with $\Delta t = 0.05$ are presented. For clarity, only the droplet at $t = 0$, 25, 50, 80 and 110 are shown. These times are selected since the interfaces do not overlap each other when plotted in the same figure. For this problem, very fine spatial mesh is required if compared to the previous case. This fact will be explained later. It can be seen that a mesh of 360×200 CVs with $\Delta t = 0.10$ gives spatial and temporal independent solution. Subsequent computations are made using this spatial grid and time step size. The present solutions obtained with and without GMC are shown in Figs. 4-5c and 4-5d. Without GMC, the tail of the droplet is shorter at $t = 110$, an indication of mass loss. The solution with GMC is compared with that of the VOF in Fig. 4-5b. For the VOF solution, the same control volume size is used. The present solution agrees well with that of the VOF.

Figure 4-6 shows the fluid velocity profiles at a few selected locations for $t = 110$. The fluid properties of the two fluids do not differ much. Therefore, this velocity field would be qualitatively similar to that of other times even if the droplet is at different locations. There are two regions of low velocity, i.e. regions near the upper corner of the first bend and the lower corner of the second bend. These regions are circled using dotted line in Fig. 4-6 for clarity. In each of these corners, a small region of recirculation is detected. Let the droplet be separated qualitatively into two portions, a portion near the upper corner and another portion consists of the rest of the droplet. As the droplet flows through the first bend, the portion of the droplet near the upper wall moves with a much lower velocity. The rest of the droplet experiences a higher velocity. Therefore, the portion of the droplet near the upper corner will be increasingly ‘lagged’ behind. This creates a long and thin tail. This process repeats as the droplet flows through the second bend, forming the second tail. In order to capture the formation and its subsequent development of these tails properly, a very fine mesh is required.

Figure 4-7 shows the effect of surface tension on the droplet evolution. Surface tension is set to $\sigma = 0.01$ (Fig. 4-7a) and 0.05 (Fig. 4-7b) respectively. For the case of $\sigma = 0.01$, one tail forms as the droplet is flowing through the first bend. This tail is shorter and thicker if compared to the case without surface tension ($\sigma = 0$). Such a shape gives a smaller interfacial area, consistent with the effect of surface tension that minimizes interfacial area. The same applies to the second tail. When the surface tension coefficient is increased to $\sigma = 0.05$, surface tension effect becomes more profound. For a smaller σ, the first tail tends to form around $t = 50$. This tendency is suppressed by the surface tension force to the extent that no obvious tail is formed at $t = 80$. At $t = 110$, a small thick tail develops after the second bend. It is expected if further computations are made, this tail will become shorter and thicker. A portion of Fig. 4-7a is enlarged in Fig. 4-8a showing the effect of GMC. The prediction without GMC is obviously different at the two blunt tails. Careful examination of Fig. 4-8a reveals that the size of the droplet is smaller for the case without GMC. A parameter called mass error is introduced to examine the mass losses. It is given by

$$M_{err} = \left| \frac{M_d - M_c}{M_d} \right| \tag{4-1}$$

The mass error represents the percentage of mass surplus or loss. Figure 4-8b shows the mass errors with GMC and without GMC. For the case without GMC, the mass error increases with time. This is an indication of either mass surplus or loss of the reference fluid (fluid 1 in this case). The droplet losses around 5% of its original mass at $t = 110$. Base on the trend of the mass error, more mass loss is expected as time passes. When GMC is used, the mass error of the reference fluid remains well in the order of 10^{-16}, an indication of "perfect" mass conservation.

4.4 Droplet Flow in a Constricted Channel

Figure 4-9 shows a droplet of fluid 1 suspended in a constricted channel filled with fluid 2. The channel is of length 2 unit. It has a sudden contraction followed by a sudden expansion. At the inlet, the channel height is 1.0 unit. Then, the height contracts abruptly to $W = 0.2$ to form a smaller channel of length $L = 0.7$, after which it expands to its initial height. For ease of discussion, this smaller channel is henceforth referred as the small channel. The details of the channel geometry are given in Fig. 4-9. The droplet has a diameter of $d_d = 0.40$ and is initially suspended at $(x_d, y_d) = (0.3, 0.5)$. The densities and viscosities for fluid 1 are 2 and 2, and for fluid 2 are 1 and 1 respectively. Initially, both fluids are at rest. A stream of fluid 2 then flows into the channel with a uniform velocity of $u_{in} = 0.01$ at the inlet. The droplet is carried by the stream and squeezed through the small channel eventually. Large deformation of the droplet is expected as the droplet has a diameter larger than the size of the small channel.

The effect of spatial grids and time step sizes on the solution is first investigated. Two solutions obtained using 100×50 CVs with $\Delta t = 0.10$ and 200×100 CVs with $\Delta t = 0.05$ are presented in Fig. 4-10a. Instead of the whole computational domain, only the portion of the small channel with the droplet, which is of interest, is shown. The two solutions agree with each other very well. Therefore, 100×50 CVs with $\Delta t = 0.10$ is enough to achieve spatial and temporal independent solution. This grid and time step size is used for the subsequent computations. For these computations, GMC is used.

Generally, the fluid flows faster in the small channel. A lower pressure is developed in the small channel, sucking the droplet into the small channel. This creates a cusp at the leading edge of the droplet. No slip condition is enforced at all walls, including those of

the small channel. A typical velocity profile across the small channel for $t = 5$ is shown in Fig. 4-10a. In the middle of the small channel, the fluid particles flow faster than those near the wall. Since the cusp is driven by a larger velocity at the middle of the channel, it becomes longer and sharper. Once in the small channel, the deformed droplet is squeezed by the main stream through the small channel. At the exit of the small channel, the flow expands since there is a sudden increase in cross sectional area. At this point, the v velocity component is no longer negligible.

From $t = 10$ to $t = 25$, mass (fluid 1) is transferred from the 'tail' of the droplet to the leading cusp. This is shown in Fig. 4-10b which depicts an enlarged portion of Fig. 4-10a for $t = 25$. Velocity vectors are also presented for the ease of explanation. The velocity in the 'tail' is larger than that in the leading cusp. This suggests that mass is transferred from the 'tail' and accumulated in the leading cusp. As a result, the leading cusp swells. This process is accompanied by shrinkage of the 'tail' as it is pushed by the main stream. The 'tail' disappears completely at $t = 30$ as the droplet emerges from the small channel. The emerged droplet is further deformed by the hydrodynamic force downstream of the flow field.

Figure 4-10c shows the mass errors with GMC and without GMC. Without GMC, the mass error remains finite, in the order of 10^{-2} to 10^{-3}. There is either mass surplus or mass loss. With GMC, the mass error reduces to machine zero (10^{-16}). This shows that GMC is a necessity to ensure mass conservation. Therefore, GMC is used in the subsequent computations.

The present solution is compared to that of VOF in Figs. 4-11a. The spatial and temporal independent VOF solution is obtained using 200×100 CVs with $\Delta t = 0.10$. The present

solutions are in good agreements with that of VOF both qualitatively and quantitatively. The effect of surface tension on the droplet evolution is shown in Fig. 4-11b. The surface tension coefficient is set to $\sigma = 0.05$. The surface tension force acts to smooth interface with high curvature. In the case of no surface tension (Fig. 4-11a), both the leading cusp and the 'tail' of the droplet are of large curvature, i.e. pointed. When surface tension is present, the pointed nature of both the cusp and 'tail' is suppressed.

4.5 Two-fluid Flow with Variable Surface Tension (Marangoni Effect)

4.5.1 Marangoni Force Driven Stratified Two-fluid Flow

Figure 4-12 shows a schematic of two stratified fluid layers. These fluids, i.e. fluid 1 and fluid 2, are immiscible in each other. The thickness of fluid 1 and fluid 2 are W_1 and W_2 respectively. They are separated by the F-F interface. There exists a variation of surface tension along the F-F interface. Surface tension varies linearly with x, i.e. $\frac{d\sigma}{dx} = const$. Such a surface tension gradient induces a net force tangential to the F-F interface (Marangoni force) dragging both layers into motion. It drives the fluids at the F-F interface to flow towards region of higher surface tension. Since the fluid layers extend to infinity, the F-F interface remains flat. Under such a condition, the capillary force (induced by the curvature of the F-F interface) acting normal to the F-F interface is zero.

This is actually a one-dimensional problem with $u(y)$ and $v = 0$. An analytical expression can be derived for $u(y)$ (see Appendix A) as

$$u = \frac{1}{\mu_i}\frac{dp}{dx}\frac{y^2}{2} + \frac{A_i}{\mu_i}y + \frac{B_i}{\mu_i} \tag{4-2a}$$

where

$$i = \begin{cases} 1, & \text{if } 0 \le y < W_1 \\ 2, & \text{if } W_1 \le y \le W \end{cases} \tag{4-2b}$$

$$A_1 = f\frac{d\sigma}{dx} - W_1\frac{dp}{dx} \tag{4-2c}$$

$$B_1 = 0 \tag{4-2d}$$

$$A_2 = -W_1\frac{dp}{dx} - \frac{d\sigma}{dx} + \frac{d\sigma}{dx}f \tag{4-2e}$$

$$B_2 = \left(W_1 W - \frac{W^2}{2}\right)\frac{dp}{dx} + W\frac{d\sigma}{dx} - W\frac{d\sigma}{dx}f \tag{4-2f}$$

$$f = \frac{\left(\frac{{W_1}^2}{2\mu_1} - \frac{{W_2}^2}{2\mu_2}\right)\frac{dp}{dx} + \frac{W_2}{\mu_2}\frac{d\sigma}{dx}}{\left(\frac{W_1}{\mu_1} + \frac{W_2}{\mu_2}\right)\frac{d\sigma}{dx}} \tag{4-2g}$$

Computation is made on a domain of height $W = 2$ and length $L = 1$. At $x = 0$ and $x = L$, $\frac{\partial u}{\partial x} = 0$. The F-F interface is held at $y = 1.2$, i.e. $W_1 = 1.2$ and $W_2 = 0.8$. For $\rho_1 = \rho_2 = 1$ and $\frac{d\sigma}{dx} = 0.01$, the following combinations of viscosities are investigated:

(a) $\mu_1 = 1$ and $\mu_2 = 10$

(b) $\mu_1 = 10$ and $\mu_2 = 10$

In evaluating the velocity profile from Eq. (4-2), $\frac{dp}{dx}$ is determined from the computations.

Figures 4-13a and 4-14a show the velocity profile obtained using 20×40, 40×80 and 60×120 CVs. It can be seen than 40×80 CVs is sufficient to achieve grid independent solution. For the case where the viscosities are identical (Fig. 4-14a), there is no

variation of properties across the interface. The flow becomes essentially a single fluid flow with additional surface force (due to surface tension) at the F-F interface. Therefore, even a mesh of 20×40 CVs is sufficient to capture all the essential features of the solution.

Figures 4-13b and 4-14b show the comparison between the analytical and the present solution. The computed velocity profiles are in good agreement with that of the analytical solution. This validates the present calculation of the Marangoni force. The peak velocity for the viscosity combination of $\mu_1 = 1$ and $\mu_2 = 10$ is around 0.00070. It is much higher than that of the case where $\mu_1 = 10$ and $\mu_2 = 10$, which is only around 0.00028. This is expected as the same Marangoni force is now acting on two fluid layers of large viscosity.

For the viscosity combination of $\mu_1 = 1$ and $\mu_2 = 10$, the effect of the F-F interface location on the velocity profile is shown in Fig. 4-15. The driving Marangoni force acts at the F-F interface. The wall effect is to retard the flow. When the driving Marangoni force is in close proximity to the wall ($W_1 = 0.4$ or $W_1 = 1.6$), wall effect becomes stronger. Therefore, the flow can only achieve a smaller peak velocity. This generally leads to a lower flowrates for both fluids. The wall effect is more profound for the case of $W_1 = 1.6$ as the viscosity of the fluid between the F-F interface and the wall closer to it (upper wall) is larger and therefore a stronger resistance to flow is encountered. The maximum peak velocity is achievable if the F-F interface is around $W_1 = 0.9$.

4.5.2 Droplet Flow in a Micro T-junction with Thermocapillary Effect

T-junctions or termed T-shaped constructs are the building blocks of highly complex tree-shaped flow architectures (Bejan et al., 2000 and Bejan and Lorente, 2006). Figure 4-16 shows a fluid 1 droplet of length l_d in a single micro T-junction. Fluid 2 at temperature T_{ref} flows into the micro T-junction with a fully developed velocity profile of u_{in} at the inlet. This corresponds to a mean velocity of u_m. As fluid 2 flows, it carries the droplet.

An asymmetric temperature field is induced in the T-junction by applying a heat flux q at the selected locations (Fig. 4-16). The remaining walls of the channel are properly insulated. As a result, the temperature dependent surface tension $\sigma(T)$ varies along the F-F interface. σ is assumed to vary linearly with temperature, i.e.

$$\sigma = \sigma_o + \frac{d\sigma}{dT}\left(T - T_{ref}\right) \tag{4-3}$$

where σ_o is the surface tension at temperature T_{ref}. The variation of σ induces an additional interfacial force (Marangoni force) on the droplet. A larger temperature gradient creates a larger surface tension gradient and therefore generates a larger Marangoni force. This suggests that the net force on the droplet, and thus its motion, can be controlled by adjusting the heater power.

Driven by the pressure gradient and the Marangoni force, fluid 2 together with the droplet flows out via outlet A or B. These outlets are maintained at the same pressure with a fully developed temperature profile.

Results are presented in dimensionless form for convenience. The present problem is

governed by a total of 8 dimensionless numbers: droplet length to channel width ratio ($\frac{l_d}{W}$), density ratio ($\frac{\rho_1}{\rho_2}$), viscosity ratio ($\frac{\mu_1}{\mu_2}$), thermal diffusivity ratio ($\frac{\alpha_1}{\alpha_2}$), Prandtl number ($\mathrm{Pr}$), Reynolds number ($\mathrm{Re}$), Capillary number ($Ca$) and Marangoni number ($Ma$). However, of all the dimensionless numbers, only variation of Ma is considered as the effect of the Marangoni force on the droplet motion is the sole interest. Pr, Re, Ca and Ma are defined as

$$\mathrm{Pr} = \frac{\mu_2}{\rho_2 \alpha_2} \tag{4-4}$$

$$\mathrm{Re} = \frac{\rho_2 u_m W}{\mu_2} \tag{4-5}$$

$$Ca = \frac{u_m \mu_2}{\sigma_o} \tag{4-6}$$

$$Ma = \frac{\left|\frac{d\sigma}{dT}\right| \Delta T}{\mu_2 u_m} \tag{4-7a}$$

ΔT in Ma is related to the heat flux q. Assumed that q increases the fluid 2 temperature flowing out at outlet A by ΔT, i.e.

$$qA \sim 0.5 \dot{m} c_{p2} \Delta T$$

$$q(3W) \sim 0.5(\rho_2 u_m W) c_{p2} \Delta T$$

$$\Delta T \sim \frac{6q}{\rho_2 u_m c_{p2}} \tag{4-7b}$$

This gives a Ma in term of the applied heat flux q.

$$Ma = \frac{6q\left|\frac{d\sigma}{dT}\right|}{\rho_2 c_{p2} \mu_2 u_m^2} \tag{4-7c}$$

The dimensionless time t^* and temperature T^* are given by

$$t^* = \frac{t u_m}{W} \tag{4-8}$$

$$T^* = \frac{T - T_{ref}}{\Delta T} \tag{4-9}$$

For demonstration, computations are made for a micro T-junction of $W = 400\,\mu\text{m}$. The dimensionless numbers are set to $\frac{l_d}{W} = 1.1$, $\frac{\rho_1}{\rho_2} = 1.0961$, $\frac{\mu_1}{\mu_2} = 0.0192$, $\frac{\alpha_1}{\alpha_2} = 1.1078$, $\text{Pr} = 441.9882$, $\text{Re} = 0.0175$ and $Ca = 0.00625$. $Ma = 0$, 40 and 80 are considered.

Figure 4-17 shows the evolution of the droplet obtained with different mesh sizes. For this particular case, the heater is switched off giving $Ma = 0$. A mesh of 63×150 CVs with a time step of $\Delta t^* = 1.5625 \times 10^{-4}$ is sufficient to achieve grid independent solution. Therefore, subsequent computations are made with this mesh and time step size. The droplet is much larger than the either of the outlet channel. It split into two daughter droplets of equal size. This is expected given the symmetry of the flow field. Each of these daughter droplets leaves the channel via one of the outlets.

As Ma is increased to 40, an asymmetric temperature field with strong temperature gradient at the upstream of branch A is generated. Figure 4-18a shows the induced dimensionless temperature field. The induced Marangoni force tends to drive the droplet towards branch A. As a result, a larger portion of the droplet is biased to flow into branch A as shown in Fig. 4-18b. The droplet is now split unequally with a larger daughter droplet forms in branch A.

Figure 4-19 shows the droplet evolution for $Ma = 80$. No splitting of the droplet occurs. In this case, the induced Marangoni force is so large that the whole droplet is driven to outlet A. The flow field as the droplet enters branch A is shown in Fig. 4-20. The asymmetric flow field is obvious even in Fig. 4-20a. A circulation is setup in the lower lobe of the droplet (Figs. 4-20e-j) driving the whole droplet into branch A.

The two cases of non-zero Ma suggest that a temperature gradient can be used to (1) split a droplet or droplet into two daughter droplets of controllable sizes and (2) switch a droplet or droplet into a desired branch in a bifurcating microchannel.

4.5.2.1 Importance of Artificial Viscosity

The importance of artificial viscosity is now discussed. In the F-F interface capturing procedure, the F-F interface is encapsulated in a band of finite thickness where the fluid properties change smoothly across it. The thickness of this band is currently set to 3 CVs. For the above computations, artificial viscosity is turned on. Artificial viscosity is added to the region outside of the band, i.e. beyond 1.5 CVs from the F-F interface.

The proposed artificial viscosity approach in ensuring numerical stability will be demonstrated for the case where the droplet splits equally ($Ma = 0$). Figure 4-21 shows the computational domain with the micro T-junction created using the block-off region approach of Patankar (1980). The purpose of creating the long blocked-off region along branches A and B will be explained later.

Three approaches, i.e. (1) without artificial viscosity ($\lambda = 0$ in Eq. 2.3), (2) with artificial viscosity added to the whole computational domain including at the interface ($\lambda = 6.7 \times 10^{-7}$ and $n = 0$) and (3) with artificial viscosity added to the region beyond 1.5 CVs from the F-F interface ($\lambda = 6.7 \times 10^{-7}$ and $n = 1.5$), are considered. Figures 4-22 show the evolution of the level-set function obtained with these approaches. The level-set function is shown for the whole computational domain as the behavior of

level-set function in the blocked-off region is of interest too. In these contour plots of the level-set function, the zero level-set (i.e. F-F interface) is drawn slightly thicker than other constant level-sets. For the purpose of comparison, the predicted F-F interfaces are enlarged and superimposed. In order to show the detailed history of the level-set function evolution leading to possible numerical instability, contour plots for the level-set function are given at 11 successive t^*.

Without artificial viscosity (approach 1), the level-set function is reasonably smooth up to $t^* = 0.1563$ (Fig. 4-22b). At $t^* = 0.3125$ (Fig. 4-22c), small disturbances (kinks) start to appear at the center of both branches A and B. These small disturbances amplify when propagating to other region of the domain. Finally, these disturbances reach the F-F interface at around $t^* = 0.6250$ (Fig. 4-22e). As the disturbances have just reached the F-F interface and yet to distort it, the predicted F-F interface up to $t^* = 0.6250$ (Fig. 4-22e) is considered to be correct. The F-F interface is then gradually distorted by these disturbances. The distorting effect of the disturbances becomes more and more obvious until it is so profound that the droplet even loses its symmetry (Fig. 4-22j). The solution blows up eventually. It is therefore important to damp away these disturbances once arise. This leads naturally to approach (2).

In approach (2), artificial viscosity is added to the whole domain including at the F-F interface. Although this damps away the disturbances, it modified the F-F interface evolution by including an unphysically damping mechanism at the F-F interface. Comparison of the predicted F-F interface with that of approach (1) for time up to $t^* = 0.6250$ (Fig. 4-22e) shows that approach (2) changes the F-F interface evolution. Besides, as the F-F interface approaches the long blocked-off region along branches A and B, the F-F interface unphysically and incorrectly diffuses into this region (Figs.

4-22g-j). The long blocked-off region is added to capture such a phenomenon. Both changing the F-F interface evolution and diffusing the F-F interface into blocked-off region are highly undesirable.

To overcome these undesirable effects of adding artificial viscosity, approach (3) is proposed. Instead of adding artificial viscosity over the whole domain, it is now added in the region 1.5 CVs beyond the F-F interface. Careful comparison is made on the predicted F-F interface for approach (1) and (3) in Figs. 4-22a-e. The F-F interfaces predicted by both approaches match each other. This demonstrates that the added artificial viscosity does not alter the F-F interface. Besides, the level-set function remains smooth even up to $t^* = 2.5$ (Fig. 4-22k). Any disturbance arises in the domain is damped. As a result, no disturbance is noticed throughout the computational domain for all time. Of the three approaches, only with approach (3) employed can the computation be completed successfully.

It is clear than if there is no artificial viscosity added, any disturbance however small or far from the F-F interface would build up and end up at the F-F interface eventually. This leads to the distortion of the F-F interface and blow up of the solution. Therefore, it is beneficial to cautiously damp away any disturbance employing approach (3). If desired, the idea in approach (3) can be extended to employing artificial viscosity only to specific regions deemed vulnerable to disturbances of the aforementioned nature.

A final remark is given for the selection of λ. It is the author's experience that only the order of magnitude of λ is important. The selection of λ is performed via numerical experimentation. For a case where the solution is known to blow up because of numerical instability of the above nature, approach (3) is used starting with a very small

λ, e.g. $\lambda = 1 \times 10^{-10}$. λ is increased gradually by increments of 1 order of magnitude until computation can be completed successfully.

4.6 Pressure Driven Stratified Two-fluid Flow in a Straight Channel

Figure 4-23 shows two immiscible fluid layers flow a distance L of a channel with height W. The F-F interface location is given by $y = \delta$. For a given set of densities (ρ_1 and ρ_2) and mass flowrates ($\dot{M}_1$ and $\dot{M}_2$), the inlet F-F interface location (δ_{in}) determines the inlet velocities of both fluids ($u_{in,1}$ and $u_{in,2}$). As the flow develops, the velocity profile at every section changes along the x-direction. As a result, the F-F interface evolves along the streamwise direction. Once the fully developed region is reached ($x = L_E$), the velocity profile and the F-F interface location (δ_E) become independent of x.

Fluids of identical properties are first considered. Then, the case where the fluids properties are different is investigated. The capability of LMC in ensuring mass conservation is demonstrated in both situations.

4.6.1 Fluids of Identical Properties

For the channel geometry, $L = 1$ and $W = 1$. Two immiscible fluids with the same densities ($\rho_1 = \rho_2 = \rho$) and viscosities ($\mu_1 = \mu_2 = \mu$) are considered. Surface tension coefficient is set to zero. With this choice of properties, the velocity profile at every x is the single-phase flow velocity. To initiate this study, the inlet velocities of the two fluids are also set to the same value, i.e. $u_{in,1} = u_{in,2} = 1$. The inlet F-F interface

location is $\delta_{in} = 0.3$. This gives a mass flowrate ratio of $\dot{M}_1 / \dot{M}_2 = 3/7$.

The effects of grid resolutions on the F-F interface location with and without LMC are shown in Fig. 4-24. Computations are carried out using 10×10, 20×20, 30×30, 40×40, and 50×50 CVs. It can be seen that the F-F interface location do not change when 40×40 and 50×50 CVs are used. As a result, unless otherwise specified, all subsequent results are obtained using 40×40 CVs.

Without LMC to ensure mass conservation, the fully developed F-F interface location varies with grid resolution before converging to its grid independent solution. It is interesting to point out that with LMC, the F-F interface location in the fully developed region is the same irrespective of the number of CV used. For a quantitative analysis, a mass error is defined.

$$\dot{M}_{err} = \left| \frac{\dot{M}_{in} - \dot{M}}{\dot{M}_{in}} \right| \tag{4-10}$$

In Eq. (4-10), $\dot{M}_{in}$ and $\dot{M}$ are the inlet mass flowrate and the calculated (local) mass flowrate respectively. $\dot{M}_{err}$ is calculated for both fluids. The mass errors for fluid 1 and fluid 2 are shown in Fig. 4-25. Without LMC, the mass errors are finite. These mass errors reduce to machine zero (10^{-16}) with LMC. For further comparisons, the "exact" F-F interface location is calculated and compared with the numerical prediction. The "exact" solution is obtained by ensuring the conservation of mass of fluid 1 using the discrete local single-phase velocity profile. For ease of discussion, assume the area occupied by fluid 1 spans from the first CV to part of the CV labeled N at a given x as shown in Fig. 4-26. The F-F interface location δ can be calculated as

$$\delta = \sum_{j=1}^{N-1} \Delta y_j + f\Delta y_N \tag{4-11a}$$

where f is the fraction of the area of CV labeled N occupied by fluid 1. The fraction f can be obtained by ensuring the conservation of mass of fluid 1. Let the mass flowrate into CV labeled j be $\Delta\dot{M}_j$. Then, the mass flow rate of fluid 1 can be written as

$$\dot{M}_{in,1} = \sum_{j=1}^{N-1} \Delta\dot{M}_j + f\Delta\dot{M}_N$$

or

$$f = \frac{\dot{M}_{in,1} - \sum_{j=1}^{N-1} \Delta\dot{M}_j}{\Delta\dot{M}_N} \tag{4-11b}$$

Figure 4-27a shows the F-F interface location and the velocity profiles at six streamwise locations with LMC employed. The fully developed velocity profile is identical to the exact solution from single-phase flow. The F-F interface location agrees with the "exact" solution exactly. This shows that with LMC, the F-F interface is correctly captured.

Figure 4-27b shows the ability of the procedure in predicting the F-F interface location with a non-uniform inlet velocity profile. Similar to the previous problem, the inlet F-F interface location is $\delta_{in} = 0.3$. However, the inlet velocities are $u_{in,1} = 2$ and $u_{in,2} = 1$. This results in a mass flowrate ratio of $\dot{M}_1 / \dot{M}_2 = 6/7$. From Fig. 4-27b, as expected, the single-phase velocity profile is recovered in the fully-developed region. The predicted F-F interface location compares well with the "exact" solution. Comparing Figs. 4-27a and 4-27b, fluid 1 occupies more of the flow area when the inlet velocity is increased.

The effect of surface tension on the flow is now considered. A larger entry length is expected with the presence of surface tension. The length of the domain is increased to $L = 2$. The inlet velocities of both fluids are equal, $u_{in,1} = u_{in,2} = 1$. To investigate the effect of surface tension, the Reynolds and capillary numbers are defined as

$$\mathrm{Re} \equiv \frac{\rho u_{in} W}{\mu} \tag{4-12}$$

$$Ca \equiv \frac{u_{in} \mu}{\sigma} \tag{4-13}$$

A case with $\mathrm{Re} = 0.01$ and $Ca = 0.1$ is first considered. For this problem, the inlet F-F interface location is set to $\delta_{in} = 0.3$. The effect of different grid sizes on the F-F interface location along the streamwise direction is shown in Fig. 4-28. It can be seen that grid independent solution is achieved with a mesh of 40 × 20 CVs. Unless otherwise specified, 40 × 20 CVs are used in the subsequence computations. It is obvious that from Fig. 4-28 that there is no noticeable change in the interface location beyond $x/W = 1.5$, with the F-F interface settling down at around $\delta_E / W = 0.36$. This indicates that the flow becomes fully-developed at $x/W = 1.5$. Although not shown, mass is conserved to machine zero with LMC.

Figure 4-29 shows the F-F interface location and the velocity field along the x-direction. Both are plotted up to $x/W = 1.0$ where changes are significant. The present solution is compared with the solution obtained using the VOF method. It can be seen that the present solution agree well with that of the VOF.

The effect of surface tension expressed in terms of Ca on the interface evolution is shown in Fig. 4-30. For these computations, σ is varied to obtain different Ca. Therefore, the Reynolds number is still maintained at $\mathrm{Re} = 0.01$. The limiting case of

$Ca = \infty$ corresponds to the situation where the surface tension effect is negligible. The interface locations predicted by VOF are superimposed for the purpose of comparison. The present solutions are in good agreement with that of the VOF. Once fully-developed flow is attained, the interface converges to the same value irrespectively of the Ca. This indicates that surface tension does not affect the fully-developed flow region. As Ca decreases, surface tension becomes more and more dominant. The role of surface tension is to minimize the F-F interfacial area. For the present flow configuration, the minimum interfacial area is achieved by having a flat surface, i.e. with a large radius of curvature. In another word, surface tension "flattens" the interface. As the boundary layer develops in the inlet region, curvature of the interface is created. This non-zero interface curvature leads to a surface tension force that tends to "flatten" the interface. This in turns hinder the development of the boundary layer. Therefore, for smaller Ca flow where the surface tension force is larger, the flow develops slower.

4.6.2 Fluids of Different Properties

In this problem, the flow of two immiscible fluids of different properties is examined. For this type of problem, the fully developed velocity profile and F-F interface location are functions of the viscosity ratio (μ_1 / μ_2) and the volumetric flowrates ratio ($\dot{V}_1 / \dot{V}_2$) and are independent of the inlet F-F interface location (δ_{in}) (Bird et al., 1971 and Churchill, 1988). For demonstration purposes, a channel with $L = 2$ and $W = 1$ is studied. The density ratio ρ_1 / ρ_2, mass flowrate ratio $\dot{M}_1 / \dot{M}_2$, viscosity ratio μ_1 / μ_2 are taken as 2, 0.837, and 10 respectively. These values are chosen so that the fully-developed F-F interface location is $\delta_E / W = 0.5$ in the fully developed region. A grid independent study shows that 80×40 uniformly spaced control volumes produces grid independent solution. Figure 4-31a shows the evolutions of the interface for three

values of the inlet interface locations δ_{in}/W namely, 0.3, 0.5 and 0.7 respectively. As expected, the interfaces evolve along the axial direction. Downstream from the entrance, all interfaces reach their fully developed value of 0.5. It is interesting to note that the interface developed faster when $\delta_{in}/W = 0.7$ (than when $\delta_{in}/W = 0.3$). This will be explained later. The associated mass errors are show in Fig. 4-31b. This demonstrates the capability of LMC in ensuring mass conservation even the properties of the fluids are different.

Figures 4-32 shows the evolutions of the velocity fields and interfaces for δ_{in}/W of 0.3 and 0.7. Once fully developed, all velocity profiles settle to the same shape. The predicted fully-developed velocity profiles compare very well with the exact solution of Bird et al. (1971). Although not shown, the interface profiles in the developing region compare well with the "exact" solution given by Eq. (4-11). From Fig. 4-32b, it can be seen that the inlet velocity profile with $\delta_{in}/W = 0.7$ is closer to the fully-developed profile than the inlet velocity profile when $\delta_{in}/W = 0.3$. As a result, the interface developed faster when $\delta_{in}/W = 0.7$. Churchill (1988) derived the fully developed interface location as function of μ_1/μ_2 and $\dot{V}_1/\dot{V}_2$. Figure 4-33 shows the comparisons between the present computations and the exact solutions of Churchill (1988). It can be seen that the present procedure captures the F-F interface correctly for the range of viscosity and volumetric flowrate ratios considered.

The effect of surface tension is again considered. A uniform inlet velocity of $u_{in,1} = u_{in,2}$ is employed. ρ_1/ρ_2, μ_1/μ_2, $\dot{V}_1/\dot{V}_2$ and Re are set to 2.0, 2.0, 3/7 and 0.01 respectively. Since the fluid properties are different, the Reynolds and the capillary numbers are redefined using the properties of fluid 2.

$$\mathrm{Re} \equiv \frac{\rho_2 u_{in} W}{\mu_2} \tag{4-14}$$

$$Ca \equiv \frac{u_{in} \mu_2}{\sigma} \tag{4-15}$$

Other than Re and Ca, the Eötvös number characterizing the relative importance of gravitational force to surface tension force is defined.

$$Eo \equiv \frac{|\rho_1 - \rho_2| g W^2}{\sigma} \tag{4-16}$$

The importance of gravity is first investigated. As seen in Fig. 4-34, the interface profile is not affected by gravity as long as $Eo \le 1$. As Eo decreases with the channel size, the effect of gravity becomes less important in microchannels. It is also noticed that the development length increases as the channel becomes smaller (smaller Eo). There seems to exist a "maximum" development length. Once this length is reached, further decrease in Eo does not alter the development length. As the solutions are invariant for $Eo \le 1$, Eo is set to 0. As a result, the development lengths for the remainder of this article are the maximum possible lengths.

Figure 4-35 shows the F-F interface together with the velocity profiles at selected streamwise locations. The VOF prediction is superimposed on the same figure. There is a good agreement between the present prediction and that of the VOF method for both the F-F interface and velocity profiles. The F-F interface settles down at around $\delta_E / W = 0.39$. If compared to the case where the properties of the fluids are the same (Fig. 4-29), the fluid 1 layer becomes thicker. This can be explained by the fact that a more viscous fluid 1 produces a thicker boundary layer. Although the mass flowrate of fluid 1 is doubled, its effect on the F-F interface location is not obvious. Its effect can only be noticed if very large density ratio ρ_1 / ρ_2 is used.

Figure 4-36 shows the pressure distribution across the streamwise direction, starting from $x/W = 0.2$. For comparison to be made, the pressure field at a given axial location is adjusted by adding a constant so that the pressure at the lower plate is zero. Therefore, the axial pressure gradient $\frac{\partial p}{\partial x}$ cannot be inferred from this figure. The pressure jump across the interface is obvious. However, the jump is not sharp and abrupt. In the CSF surface tension formulation, the interface is assumed to have a finite thickness of 2ε. The pressure would vary smoothly across this interfacial thickness. Therefore, a "sharper" or more "abrupt" pressure jump would be predicted by using a smaller ε. Nevertheless, the magnitude of pressure jump across the interface remains unaltered and is captured correctly. The pressure jump is larger in the developing region because of a larger curvature. The pressure jump reduces gradually as the curvature decreases along the streamwise direction. Comparison is made with the pressure field predicted by VOF. There is good agreement between the two predictions except at $x/W = 0.2$. At this section, although both predict a similar trend, the pressure distribution is quantitatively different. The maximum error $(p_{VOF} - p_{present})/(p_{MAX} - p_{MIN})$ (all values at $x/W = 0.2$) is around 6%.

The F-F interface profiles for $Ca = 0.1, 0.2$ and ∞ are shown in Fig. 4-37. Also shown are the predictions of the VOF method. Good agreement between the two methods is achieved. A trend similar to the case where the properties of both fluids are identical is observed.

For flow without surface tension, as mentioned, the fully developed velocity profile and F-F interface location are functions of the viscosity ratio (μ_1/μ_2) and the volumetric flowrates ratio ($\dot{V}_1/\dot{V}_2$) and are independent of the inlet F-F interface location (δ_{in})

(Bird et al., 1971 and Churchill, 1988). This is still valid for the case with surface tension because surface tension only affects the flow characteristics in the developing region. For demonstration, the volumetric flowrate ratio $\dot{V}_1/\dot{V}_2$ and viscosity ratio μ_1/μ_2 are fixed at 3/7 and 2 respectively. The inlet velocities of both fluids have to be modified accordingly to maintain the same volumetric flowrate for different inlet interface locations. Figure 4-38 shows the F-F interface profiles for $\delta_{in}/W = 0.3$, 0.5 and 0.7 with and without surface tension. Although the interface locations at the inlet are different, all the fully-developed interfaces converge to the same location even with the presence of surface tension.

4.7 Pressure Driven Stratified Two-fluid Flow in a Double-Bend

Figure 4-39 shows the schematic for a stratified two-fluid flow in a double-bend. The term "stratified" in this case is used loosely for the "stratification" of the fluids on the walls. The initial thickness of fluid 1 at the inlet is δ_{in}. A uniform inlet velocity of $u_{in,1} = u_{in,2}$ is employed. The definitions of the Reynolds and the capillary numbers follow Eqs. (4-12) and (4-13). ρ_1/ρ_2, μ_1/μ_2, $\dot{V}_1/\dot{V}_2$ and Re are set to 2.0, 2.0, 1.0 and 0.01 respectively. The detailed geometry is given in Fig. 4-40. For this flow geometry, much larger curvature is induced when the flow negotiates the bend. Thus, the overall effect of surface tension on the flow field is expected to be more obvious.

Before proceeding further, it is worth digressing for awhile to discuss the LMC procedure. The original LMC procedure makes use of the mass flowrate at every streamwise section to correct the interface to ensure mass conservation. However, for the present flow geometry, the streamwise direction does not always align with either of the coordinate axes. It changes from the x-direction to the y-direction after the first bend,

then back to the x-direction again after the second bend. Complications may arise during computation if mass flowrate at every streamwise section is used to correct the interface, especially at the bends. Fortunately for the present flow geometry, for the flow to travel from the inlet to the outlet (left to right), the mass flowrate at every x location remains constant irrespective of the stremwise direction of the flow. With this, the mass flowrate at every x-section is used to correct the interface. Therefore, no additional modification on the localized mass correction procedure is required.

Figure 4-40 shows the F-F interface profile for $Ca = 0.1$ obtained using 40×20, 80×40 and 160×80 CVs. Grid independent solution is obtained using 80×40 CVs. All the subsequent computations are made using the same number of CVs. It is interesting to note that the essential features of the interface are captured even with a coarse mesh of 40×20 CVs.

The F-F interface profile and the velocity field with and without LMC are shown in Fig. 4-41. Both sets of results are the grid independent solutions. Different F-F interface profiles and velocity fields are predicted. As a result, mass correction must be performed for this problem to ensure proper mass conservation. The difference of the F-F interface and velocity predicted is more profound at the bends area where curvature is larger. The mass errors for fluids 1 and 2 are shown in Fig. 4-42. Without LMC, the mass errors are finite. These mass errors reduce to machine zero (10^{-16}) with LMC, an indication of ”perfect” mass conservation.

Figure 4-43 shows the velocity vectors plot for the solution obtained using 160×80 CVs. This fine mesh solution is selected so that small vortices could be detected. Only one in every five velocity vectors is shown to avoid over-crowding the figure. The velocities at

the two "boxed" corners are extremely small and hence could not be shown. These regions are enlarged and plotted with the unit velocity vectors. For these enlarged figures, all velocity vectors are shown. It is clear that there is a vortex at each of the corner, an indication of recirculation. Figure 4-44 shows comparisons between the present prediction and the VOF method. All the velocity profiles show the variation of u across the streamwise section, but the third velocity profile shows the variation of v instead. These predictions agree well quantitatively for both interface location and velocity field. There is no noticeable change in the F-F interface location downstream of around $x/W = 1.4$. This implies that the flow is fully-developed. The pressure jump across the F-F interface is shown in Fig. 4-45. The jump is larger in the bend area where the curvature is large. The prediction of VOF is also shown for comparison where reasonable agreement is obtained.

As the presence of surface tension alters the F-F interface, the flow field would generally be affected. Figure 4-46 shows the effect of surface tension on the flow field. The F-F interfaces without surface tension ($Ca = \infty$) and with surface tension ($Ca = 0.1$) are shown. The effect of surface tension is most profound at the two bends. With surface tension present, the F-F interface profile changes, thinning either one of the fluids. This is accompanied by a redistribution of the velocity field with the peak of the velocity profile shifting towards the thinning fluid to maintain the same mass flowrate. For example, at $y/W = 0.5$, surface tension causes a thinning of fluid 1. The change of the v-velocity profile is obvious with the peak shifted towards fluid 1. As the flow becomes fully developed at around $x/W = 1.4$, the two interface collapse to a single straight line, i.e. of zero curvature. With zero curvature, there is no surface tension effect. Hence, the velocity profile for with and without surface tension collapse to a single curve.

4.8 Flow around Stationary, Forced and Freely Rotating Cylinders

The proposed F-S interface tracking procedure is first validated using (1) flows around stationary, (2) flow around forced rotating and (3) flow around freely rotating circular cylinders. Figure 4-47 shows a circular cylinder of diameter d, centered at (x_c, y_c) in a two-dimensional channel. The length and height of the channel are L and W respectively. The average inlet velocity of the fluid is u_m. The moving fluid exerts a drag force F_D and lift force F_L on the cylinder. The Reynolds number Re, the lift coefficient C_L and the drag coefficient C_D are defined as

$$\mathrm{Re} = \frac{\rho u_m d}{\mu} \tag{4-17}$$

$$C_L = \frac{2F_L}{\rho u_m^2 d} \tag{4-18}$$

$$C_L = \frac{2F_D}{\rho u_m^2 d} \tag{4-19}$$

The drag forces on flow around a stationary and non-rotating cylinder in an infinite domain subjected to a uniform inlet velocity are predicted. Both the length L and height W are set to 200 times the diameter d to simulate an infinite domain. Non-uniform mesh with finer mesh clustered around the cylinder is used to capture the flow field near the cylinder. The predictions, obtained using the proposed approach are tabulated in Table 4-1a. The present predictions compare well with available results up to Re = 40.

The same problem is repeated but now, with the cylinder rotating at a constant angular velocity Ω. In addition to the Reynolds number Re, a dimensionless angular velocity $\beta = \Omega d/(2u_m)$ is defined to characterize the flow. Table 4-1b shows comparisons between the current predictions and available data. As expected, the angular rotation

generates a non-zero lift force leading to a non-zero C_L. The present solutions compare well with those obtained from the full Navier-Stokes (NS) equations (Ingham and Tang, 1990) and using Series Expansion (SE) (Tang and Ingham, 1991) solutions.

In the next problem, a stationary (non-translating) cylinder is placed off centered with an eccentricity $e = (2y_c - W)/(W - d)$ between two parallel plates. The length L, height W and x_c are 27.5d, 4d and 7.5d respectively. Fully-developed flow enters the channel at $x = 0$. The characteristic velocity and characteristic length are the maximum inlet velocity (at $y = W/2$) and the diameter of the cylinder respectively. As the cylinder is placed eccentrically, lift force and torque are generated. Two situations namely, (1) fix (non-rotating) cylinder and (2) freely rotating cylinder are investigated. Table 4-1c shows comparisons between the present computations and available results of Juárez et al. (2000). Again, the lift and drag coefficients match available solutions well for both cases. The dimensionless angular velocity β for both cases are also tabulated for completeness.

The procedure is validated against flows around stationary (non-translating) cylinder which can rotates about a fixed stationary axis. Further validation is made for the case with translational motion. The case of a settling circular cylinder under gravity is selected and presented next.

Table 4-1: C_D for flow around a stationary cylinder.

Re	Present	(1)	(2)	(3)	(4)	(5)	(6)	(7)	(8)
1	11.596	-	-	9.94	-	-	-	11.00	12.55
10	2.855	2.81	2.78	2.67	-	-	-	3.15	-
20	2.065	2.01	2.01	2.08	2.05	2.03	2.22	2.36	-
40	1.547	1.54	1.51	1.73	1.52	1.52	1.48	1.85	-

Note: (1) Silva et al. (2003)
(2) Park et al. (1998)
(3) Sucker and Brauer (1975)
(4) Dennis and Chang (1970)
(5) Ye et al. (1999)
(6) Triton (1959)
(7) White (1991)
(8) Tomotika and Aoi (1951)

Table 4-2: C_L and C_D for flow around a forced rotating cylinder.

		C_L			C_D		
		(9) & (10)			(9) & (10)		
Re	β	NS	SE	Present	NS	SE	Present
5	0	0	0	6.4596E-13	3.947	3.947	4.1239
5	0.5	1.389	1.384	1.3979	3.916	3.929	4.0917
5	1.0	2.838	2.768	2.8142	3.849	3.875	3.9958
20	0	0	0	2.13E-14	1.995	1.995	2.0512
20	0.5	1.283	1.271	1.2653	1.973	1.959	2.0164
20	1.0	2.617	2.541	2.5618	1.925	1.886	1.9138
60	0	0	0	3.3054E-12	1.279	1.279	1.3094
60	0.5	1.109	1.085	1.0591	1.251	1.264	1.2812
60	1.0	2.249	2.170	2.1983	1.207	1.219	1.1876

Note: (9) Ingham and Tang (1990)
(10) Tang and Ingham (1991)

Table 4-3: C_L and C_D for flow around a freely rotating cylinder.

		Ω	β	C_L		C_D	
Re	*e*	(11)	Present	(11)	Present	(11)	Present
100	5/6	0 (static)	0	-0.3798	-0.37383	0.9440	0.93407
100	5/6	0.0682 (freely rotating)	0.07497	-0.4644	-0.46332	0.8949	0.88416

Note: (11) Juárez et al. (2000)

4.9 Sedimentation of a Circular Cylinder between Parallel Plates

Figure 4-48 shows the schematic of the problem. A circular cylinder of diameter d is placed at $(0, y_c)$ between two parallel plates spaced $4d$ apart. The cylinder, which is heavier than the fluid, is initially at rest. When it is released, it travels downward due to gravity. It will eventually reach its terminal velocity u_T. The diameter of the cylinder and its terminal velocity are the characteristic length and the characteristic velocity respectively. The trajectories of the cylinder ($\mathrm{Re} = 0.522$) released at different lateral location off the centerline are shown in Fig. 4-49. The results from the present computation compare well with those reported in the literature (Feng et al., 1994). As seen, the cylinder drifts towards the centerline for the Re studied.

4.10 Flow of Particles in a Microchannel System

Figure 4-50 shows a microchannel system with two inlets (A and B) and two outlets (C and D). A primary stream of carrier fluid flows into the system via inlet A. Another secondary stream of carrier fluid carrying particles is injected into the primary stream through inlet B. The fluid merges, flows through a constriction and exits through one of the two outlets (C and D). The motion of the particle is determined by the resultant force due to hydrodynamics and inertia effects. The inertia of the particle acts to maintain its original course and the hydrodynamic force steers the particle to travel along the streaklines. Therefore, as the inertia of particle increases, the motion of the particle deviates from the streakline of the carrier fluid. Depending on the flow condition, particle size and etc, a particle can exit through either one of the exits.

The motion of a single circular particle is first considered. The particle initially located at (x_c, y_c) is at rest. Water, with a density and a viscosity of 1000 kg/m^3 and 0.001

Ns/m^2 respectively, is used as the carrier fluid. The inlet velocities u_A and u_B are set to 1000 μm/s and 4000 μm/s respectively.

The motion of a 30-μm diameter aluminum particle initially located at $(140,104)$ is investigated. Figure 4-51 shows the trajectories of the particle obtained using a time step size of $\Delta t = 2.50\times10^{-5}$ s with 151×118 CVs and $\Delta t = 1.25\times10^{-5}$ s with 302×236 CVs. The locations of the particle for every 1.25×10^{-2} s are shown for comparison purposes. It can be seen that a time step size of $\Delta t = 2.50\times10^{-5}$ s with 151×118 CVs produces grid independent solution. As a result, all subsequent computations are performed using this time step and mesh size. As expected, the particle gains speed (particles spaced further apart for a fixed $\Delta t = 1.25\times10^{-2}$ s) reaching a maximum velocity inside the constriction. As the flow bifurcates and leaves through the two exits, the particle slows down and travels towards exit C.

Figure 4-52 shows the effect of particle size on its trajectory. Initially, aluminium particles of two different diameters, i.e. 30 μm and 50 μm are placed at $(137,104)$. The particles travel along two different trajectories. The 30 μm and 50 μm particles are carried by the carrier fluid to outlet C and outlet D respectively. The locations of the particle for every 2.5×10^{-2} s are shown for comparison purposes.

Figure 4-53 shows the effect of particle density on its trajectory. The particles are initially placed at $(140,104)$. The densities of the particles are set to 2700 kg/m^3 (aluminum) and 8960 kg/m^3 (copper). The hydrodynamic force on these particles of different densities but of identical size does not vary much. However, a denser particle

implies a larger mass. The acceleration caused by the same hydrodynamic force on a denser particle is therefore smaller. As a result, denser particle moves with a lower velocity and takes longer time to reach the outlet. This effect is more obvious after the particles enter the T-junction.

Figure 4-54a shows the trajectories of three copper particles flowing in the microchannel system. There are two circular and an elliptical copper particles. A 30-μm diameter circular particle is initially located at $(125,32.5)$. A larger (35-μm diameter), circular particle is initially located at $(163,71.5)$. The major and minor axes of the elliptical particle are 45 and 30μm respectively. This elliptical particle is initially located at $(135,117)$. All three particles are initially at rest. The larger circular and the elliptical particles are driven to outlet C while the smaller circular particle is carried to outlet D. The positions of these particle at eight time steps namely, $t = 0$, 0.025, 0.050, 0.075, 0.100, 0.125, 0.150 and 0.1675s are shown. The velocity of these particles is highest when they are flowing through the constriction.

Figure 4-54b shows the trajectories of two complex shaped copper particles in the microchannel system. The local distance function of each particle is obtained by merging the distance functions for two smaller elliptical particles of identical size. Particle 1 consists of two small elliptical particles of each with major and minor axes of 55μm and 30μm respectively. These two small elliptical particles are initially located at $(140,130)$ but orientated with their major axes perpendicular to each other. Particle 2 is formed from two small elliptical particles identical to those of particle 1 with each initially located at $(140,65)$ and $(140,52)$ respectively and their major axes orientated perpendicular to each other. The positions of particles 1 and 2 at $t = 0$, 0.025, 0.050, 0.075, 0.100, 0.125 and 0.150s are shown. Both particle 1 and 2 are driven to outlet D.

This example demonstrates the idea of merging a few distance functions (for simple shaped particles, .e.g. elliptical particle) to form the local distance function for more geometrically complex particle or solid. With this, the present F-S interface tracking procedure can therefore be employed to investigate the flow of particles or solids with complex geometries.

4.11 Electrophoresis of Circular and Elliptical Particles

Figure 4-55 shows a charged circular particle in a microchannel. Both the particle and the wall are non-conducting. The particle is subjected to an electrical field given by

$$\vec{E} = -\nabla\varphi \tag{4-20}$$

An applied electrical field parallel to the *x*-axis is considered. For such an electrical field, the following boundary conditions are prescribed for the electrical potential φ.

$$x = 0,\ \varphi = \varphi_1 \tag{4-21a}$$

$$x = L,\ \varphi = \varphi_2,\ \varphi_2 < \varphi_1 \tag{4-21b}$$

$$y = 0 \text{ or } y = W,\ \frac{\partial\varphi}{\partial y} = 0 \tag{4-21c}$$

With these, the applied electrical field can be expressed as

$$E = \frac{\varphi_1 - \varphi_2}{L} \tag{4-22}$$

Thin EDLs form at both the particle and the wall surfaces. The formation of EDLs at the surfaces set the fluid in motion and consequently drives the particle.

A case where the particle is placed in the proximity of a charged infinite plane wall is first considered. The steady-state translational and angular velocities of the particle are of interest. To simulate an infinite domain, the length and height of the domain is set to $L = 600d$ and $W = 300d$. The selection of these dimensions is performed with the

domain successively enlarged until there is no effect of the domain size on the solution. For computational purpose, non-uniform mesh with very fine mesh around the particle is employed. The circular particle has a diameter of $d = 20$ μm and is initially located at $(x_c, y_c) = (0.5L, 30)$. The zeta potentials of the wall and the particle are $\zeta_S = -50 \times 10^{-3}$ V and $\zeta_W = -100 \times 10^{-3}$ V respectively. The steady-state solution does not depend on the density of the particle. The density of the particle merely dictates the time taken to achieve steady-state. For computational purpose, it is set to $\rho_S = 8960$ kgm^{-3}.

The same phenomenon has been investigated analytically by Keh et al. (1991). They provided analytical expressions for the translational and angular velocities of the particle. Figures 4-56 show the comparison of the translational and angular velocities. The present predictions match with the analytical solutions.

The particle moves in the positive *x*-direction. To explain this, consider the scenario in Fig. 4-57. If the wall is absent, the electrophoretic velocity of the particle under the same applied electric field is given by

$$U_e = \frac{\varepsilon_e \zeta_S E}{\mu} \text{ (-ve)} \tag{4-23}$$

as ζ_S is negative. Therefore, the particle moves electrophoretically in the negative *x*-direction. This is however not necessary true if the wall is present. On the wall, the slip velocity is

$$u\big|_{y=0} = \left(\frac{\varepsilon_e \zeta_W}{\mu} \right) \frac{\partial \varphi}{\partial x} \text{ (+ve)} \tag{4-24}$$

as both ζ_W and $\frac{\partial \varphi}{\partial x}$ are negative. The EDL at the wall drives the flow in the positive *x*-direction. As the particle is close to the wall, it is strongly influenced by the velocity

field generated by the EDL at the wall. For the situation considered, $u|_{y=0}$ is twice as strong as U_e (because of the different in zeta potentials). The flow field induced by the EDL at the wall overcomes that of the particle. The net effect is therefore driving the particle in the positive *x*-direction.

A case where the size of the particle is comparable to that of the microchannel is now considered. The length and height of the microchannel are set to $L = 400$ μm and $W = 200$ μm respectively. A circular particle of density $\rho_S = 8960$ kgm^{-3} and diameter $d = 80$ μm is initially suspended at $(x_c, y_c) = (200,100)$. Solutions are obtained for neutral ($\zeta_S = 0$), positively ($\zeta_S = +51\times10^{-3}$ V) and negatively ($\zeta_S = -204\times10^{-3}$ V) charged particles. The zeta potential of the wall is set to $\zeta_W = -102\times10^{-3}$ V.

A grid independent study shows that a mesh of 82×43 CVs with $\Delta t = 1.25\times10^{-4}$ is sufficient to achieve grid independent solution (Fig. 4-60a). The velocity vectors inside the solid are due the implementation of the no-slip boundary conditions inside the solid. This mesh and time step size is used for the subsequent computations. The particle is located at the center of the microchannel, it experiences neither vertical translation nor rotation. Figure 4-58 shows the instantaneous location of the particles with different zeta potentials. The translational velocity U of the particle is given by the gradient of the graph. For all cases, the gradient is constant. This implies that the particles accelerate in a very short time to a constant velocity and move with that constant velocity thereafter. This is not unexpected as the inertia force is negligible in such a small scale channel.

The induced electro-osmotic flow is in the positive *x*-direction. A neutral particle thus flows in the positive *x*-direction. Figure 4-59 shows the velocity field around the neutral particle at $t = 0.05$, 0.10, 0.15 and 0.20. No distortion of the velocity field is observed. This indicates that the particle flows with the same velocity as the fluid.

When the particle is charged, an additional electrophoretic flow is induced around the particle. It pushes a positively charged particle to flow in the positive *x*-direction. With both electro-osmotic and electrophoresis effects acting in the same direction, the particle flows with a higher velocity as implied by a larger gradient in Fig. 4-58. The velocity field around the positively charged particle is shown in Fig. 4-60. Since the particle is flowing faster than the fluid, a low pressure region is created at the trailing edge. Fluid is drawn into this region. On the other hand, a high pressure region is created at the leading edge, pushing the fluid to move forward.

For the negatively charged particle, the electrophoretic effect tends to drive it in the negative *x*-direction. As the particle is highly negatively charged, the electrophoretic effect is strong enough to overcome the electro-osmotic effect. As a result, the particle is driven to flow in the negative *x*-direction creating regions of high velocity between the particle and the walls (Fig. 4-61).

Finally, the application of the present model to electrophoresis of multiple particles is demonstrated. Instead of only one, there are a total of three particles in the microchannel. These particles are labeled 1, 2 and 3 (Fig. 4-62a). The semi-major, semi-minor axes, initial location and zeta potential of the particles are:

Particle 1: 50μm, 40μm, $(120,60)$, -306×10^{-3} V

Particle 2: 50μm, 50μm, $(180,150)$, $+61\times10^{-3}$ V

Particle 3: 40μm, 30μm, $(220,70)$, 0 V

The directions of the particle movement are indicated by the arrows. The motions of the particles are qualitatively similar to the above case study. The velocity fields around the particles at $t = 0.04$, 0.08 and 0.15s are shown in Figs. 4-62b-d.

4.12 Flow of Particle-Encapsulated Droplet through a Constricted Microchannel

Figure 4-63 shows a particle-encapsulated droplet flowing in a constricted microchannel. Three phases are involved in the present problem, i.e. the carrier fluid (fluid 1), the droplet (fluid 2) and the solid particle (a solid phase). The circular particle is located at (x_c, y_c). It has a diameter of d. This particle is encapsulated in a circular droplet of diameter d_d and located at (x_d, y_d). The carrier fluid flows into the microchannel with a uniform velocity of u_{in} at the inlet. As it flows, it exerts a hydrodynamic force on the droplet in the form of surface stress, carrying the droplet with it. Meanwhile, the fluid particles in the droplet impinge on the surface of the solid particle. An exchange of momentum occurs. This generates a hydrodynamic force on the solid particle. As a result, the solid particle undergoes both translational and rotational motions. The droplet, together with the particle encapsulated, is therefore carried by the pressure driven immiscible carrier fluid.

For demonstration, a particle of diameter $d = 40$ μm and is initially suspended at $(150,99.5)$ is studied. It has a density of $\rho_S = 2700$ kg/m^3. The particle is encased by a droplet of diameter $d_d = 170$ μm and located at $(150,99.5)$. The density ρ_1 and viscosity μ_1 of the droplet are set to 1000kg/m^3 and 0.001Ns/m^2 respectively. The

density ρ_2 and viscosity μ_2 of the carrier fluid are 800 kg/m^3 and 0.01 Ns/m^2 respectively. Surface tension σ is set to 1×10^{-4}N/m. The inlet velocity of fluid 2 is 2000μm/s. Artificial viscosity is switched on with $\lambda = 4\times10^{-9}$ and $n = 1.5$ (determined experimentally). These parameters are retained in all the subsequent cases unless stated otherwise.

The evolution of the F-F interface and the motion of the particle are shown in Figure 4-64a. Solutions obtained using uniform meshes of 173×41 CVs with $\Delta t = 4.0\times10^{-5}$s and 346×82 CVs with $\Delta t = 2.0\times10^{-5}$s. Both the F-F and F-S interfaces do not show any noticeable difference for these mesh sizes. Therefore, a mesh of 173×41 CVs with $\Delta t = 4.0\times10^{-5}$s is sufficient to achieve grid and temporal independent solution. The droplet undergoes significant change in shape when it is squeezed through the constriction. Surface tension keeps the F-F interface smooth, minimizing the droplet surface area. The particle which is initially located at the center of the droplet is increasing pushed toward the front portion of the droplet. As the droplet emerges from the constriction, the droplet is more "bullet-like". In this computation, GMC is employed with fluid 1 used as the reference fluid. The mass errors for computations with and without GMC are shown in Fig. 4-64b. There is around 10% mass loss at the end of the computation if GMC is not used. Only with GMC employed, the mass of fluid 1 is well conserved.

The effect of the carrier fluid viscosity is shown in Fig. 4-65. Three different viscosities, i.e. 0.001, 0.005 and 0.010 Ns/m^2 are considered. The droplet and the particle at t = 0, 0.025, 0.050, 0.075, 0.100, 0.125 and 0.150s are shown alternatively as solid or dashed line. As μ_2 increases, the boundary layer thickness of the carrier fluid increases. This is especially evident in the constriction. The droplet is squeezed in such a way that the

F-F interface is further away from the wall. The cross-sectional area available for the droplet to flow decreases. As such, the droplet flows faster. This generates a larger hydrodynamic force on the encapsulated particle and propels it further downstream with a higher velocity. When the droplet emerges from the constriction, surface tension minimizes the F-F interfacial area by rounding out the frontal portion of the droplet. However, the effect of the boundary layer of the carrier fluid remains significant. It pushes the portions of the F-F interface near the wall to the center of the channel, compressing the droplet into more 'bullet-like' shape for larger carrier fluid viscosity.

The evolutions of the particle-encapsulated droplet with different surface tension are depicted in Fig. 4-66. σ is set to 0.5×10^{-4}, 1.0×10^{-4} or 2.5×10^{-4}N/m. The droplet and the particle at t = 0, 0.025, 0.050, 0.075, 0.100, 0.125 and 0.150s are shown. σ minimizes the F-F interfacial area. For a circular droplet, it maintains the circular shape of the droplet as the F-F interfacial area is minimal. Therefore, σ acts to resist any stretching of the droplet by the flow field. Larger σ implies more resistance to deformation and thus smaller stretching. When the droplet flows into the constriction, severe stretching occurs. For the case of larger σ, stretching is smaller with the frontal and rear portion of the droplet rounded out more. This is depicted lucidly in the F-F interface at t = 0.050 and 0.100s. The droplet flows slower given an increase in cross-sectional area for it to flow. A smaller hydrodynamic force acts on the encapsulated particle. Therefore, the particle moves slower. After the droplet emerges from the constriction, σ tries to restore the circular shape of the droplet, lowering the velocity of the F-F interface in the frontal portion of the droplet. This is because the surface tension force which is tangential to the interface has a backward component. Such a slowdown in the F-F interface movement causes the particle to break out from

the encapsulation for the case of $\sigma = 2.5 \times 10^{-5}$ N/m.

The effect of different particle density is now investigated. Three different particle densities are considered, i.e. 2700, 6000 and 8960kg/m^3. When the particle is impulsively acted upon by the hydrodynamic force, the inertia effect is found significant only in a very short period of time. Figure 4-67 shows the variation of the particle streamwise velocity U over this period of time beyond which no obvious dependent of U on the particle density is observed. Since the particles are of the same size, a larger particle density implies a larger mass. The inertia is larger and therefore it has more resistance to motion. The denser particle experiences a smaller acceleration and thus moves with a smaller velocity. It takes a slightly longer time to attain particle density independent U. The distance covered in this time interval is only about 20-30μm which is relatively small compared to the total distance the particle will travels downstream (around 700μm). This indicates that the effect of particle density on the overall movement of the particle is not obvious. Therefore, no obvious effect on the F-F interface is observed as shown in Fig. 4-68.

4.13 Flow of Particle-Encapsulated Droplets in a Microchannel System

Figure 4-69 shows a particle-encapsulated droplet in a microchannel system. The 80μm diameter droplet is initially suspended at $(150,117)$. The density and viscosity of the droplet are $\rho_1 = 2000$ kg/m^3 and $\mu_1 = 0.002$ Ns/m^2 respectively. A circular solid particle of diameter $d = 30$ μm and density $\rho_S = 8960$ kg/m^3 is encased in the droplet. At both inlets A and B, fluid 2 flows into the microchannel with velocities of $u_A = 1000$ μm/s and $u_B = 4000$ μm/s respectively. Its density and viscosity are

$\rho_2 = 1000$ kg/m^3 and $\mu_2 = 0.001$ Ns/m^2 respectively. Surface tension is set to $\sigma = 1\times10^{-5}$ N/m for demonstration purpose. Artificial viscosity is switched on with $\lambda = 4\times10^{-9}$ and $n = 1.5$ (determined experimentally).

Figure 4-70a shows the evolutions of the F-F and F-S interfaces. It is clear that a mesh of 152×102 CVs with $\Delta t = 1.25\times10^{-4}$ s is sufficient to capture all the essence of the interfaces. There are two situations where the particle is prone to break out from the droplet. These are (1) as the droplet flows through the constriction and (2) as the droplet is making a turn. For (2), the inertia of the particle is larger than the droplet. A larger force is required for the particle to make the same turn. Therefore, it does not follow exactly the droplet trajectory and tend to break out from the droplet. It should be pointed out that as the droplet turns into branch D, the encapsulated particle breaks out from the droplet. Computation is stopped at $t = 0.1100$ s as post break out flow is not the present interest. Such a computation involves a three-phase contact line problem which is not addressed in the present study.

The evolutions of the particle-encapsulated droplet with and without GMC are show in Fig. 4-70b. Different F-F and F-S interfaces are predicted. The droplet for the case without GMC is increasingly smaller than that with GMC after it emerges from the constriction. The mass error for the reference fluid (fluid 1) is shown in Fig. 4-70c. Without GMC, the mass loss of the particle-encapsulated droplet is increasing over time. Substantial mass up to almost 30% is lost at the end of the computation. With acute mass loss, even the F-S interface can be affected as the flow field changes due to a small "droplet". Again, GMC conserves the reference fluid mass well.

The application of the present model for the case of two particle-encapsulated droplets is now presented. A second droplet is added. This droplet of diameter 100μm is located at $(70,306)$. It encases an elliptical particle with major and minor axes of 44μm and 30μm respectively. The particle is initially located at the center of the droplet. Figure 4-71 shows the evolution of the F-F and F-S interfaces. One in every five velocity vectors is shown to avoid overcrowding the figure. The elliptical particle encapsulate-droplet is trailing the circular particle-encapsulated droplet given the smaller driving flow at inlet A. The elliptical particle undergoes obvious rotational motion. Examination of velocity field suggests that the circular and elliptical particles are driven to outlet D and C respectively. Computation is stopped at $t = 0.1250$ s when the circular particle breaks out from the droplet.

4.14 Concluding Remarks

In this chapter, the proposed three-phase flow model is applied to a variety of multiphase problems. The F-F interface capturing procedure is validated against droplet flows and stratified two-fluid flows in various channels. For these cases, the F-F interface evolutions are predicted and compared with that of the VOF method whenever possible. Good agreements are achieved for these comparisons. Good mass conservation is demonstrated for droplet flows with GMC employed and stratified two-fluid flows with LMC employed. For flow with complex geometry, e.g. droplet flow in a micro T-junction with thermocapillary effect, the proposed artificial viscosity addition plays a decisive role in ensuring smoothness in the advection of level-set function. This enhances numerical stability tremendously.

F-S interface tracking procedure is validated against (1) flow around stationary, forced

and freely rotating cylinders and (2) sedimentation of a cylinder between parallel plates. In these cases, the results compared well with the existing literatures. The capability of the F-S tracking procedure is demonstrated for both pressure and electrically driven flow of a single and multiple particles in microchannels. The application of the procedure to multiple geometrically complex particles is also presented.

Finally with the F-F interface capturing and F-S interface tracking procedure validated, these procedures are applied simultaneously for three-phase flow problems involving particle-encapsulated droplets flow in microchannels. GMC is shown to conserve mass well for these three-phase flow problems.

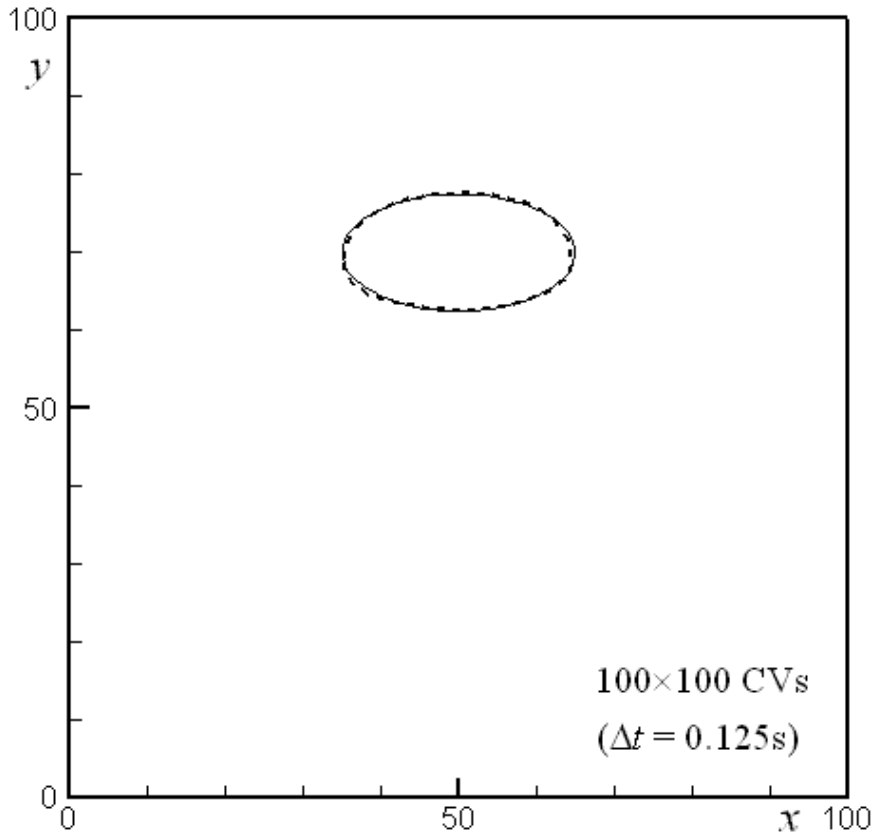

(a) An elliptical disc.

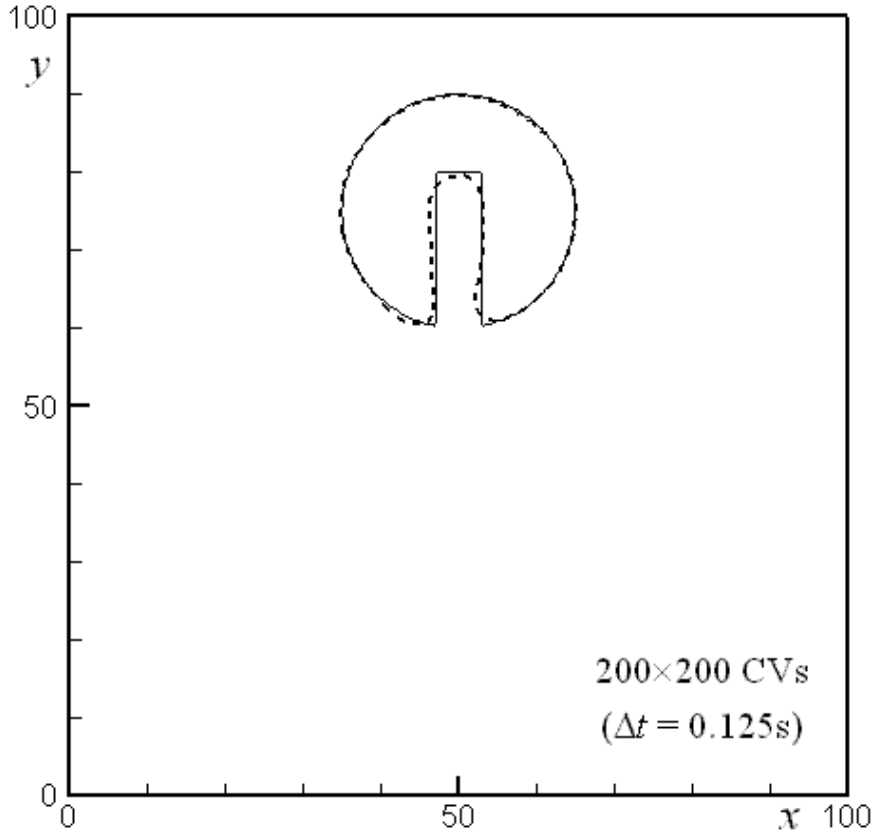

(b) A slotted circular disc.

Figure 4-1: Rigid body rotation of discs.

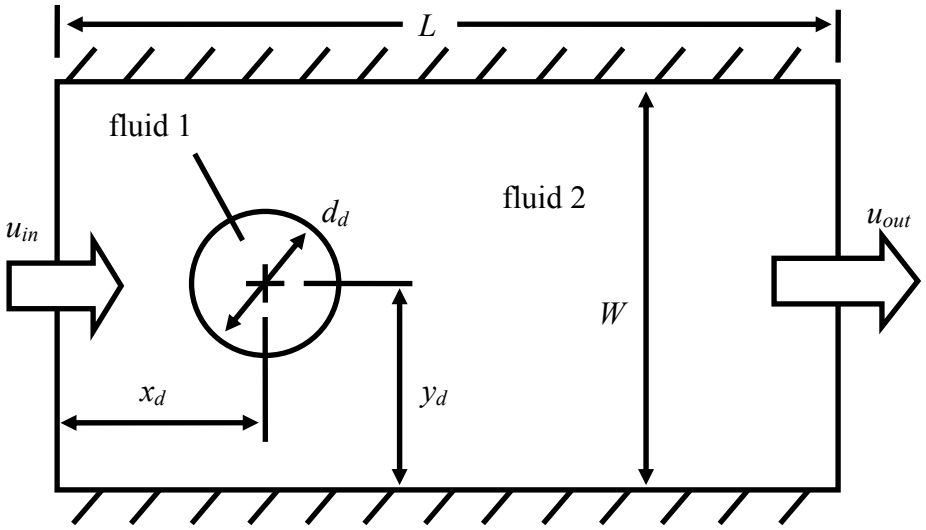

Figure 4-2: Droplet flow in a straight channel.

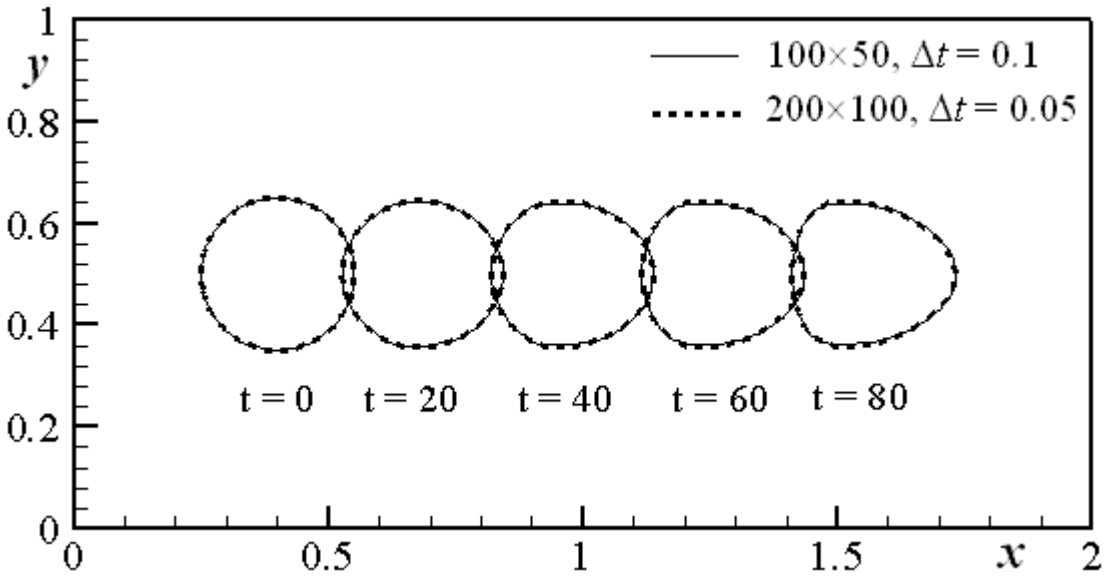

Figure 4-3a: Grid independent study.

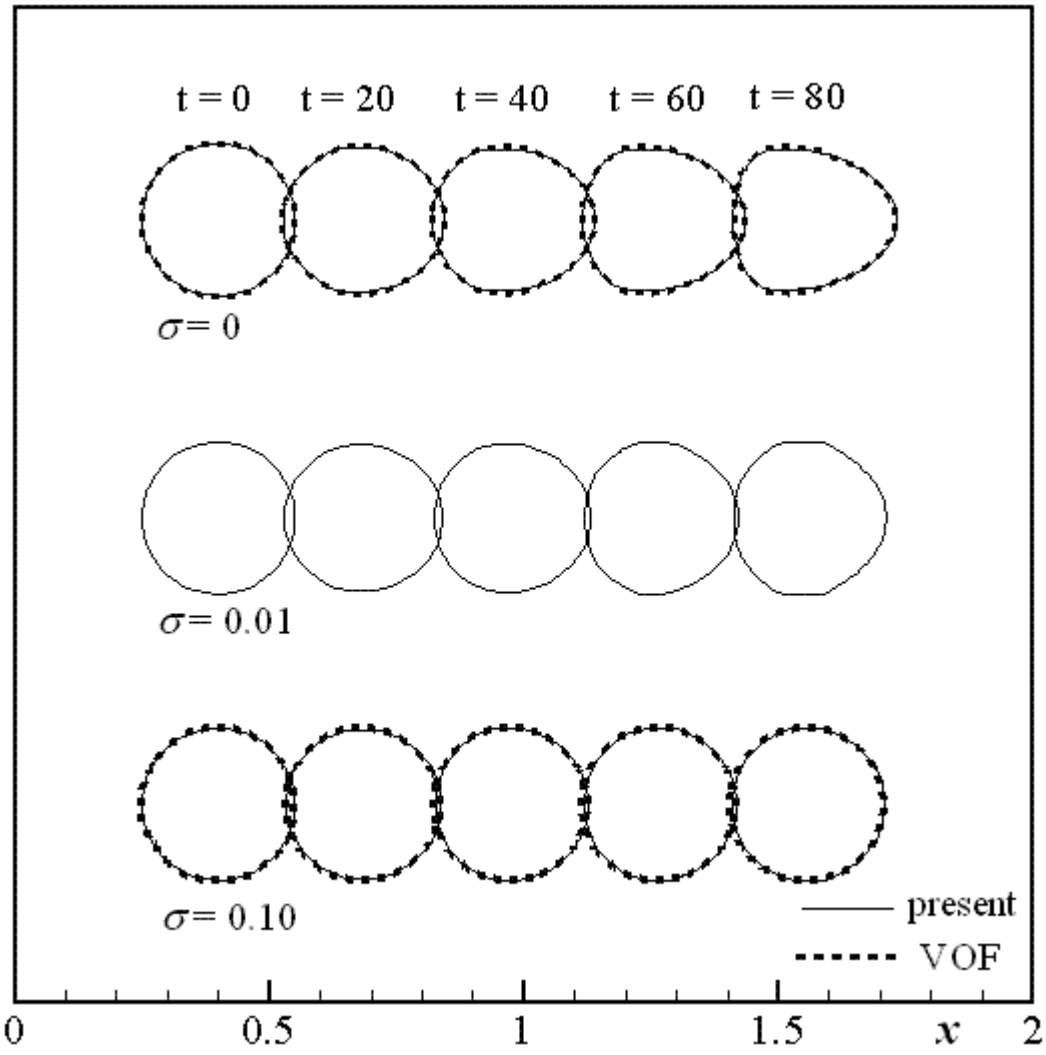

Figure 4-3b: Effect of surface tension.

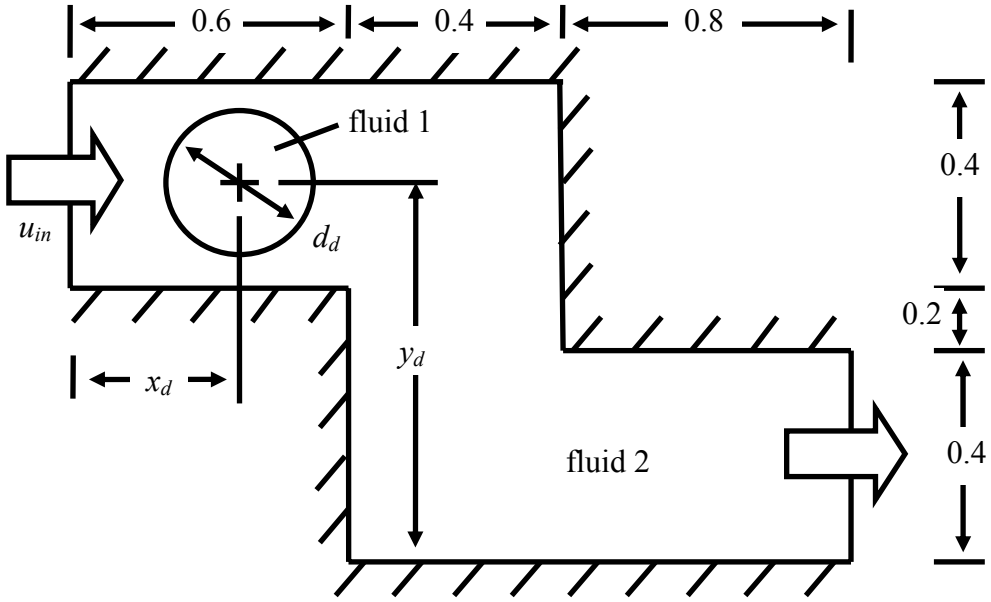

Figure 4-4: Droplet flow in a double-bend.

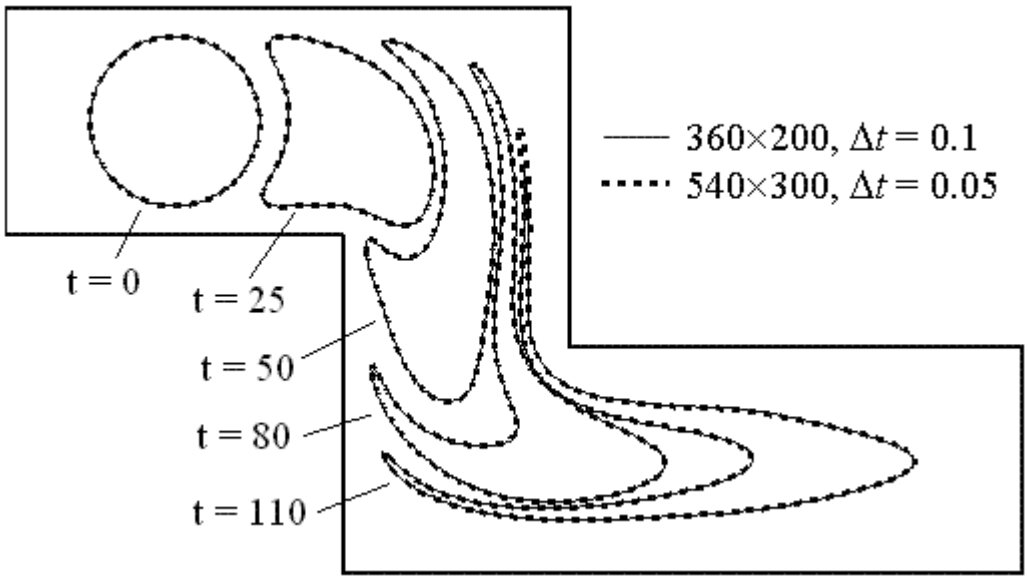

(a) Grid independent study.

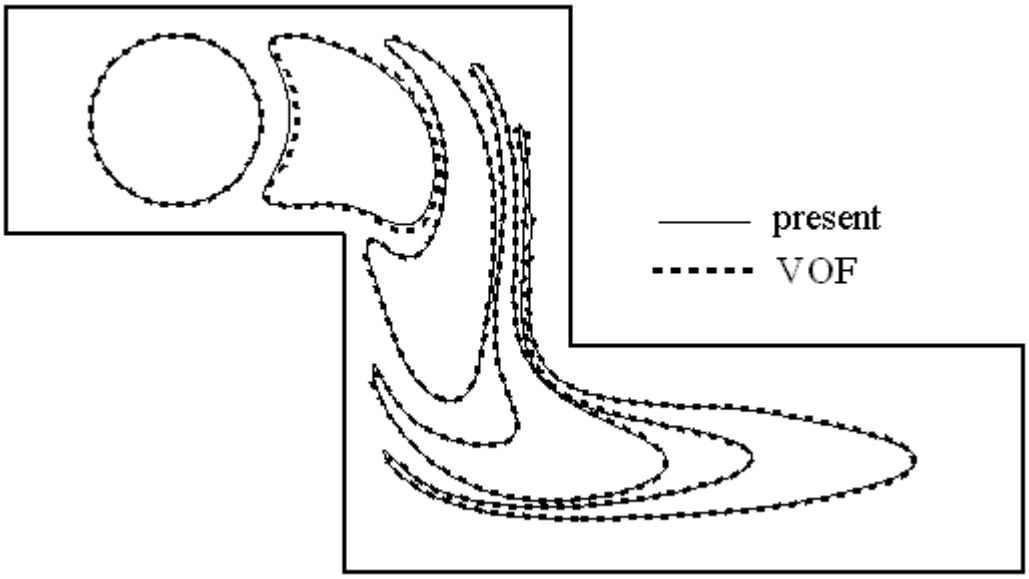

(b) Present (with GMC) and VOF comparison.

Figure 4-5: Evolution of a droplet in a double-bend without surface tension.

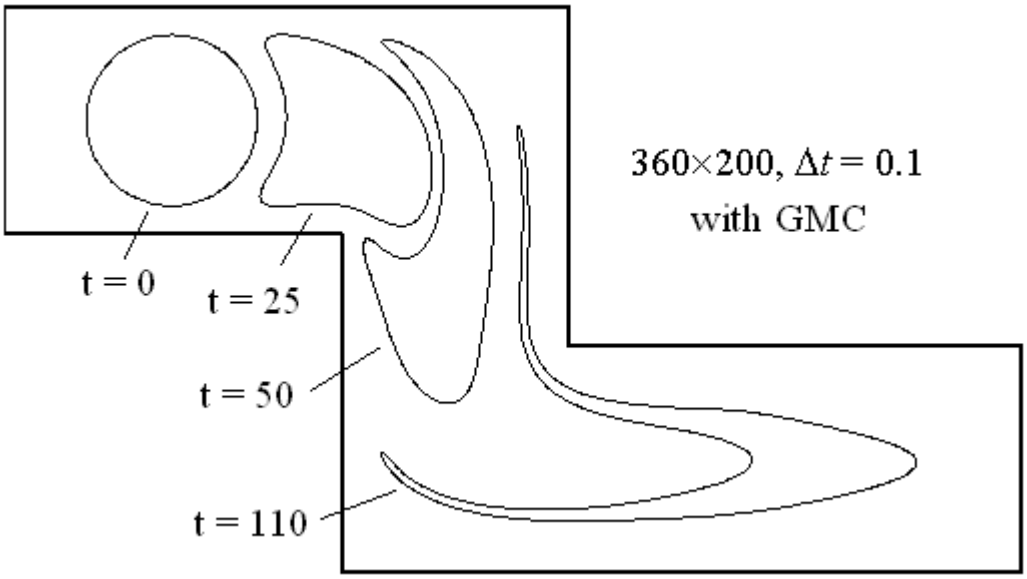

(c) Present with GMC.

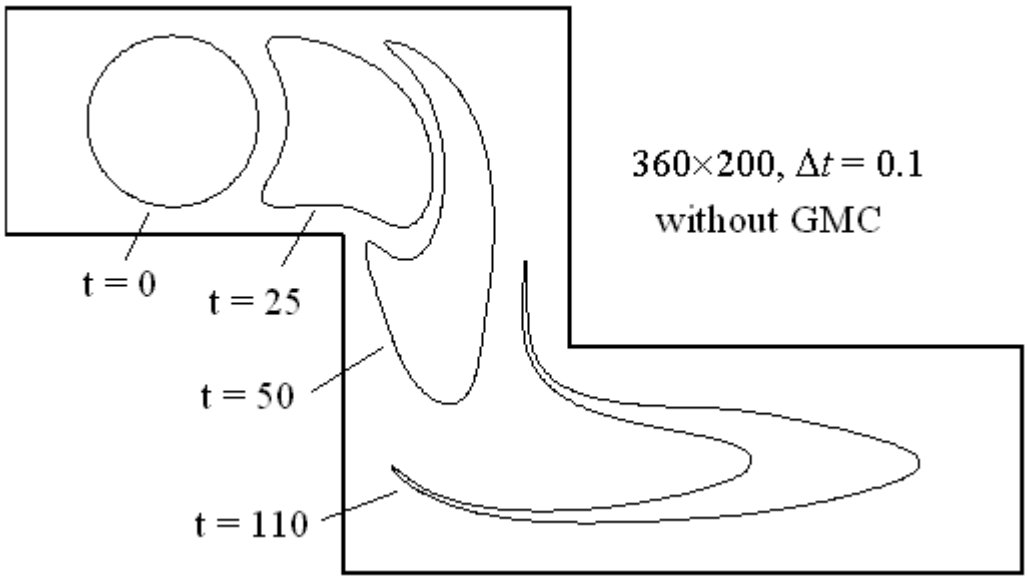

(d) Present without GMC.

Figure 4-5: Evolution of a droplet in a double-bend without surface tension.

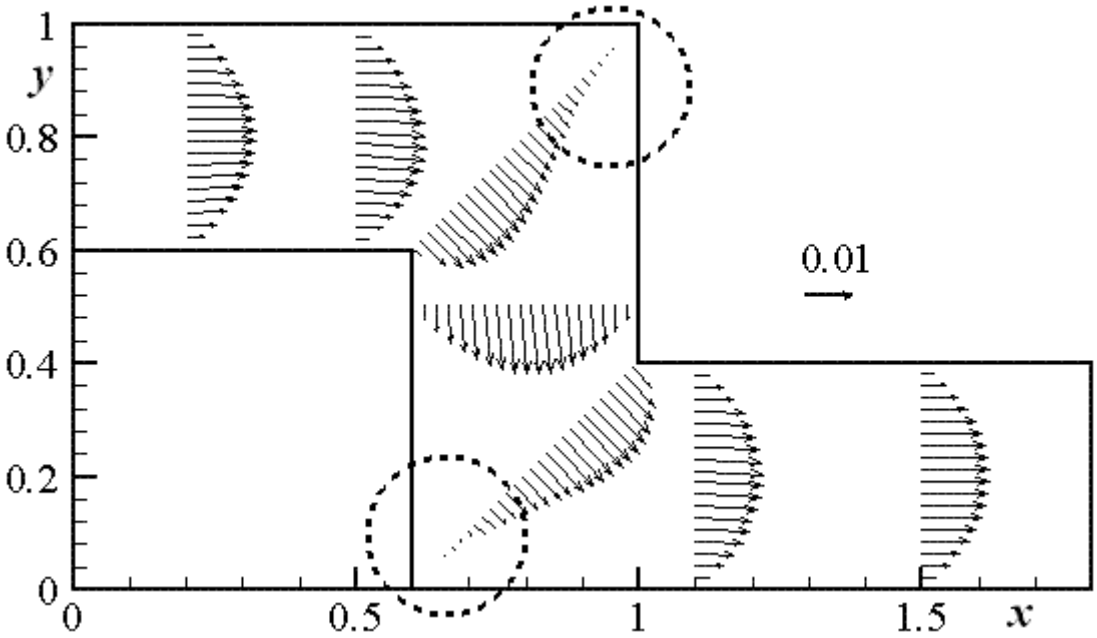

Figure 4-6: Velocity profiles for the flow in a double-bend channel at t = 110.

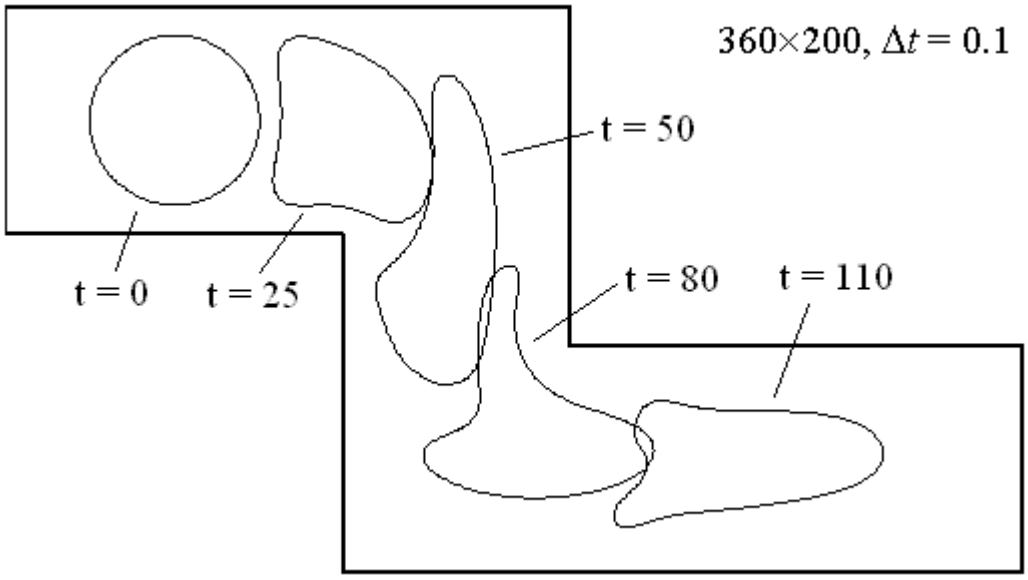

(a) $\sigma = 0.01$

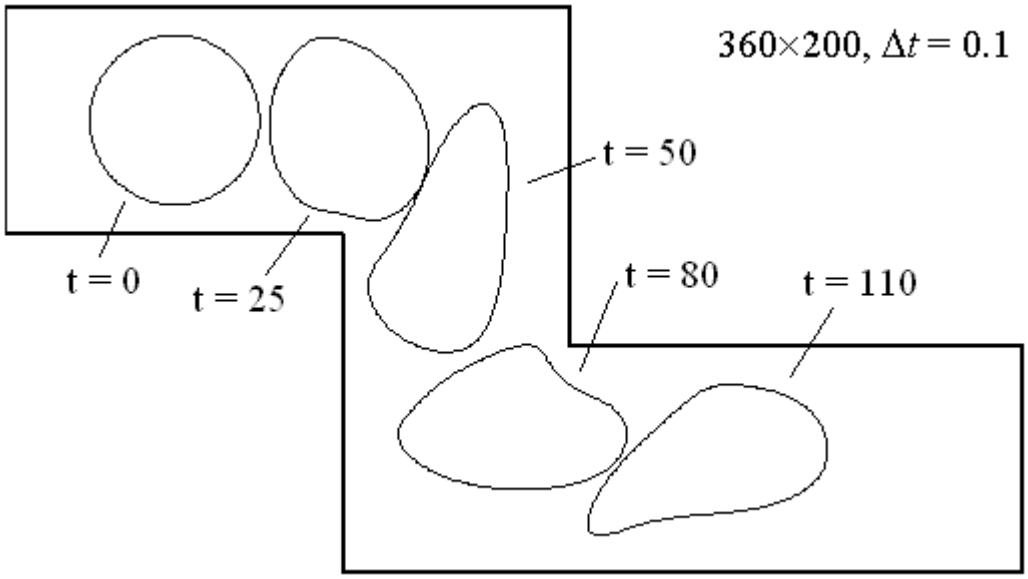

(a) $\sigma = 0.05$

Figure 4-7: Evolution of a droplet flowing in a double-bend channel with surface tension effect.

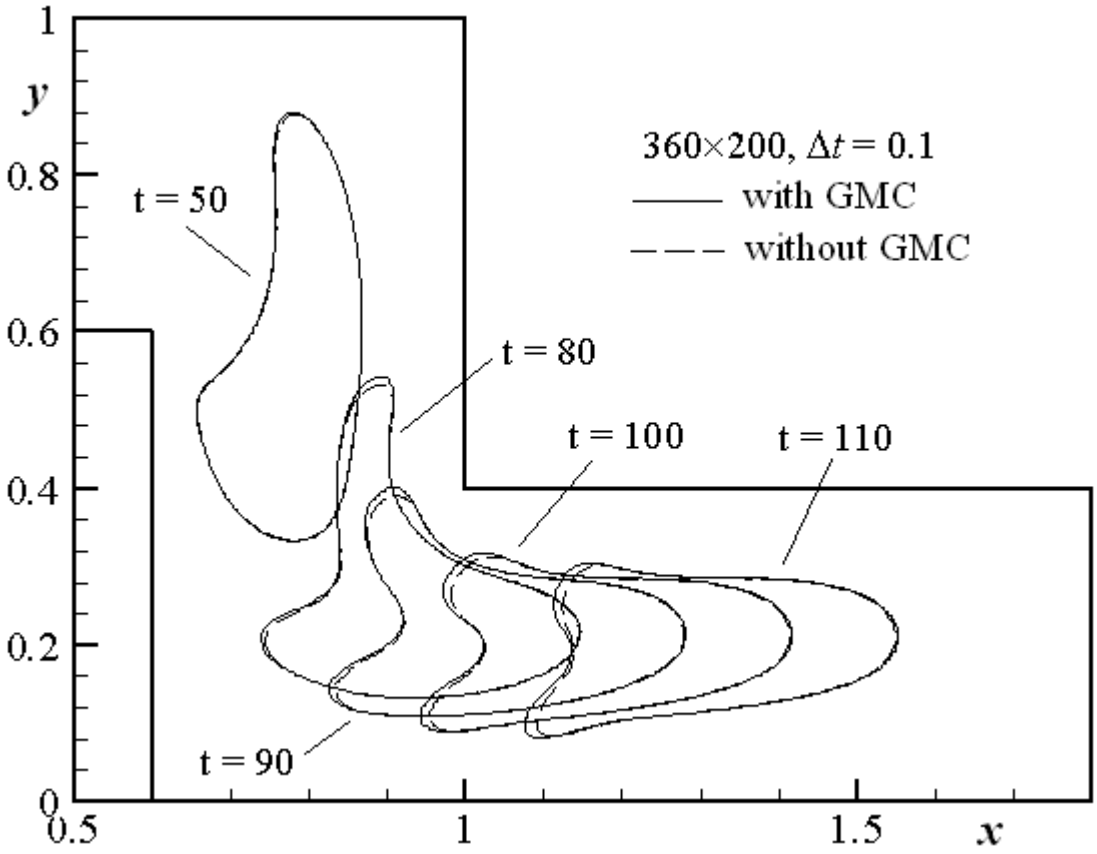

(a) Droplet interfaces.

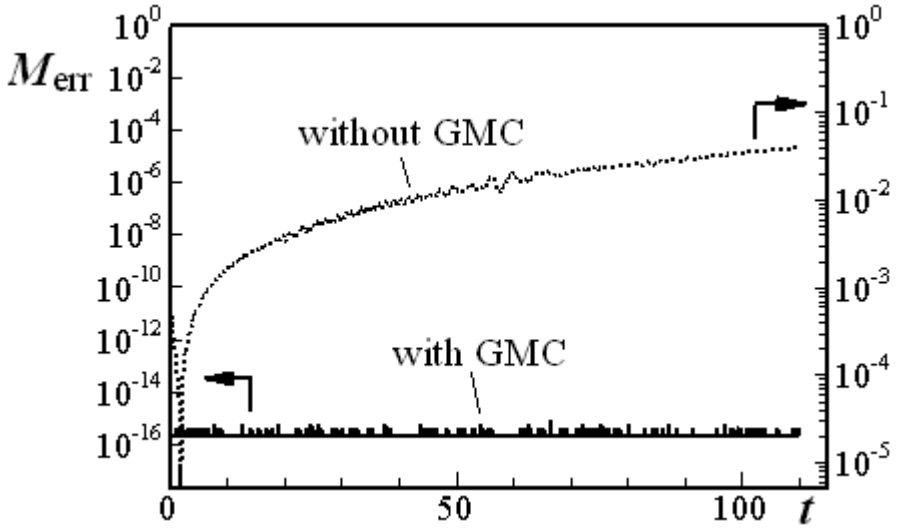

(a) Mass errors.

Figure 4-8: Evolution of a droplet flowing in a double-bend channel with surface tension effect $\sigma = 0.01$ computed with and without GMC.

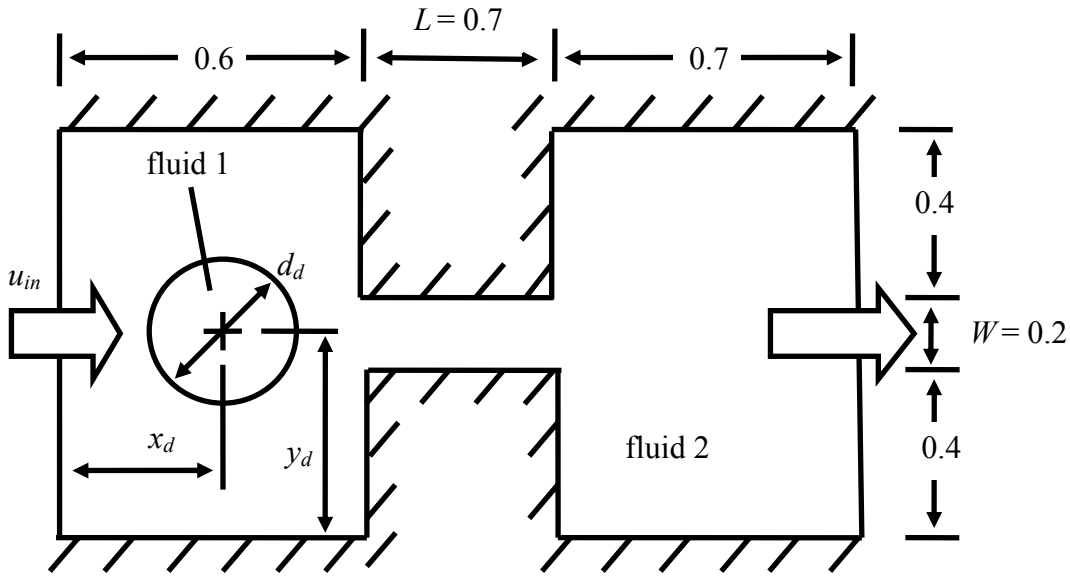

Figure 4-9: Droplet flow through a constricted channel.

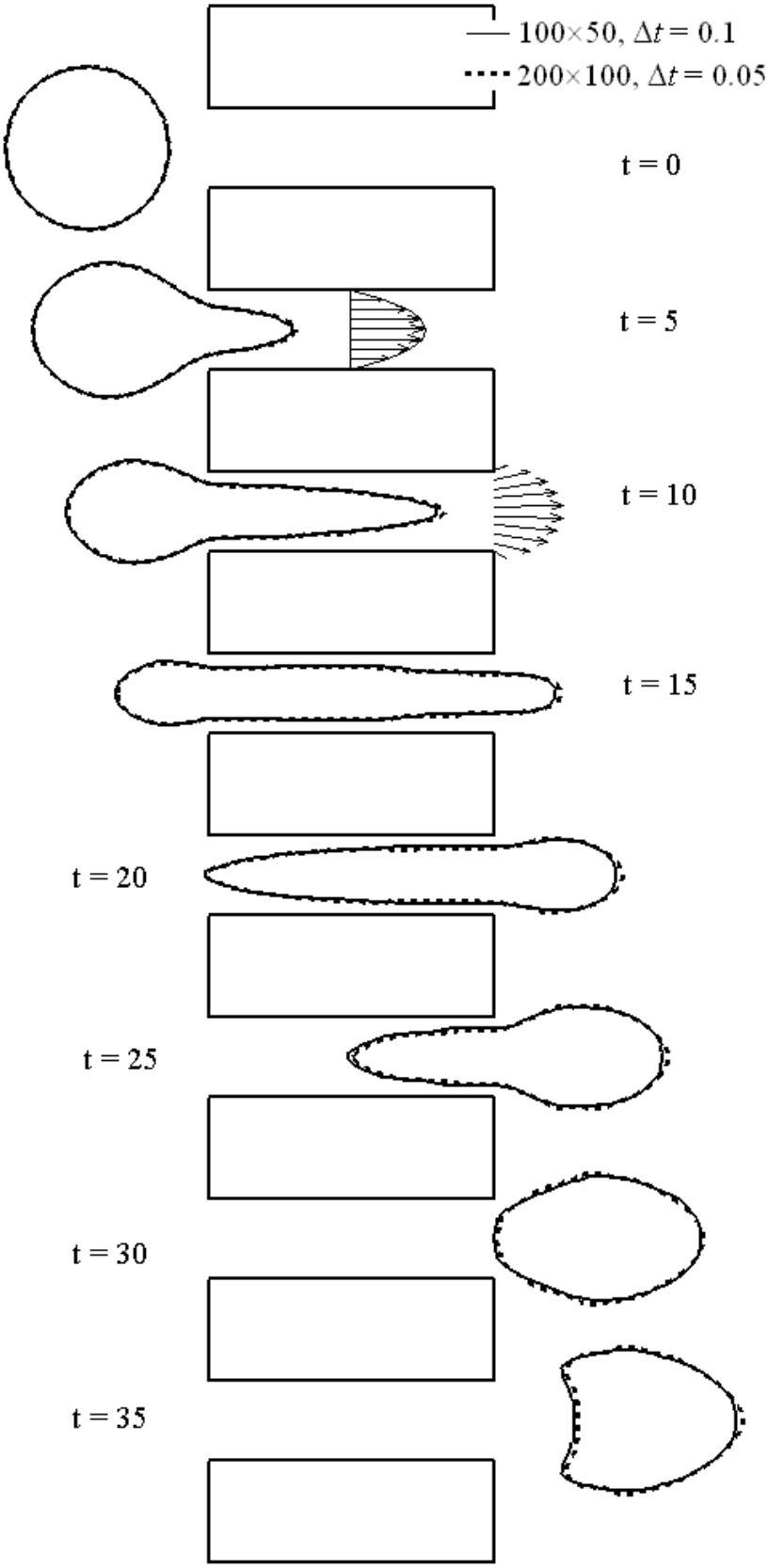

Figure 4-10a: Grid independent study for a droplet squeezed through a constricted channel.

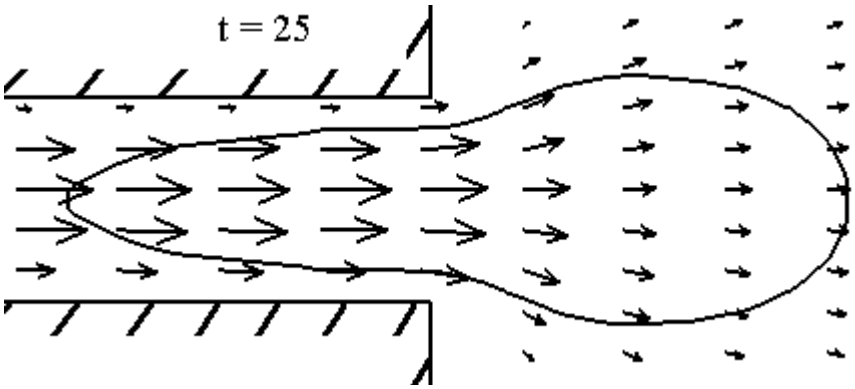

Figure 4-10b: Droplet interface and velocity vectors at $t = 25$ for a droplet squeezed through a constricted channel.

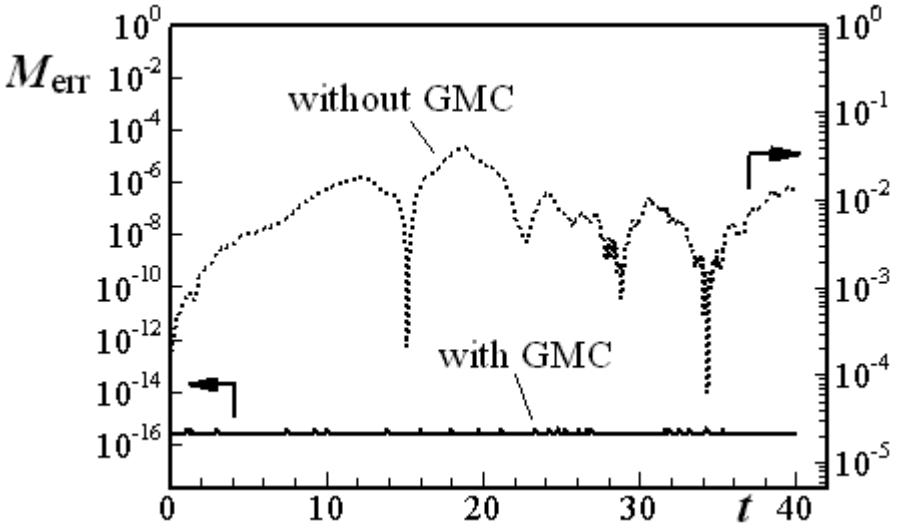

Figure 4-10c: Mass errors for a droplet squeezed through a constricted channel computed with and without GMC.

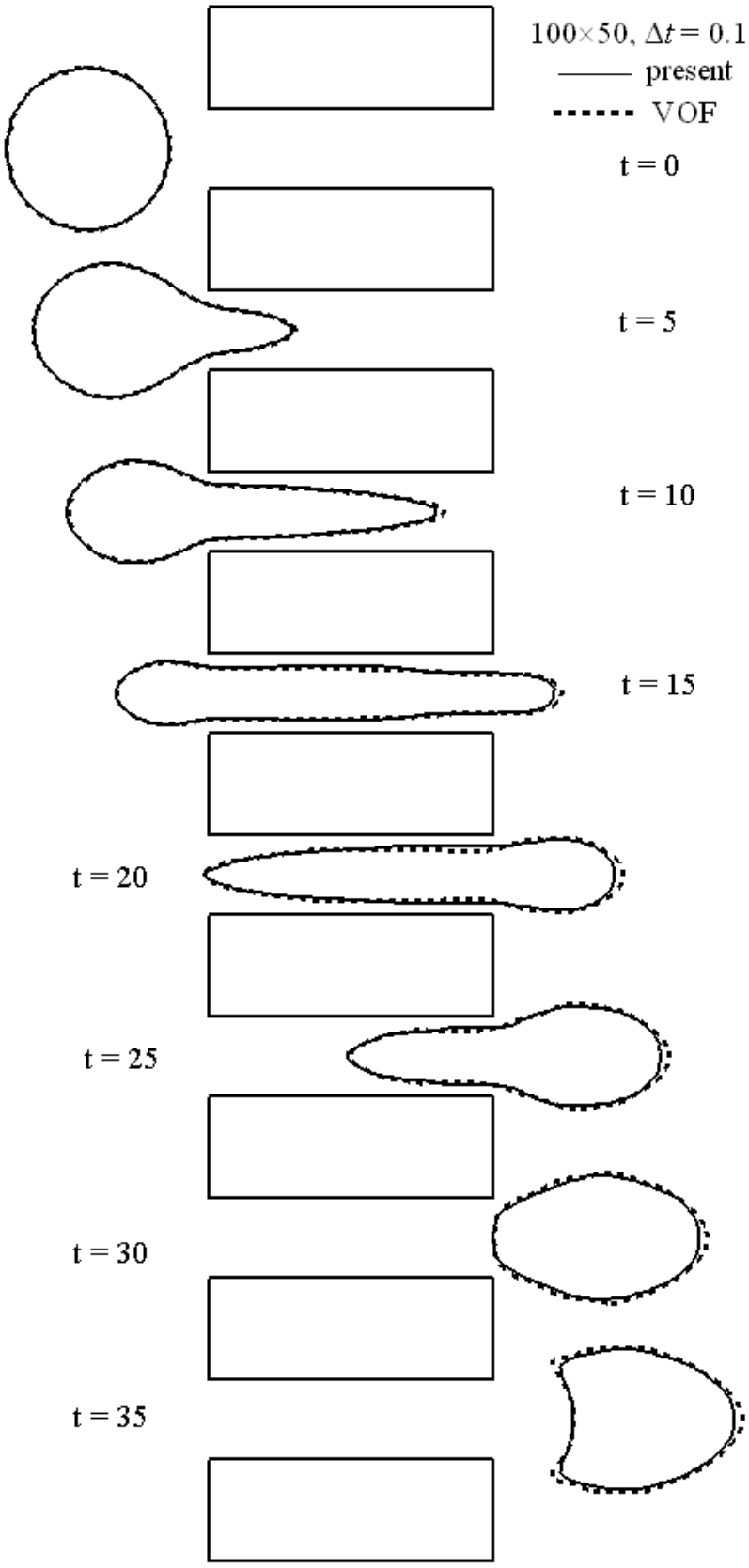

Figure 4-11a: Present and VOF comparisons for the evolution of a droplet squeezed through a constricted channel for $\sigma = 0$.

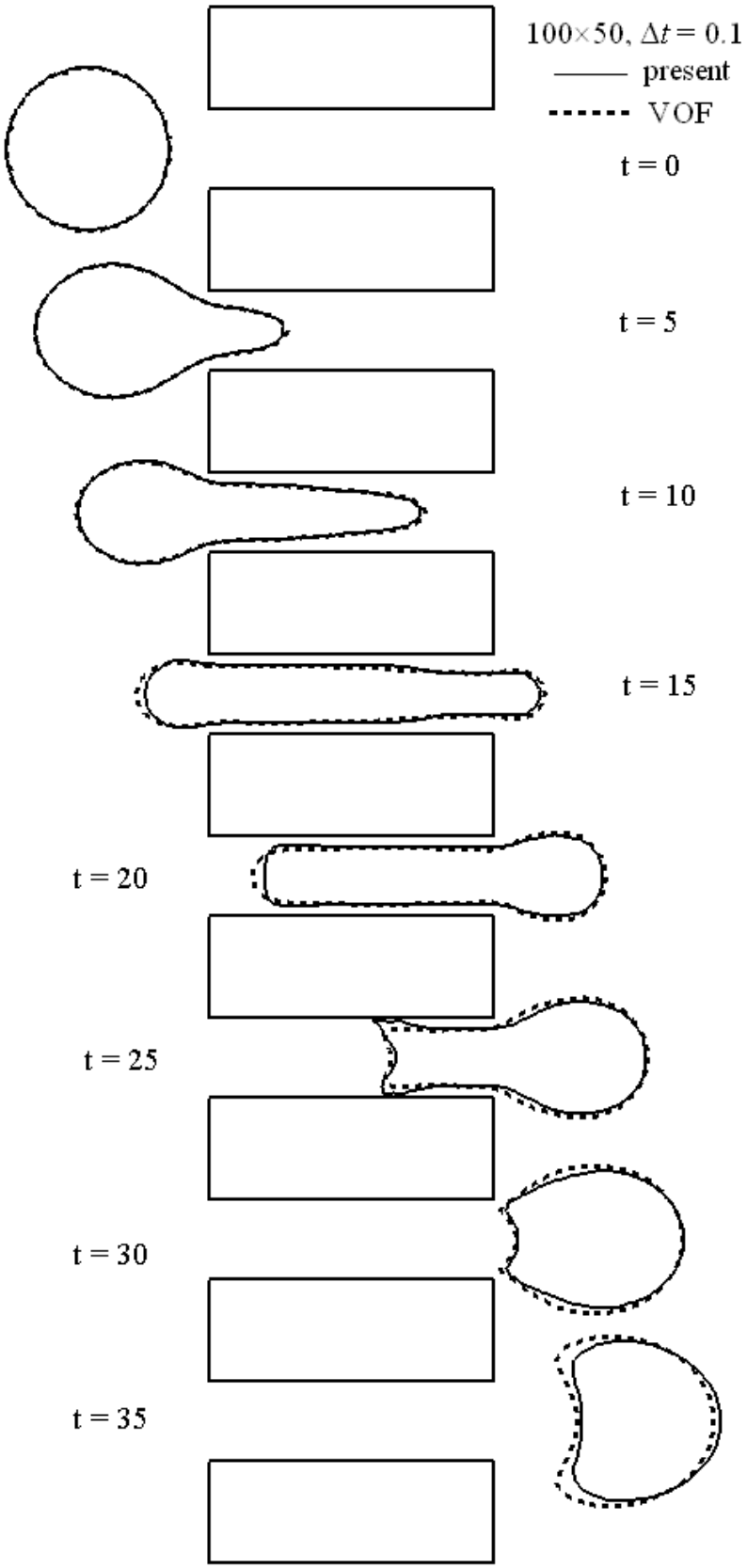

Figure 4-11b: Present and VOF comparisons for the evolution of a droplet squeezed through a constricted channel for $\sigma = 0.05$.

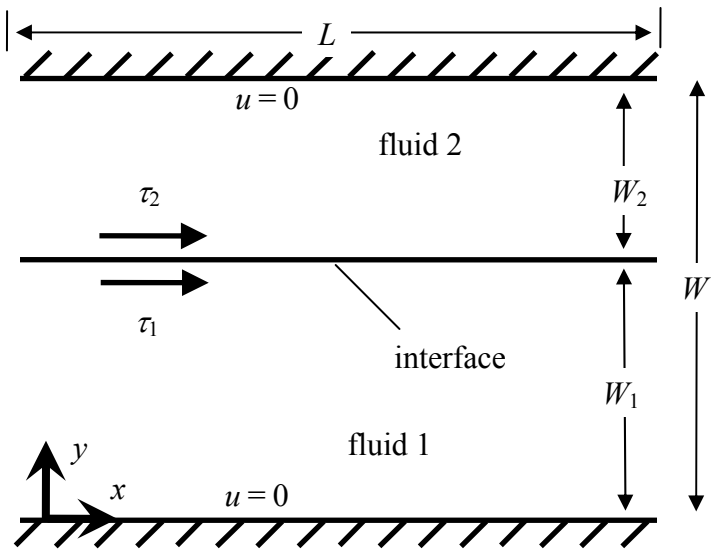

Figure 4-12: Flow of two stratified fluid layers driven by Marangoni force.

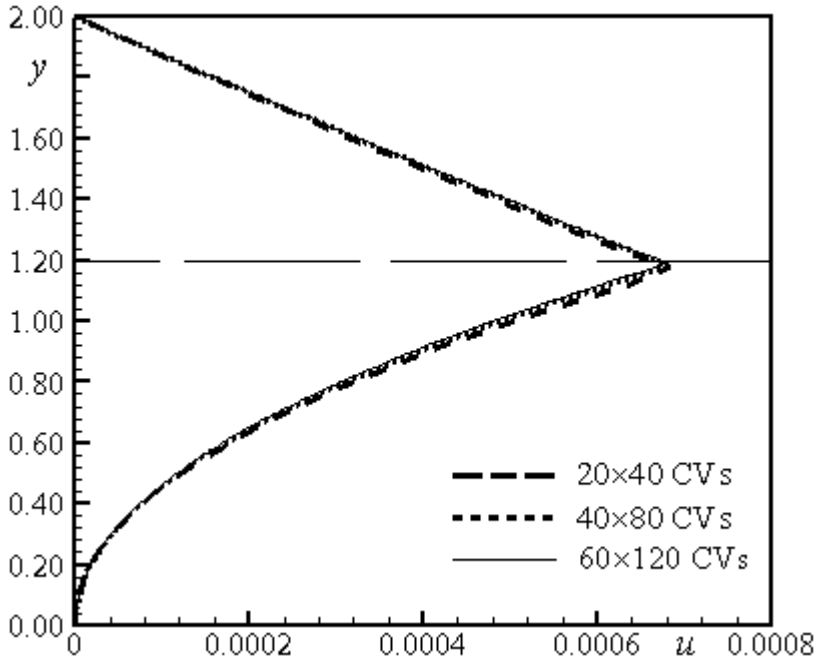

(a) Grid independent study.

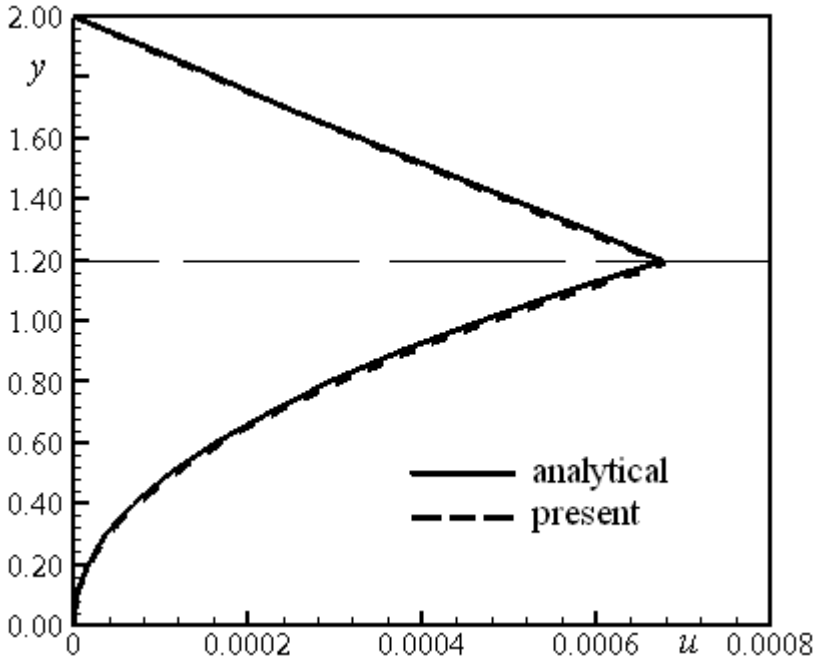

(b) Comparison between analytical and the present solution.

Figure 4-13: Velocity profile for viscosity combination of $\mu_1 = 1$ and $\mu_2 = 10$.

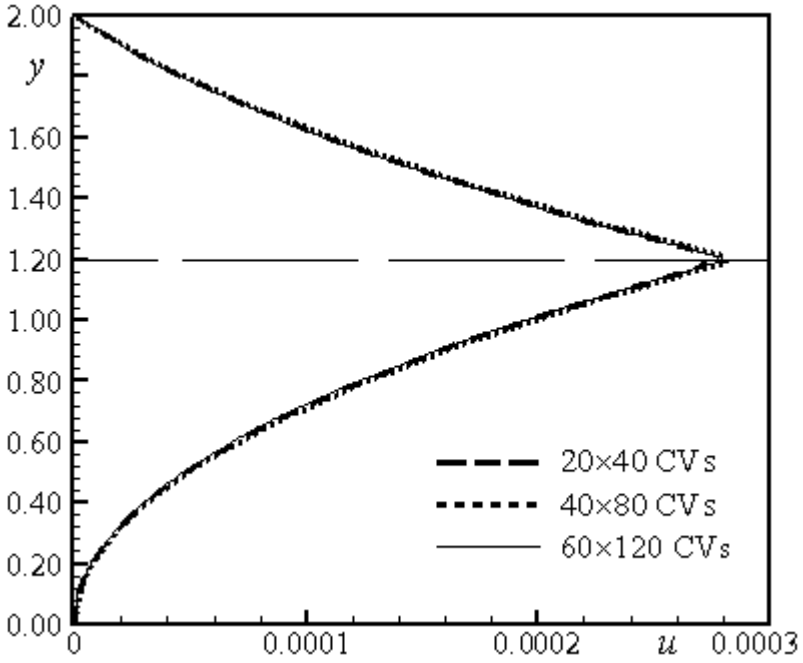

(a) Grid independent study.

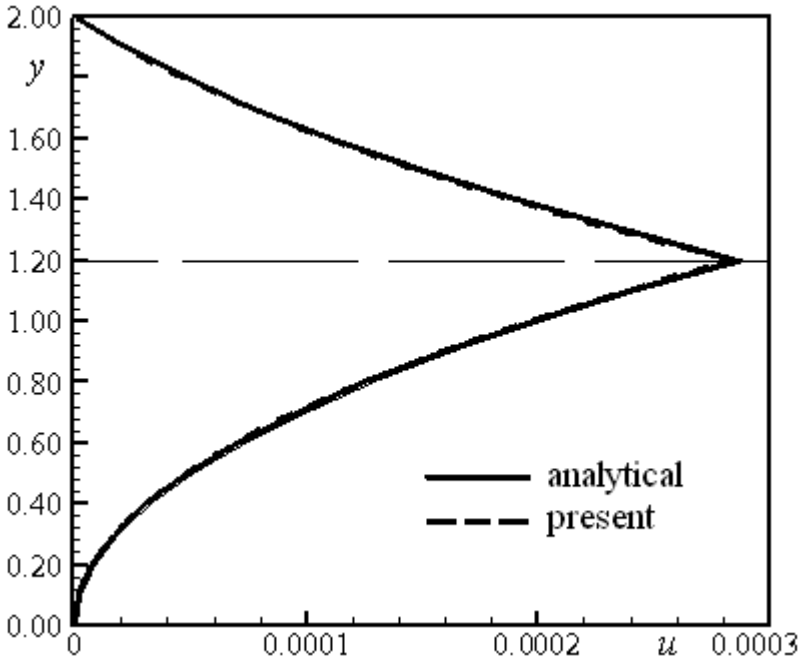

(b) Comparison between analytical and the present solution.

Figure 4-14: Velocity profile for viscosity combination of $\mu_1 = 10$ and $\mu_2 = 10$.

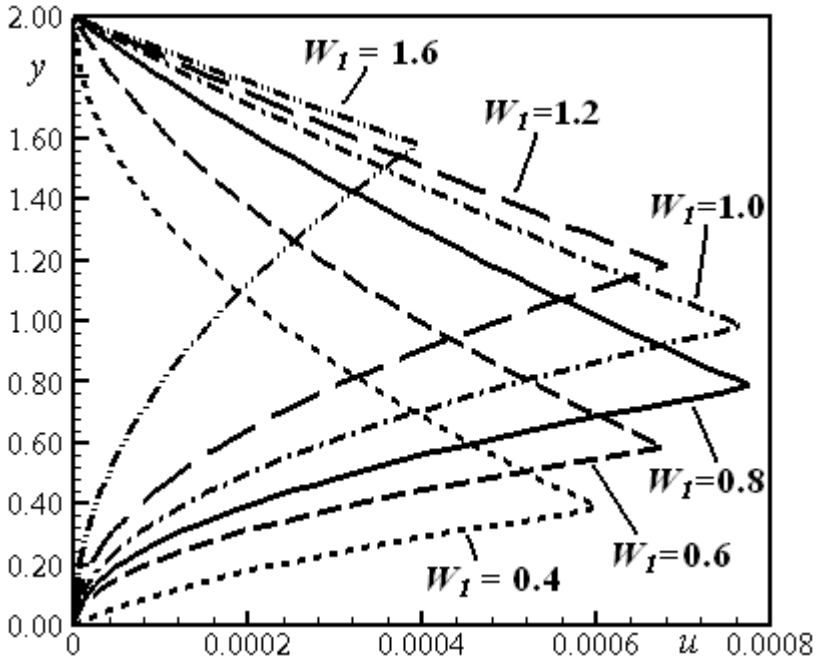

Figure 4-15: Velocity profile for viscosity combination of $\mu_1 = 1$ and $\mu_2 = 10$ with different F-F interface locations.

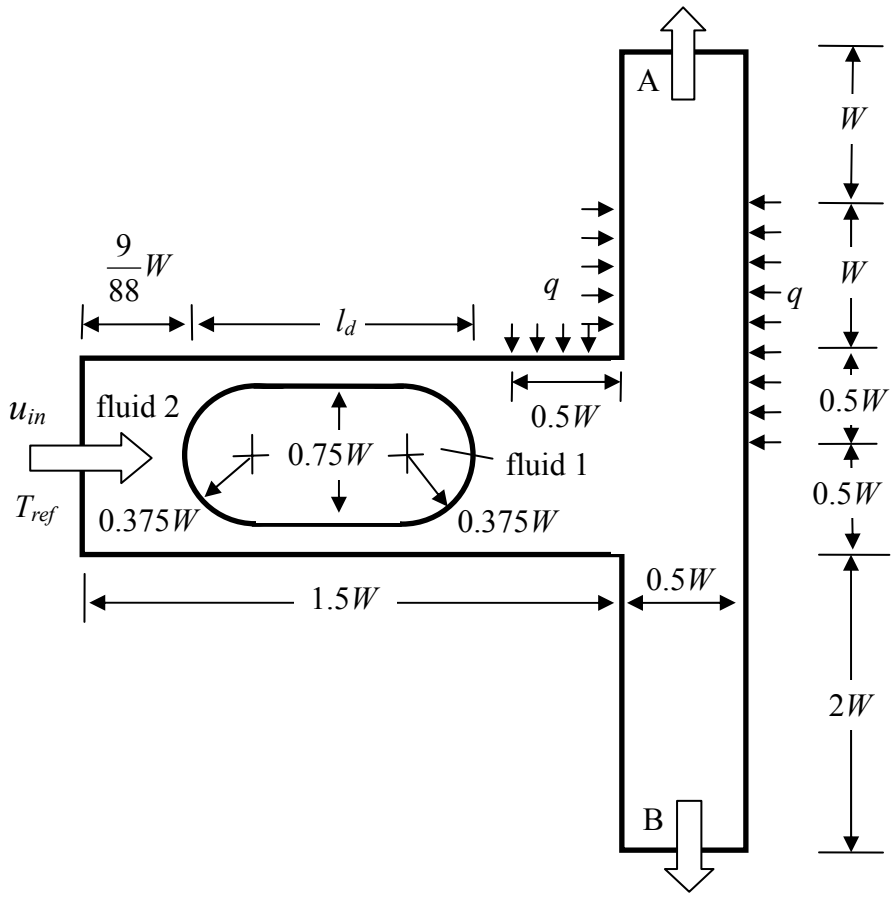

Figure 4-16: Schematic of a droplet in a micro T-junction.

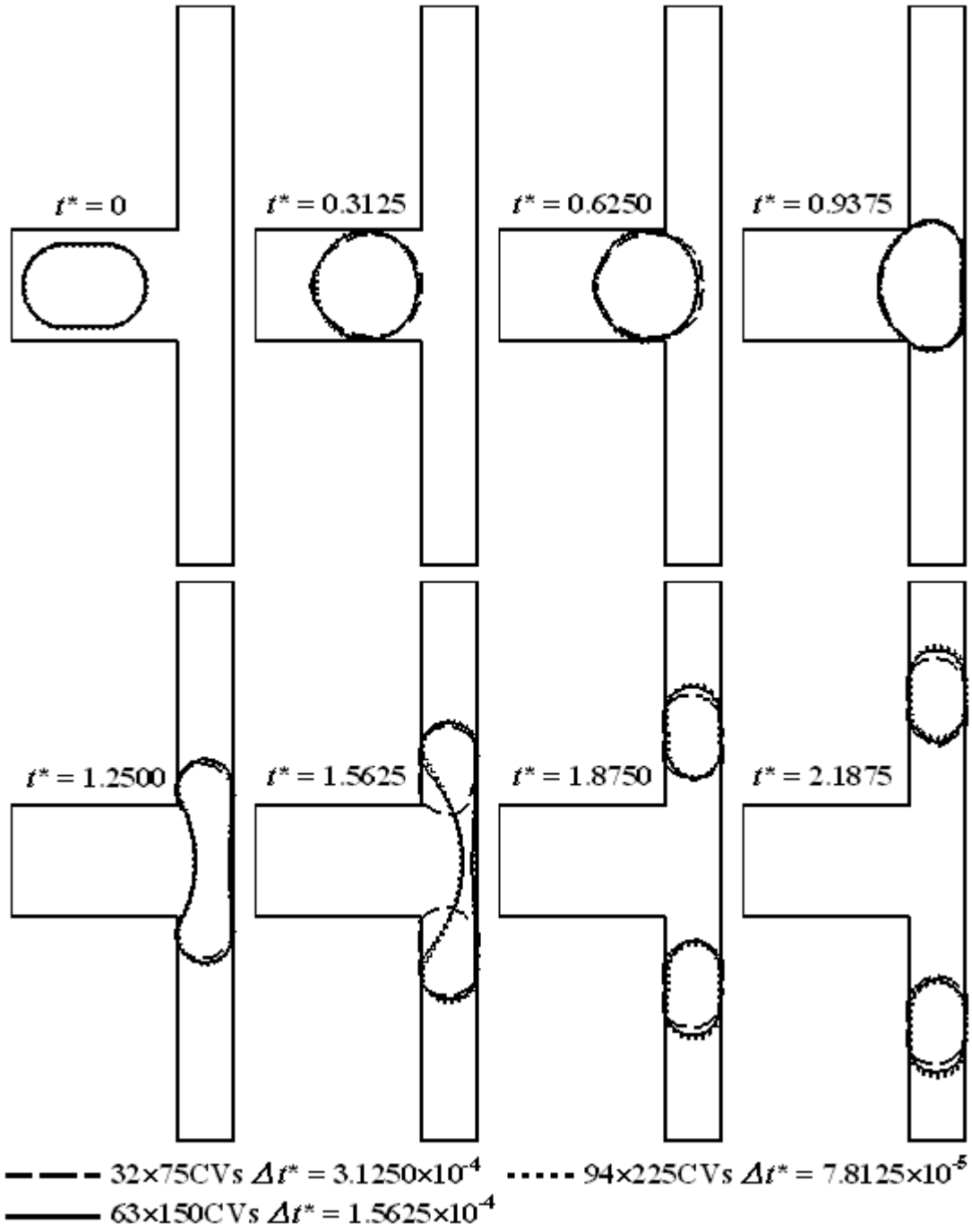

Figure 4-17: Evolution of a droplet in a T-junction for $Ma = 0$.

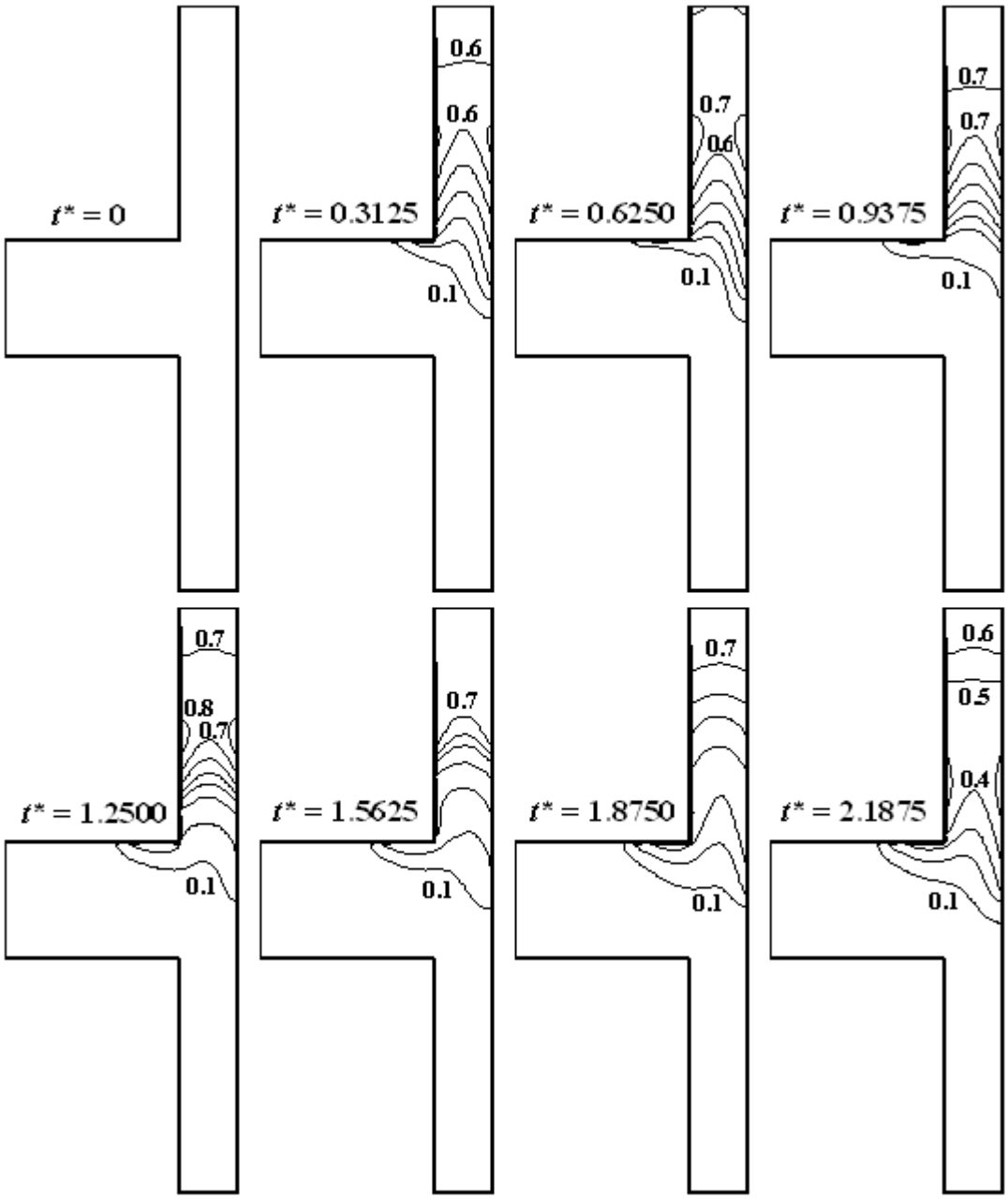

Figure 4-18a: Dimensionless temperature field in a T-junction for $Ma = 40$.

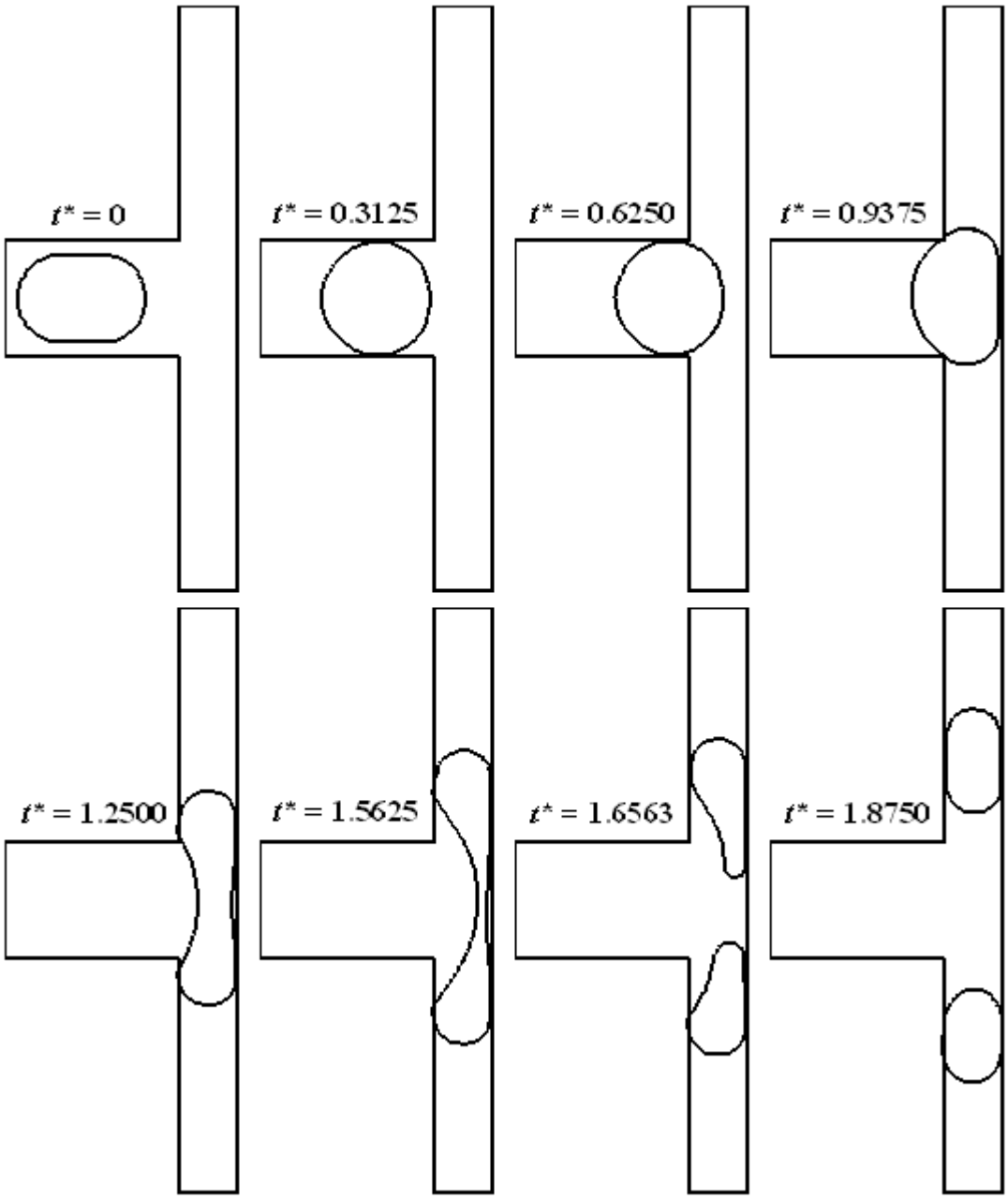

Figure 4-18b: Unequal splitting of a droplet in a T-junction for $Ma = 40$.

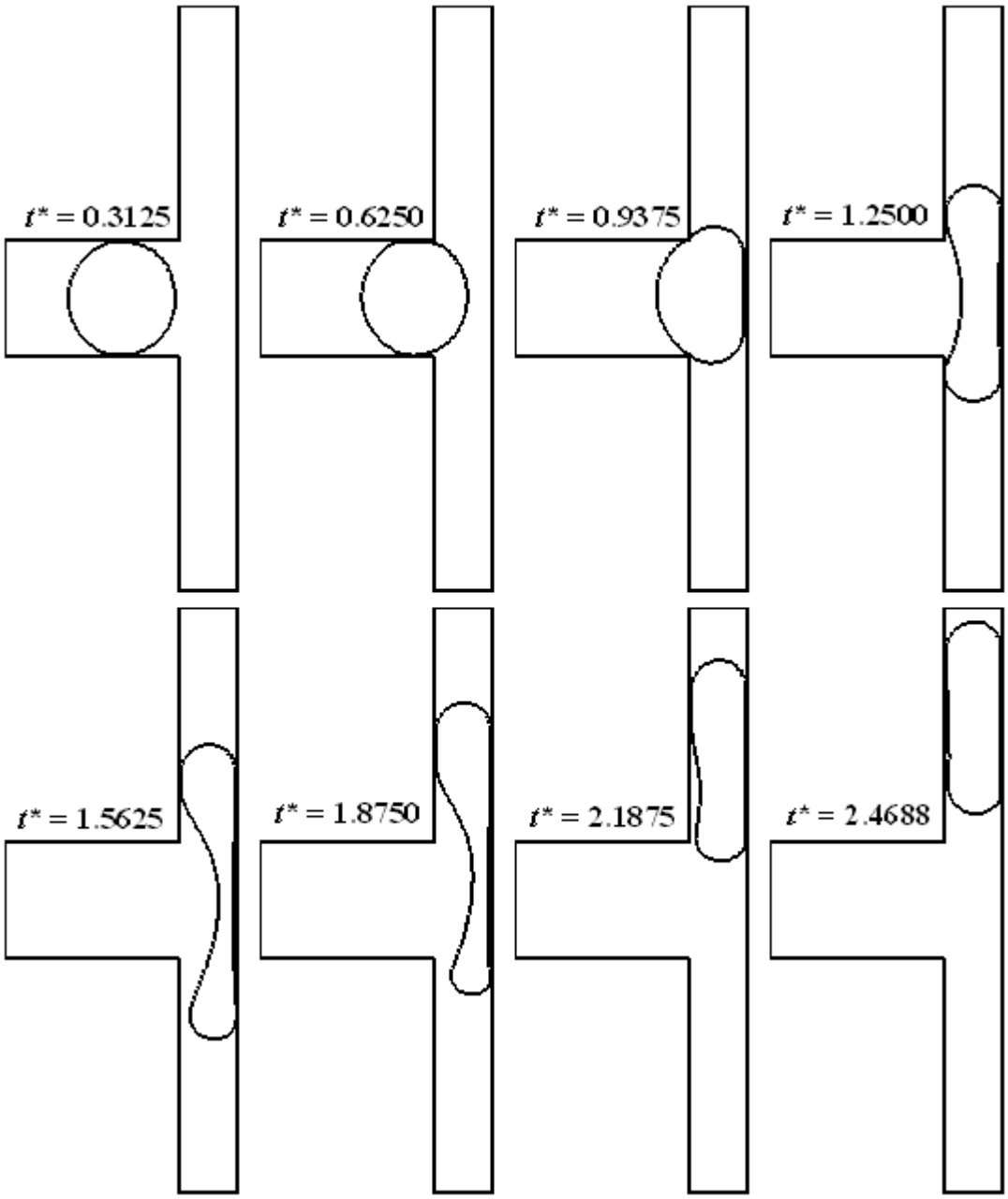

Figure 4-19: Switching of a droplet into a desired branch at a T-junction for $Ma = 80$.

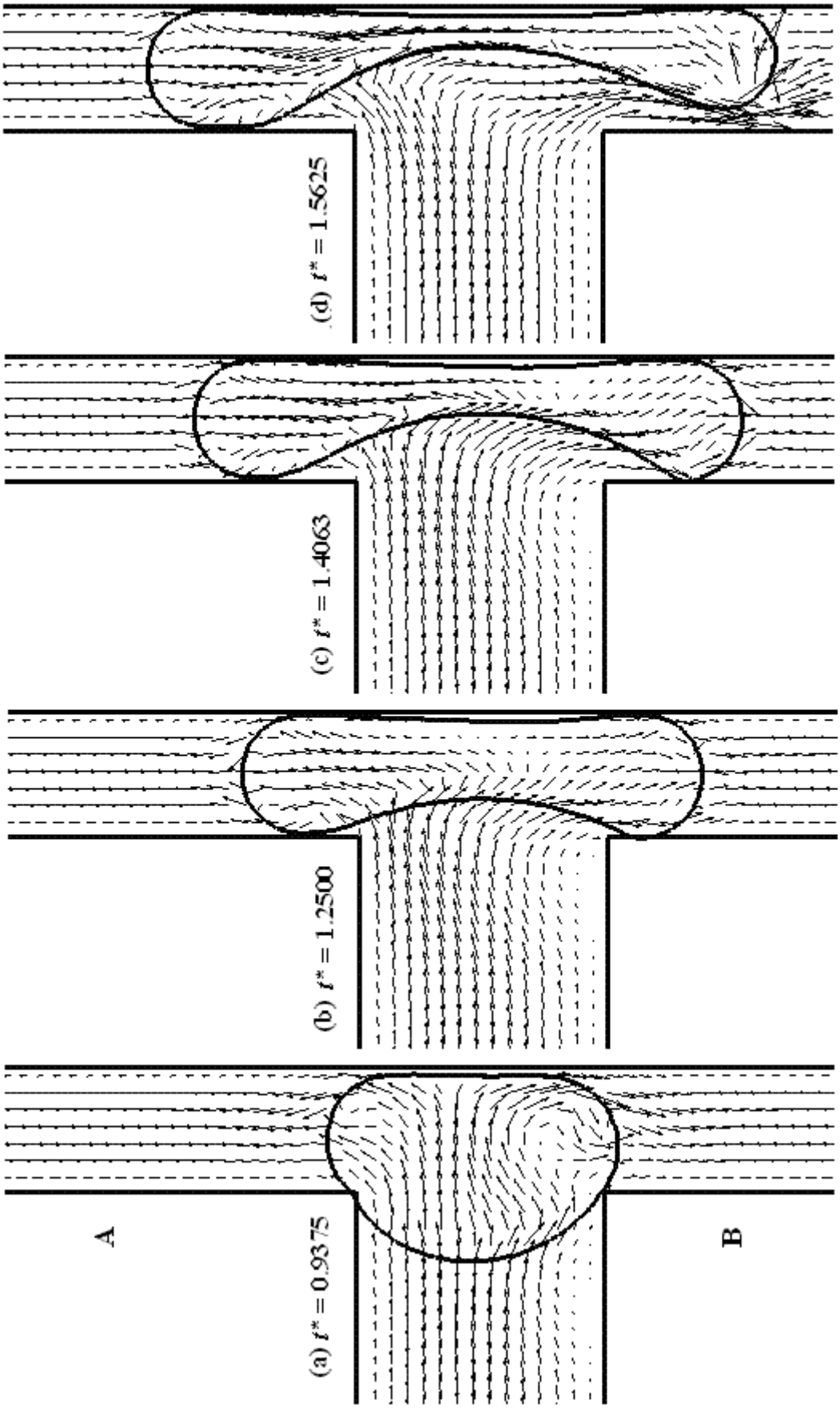

Figure 4-20: Velocity field around a droplet entering branch A.

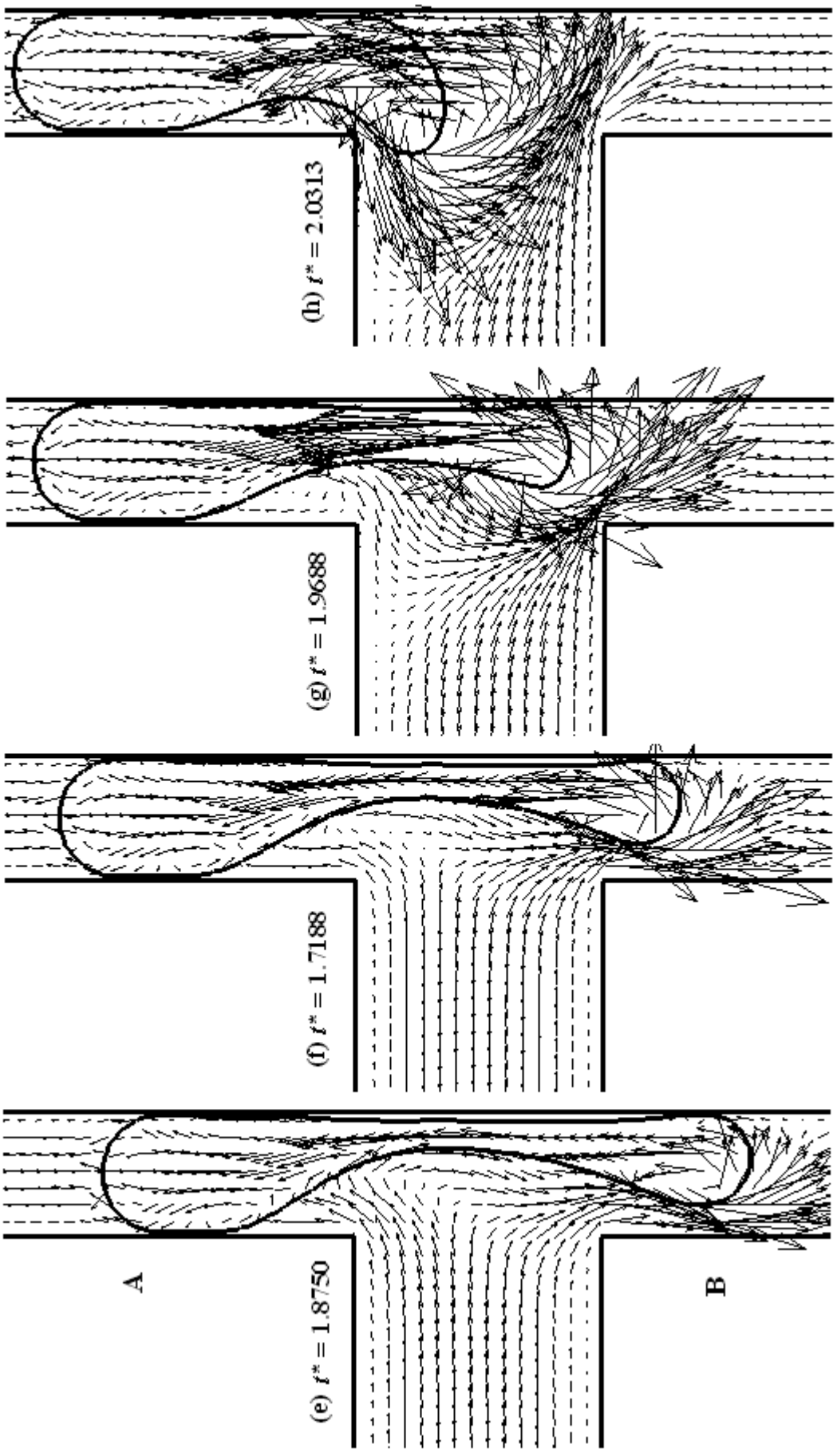

Figure 4-20: Velocity field around a droplet entering branch A.

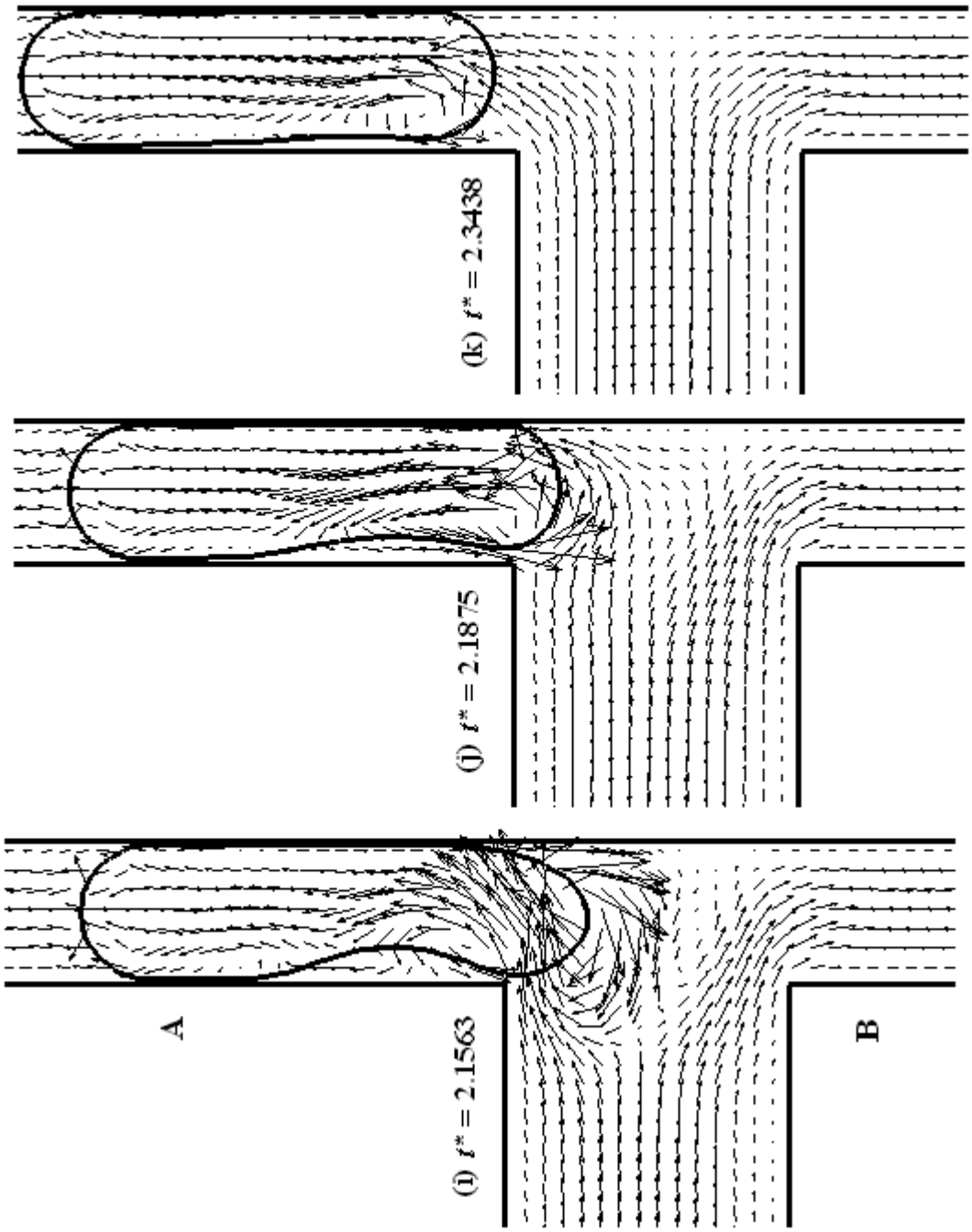

Figure 4-20: Velocity field around a droplet entering branch A.

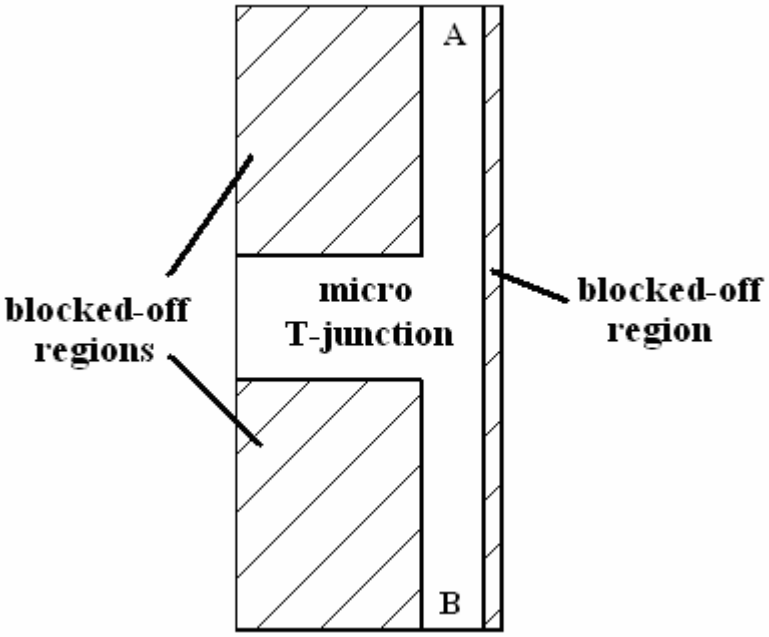

Figure 4-21: Computational domain for a micro T-junction.

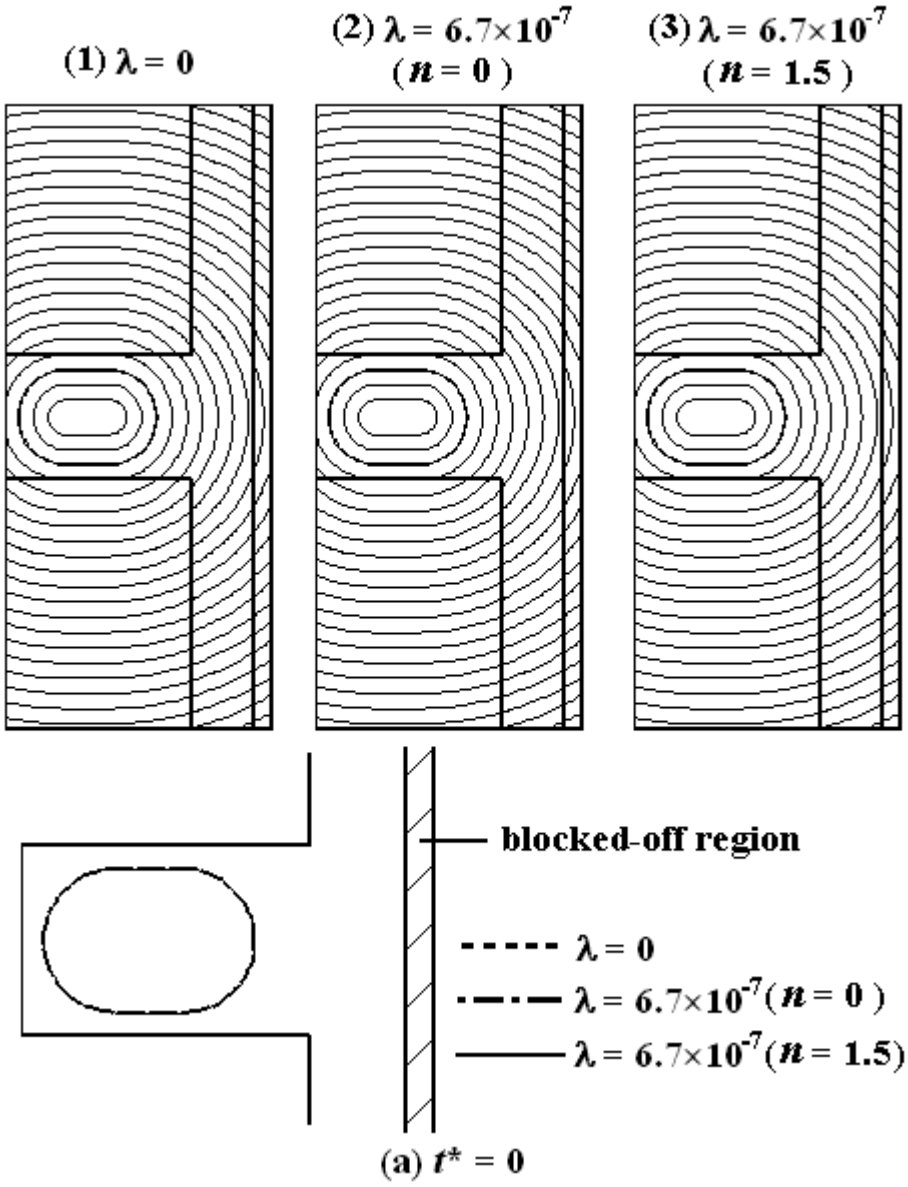

Figure 4-22: F-F interface evolution with and without artificial viscosity.

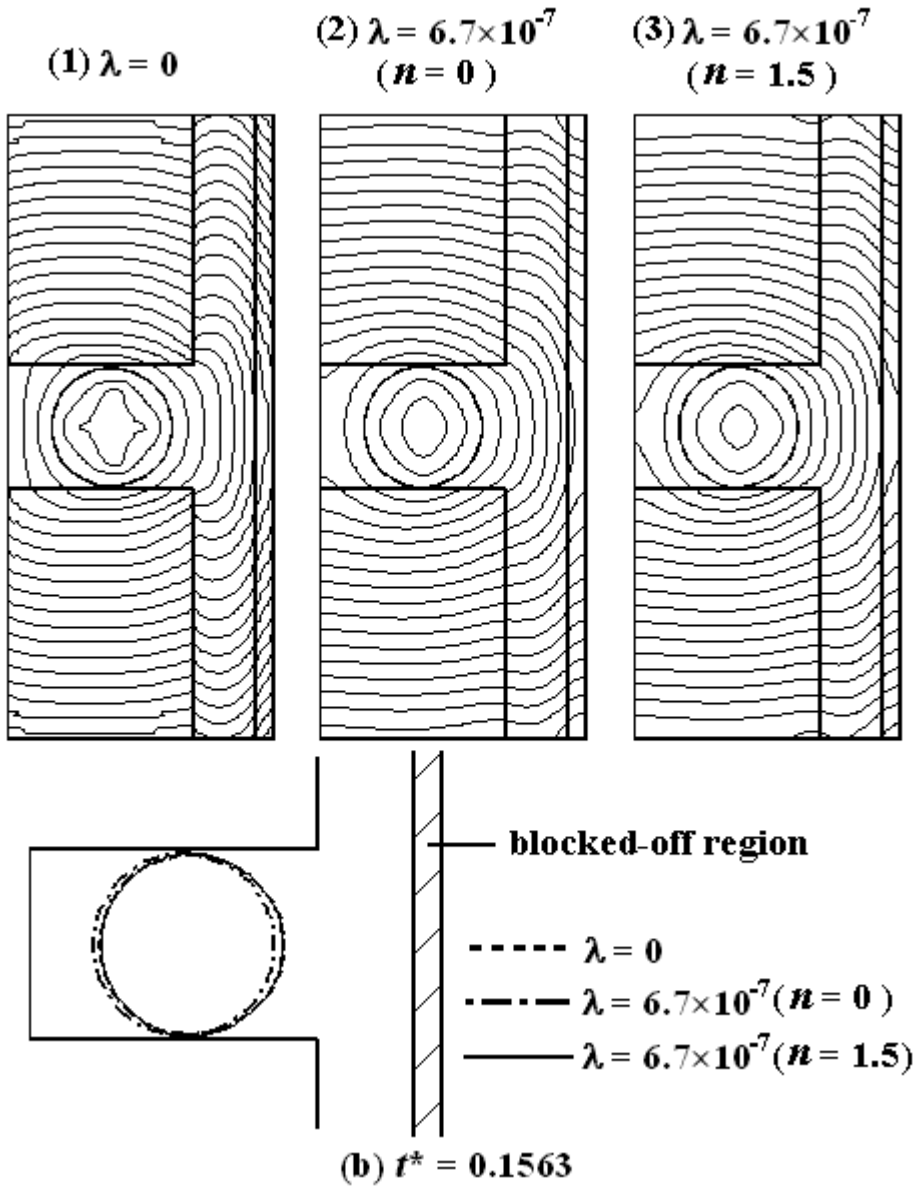

Figure 4-22: F-F interface evolution with and without artificial viscosity.

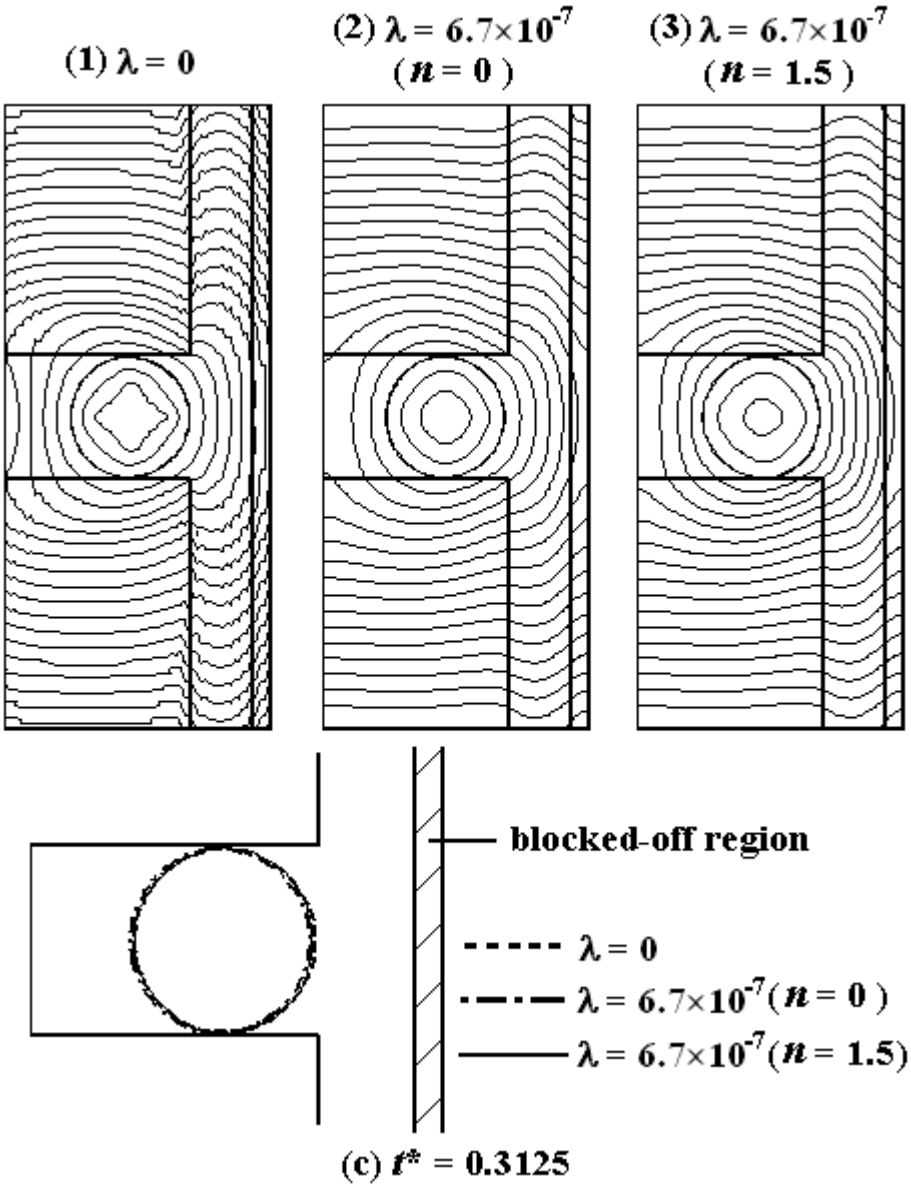

Figure 4-22: F-F interface evolution with and without artificial viscosity.

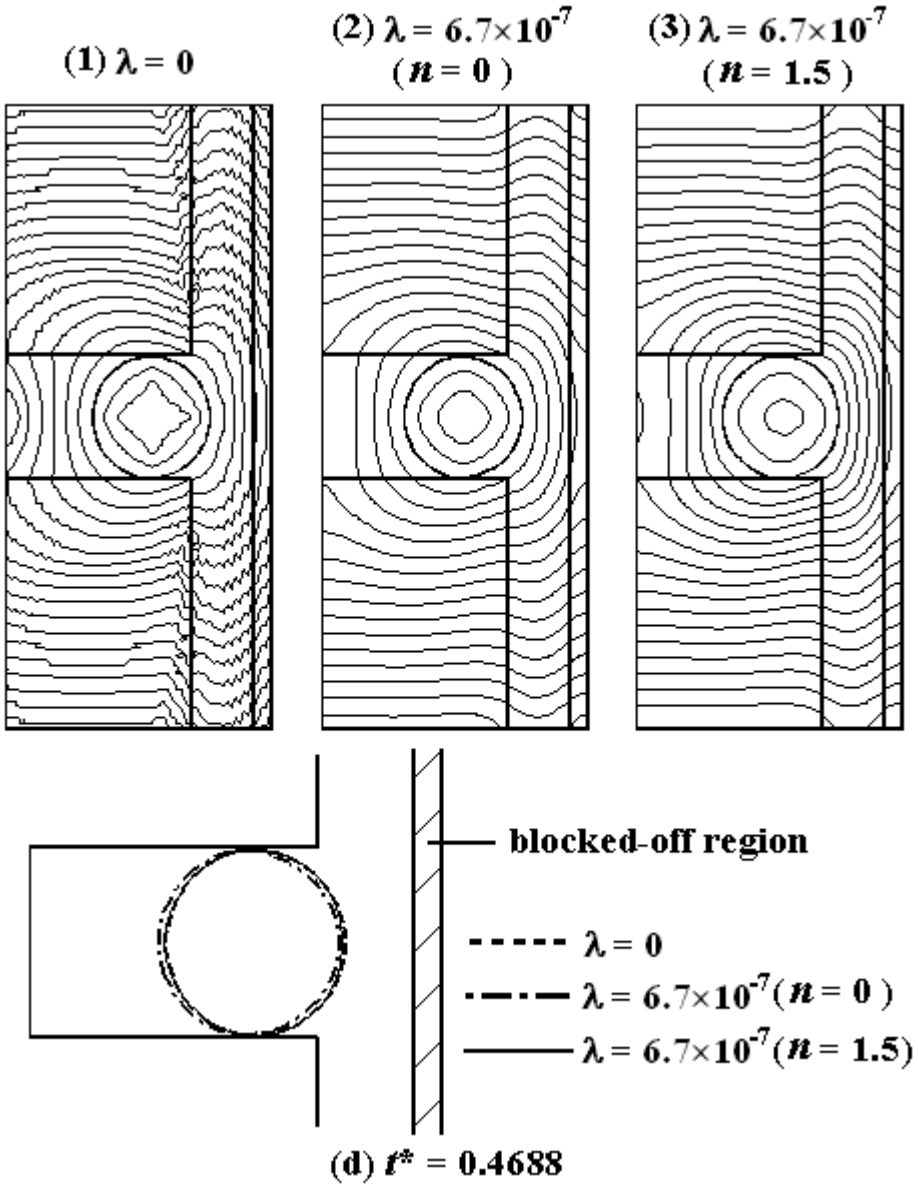

Figure 4-22: F-F interface evolution with and without artificial viscosity.

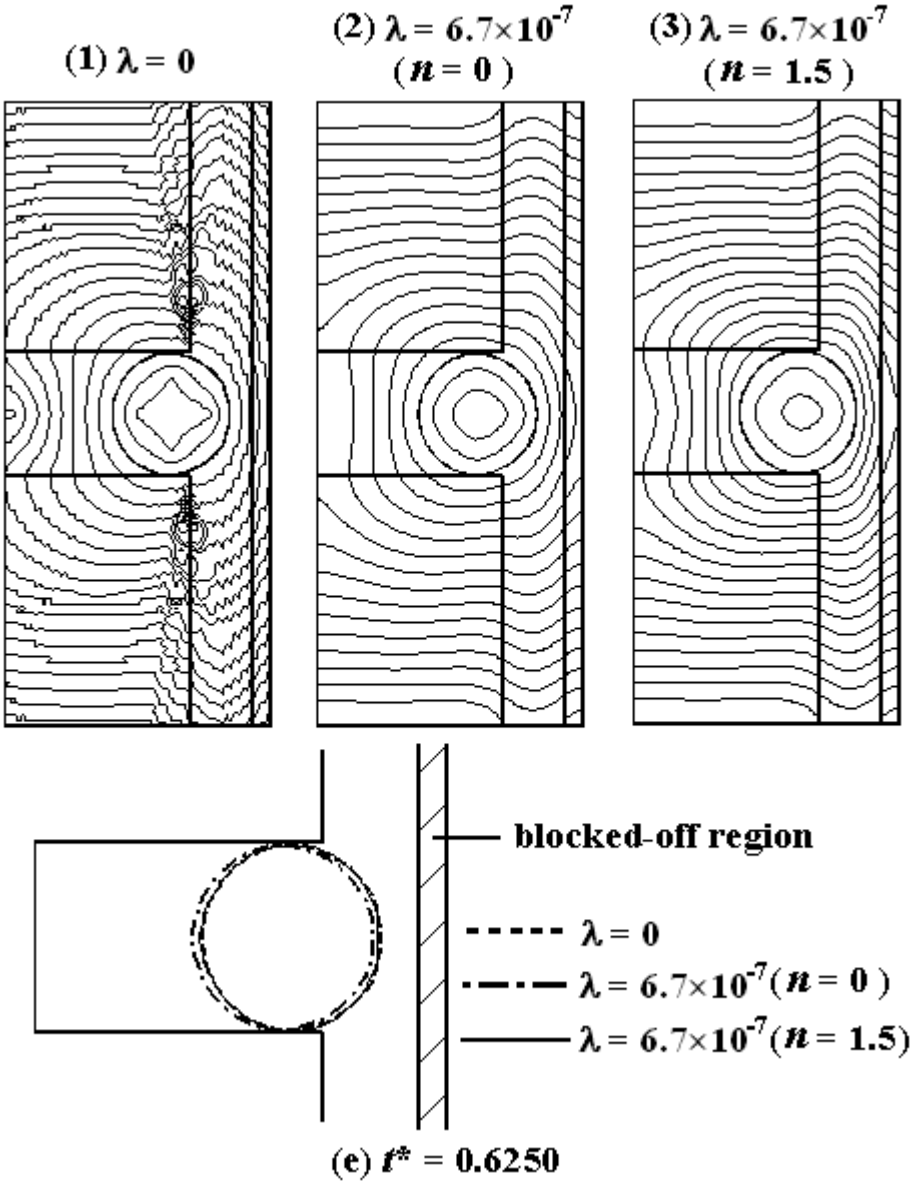

Figure 4-22: F-F interface evolution with and without artificial viscosity.

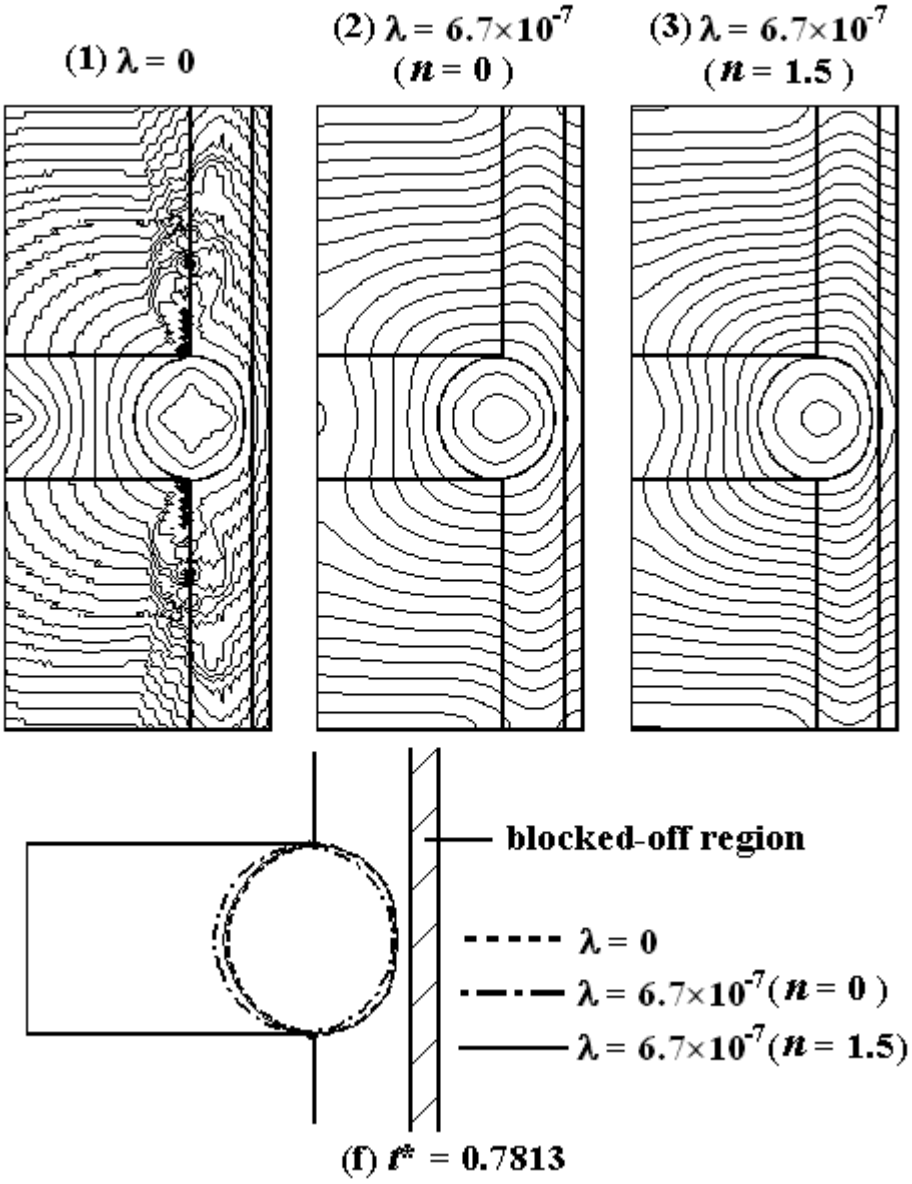

Figure 4-22: F-F interface evolution with and without artificial viscosity.

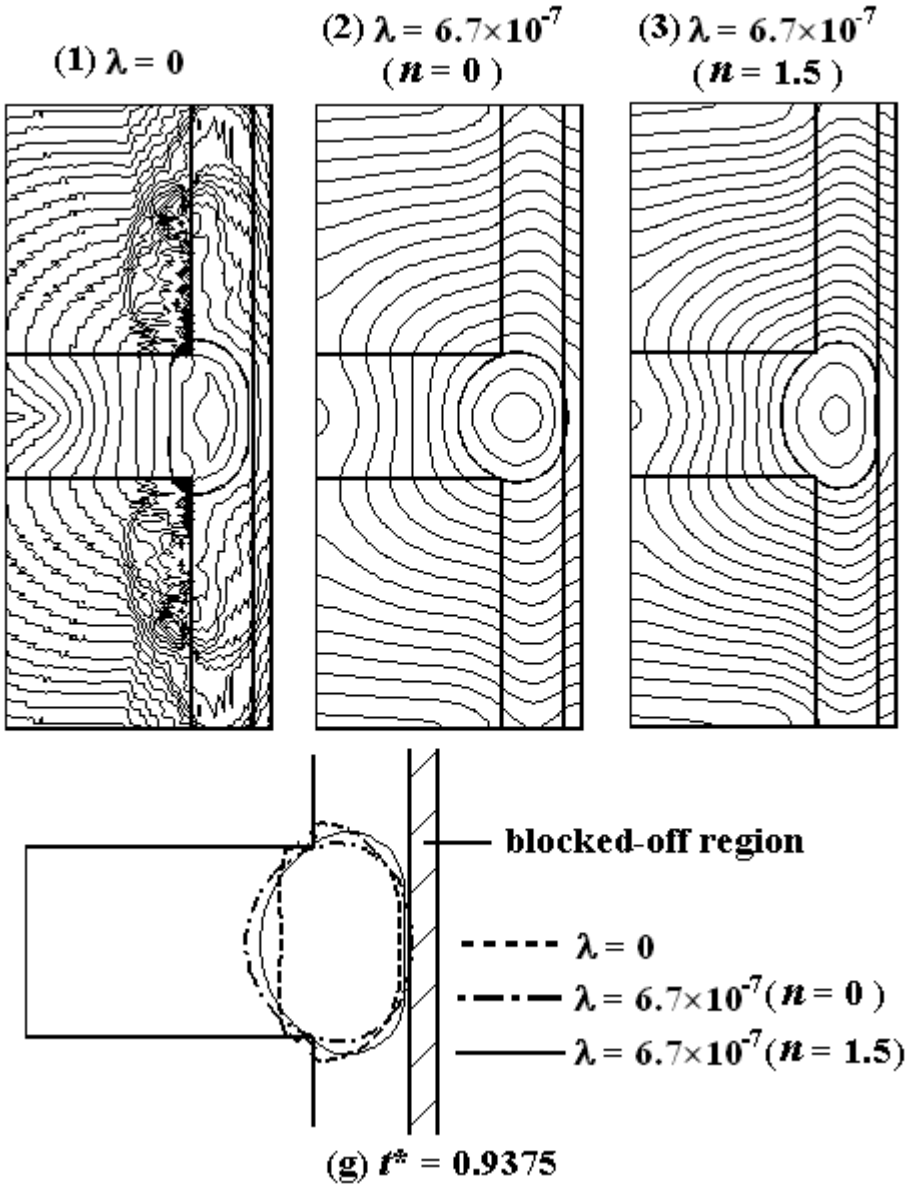

Figure 4-22: F-F interface evolution with and without artificial viscosity.

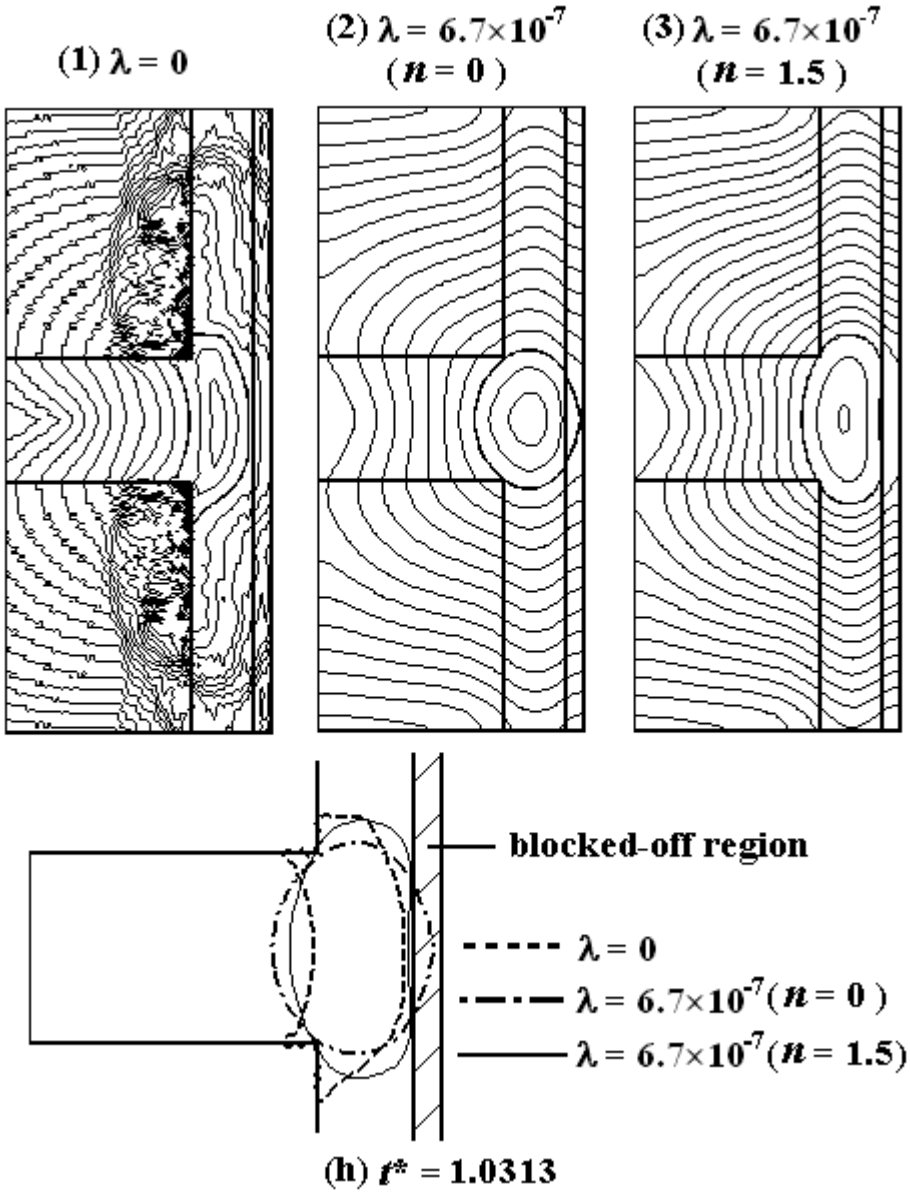

Figure 4-22: F-F interface evolution with and without artificial viscosity.

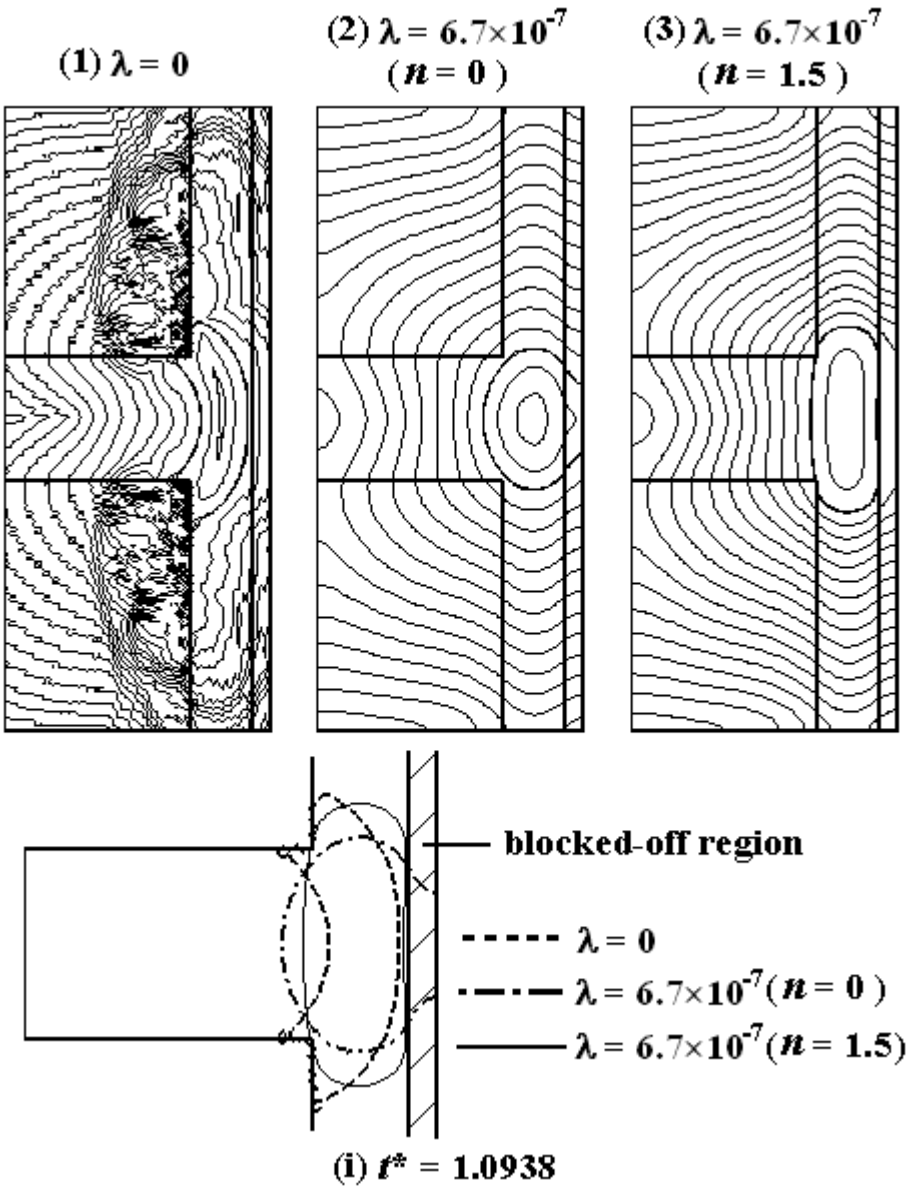

Figure 4-22: F-F interface evolution with and without artificial viscosity.

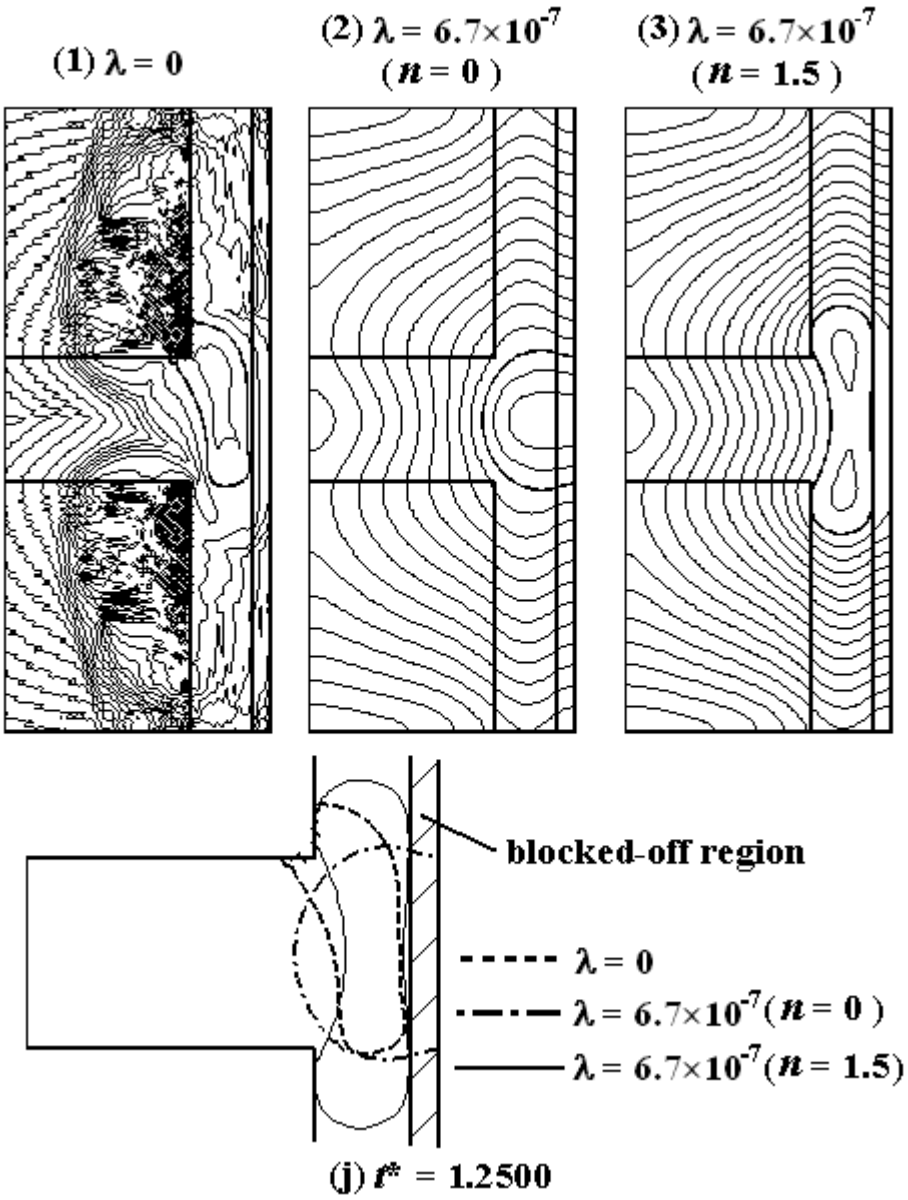

Figure 4-22: F-F interface evolution with and without artificial viscosity.

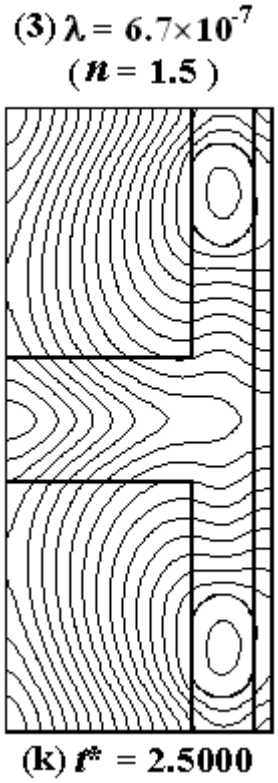

Figure 4-22: F-F interface evolution with and without artificial viscosity.

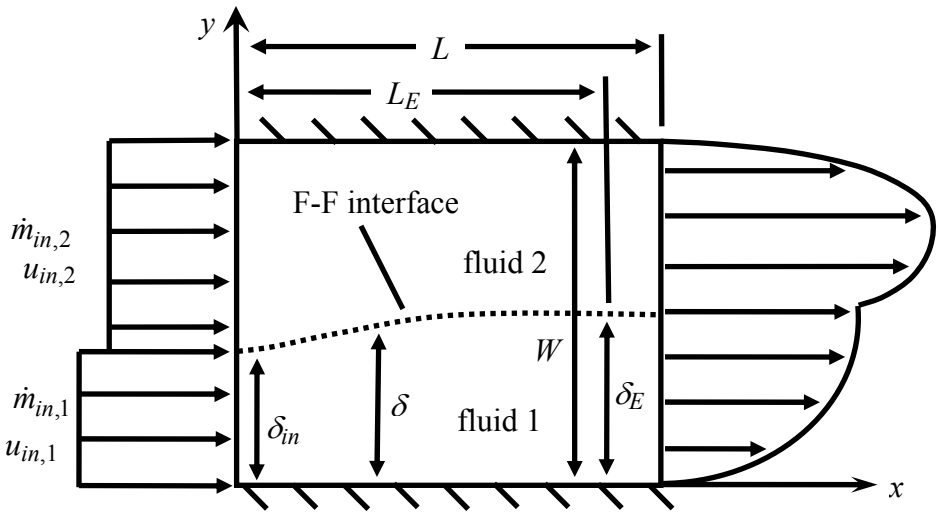

Figure 4-23: Schematic of a stratified two-fluid flow in a straight channel.

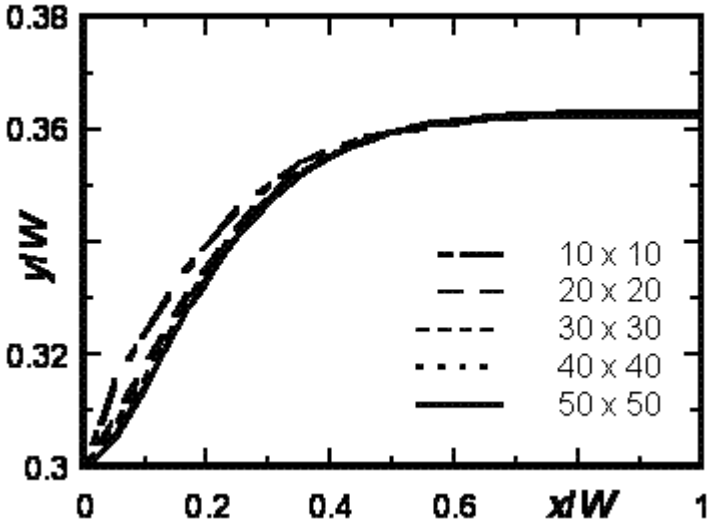

(a) With LMC.

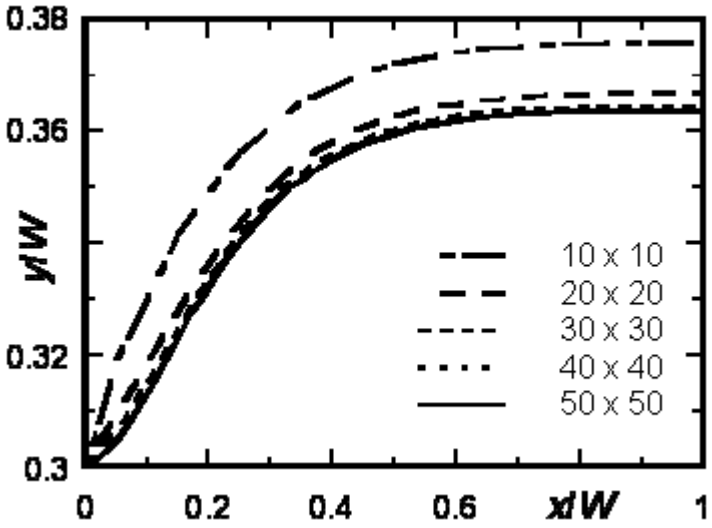

(b) Without LMC.

Figure 4-24: Grid independent study for the F-F interface location for two fluids of identical properties.

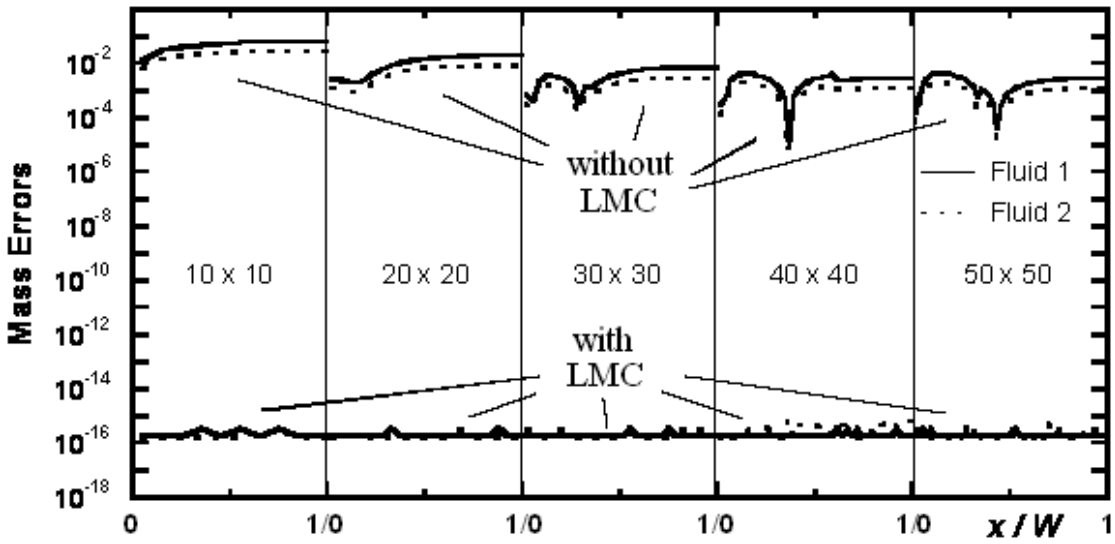

Figure 4-25. Mass errors for fluid 1 and fluid 2.

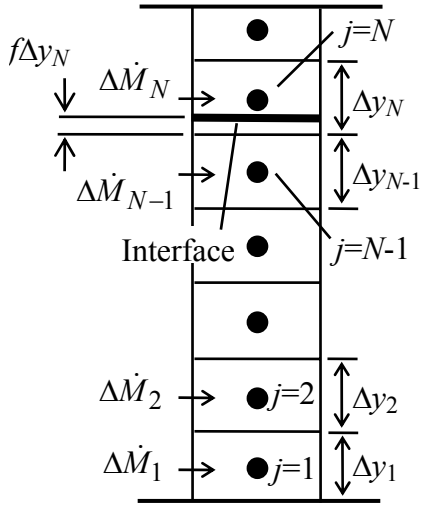

Figure 4-26: Control volumes at a given x.

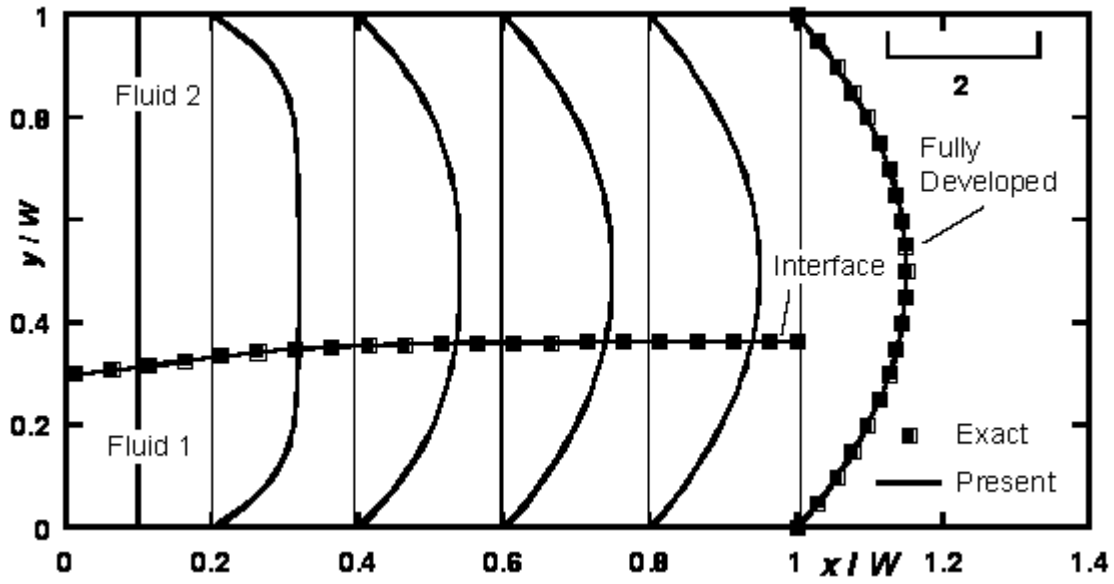

Figure 4-27a: The F-F interface location and velocity profiles for two fluids of identical properties with a uniform inlet velocity.

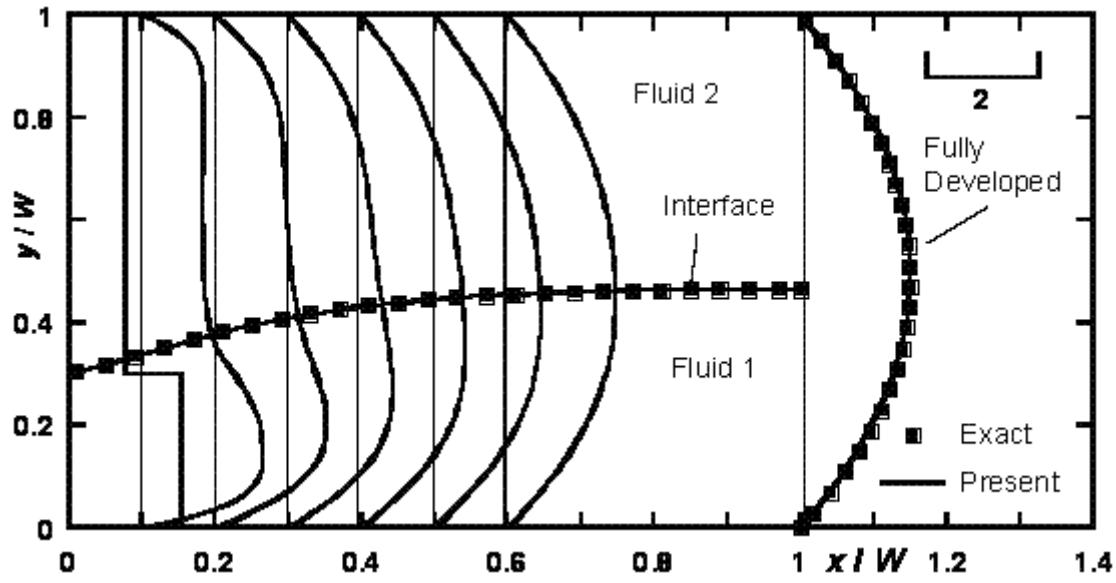

Figure 4-27b: The F-F interface location and velocity profiles for two fluids of identical properties with a non-uniform inlet velocity.

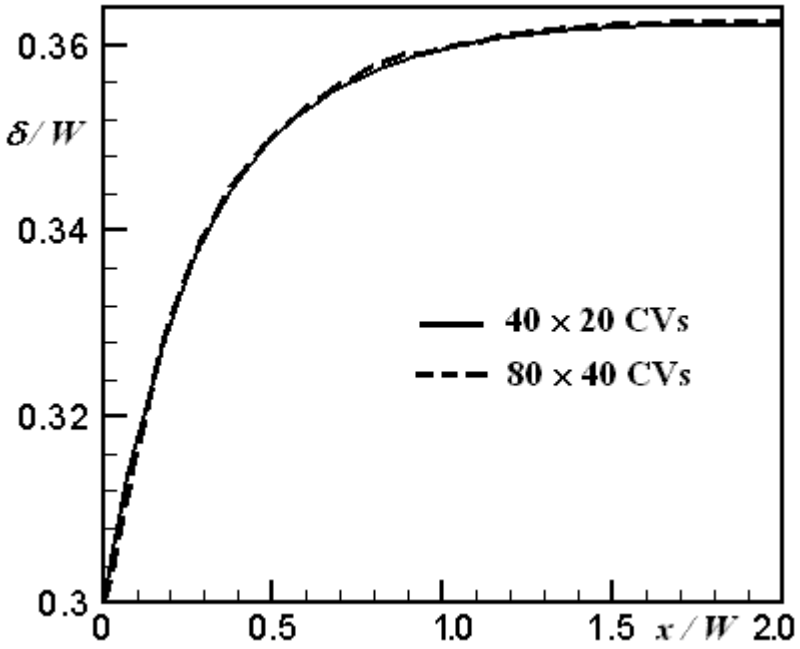

Figure 4-28: Grid independent study for the F-F interface location for two fluids of identical properties with Re = 0.01 and $Ca = 0.1$.

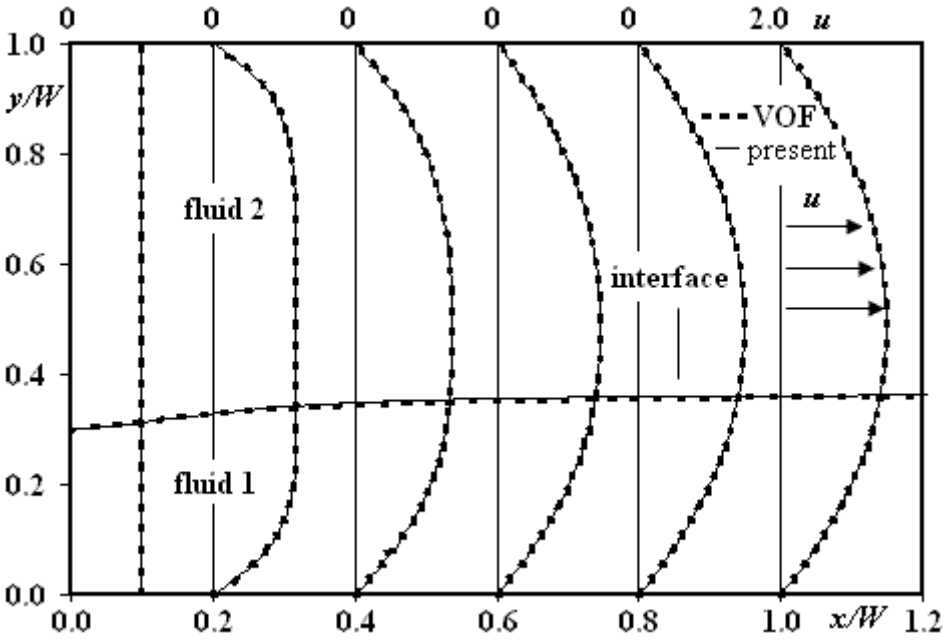

Figure 4-29: The F-F interface location and velocity profiles for two fluids of identical properties with Re = 0.01 and $Ca = 0.1$.

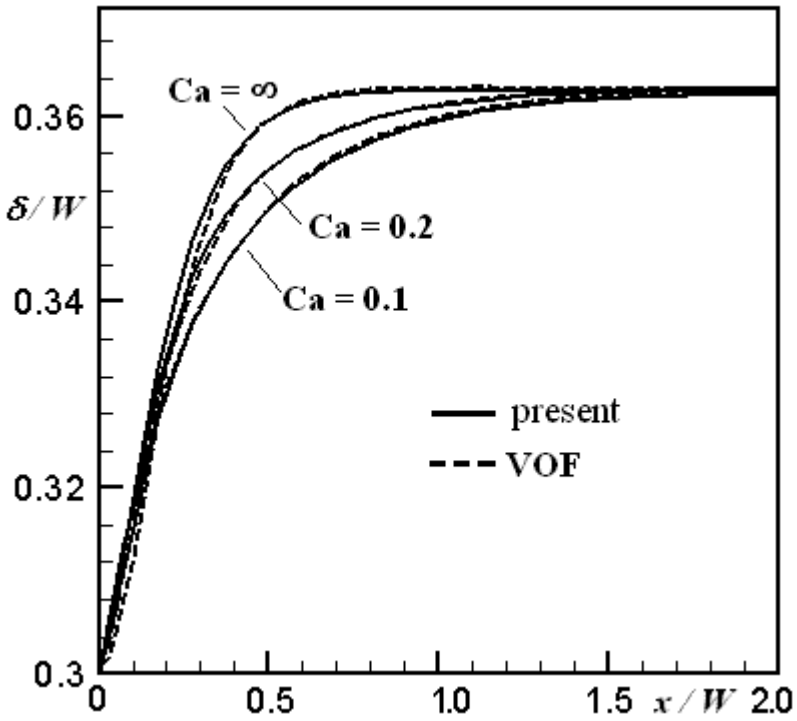

Figure 4-30: The F-F interface location for two fluids of identical properties with various Ca .

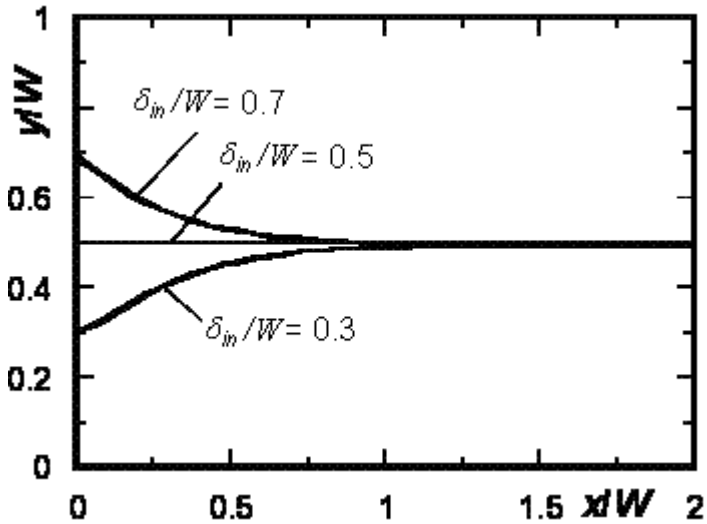

Figure 4-31a: The F-F interface location for two different fluids with various inlet F-F interface locations.

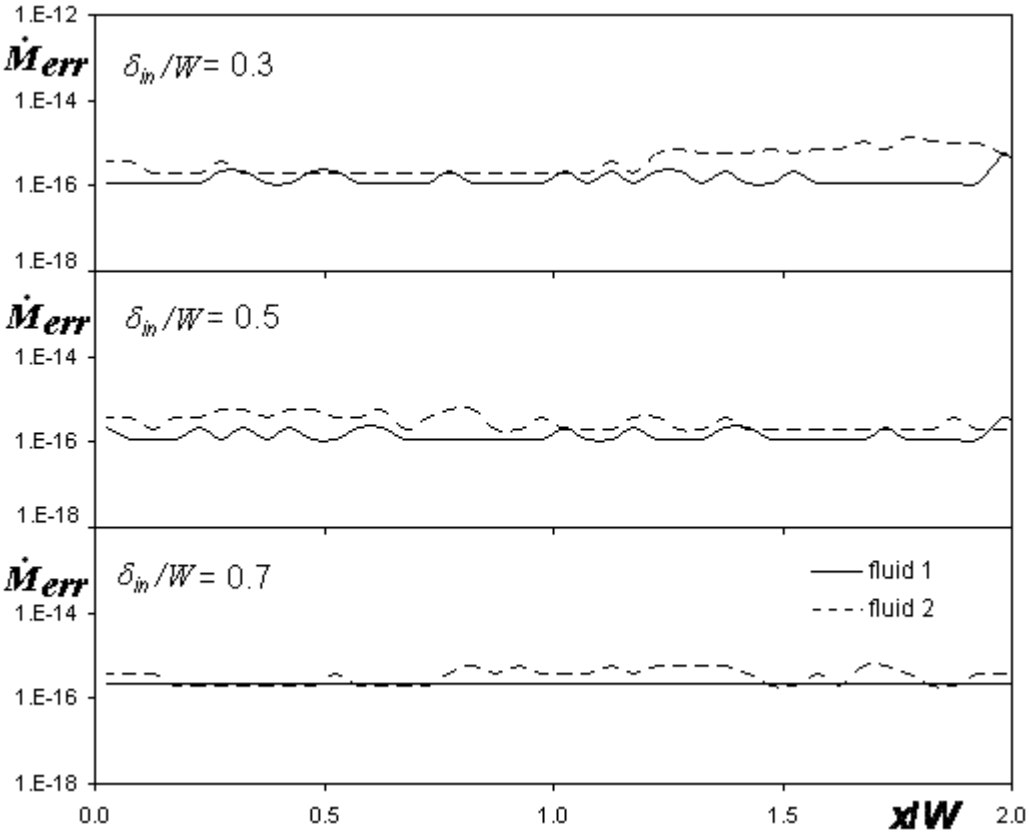

Figure 4-31b: Mass error with LMC.

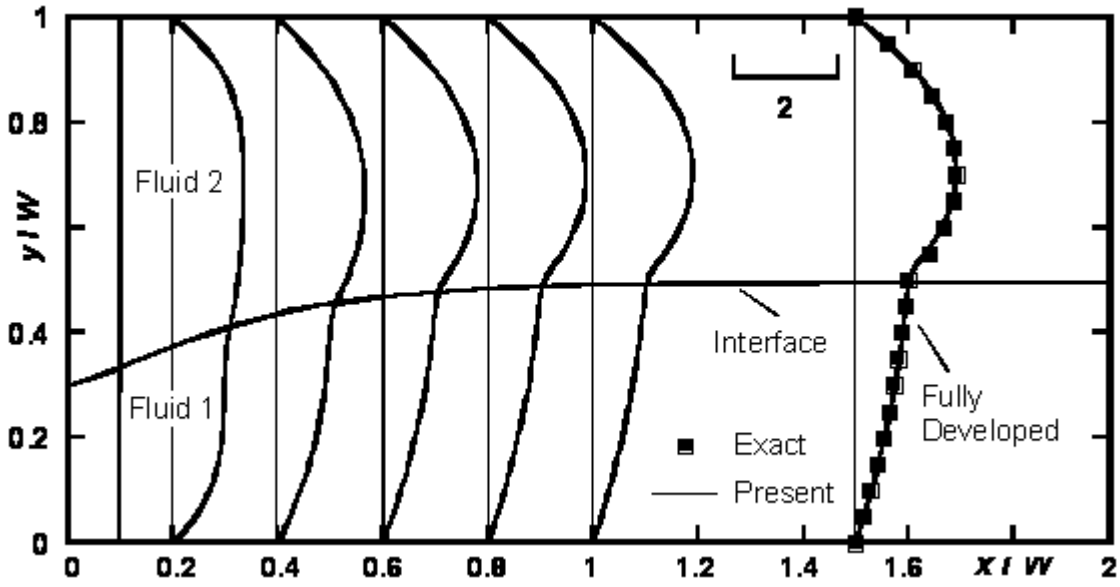

(a) $\delta_{in} / W = 0.3$.

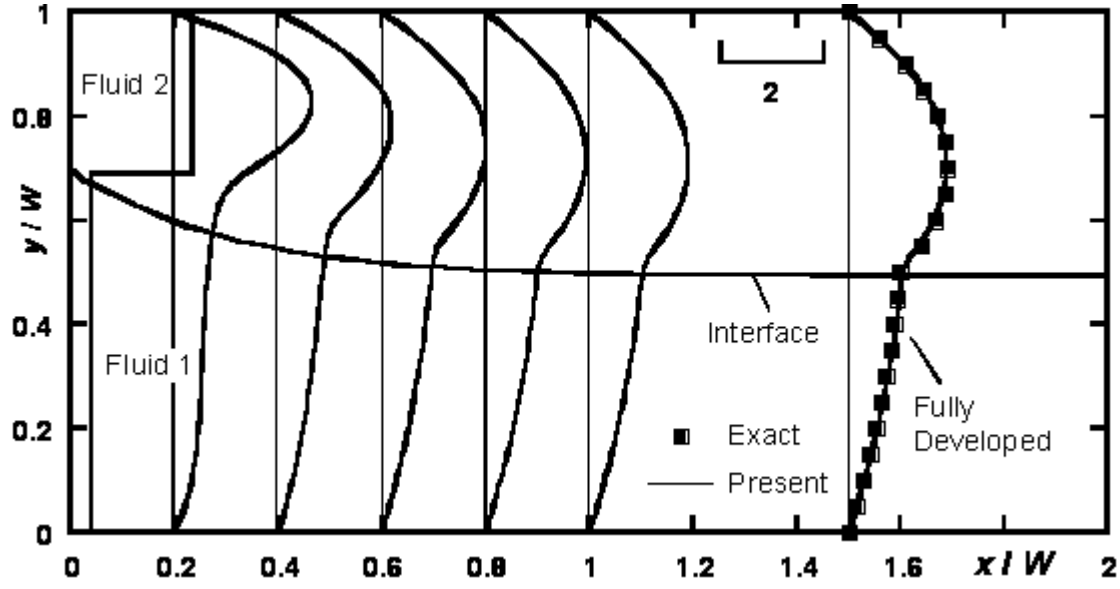

(b) $\delta_{in} / W = 0.7$.

Figure 4-32: The F-F interface location and velocity profiles for two different fluids with different inlet F-F interface locations.

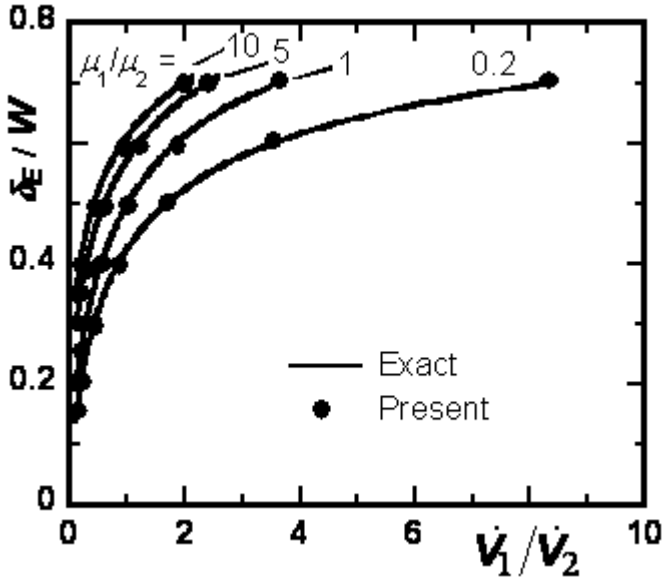

Figure 4-33: Fully-developed interface location (δ_E / W) versus volumetric flow ratio ($\dot{V}_1 / \dot{V}_2$).

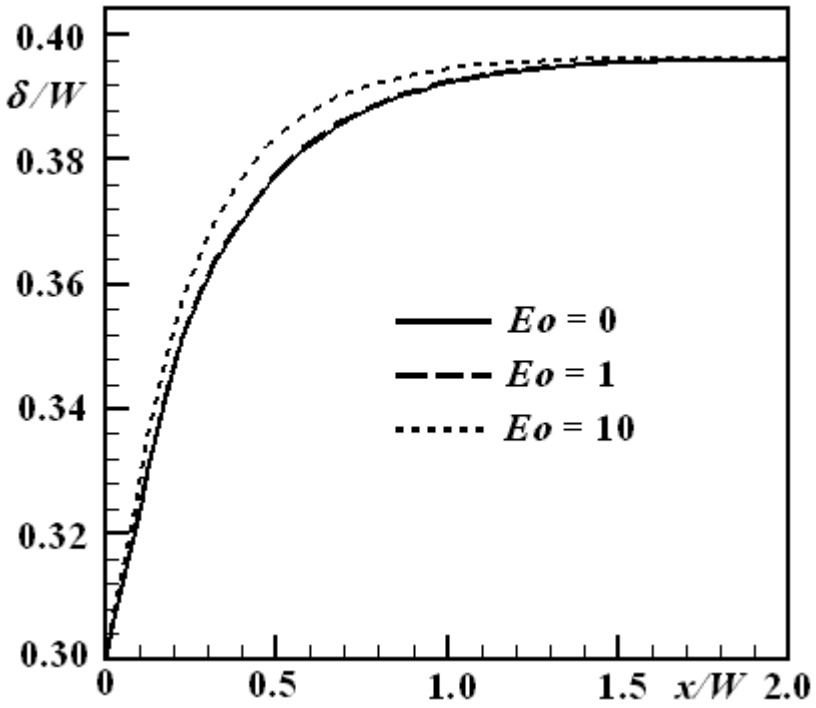

Figure 4-34: Effect of Eo on the F-F interface profile for Re = 0.01 and Ca = 0.1.

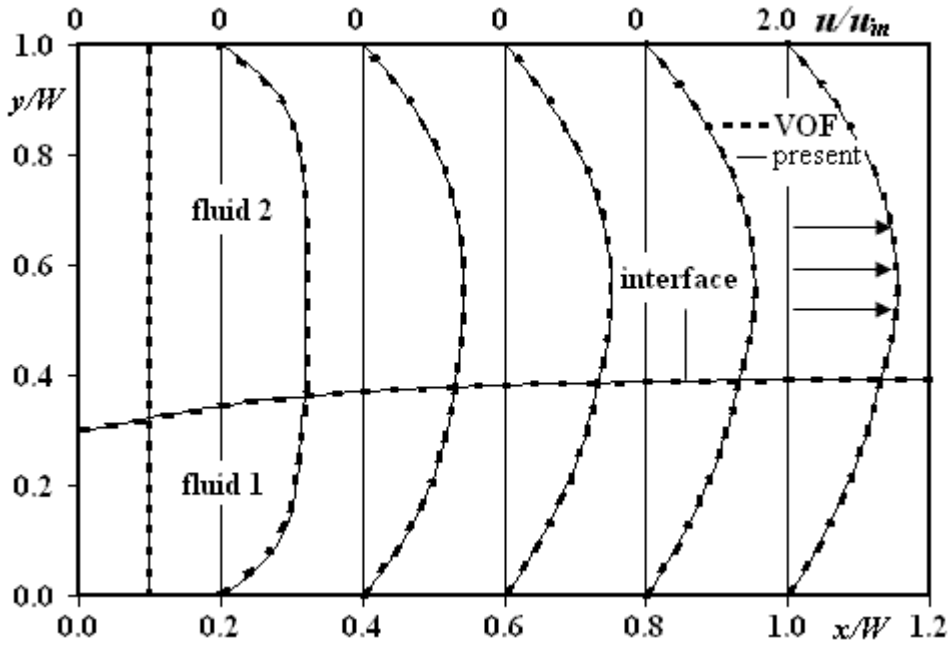

Figure 4-35: The F-F interface location and velocity profiles for two different fluids with $\delta_{in}/W = 0.3$ and $Ca = 0.1$.

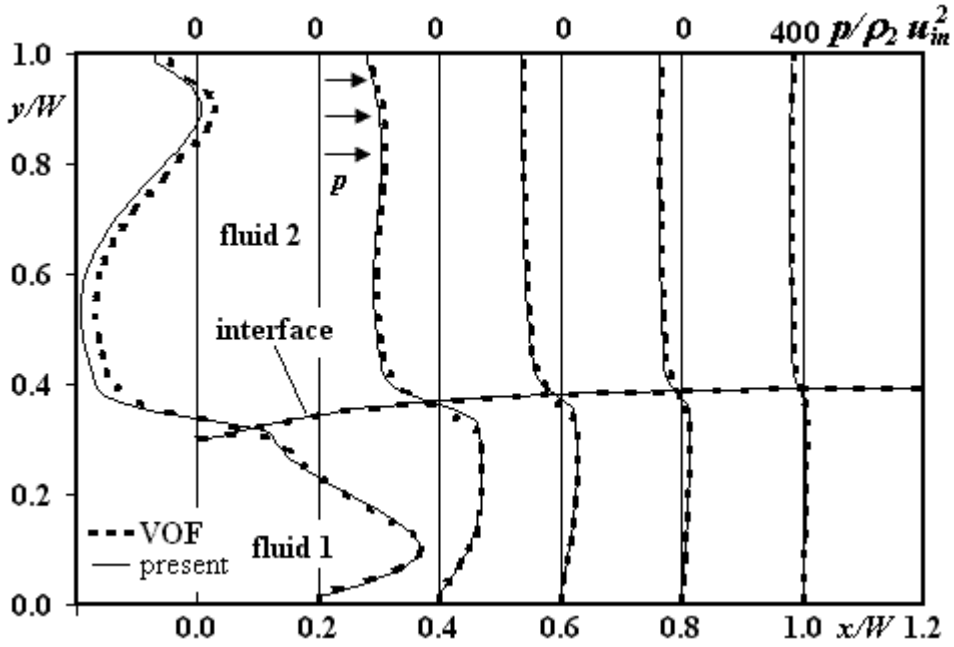

Figure 4-36: The F-F interface location and pressure distribution for two different fluids with $\delta_{in}/W = 0.3$ and $Ca = 0.1$.

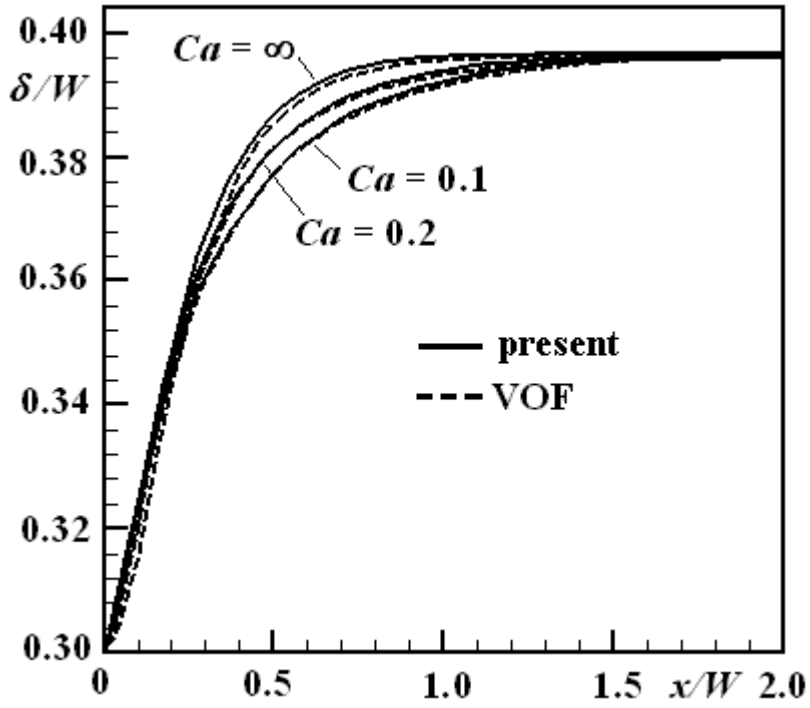

Figure 4-37: The F-F interface location for two different fluids with various Ca .

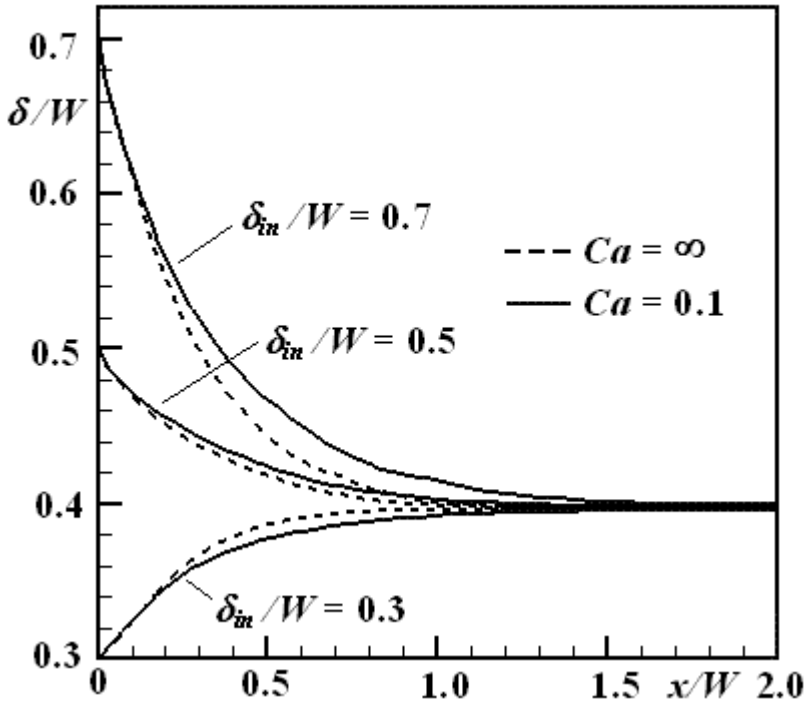

Figure 4-38: The F-F interface location for two different fluids with various inlet F-F interface locations.

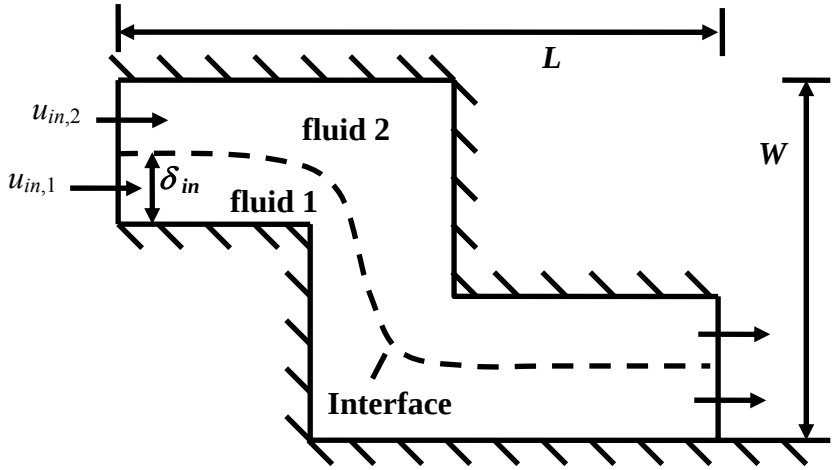

Figure 4-39: Stratified two-fluid flow in a double-bend.

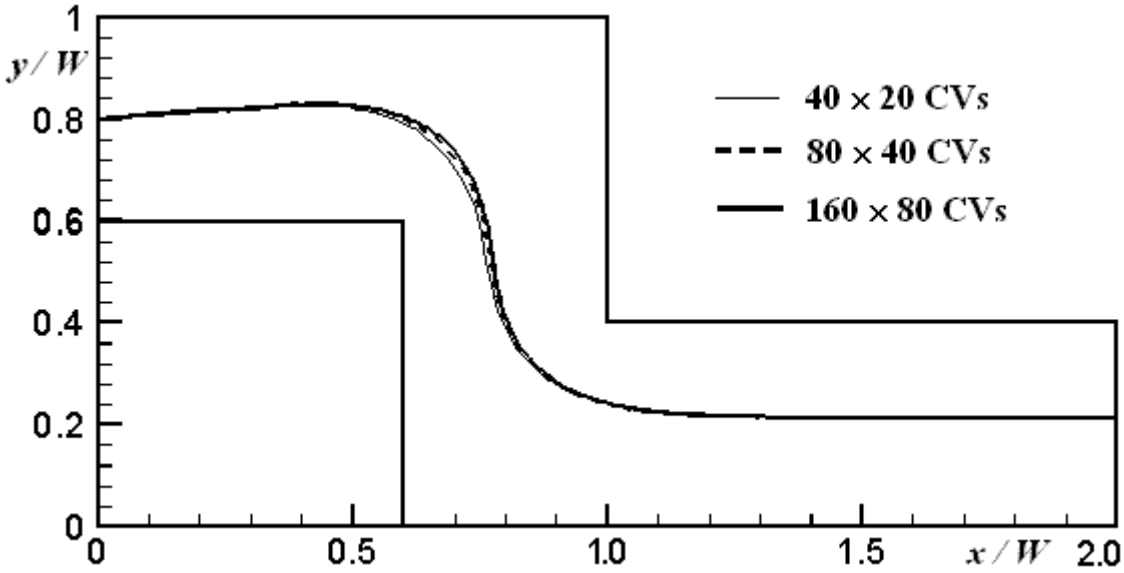

Figure 4-40: F-F interface profile in a double-bend with $Ca = 0.1$ obtained using 40×20, 80×40 and 160×80 CVs.

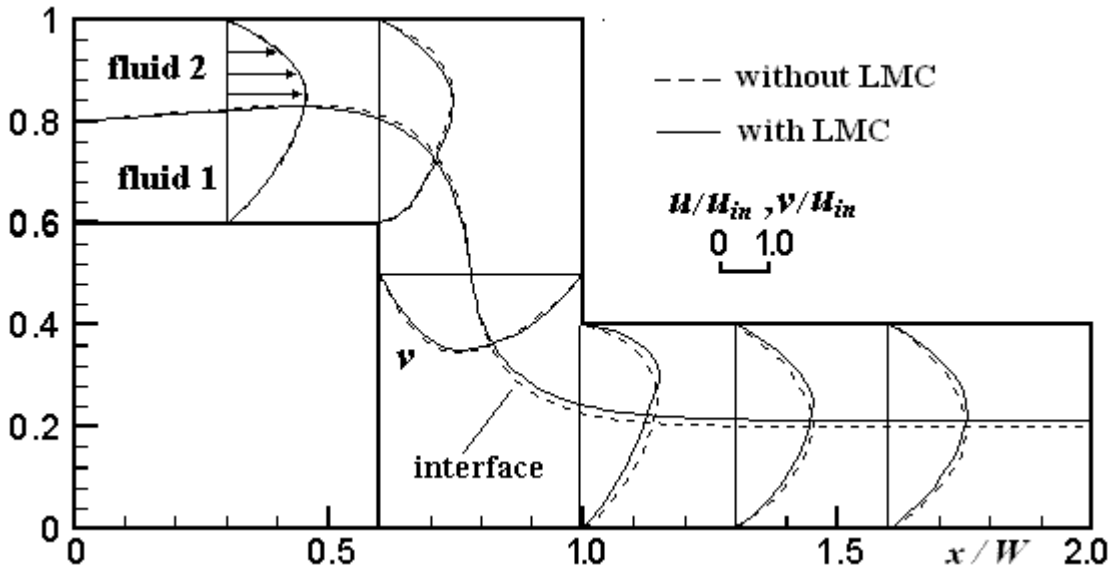

Figure 4-41: The F-F interface and velocity profiles in a double-bend with and without LMC.

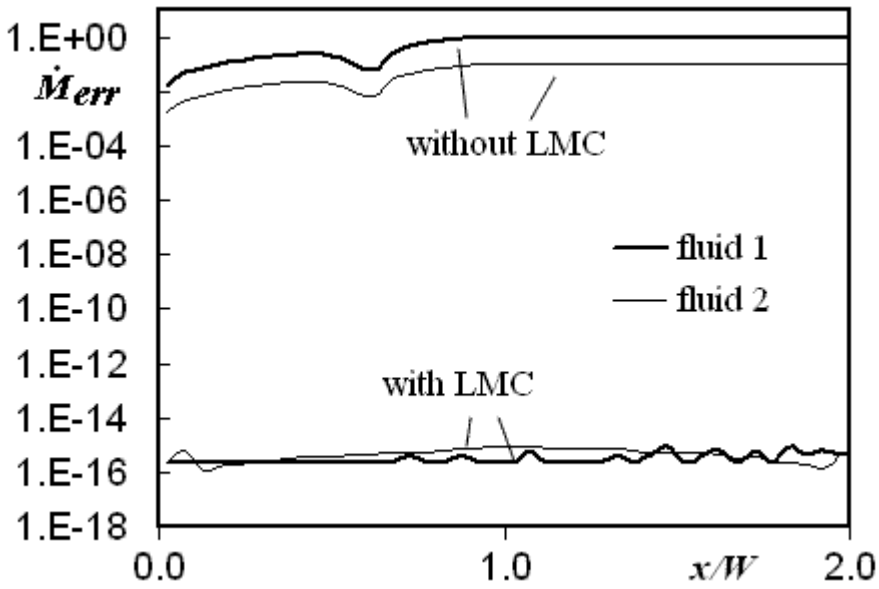

Figure 4-42: Mass error for with and without LMC.

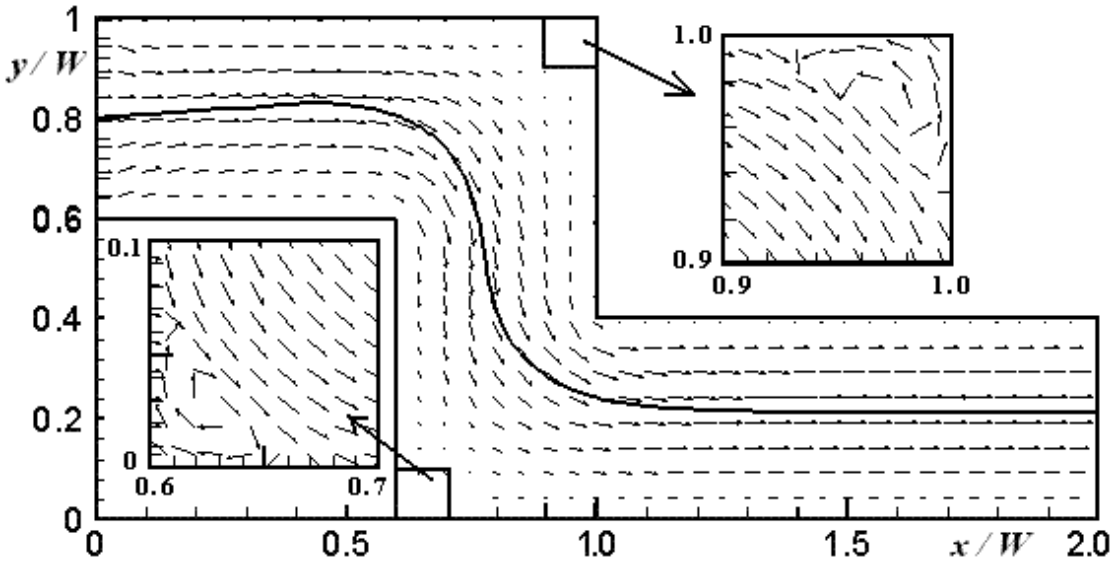

Figure 4-43: Velocity field in a double-bend with $Ca = 0.1$.

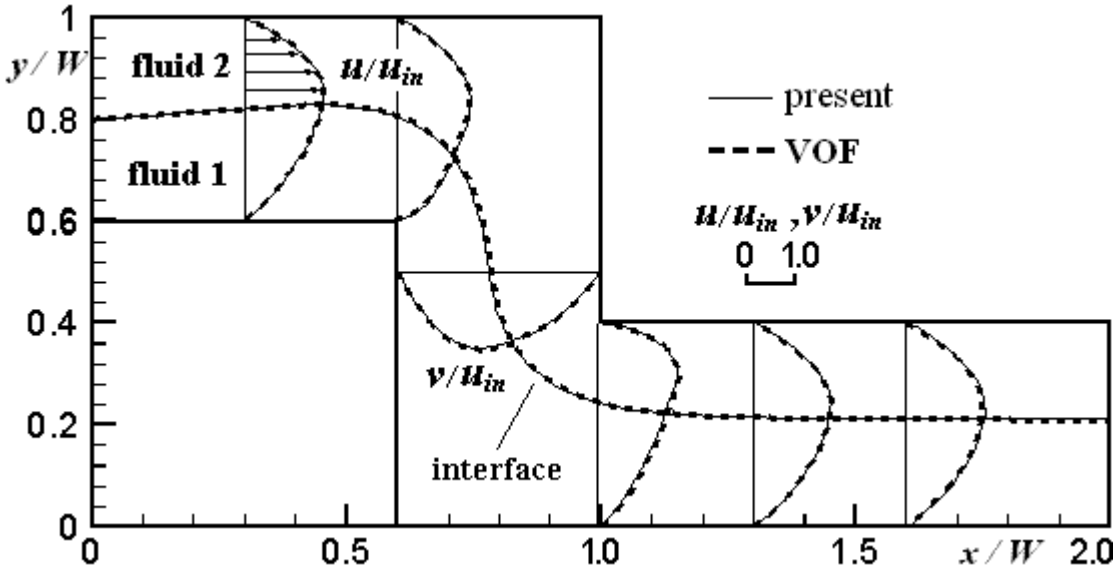

Figure 4-44: The F-F interface and velocity profiles in a double-bend with $Ca = 0.1$.

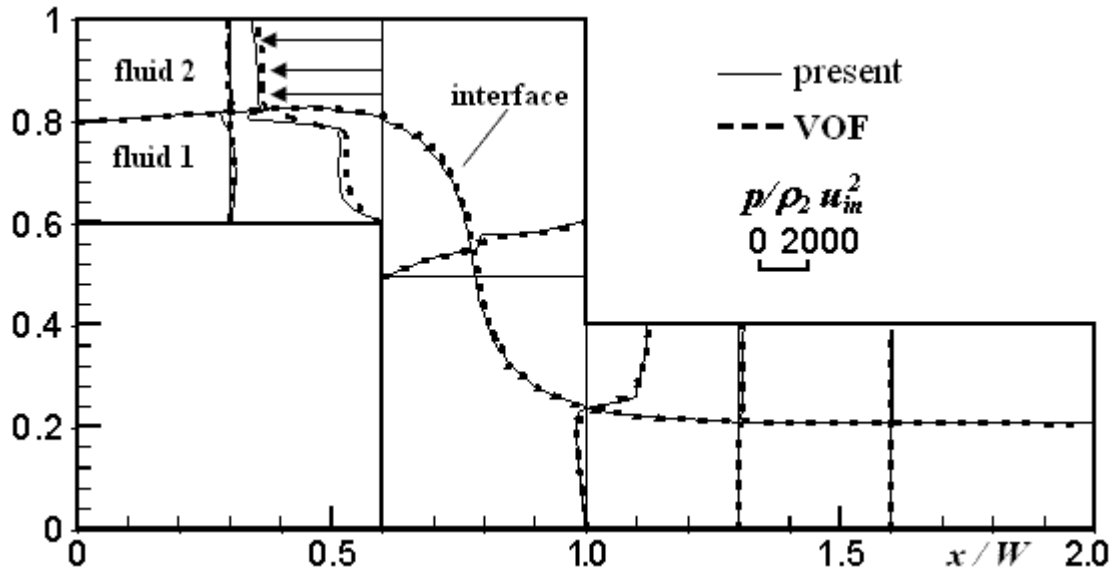

Figure 4-45: Pressure distribution in a double-bend with $Ca = 0.1$.

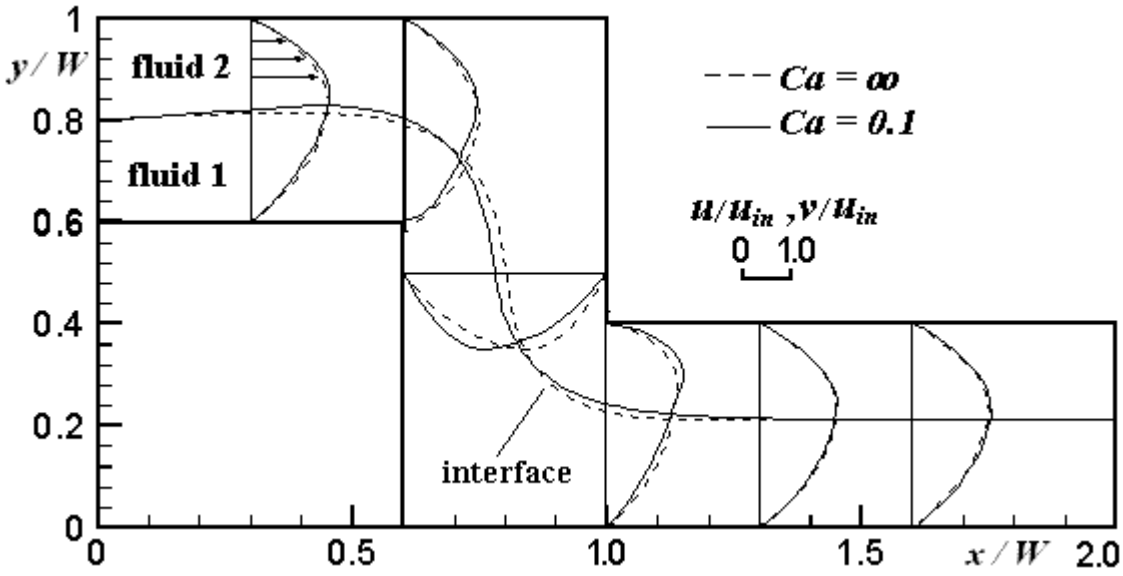

Figure 4-46: The F-F interface and velocity profiles in a double-bend with and without surface tension.

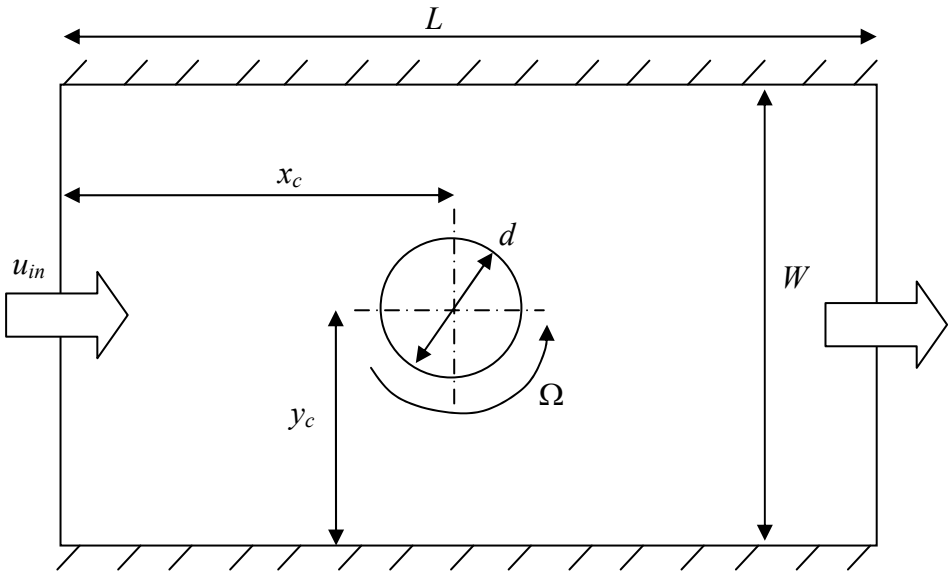

Figure 4-47: Flow around a circular cylinder in a two-dimensional channel.

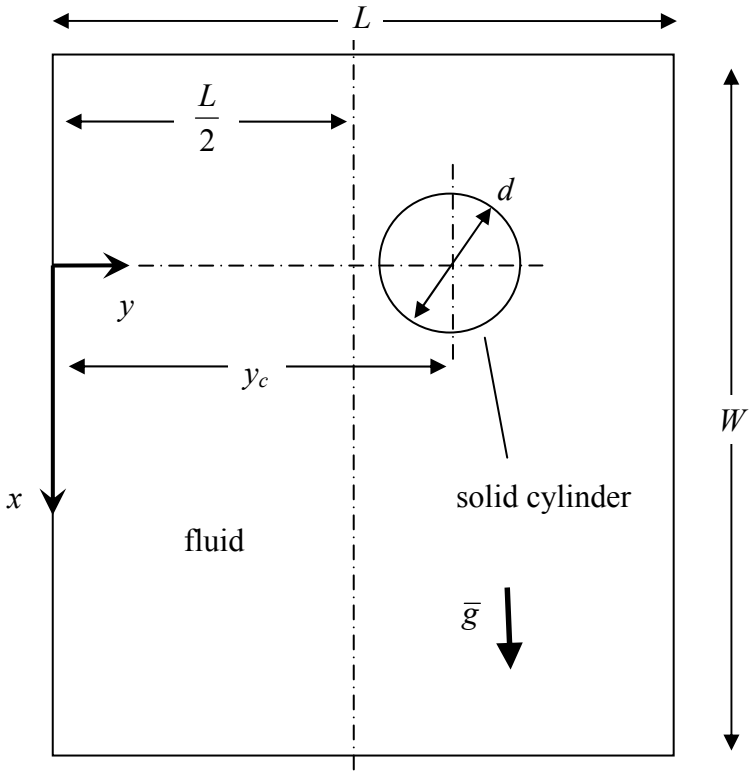

Figure 4-48: Sedimentation of a circular cylinder between parallel plates

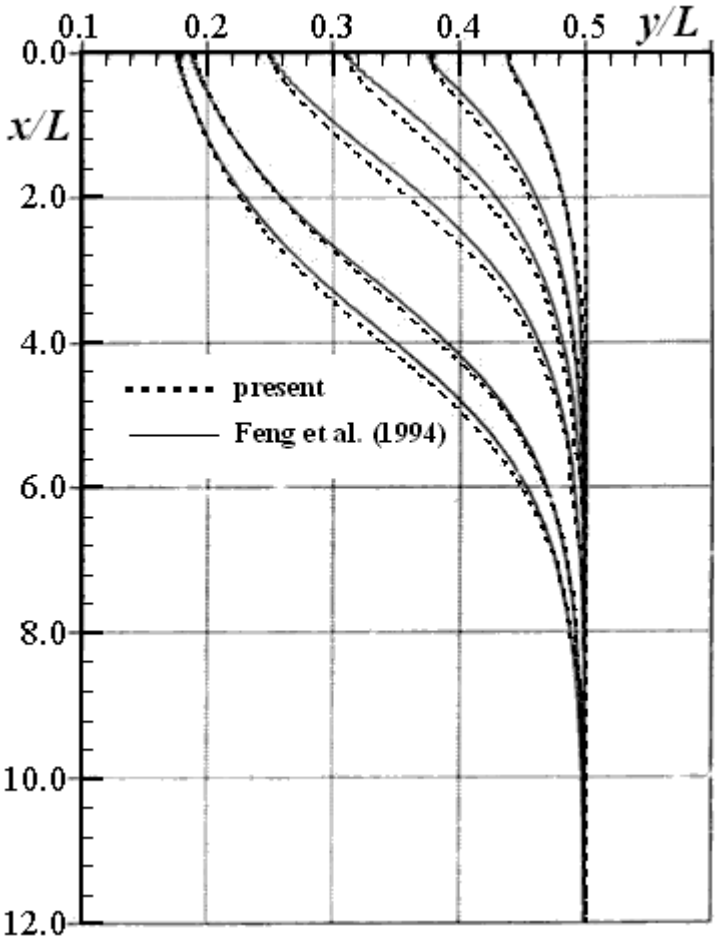

Figure 4-49: Settling trajectories of a circular cylinder under gravity for Re = 0.522 .

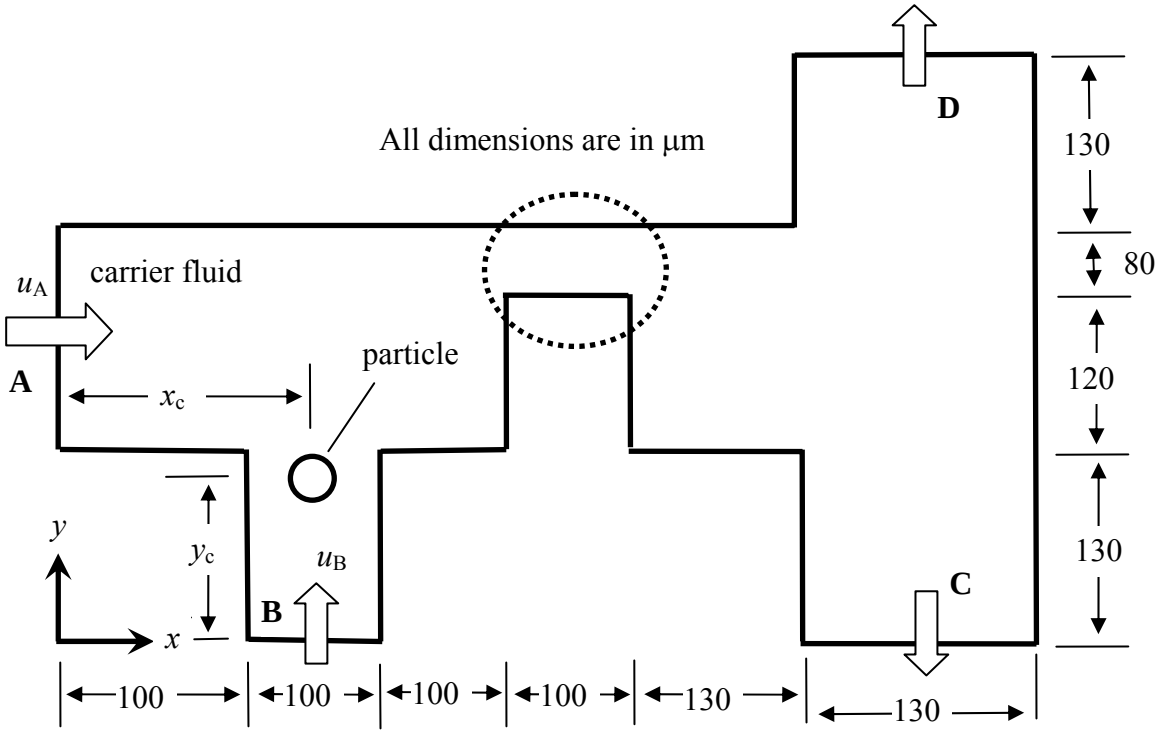

Figure 4-50: Schematic for flow of a particle in a microchannel system.

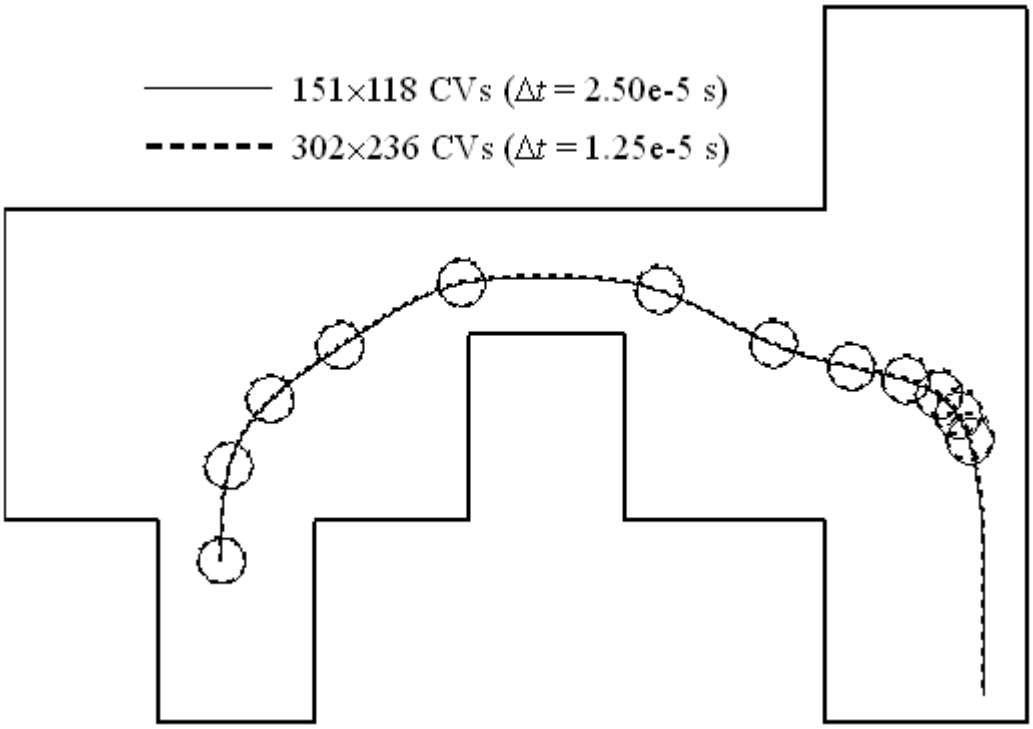

Figure 4-51: Grid independent study.

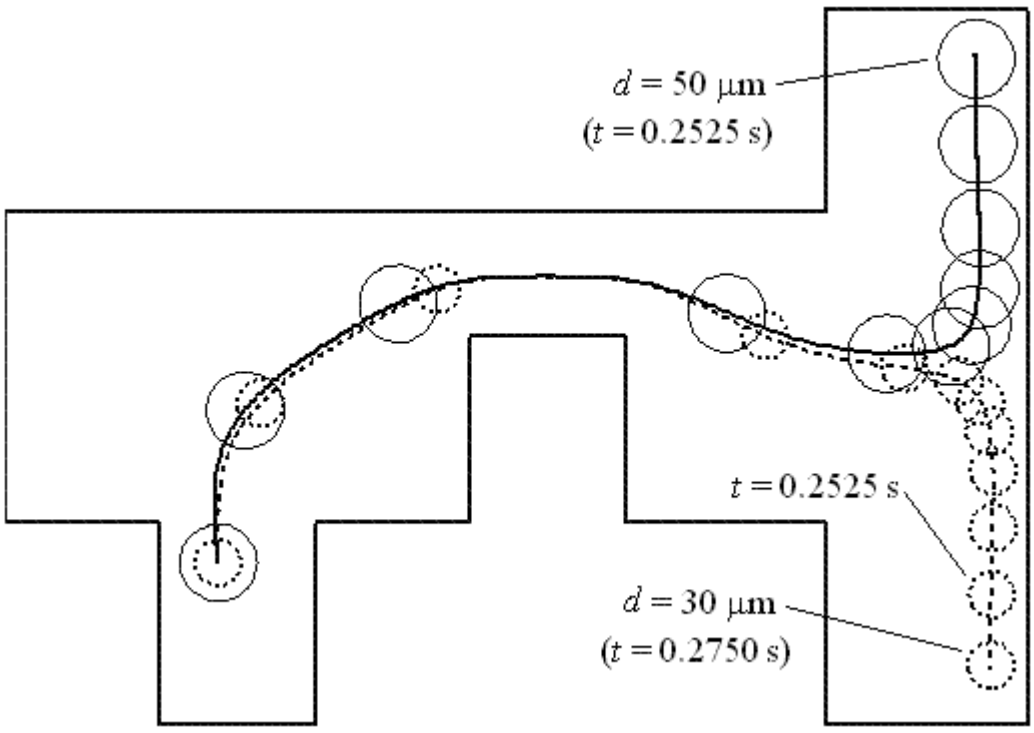

Figure 4-52: Effect of particle size on its trajectory.

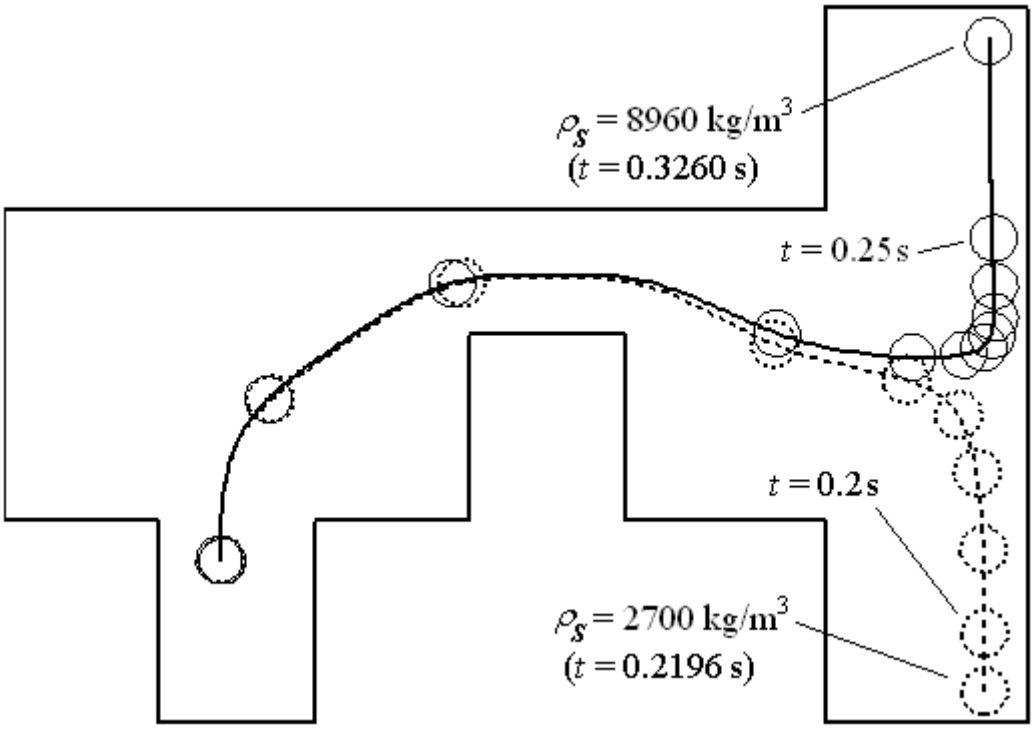

Figure 4-53: Effect of particle density on its trajectory.

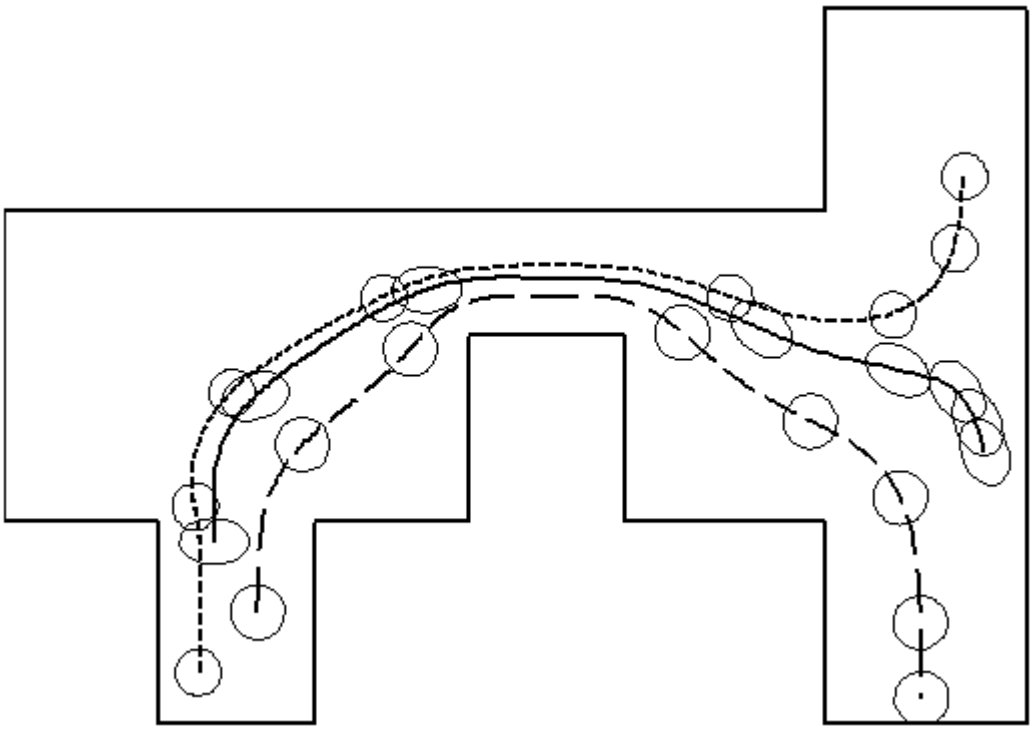

Figure 4-54a: Trajectories of three particles in a microchannel system.

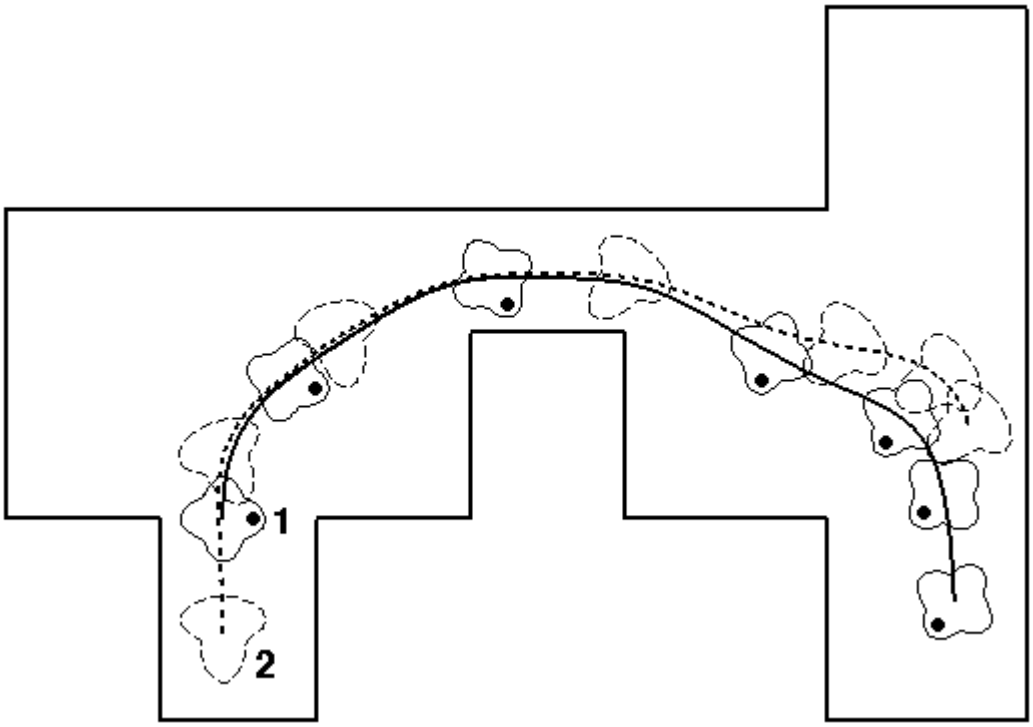

Figure 4-54b: Trajectories of two complex shaped particles in a microchannel system.

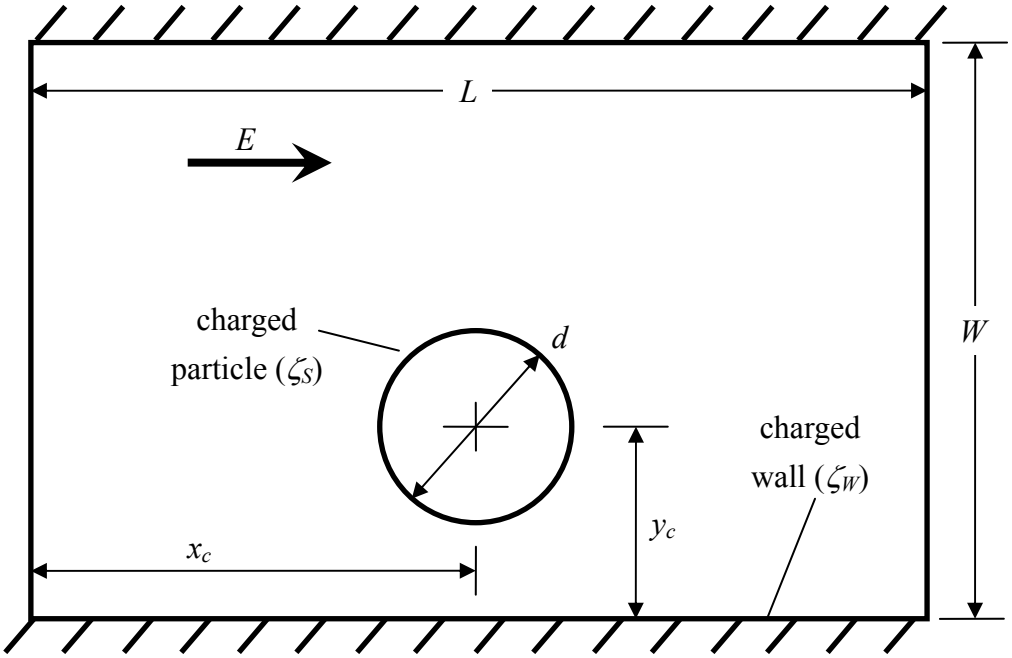

Figure 4-55: Schematic of the electrophoresis of a charged particle in a microchannel.

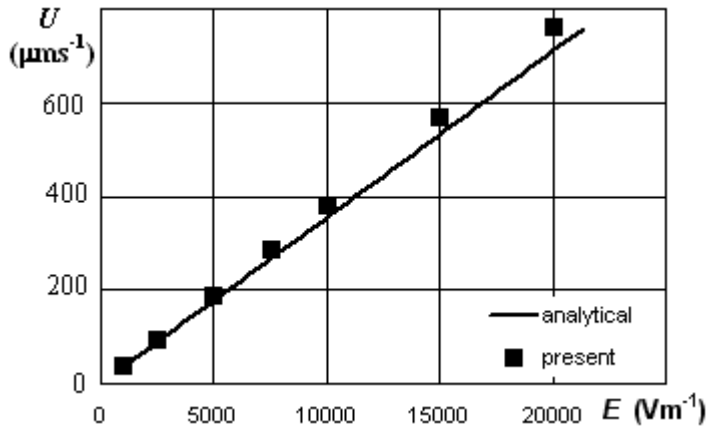

Figure 4-56a: Steady-state translational velocity of the charged circular particle.

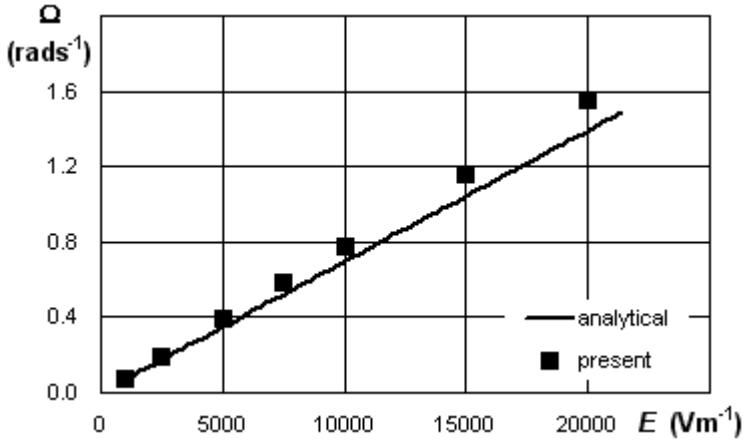

Figure 4-56b: Steady-state angular velocity of the charged circular particle.

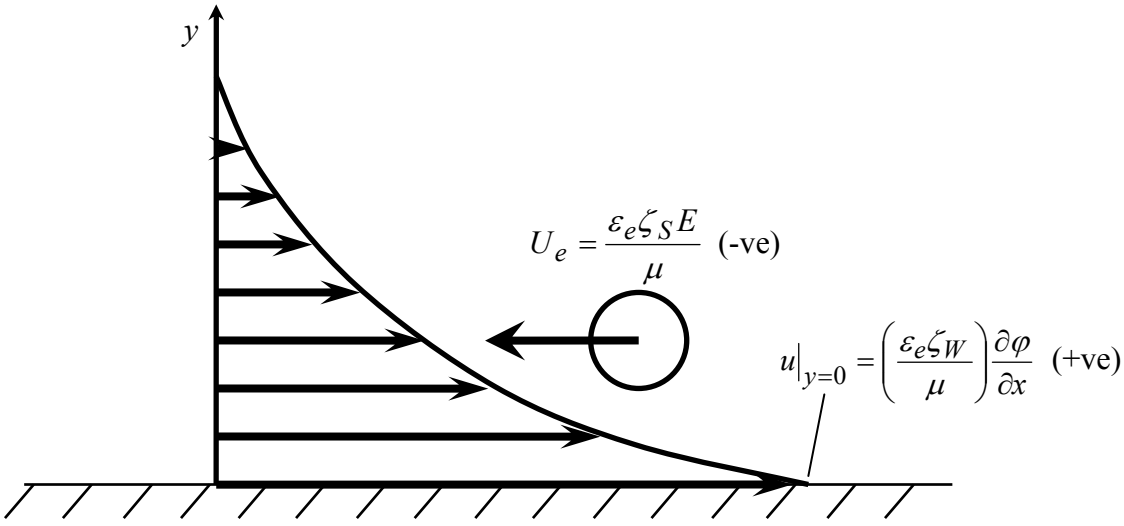

Figure 4-57: Electrokinetic effects on the wall and the particle.

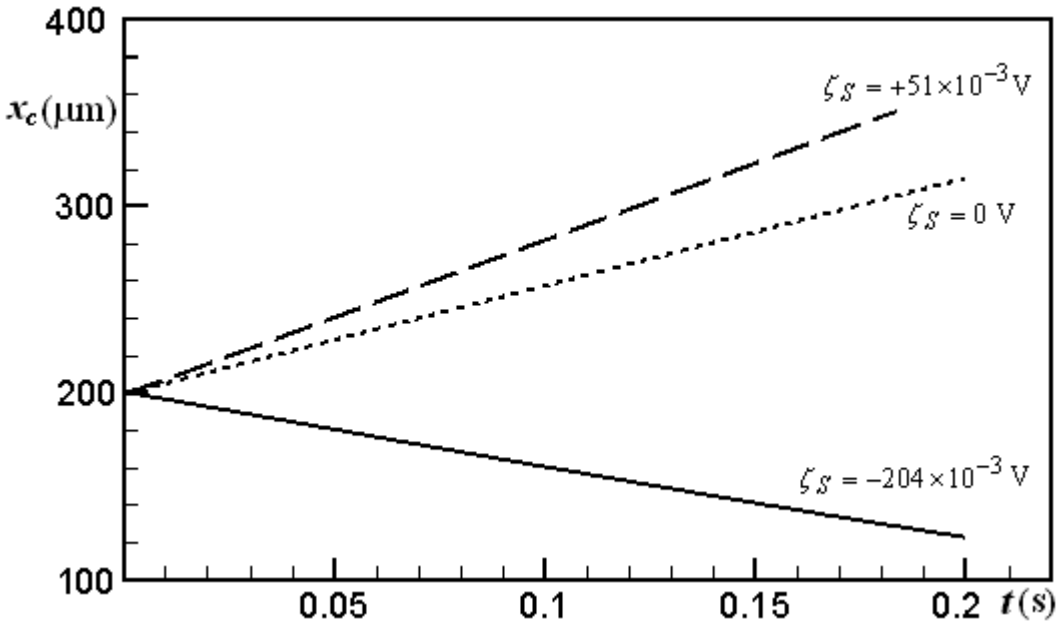

Figure 4-58: The instantaneous location of particles with different zeta potentials.

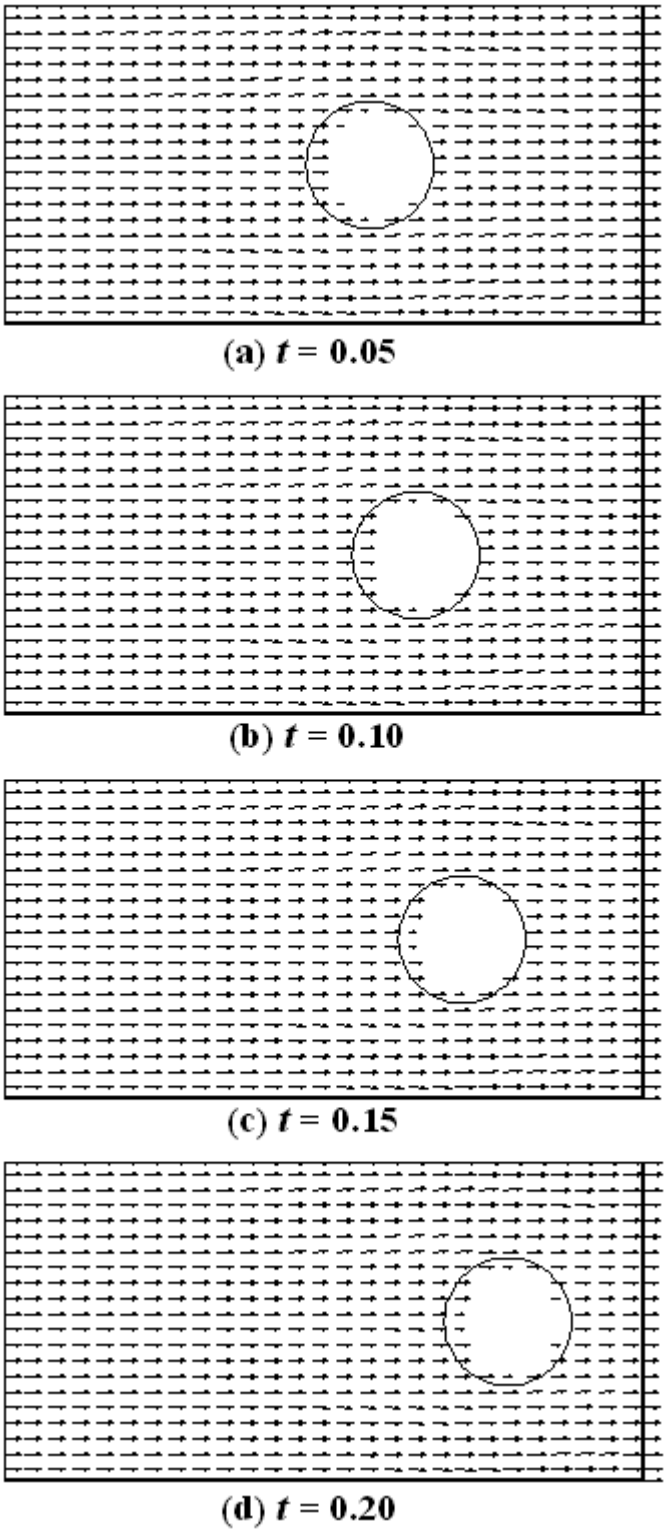

Figure 4-59: Flow field around a neutral particle.

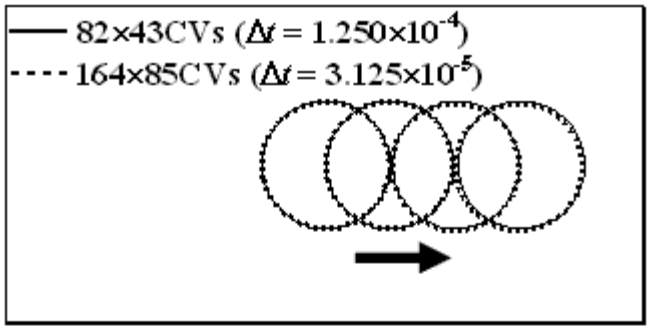

(a) grid independent study.

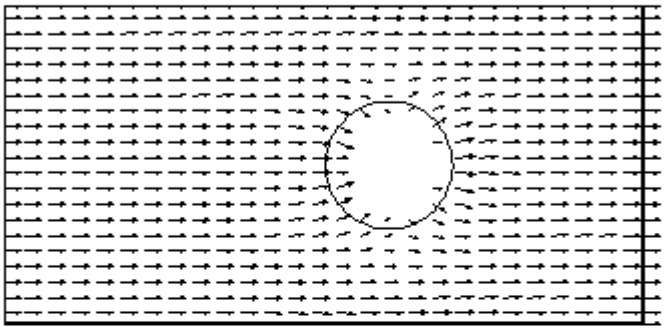

(b) t = 0.05

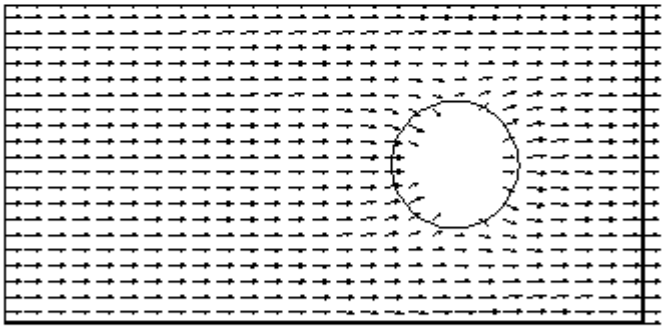

(c) t = 0.10

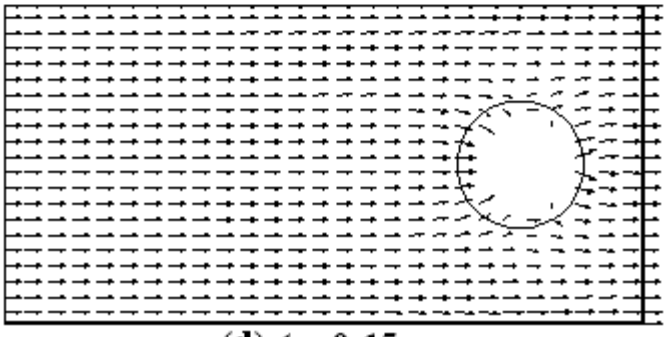

(d) t = 0.15

Figure 4-60: Flow field around a positively charged particle.

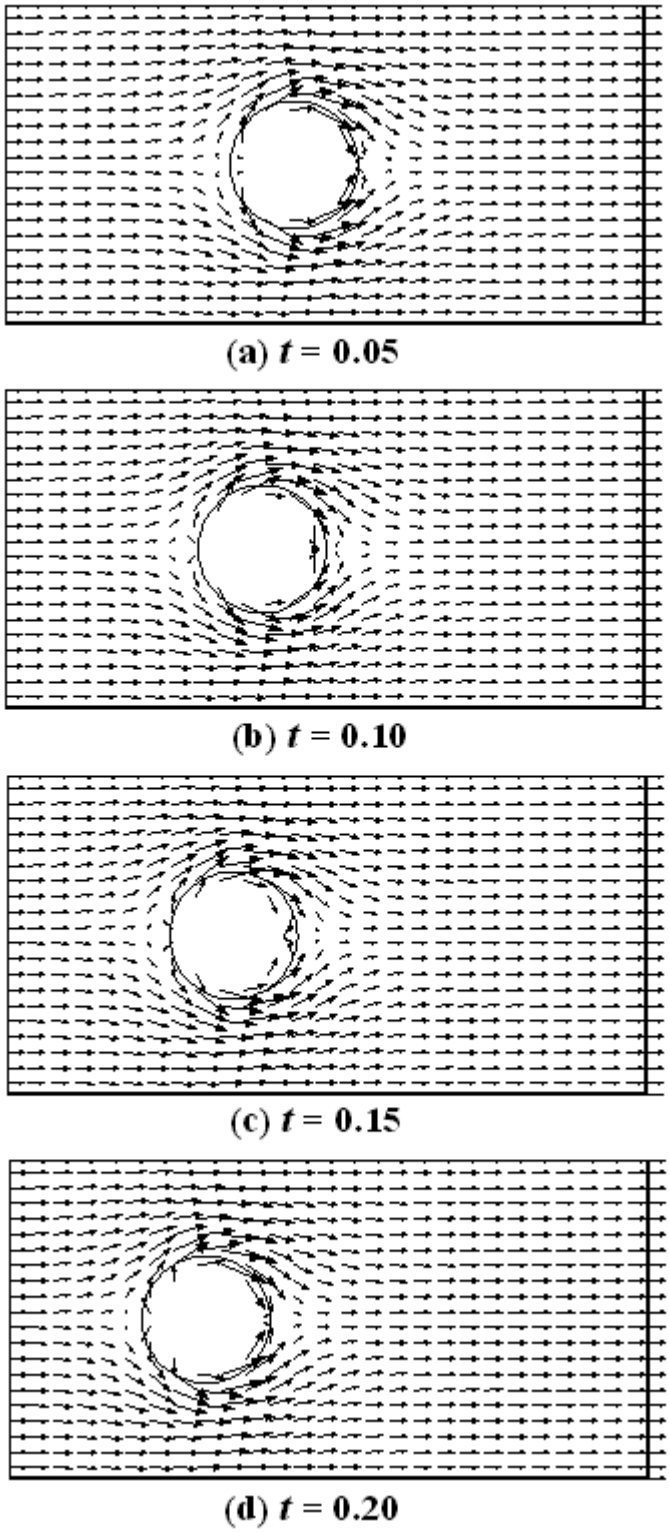

Figure 4-61: Flow field around a negatively charged particle.

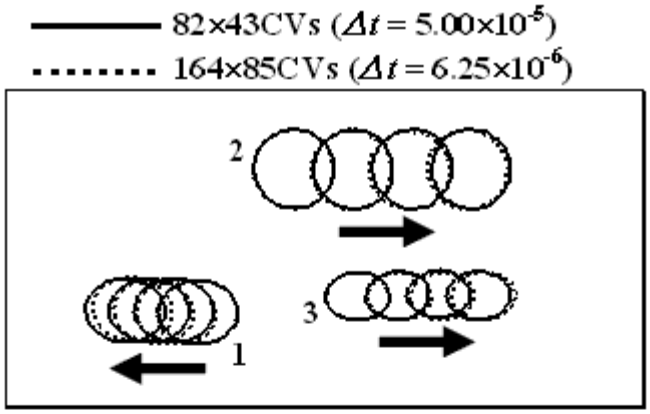

(a) grid independent study.

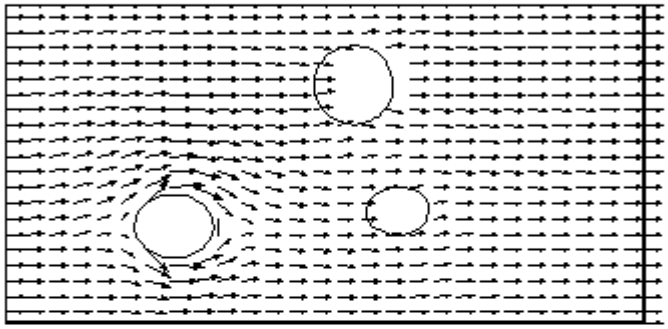

(b) t = 0.04

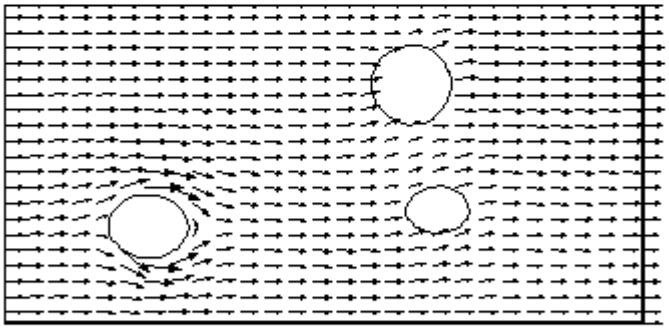

(c) t = 0.08

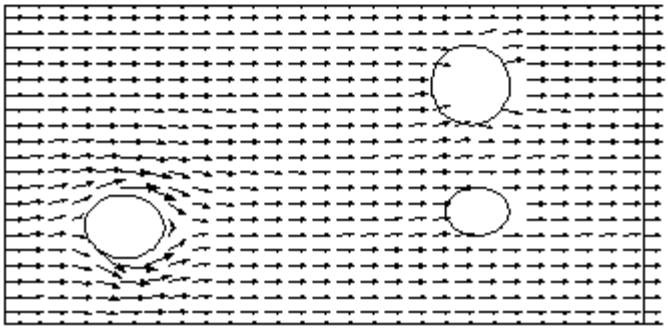

(d) t = 0.12

Figure 4-62: Electrophoresis of multiple particles.

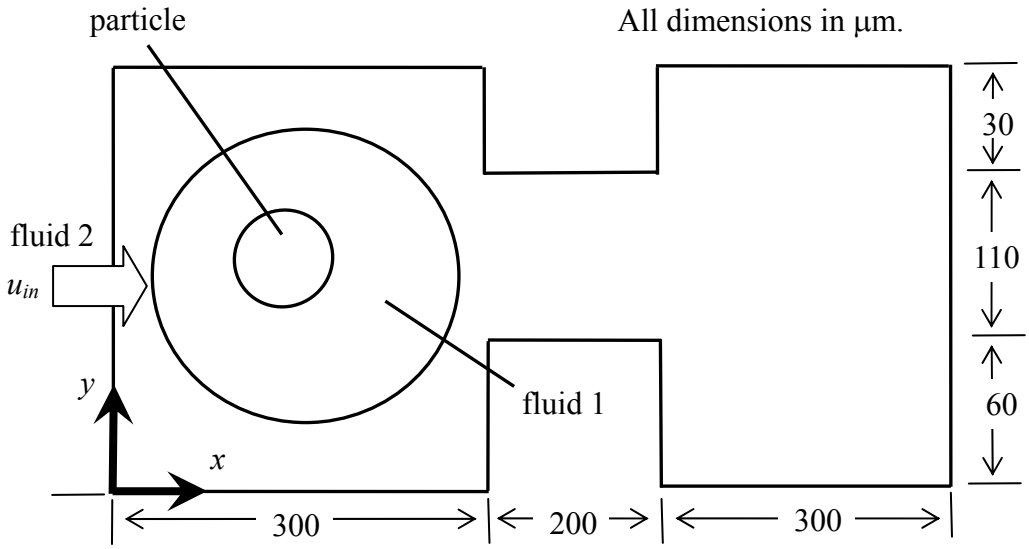

Figure 4-63: Flow of a particle-encapsulated droplet carried by an immiscible carrier fluid in a constricted microchannel.

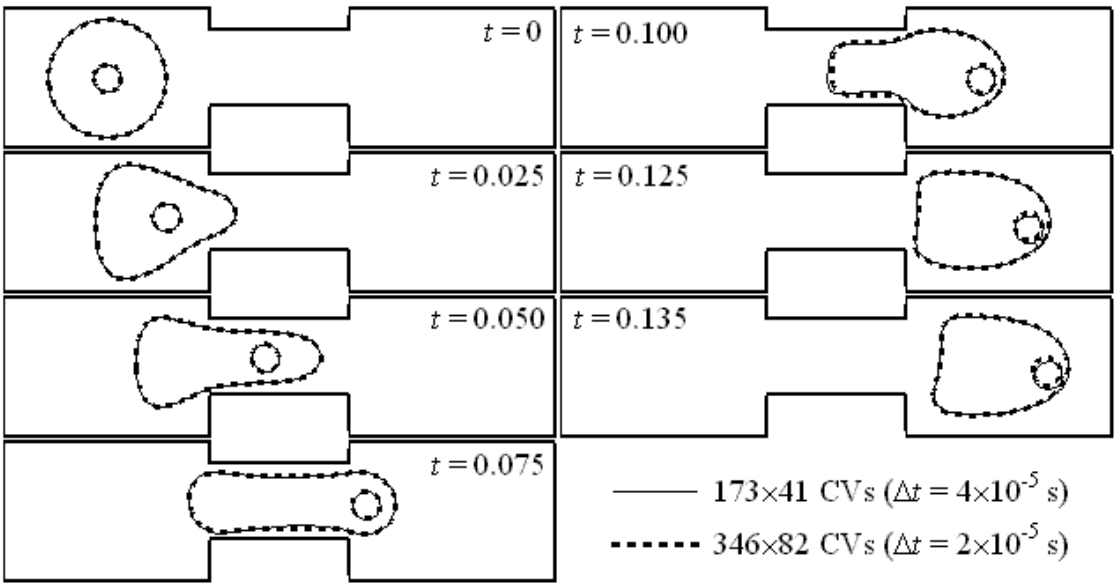

Figure 4-64a: Evolution of a particle-encapsulated droplet through a constricted microchannel.

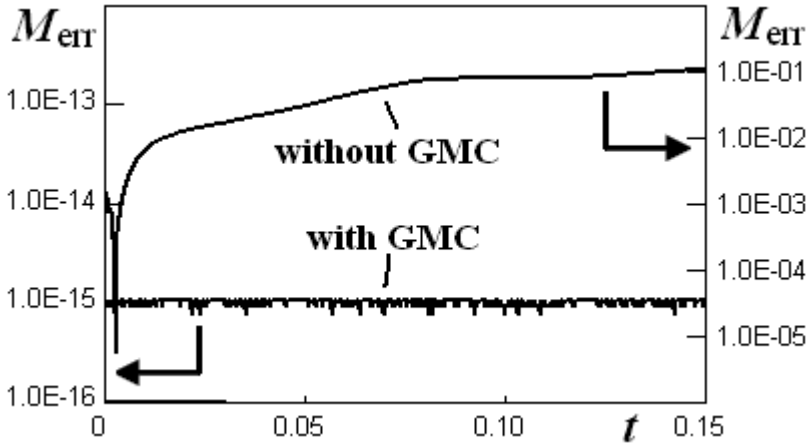

Figure 4-64b: Mass error of the reference fluid (fluid 1).

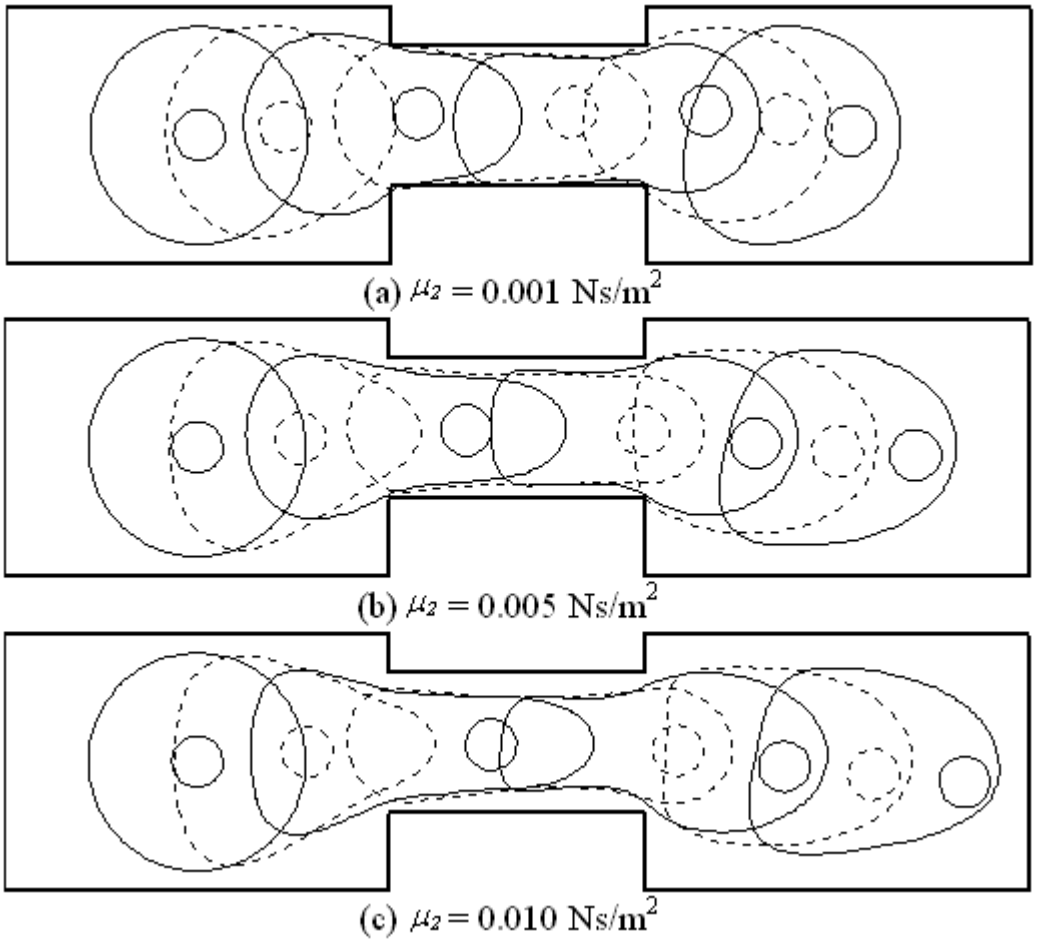

Figure 4-65: Effect of carrier fluid viscosity.

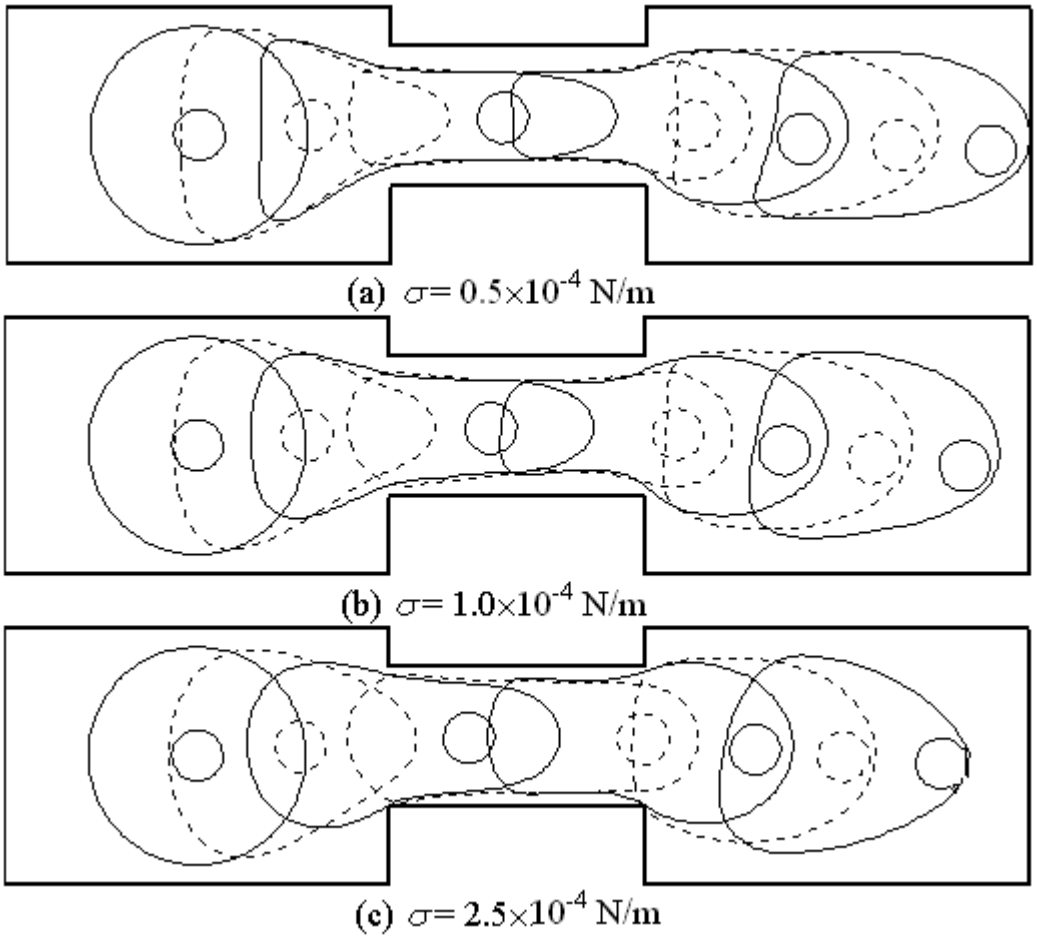

Figure 4-66: Effect of surface tension.

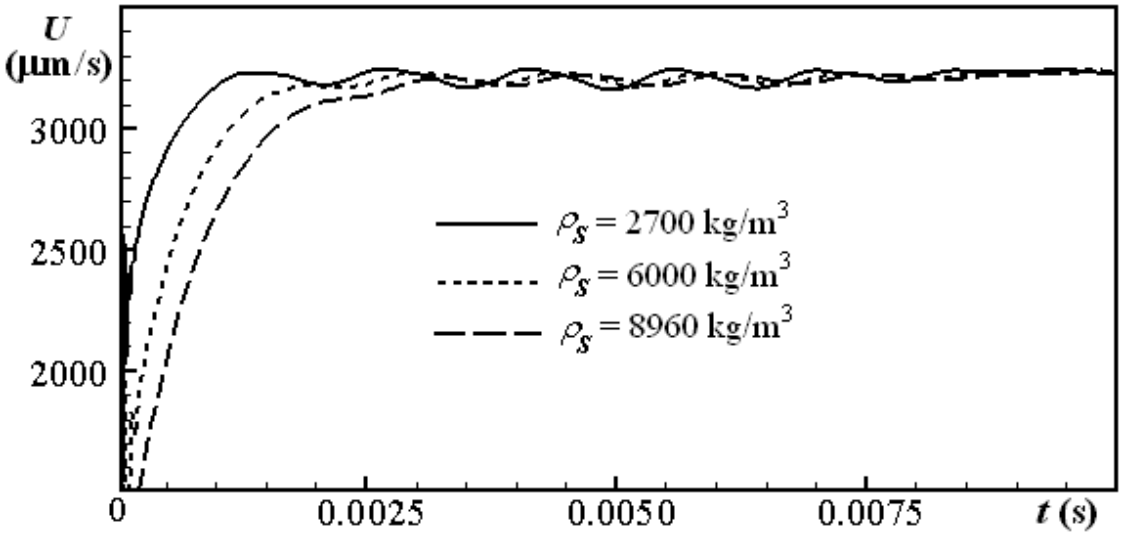

Figure 4-67: Effect of particle density on u of the particle.

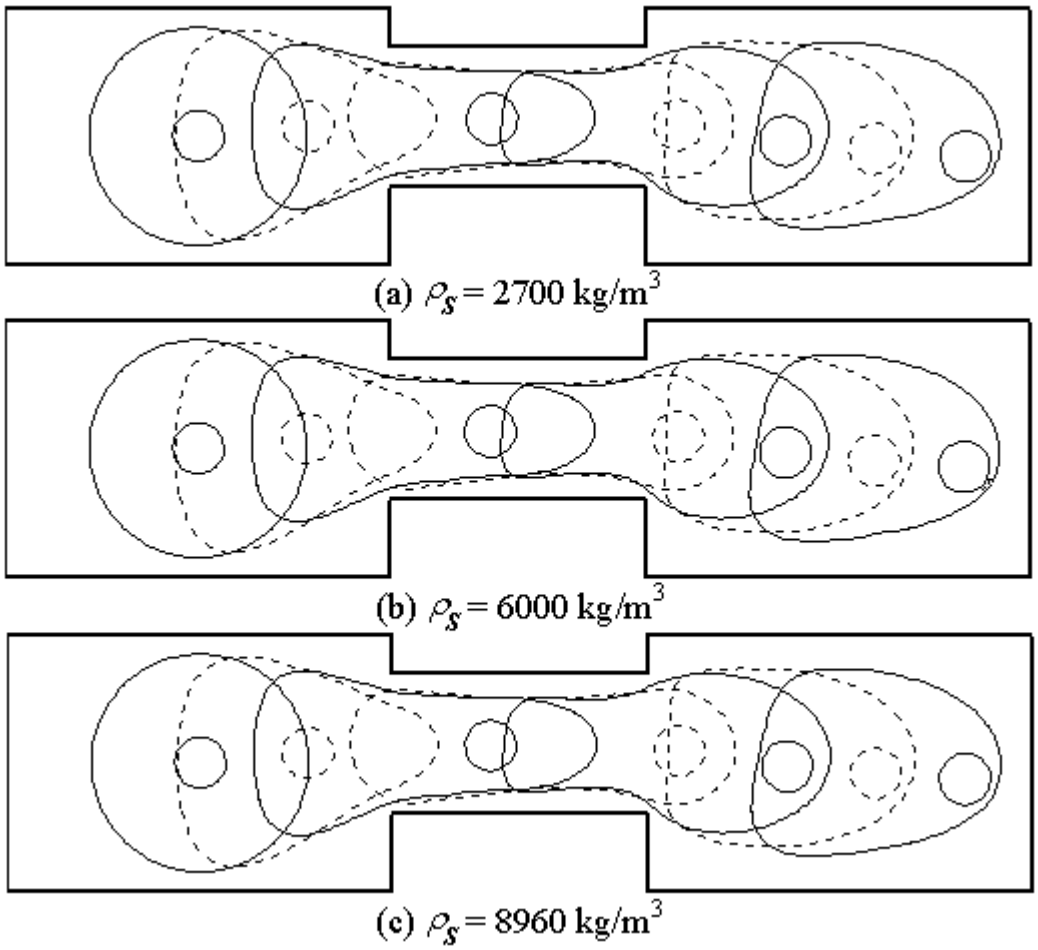

Figure 4-68: Effect of particle density.

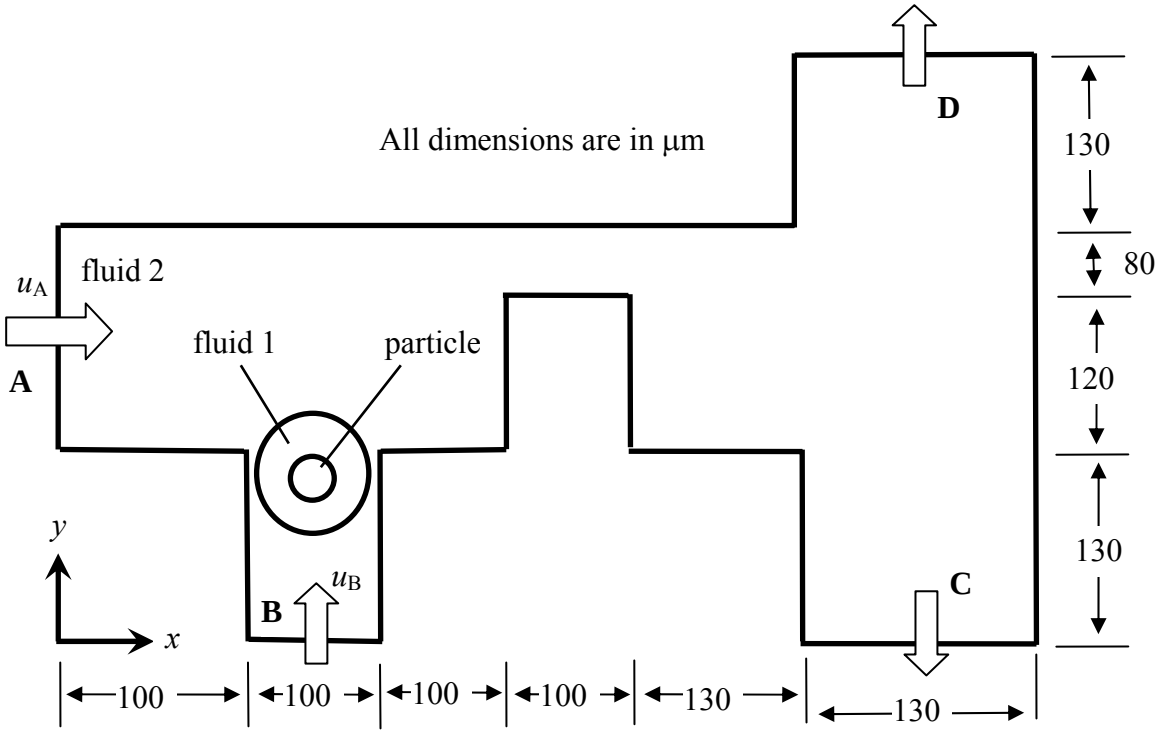

Figure 4-69: Schematic for flow of a particle in a microchannel system.

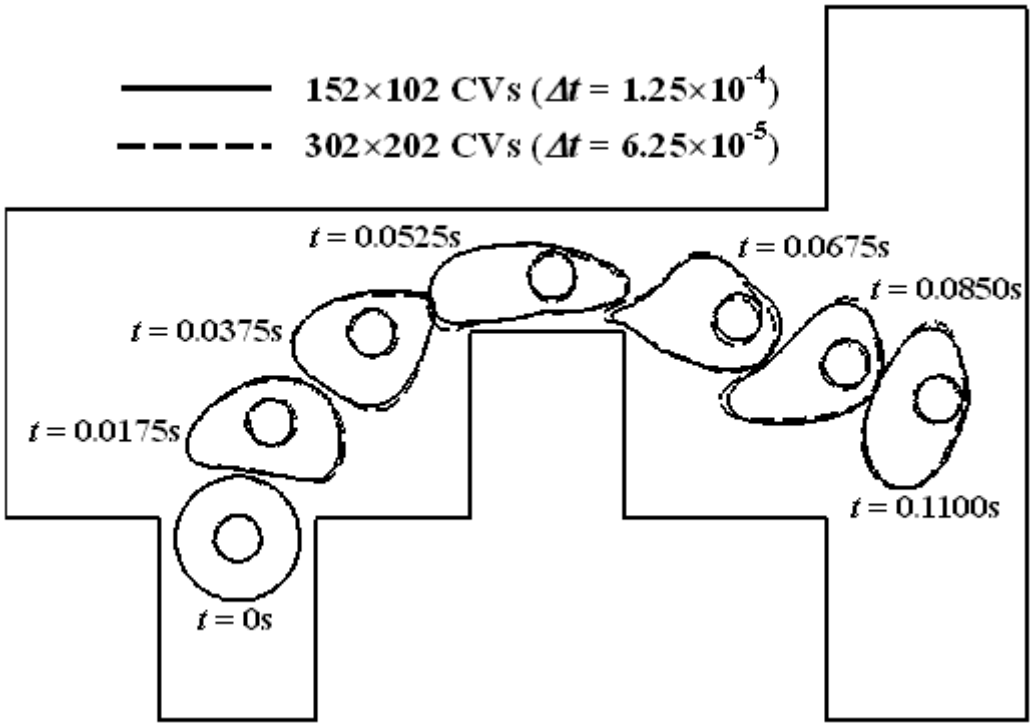

Figure 4-70a: Evolution of a particle-encapsulation droplet in a microchannel system.

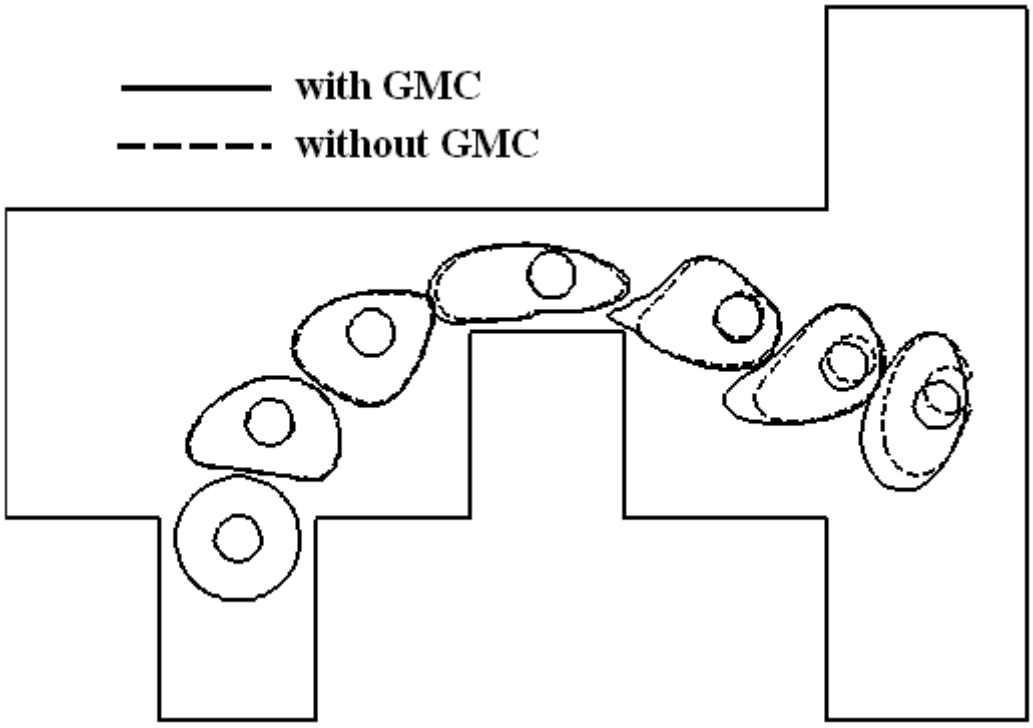

Figure 4-70b: Evolution of the particle-encapsulated droplet with and without GMC.

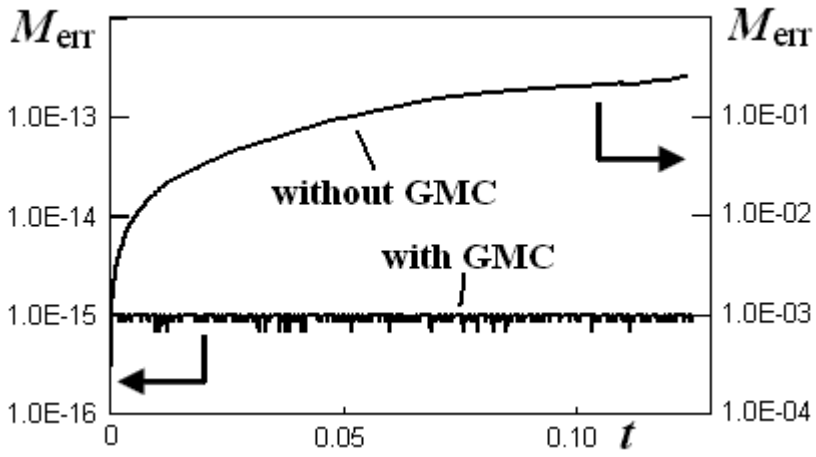

Figure 4-70c: Mass error of the reference fluid (fluid 1).

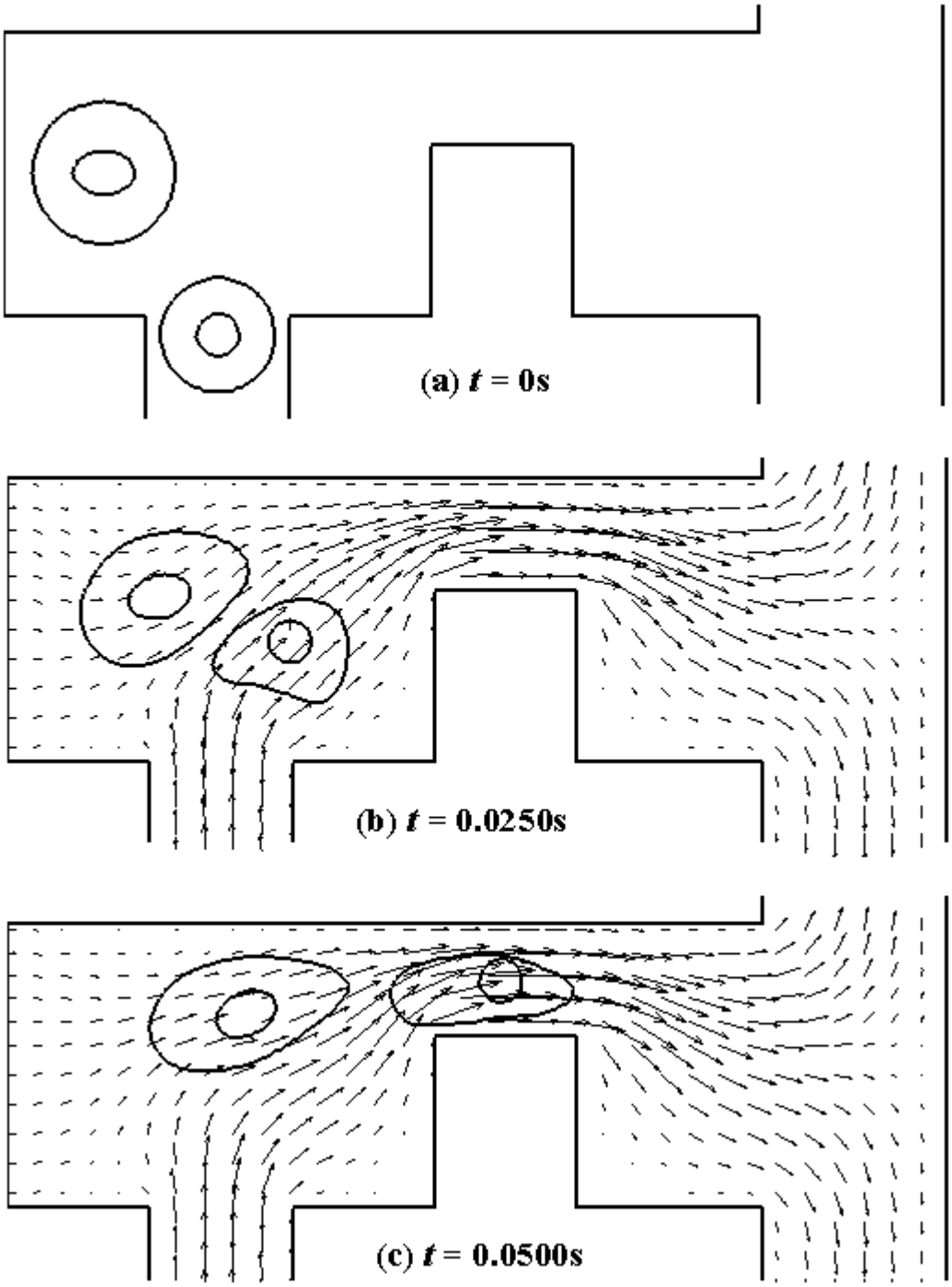

Figure 4-71: Evolution of two particle-encapsulation droplets in a microchannel system.

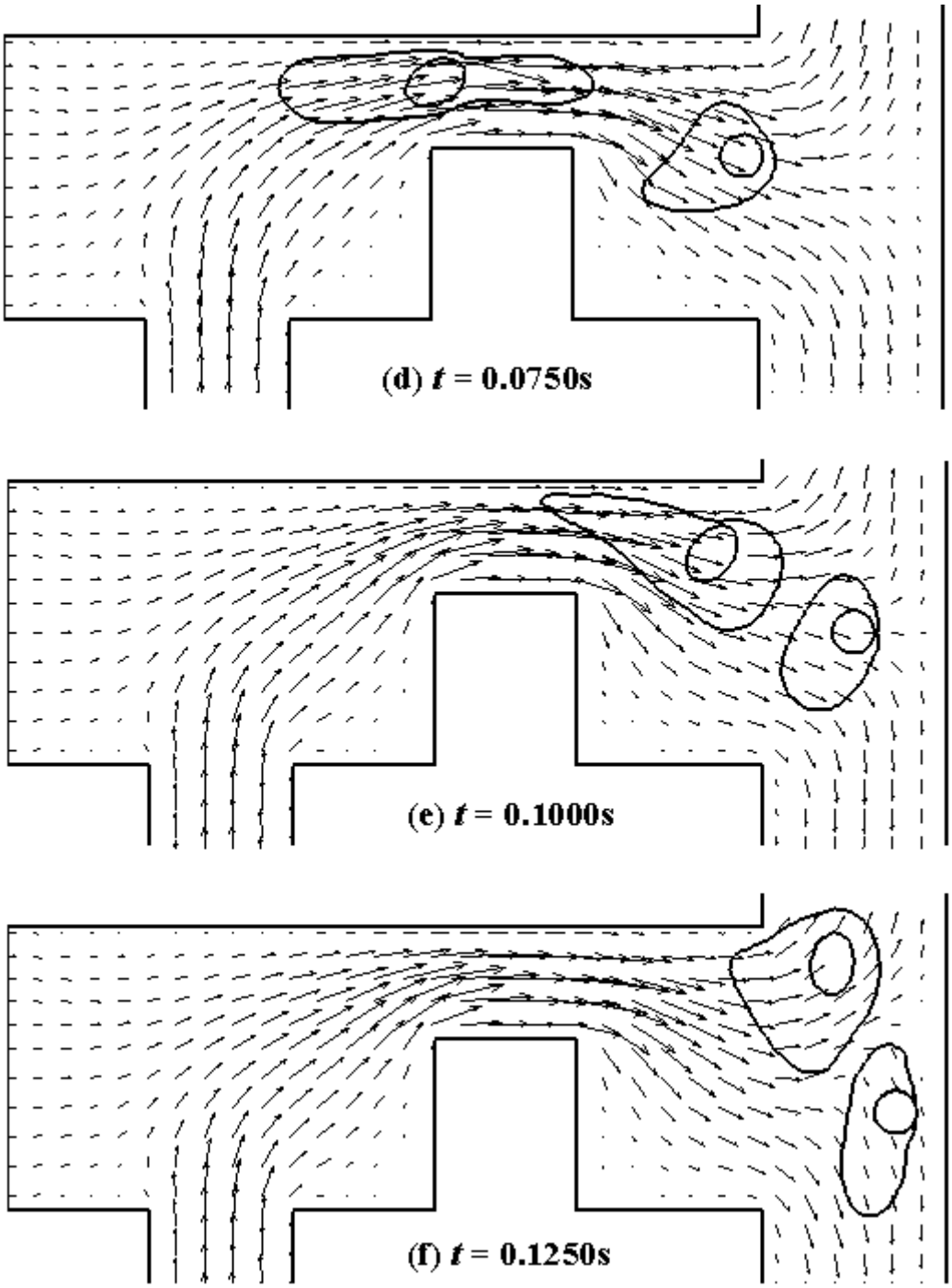

Figure 4-71: Evolution of two particle-encapsulation droplets in a microchannel system.

CHAPTER 5

CONCLUSIONS

5.1 Summary and Conclusions

Multiphase flows are encountered in many engineering applications. Micro-scale multiphase flows in particular receive intense interest recently due to its increasingly wider applications in the field of microfluidics. Unlike macro-scale multiphase flows which are dominated by inertia and gravity effects, micro-scale multiphase flows are characterized by a strong dependence on surface tension and viscosity. Multiphase flows in microfluidics includes but are not limited to liquid-gas (or vapour) flows, liquid-liquid droplet flows in digital microfluidics, liquid-solid particle flows and particle-encapsulated droplet flows. In these examples of micro-scale multiphase flows, the encountered interface can be classified either as a moving and deformable fluid-fluid (F-F) or a moving but non-deformable fluid-solid (F-S) interfaces. Both F-F and F-S interfaces play a major role in determining the flow behavior. Given the small size of these systems, numerical modeling plays a significant role in understanding the fundamental issues important to microscale multiphase flows.

In this study, a three-phase flow model with both F-F and F-S interfaces coexist together is proposed. The three phases are two fluids and a solid phase. Two limiting cases of the model are two-fluid flow and fluid-solid flow, representative of the above mentioned examples of micro-scale multiphase flows.

Among the available F-F interface prediction methods, the level-set method possesses much attractive strength over the other methods. Therefore, it is adopted as the F-F

interface capturing procedure in the present study. A weakness of the level-set method is its weak mass conservation. Two mass conservation schemes, i.e. Global (GMC) and Local (LMC) Mass Correction Schemes, are presented. While GMC is for general two-fluid flow problems, LMC is developed for stratified two-fluid flows. These schemes are extended to the situation where a third solid phase is present. Good mass conservation is demonstrated with these schemes. The level-set equation is modified to enhance numerical instability via adding artificial viscosity either to region beyond the F-F interface or specific regions deemed susceptible to numerical disturbances. The enhancement in numerical stability is demonstrated.

A new fixed-grid F-S interface tracking procedure is introduced. The solids are assumed to be a fluid of high viscosity. These solids are represented using local distance functions, offering the versatility in representing solids of complex geometries by merging a few distance functions of simple shaped solids. The motion of each solid is tracked explicitly followed by a reconstruction of its local distance function. Therefore, no deformation of the solid surface occurs. The procedure is able to handle multiple complex shaped solids. The F-F interface tracking procedure is extended to the case where there is a slip velocity at the solid surfaces as in the modeling of electrophoresis of particles.

With these interfaces capturing or tracking procedures, a set of combined conservation equations can then be written for the physical domain consists of the three phases. Surface tension effects at the F-F interface, both curvature and Marangoni driven, are incorporated using the Continuum Surface Force model. Solution of the governing equations together with the F-F interface capturing and F-S interface tracking procedures are implemented in a finite volume method.

The model is tested and validated against available analytical solutions and existing numerical results. This demonstrates simultaneously the variety of multiphase flow problems to which the current model can be applied. The case studies conducted include droplet flows in channels of various geometries, stratified two-fluid flows, pressure or electrically driven flow of particles in microchannels and particle-encapsulated droplets flows.

The present model is applicable to both micro-scale and macro-scale multiphase flows involving either the F-F, the F-S or both interfaces. It is the hope of the author that the present model will be of benefit to those involved in the investigation of these transport processes.

5.2 Suggestions for Future Work

The extension to problems with more than two fluids, i.e. with more than one F-F interface, can be made. In the present study, only one single F-F interface is captured. In the event where there are more than two fluids, there will be more than one F-F interfaces. For example, there are three different fluids and two different F-F interfaces in double emulsion droplets (Utada et. al, 2005). Each of these F-F interfaces can be captured using the same F-F interface capturing procedure.

In the tracking of the F-S interface, only the case where there is no collision among the solids or with the wall is considered. General, especially for multiple solids, collisions occur. Glowinski et al. (1999) and Glowinski et al. (2001) proposed a short ranged repulsive force model for collision modeling. Collision is assumed to occur if the distance between the two solid surfaces is less a predetermined distance (usually a factor

of the length of one computational cell) and a repulsive force is activated between the two solids. This repulsive force is added into the Newton-Euler equation of each solid preventing them to penetrate each other. Similar collision strategy can be incorporated into the present model.

Only rigid solids are considered in the present study. Non-rigidity of solids is frequently encountered. For example, cell deforms when flowing through capillary. A change in both mass and therefore geometrical shape occur when a moving solid undergoes melting or solidification. Such type of problems involving moving and deforming solids are challenging and worth pursuing given its practical importance. For these deforming solids, the F-S interface tracking procedure requires modifications to include additional physics governing the deformation of the F-S interface.

In the present three-phase flow model, the solid is confined in one of the fluids. For a more general situation, the solid may enter into the other fluid, e.g. particle break out from a droplet. Under such a condition, the problem of enforcing three-phase contact angle needs to be considered. Fortunately, for both F-F and F-S interfaces defined via level-set or distance functions, as in the present study, the contact angle and contact line conditions can be enforced using an approach proposed by Sussman (2001). Sussman (2001) devised a method to prescribe a contact angle on stationary flat surface by extending the fluid-fluid level-set function to the outside of the fluid domain, i.e. inside the solid. The level-set function inside the solid is evolved by solving a modified level-set equation. This approach was employed by Son (2005) in a two-dimensional stationary curved solid surface and by Singh and Joseph (2005) in a three-dimensional moving curved solid surface. Although for these studies, only static contact angle is prescribed, the idea can be extended to include dynamic contact angle.

The present model is formulated with minimal reference to two-dimensionality. The applicability of the present model is demonstrated for various two-dimensional multiphase flows. It is of interest to extend the present procedure to three dimensions for more realistic predictions. No new additional formulation or numerical technique is required. The model can be extended straight forward to three-dimensional flow in a dimension-by-dimension manner.

REFERENCES

Agresar, G., Linderman, J.J., Tryggvason, G. and Powell, K.G., 1998, An Adaptive, Cartesian, Front-Tracking Method for the Motion, Deformation and Adhesion of Circulating Cells, J. of Computational Physics 143(2) 346-380.

Anderson, D.M., McFadden, G.B. and Wheeler, A.A., 1998, Diffuse-interface methods in fluid mechanics, Annual Review of Fluid Mechanics 30 139-165.

Anna, S.L., Bontoux, N. and Stone, H.A., 2003, Formation of dispersions using "flow focusing" in microchannels, Applied Physics Letters 82(3) 364-366.

Annaland, M.V.S., Deen, N.G. and Kuipers, J.A.M., 2005, Numerical simulation of gas bubbles behaviour using a three-dimensional volume of fluid method, Chemical Engineering Science 60(11) 2999-3011.

Atencia, J. and Beebe, D.J., 2005, Controlled microfluidic interfaces, Science 437 648-655.

Aubry, N. and Singh, P., 2006, Influence of particle-particle interactions and particles rational motion in traveling Electrophoresis 27 703-715.

Bejan, A. and Lorente, S., 2006, Constructal theory of generation of configuration in nature and engineering, J. of Applied Physics 100 (4) 41301-1-27.

Bejan, A., Rocha, L.A.O. and Lorente, S., 2000, Thermodynamic optimization of geometry: T- and Y-shaped constructs of fluid streams, Int. J. of Thermal Sciences 39 (9-11) 949-960.

Bird, R.B., Stewart, W.E. and Lightfoot, E.N., 1971, Transport Phenomena, John Wiley & Sons Inc., New York.

Bourlioux, A., 1995, A coupled level-set volume-of-fluid for tracking material interfaces, 6th Int. Symposium on Computational Fluid Dynamics, Lake Tahoe, NV, September 4-8.

Bozzi, L.A., Feng, J.Q., Scott, T.C. and Pearlstein, A.J., 1997, Steady axisymmetric motion of deformable drops falling or rising through a homogeneous fluid in a tube at intermediate Reynolds number, J. of Fluid Mechanics 336 1-32.

Brackbill, J.U., Kothe, D.B. and Zemach, C., 1992, A continuum method for modelling surface tension, J. Computational Physics 100 335-354.

Cahn, J.W. and Hilliard, J.E., 1959, Free Energy of a Nonuniform System. III. Nucleation in a Two-Component Incompressible Fluid, J. of Chemical Physics 31 688-699.

Chang, Y.C., Hou, T.Y., Merriman, B. and Osher, S., 1996, A Level Set Formulation of Eulerian Interface Capturing Methods for Incompressible Fluid Flows, J. Computational Physics 124 449-464.

Coulliette, C. and C. Pozrikidis, C., 1998, Motion of an array of drops through a cylindrical tube, J. of Fluid Mechanics 358 1-28.

Cristini, V., Bawzdziewicz, J. and Loewenberg, M., 2001, An Adaptive Mesh Algorithm for Evolving Surfaces: Simulations of Drop Breakup and Coalescence, J of Computational Physics 168 (2) 445-463.

Dai, M. and Schmidt, D.P., 2005, Adaptive tetrahedral meshing in free-surface flow, J. of Computational Physics 208(1) 228-252.

Daly, B., 1967, Numerical study of two fluid Rayleigh-Taylor instability, Physics of Fluids 10 297-307.

De Sousa, F.S., Mangiavacchi, N., Nonato, L.G., Castelo, A., Tome, M.F., Ferreira, V.G., Cuminato, J.A. and McKee, S., 2004, A front-tracking/front-capturing method for the simulation of 3D multi-fluid flows with free surfaces, J. of Computational Physics 198(2) 469-499.

DeBar, R., 1974, Fundamentals of the KRAKEN code, Technical Report UCIR-760, Lawrence Livermore National Laboratory.

Dennis, S.C.R. and Chang, G., 1970, Numerical solutions for steady flow past a circular cylinder at Reynolds numbers up to 100, J. Fluid Mechanics 42 471.

Duchanoy, C. and Jongen, T.R.G., 2003, Efficient simulation of liquid-solid flows with high solids fraction in complex geometries, Computers & Fluids 32 1453-1471.

Enright, D., Fedkiw, R., Ferziger, J. and Mitchell, I., 2002, A Hybrid Particle Level Set Method for Improved Interface Capturing, J. of Computational Physics 183(1) 83-116.

Esmaeeli, A. and Tryggvason, G., 2003, Computations of explosive boiling in microgravity, J. of Scientific Computing 19(1-3) 163-182.

Esmaeeli, A. and Tryggvason, G., 2004, Computations of film boiling. Part 1:numerical method, Int. J. of Heat and Mass Transfer 47 5451-5461.

Feng, J., Hu, H.H. and Joseph, D.D., 1994, Direct simulation of initial value problems for the motion of solid bodies in a Newtonian fluid Part 1: Sedimentation, J. Fluid Mechanics 261 95-134.

Feng, J., Hu, H.H. and Joseph, D.D., 1994b, Direct simulation of initial value problems for the motion of solid bodies in a Newtonian fluid Part 2: Couette and Poiseuille flows, J. Fluid Mechanics 277 271-301.

Fisher, J.S. and Lee, A.P., 2004, Cell encapsulation on a microfludic platform, MicroTAS 2004, Sept 26-30, Malmo, Sweden.

Fukano, T. and Inatomi, T., 2003, Analysis of liquid film formation in a horizontal annular flow by DNS, Int. J. of Multiphase Flow 29 1413-1430.

Ghosal, S., 2006, Electrokinetic flow and dispersion in capillary electrophoresis, Annual Review of Fluid Mechanics 38 309-338.

Glimm, J., Grove, J.W., Li, X.L., Oh, W. and Sharp, D.H., 2001, A Critical Analysis of Rayleigh–Taylor Growth Rates, J. of Computational Physics 169(2) 652-677.

Glimm, J., Grove, J.W., Li, X.L., Shyue, K.M, Zeng, Y. and Zhang, Q., 1998, Three-dimensional front-tracking, SIAM J. on Scientific Computing 19(3) 702-723.

Glowinski, R., Pan, T.-W., Hesla, T.I. and Joseph, D.D., 1999, A distributed Lagrange multiplier/fictitious domain method for particulate flows, Int. J. of Multiphase Flow 25(5) 755-794.

Glowinski, R., Pan, T.-W., Hesla, T.I., Joseph, D.D. and Periaux, J., 2001, A Fictitious Domain Approach to the Direct Numerical Simulation of Incompressible Viscous Flow past Moving Rigid Bodies: Application to Particulate Flow, J. of Computational Physics 169(2) 363-426.

Glowinski, R., Pan, T.-W., Hesla, T.I., Joseph, D.D. and Periaux, J., 2000, A distributed Lagrange multiplier/fictitious domain method for the simulation of flow around moving rigid bodies: application to particulate flow, Computer Methods in Applied Mechanics and Engineering 184(2-4) 241-267.

Hardt, S. Schonfeld, F., Weise, F., Hoffmann, Ch., and Ehrfeld, W., 2001, Simulation of droplet formation in micromixers, 4th Int. Conference on Modeling and Simulation of Microsystems MSM 2001, 19-21 March, Hilton Head Island, SC, 223-226.

Harlow, F.H and Welch, J.E., 1965, Numerical calculation of time-dependent viscous incompressible flow of fluid with free surface, Physics of Fluids 8 2182-2189.

He, M., Edgar, J.S., Jeffries, G..D.M., Lorenz, R.M., Shelby, J.P. and D.T. Chiu, 2005, Selective encapsulation of single cells and subcellular organelles into picoliter and femtoliter-volume droplets, Analytical Chemistry 77(6) 1539-1544.

Hirt, C.W. and Nichols, 1981, Volume of fluid (VOF) method for the dynamics of free boundaries, J. of Computational Physics 39 201-225.

Hirt, C.W. and Sicilian, J.M., 1985, A Porosity Technique for the Definition of Obstacles in Rectangular Cell Meshes, Proc. Fourth International Conf. Ship Hydro., National Academic of Science, Washington, DC, Sept. 1985.

Hou, T.Y., Lowengrub, J.S. and Shelley, M.J., 2001, Boundary Integral Methods for Multicomponent Fluids and Multiphase Materials, J. of Computational Physics 169(2) 302-362.

Hu, H.H., Joseph, D.D. and Crochet, M.J., 1992, Direct simulation of fluid particle motions, Theoretical Computational Fluid Dynamics 3 285-306.

Hu, H.H., Patankar, N.A. and Zhu, M.Y., 2001, Direct Numerical Simulations of Fluid–Solid Systems Using the Arbitrary Lagrangian–Eulerian Technique, J. of Computational Physics 169(2) 427-462.

Ingham, D.B. and Tang, T., 1990, A numerical investigation into the steady flow past a rotating circular cylinder at low and intermediate Reynolds numbers, J. of Computational Physics 87 91-107.

Jacqmin, D., 1999, Calculation of Two-Phase Navier–Stokes Flows Using Phase-Field Modeling, J. of Computational Physics 155(1) 96-127.

Jiang, L, Wong, M. and Zohar, Y., 2001, Forced convection boiling in a microchannel heat sink, J. of Microelectromechanical System 10 80-87.

Juárez, H., Scott, R., Metcalfe, R. and Bagheri, B., 2000, Direct simulation of freely rotating cylinders in viscous flows by high-order finite element methods, Computers & Fluids 29 547-582.

Kang, K.H., Kang, Y., Xuan, X. and Li., D., 2006, Continuous separation of microparticles by size with Direct current-dielectrophoresis, Electrophoresis 27 694-702.

Keh, H.J., Horng, K.D. Kuo, J., 1991, Boundary effects on electrophoresis of colloidal cylinders, J. of Fluid Mechanics 231 211-228.

Kim, S., Lorente, S. and Bejan, A., 2006, Vascularized materials: tree-shaped flow architectures matched canopy to canopy, J. of Applied Physics 100 (6) 63525-1-8.

Kim, D. and Choi, H., 2006, Immersed boundary method for flow around an arbitrarily moving body, J. of Computational Physics 212(2) 662-680.

Kim, J., 2005a, A diffuse-interface model for axisymmetric immiscible two-phase flow, Applied Mathematics and Computation 160 589-606.

Kim, J., 2005b, A continuous surface tension force formulation for diffuse-interface models, J. of Computational Physics 204(2) 784-804.

Kim, J., Kang, K. and Lowengrub, J., 2004, Conservative multigrid methods for Cahn–Hilliard fluids, J. of Computational Physics 193(2) 511-543.

Lakehal, D. and Meier, M. and Fulgosi, M., 2002, Interface tracking towards the direct simulation of heat and mass transfer in multiphase flows, Int. J. of Heat and Fluid Flow 23 242-257.

Lakehal, D., Meier, M., Davis, J., Smith, B.L. and Yadigaroglu, G., 2001, Interface tracking for the prediction of interfacial dynamics and heat/masss transfer in multiphase flows, Thermal Sciences Online 2001(2) 1267-1274, ISSN 961-91393-0-5.

Leveque, R.J., 2002, Finite Volume Methods for Hyperbolic Problems, Cambridge University Press, UK.

Link, D.R., Anna, S.L., Weitz, D.A. and Stone, H.A., 2004, Geometrically Mediated Breakup of Drops in Microfluidic Devices, Physical Review Letters 92(5) 054503.

Lopez, J., Hernandez, J., Gomez, P. and Faura, F., 2005, An improved PLIC-VOF method for tracking thin fluid structures in incompressible two-phase flows, J. of Computational Physics 208(1) 51-74.

Lorstad, D. and Fuchs, L., 2004, High-order surface tension VOF-model for 3D bubble flows with high density ratio, J. of Computational Physics 200(1) 153-176.

Lossasso, F., Fedkiw, R. and Osher, S., 2006, Spatially adaptive techniques for level set methods and incompressible flow, Computers and Fluids (in press).

Magnaudet, J., Rivero, M. and Fabre, J., 1995, Accelerated flows around a rigid sphere or a spherical bubble. Part I. Steady straining flow, J. of Fluid Mechanics 284 97-136.

Marchandise, M. and Remacle, J.-F., 2006, A stabilized finite element method using a discontinuous level set approach for solving two phase incompressible flows, J. of Computational Physics (in press).

Marella, S., Krishnan, S., Liu, H. and Udaykumar, H.S., 2005, Sharp interface Cartesian grid method I: An easily implemented technique for 3D moving boundary computations, J. of Computational Physics 210(1) 1-31.

Maruoka, A., 2003, Finite element analysis for flow around rotating body using chimera mehod, Int. J. of Computational Fluid Dynamics 17(4) 289-297.

McHyman, J., 1984, Numerical methods for tracking interfaces, Physica D 12 396-407.

McQueen, D.M. and Peskin, C.S., 1989, A three-dimensional computational method for blood flow in the heart. II. Contractile fibers, J. of Computational Physics 82(2) 289-297.

Nagrath, S., Jansen, K., Lahey Jr, R.T. and Akhatov, I., 2006, Hydrodynamic simulation of air bubble implosion using a level set approach, J of Computational Physics 215(1) 98-132.

Nichols, B.D. and Hirt, C.W., 1975, Methods for Calculating Multidimensional, Transient Free Surface Flows Past Bodies, Proc. of the 1st Int. Conf. on Numerical Ship Hydrodynamics, Gaithersburg, Maryland, October 20-23.

Noh, W. and Woodward, P., 1976, SLIC-Simple line interface calculation, 5th Int. Conference on Fluid Dynamics, Lecture Notes in Physics (A.V. Vooren and P. Zandbergen, eds.) Spinger-Verlag, 59 330-340.

Osher, S. and Fedkiw, R., 2003, Level Set Methods and Dynamic Implicit Surfaces, Springer, New York.

Osher, S. and Fedkiw, R.P., 2001, Level-set methods: An overview and some recent results, J. of Computational Physics 169 463-502.

Osher, S. and Sethian, J.A., 1988, Fronts Propagating with Curvature-Dependent Speed: Algorithms Based on Hamilton-Jacobi Formulations, J. Computational Physics 79 12-49.

Pan, T.-W. and Glowinski, R., 2005, Direct simulation of the motion of neutrally buoyant balls in a three-dimensional Poiseuille flow, Comptes Rendus Mecanique 333(12) 884-895.

Pan, T.-W., Joseph, D.D. and Glowinski, R., 2005, Simulating the dynamics of fluid–ellipsoid interactions, Computers & Structures 83(6-7) 463-478.

Park, J., Kwon, K. and Choi, H., 1998, Numerical solutions of flow past a circular cylinder at Reynolds number up to 160, KSME Int. J. 12 1200.

Patankar, S.V., 1980, Numerical Heat Transfer and Fluid Flow, Hemisphere Publisher, New York.

Peng, D., Merriman, B., Osher, S., Zhao, H.K. and Kang, M., 1999, A PDE-based fast local level-set method, J. Computational Physics 155 410-438.

Peskin C.S. and McQueen, D.M., 1989, A three-dimensional computational method for blood flow in the heart I. Immersed elastic fibers in a viscous incompressible fluid, J. of Computational Physics 81(2) 372-405.

Peskin, C.S., 1972, Flow patterns around heart valves: A numerical method, J. of Computational Physics 10(2) 252-271.

Peskin, C.S., 1977, Numerical analysis of blood flow in the heart, J. of Computational Physics 25(3) 220-252.

Peskin, C.S., 2002, The immersed boundary method, Acta Numerica, Cambridge University Press, Cambridge, UK, 1–39.

Petersson, N.A., 1999, An algorithm for assembling overlapping grid systems, SIAM J. of Scientific Computing, 20(6) 1995-2022.

Pettersen, J., 2004, Flow vaporization of CO2 in microchannel tubes, Exp. Thermal and Fluid Science 28 111-121.

Pozrikidis, C., 2001, Interfacial dynamics for Stokes flow, J. of Computational Physics 169(2) 250-301.

Qu, W. and Mudawar, I., 2003a, Flow boiling heat transfer in two-phase micro-channel heat sinks: I. Experimental investigation and assessment of correlation methods, Int. J. of Heat and Mass Transfer 46 2755-2771.

Qu, W. and Mudawar, I., 2003b, Flow boiling heat transfer in two-phase micro-channel heat sinks: II. Annular two-phase flow model, Int. J. of Heat and Mass Transfer 46 2773-2784.

Quan, S. and Schmidt, D.P., 2006, A moving mesh interface tracking method for 3D incompressible two-phase flows, J. of Computational Physics (in press).

Renardy, Y. and Renardy, M., 2002, PROST-A Parabolic Reconstruction of Surface Tension for the Volume-of-Fluid Method, J. of Computational Physics 183(2) 400-421.

Rider, W.J. and Kothe, D.B., 1998, Reconstructing volume tracking, J. of Computational Physics 141(2) 112-152.

Rider, W.J., Kothe, D.B., Mosso, S.J., Cerutti, J. and Hochstein, J.S., 1995, Volume tracking of interfaces having surface tension in two and three dimensions, AIAA Paper 95-0699.

S.W. Churchill, 1988, Viscous Flows: The Practical Use of Theory, Butterworths Publishers.

Scardovelli, R., and Zaleski, S., 1999, Direct numerical simulation of free-surface and interfacial flows, Annual Review of Fluid Mechanics 31 567-603.

Sethian, J.A. , 1999, Level Set Methods and Fast Marching Methods: Evolving Interfaces in Computational Geometry, Fluid Mechanics, Computer Vision, and Materials Science, Cambridge University Press, UK.

Sethian, J.A., 2001, Evolution, implementation and application of level set and fast marching methods for advancing fronts, J. of Computational Physics 169 503-555.

Sharma, N. and Patankar, N.A., 2005, A fast computation technique for the direct numerical simulation of rigid particulate flows, J. of Computational Physics 205(2) 439-457.

Shestopalov, I., Tice, J.D. and Ismagilov, R.F., 2004, Multi-step synthesis of nanoparticles performed on millisecond time scale in a microfluidic droplet-based system, Lab on a Chip 4(4) 316-321.

Shin, S. and Juric, D., 2002, Modeling Three-Dimensional Multiphase Flow Using a Level Contour Reconstruction Method for Front Tracking without Connectivity, J. of Computational Physics 180(2) 427-470.

Shin, S., Abdel-Khalik, S.I., Daru, V. and Juric, D., 2005, Accurate representation of surface tension using the level contour reconstruction method, J. of Computational Physics 203(2) 493-516.

Silva, A.L.F. L.E., Silveira-Neto, A. and Damasceno, J.J.R., 2003, Numerical simulation of two-dimensional flows over a circular cylinder using the immersed boundary method, J. of Computational Physics 189 351-370.

Singh, P. and Joseph, D.D., 2005, Fluid dynamics of floating particles, J. of Fluid Mechanics 530 31-80.

Son, G. and Dhir, V.K., 1997, Numerical simulation of saturated film boiling on horizontal surface, ASME J. of Heat Transfer 119 525-533.

Son, G., 2005, A level-set method for incompressible two-fluid flows with immersed solid boundaries, Num. Heat Transfer B: Fundamental 47 473-489.

Song, H., Bringer, M.R., Tice, J.D., Gerdts, C.J. and Ismagilov, R.F., 2003, Experimental test of scaling of mixing by chaotic advection in droplets moving through microfluidic channels, Applied Physics Letters 83(22) 4664-4666.

Sucker, D. and Brauer, H., 1975, Fluiddynamik bei der angestromten Zilindern, W€arme Stoffubertragung 8 149.

Sussman, M. and Fatemi, E., 1999, An Efficient, Interface-Preserving Level Set Redistancing Algorithm and Its Application to Interfacial Incompressible Fluid Flow, SIAM J. on Scientific Computing 20(4) 1165-1191.

Sussman, M. and Puckett, E.G., 2000, A Coupled Level Set and Volume-of-Fluid Method for Computing 3D and Axisymmetric Incompressible Two-Phase Flows, J. of Computational Physics 162(2) 301-337.

Sussman, M., 2001, An adaptive mesh algorithm for free surface flows in general geometries, Adaptive Method of Lines, eds. Wouwer, A.V., Saucex, Ph. and Schiesser, W.E., Chapman-Hill/CRC Press, Boca Raton, FL, 207–227.

Sussman, M., Almgren, A.S., Bell, J.B., Colella, P., Howell, L.H. and Welcome, M.L., 1999, An Adaptive Level Set Approach for Incompressible Two-Phase Flows, J. of Computational Physics 148(1) 81-124.

Sussman, M., Smereka, P. and Osher, S., 1994, A Level Set Approach for Computing Solutions to Incompressible Two-Phase Flow, J. Computational Physics 114 146-159.

Taha, T. and Cui, Z.F., 2006a, CFD modelling of slug flow inside square capillaries, Chemical Engineering Science 61(2) 665-675.

Taha, T. and Cui, Z.F., 2006b, CFD modelling of slug flow in vertical tubes, Chemical Engineering Science 61(2) 676-687.

Tan, Y.-C., Fisher, J.S., Lee, A.I., Cristini, V. and Phillip, A., 2004, Design of microfluidic channel geometries for the control of droplet volume, chemical concentration, and sorting, Lab on a Chip 4 292-298.

Tang, T. and Ingham, D.B., 1991, On steady flow past a rotating circular cylinder at Reynolds numbers 60 and 100, Computers & Fluids 19 217-230.

Tanguy, S. and Berlemont, A., 2005, Application of a level set method for simulation of droplet collisions, Int. J. of Multiphase Flow 31(9) 1015-1035.

Thorsen, T., Roberts, R.W., Arnold, F.H. and Quake, S.R., 2001, Dynamic pattern formation in a vesicle-generating microfluidic device, Physical Review Letters 86(18) 4136-4166.

Tomotika, S. and Aoi, T., 1951, An expansion formula for the drag on a circular cylinder moving through a viscous fluid at small Reynolds number, Quart. J. Mech. Appl. Math. 4 401-406.

Triton, D.J., 1959, Experiments on the flow past a circular cylinder at low Reynolds number, J. Fluid Mechanics 6 547.

Tryggvason, G., Bunner, B., Esmaeeli, A., Juric, D., Al-Rawahi, N., Tauber, W., Han, J., Nas, S. and Jan, Y.-J., 2001, A Front-Tracking Method for the Computations of Multiphase Flow, J. of Computational Physics 169(2) 708-759.

Unverdi, S.O. and Tryggvason, G., 1992, A front-tracking method for viscous, incompressible, multi-fluid flows, J. of Computational Physics 100 25-37.

Utada, A.S., Lorenceau, E., Link, D.R., Kaplan, P.D., Stone, H.A. and Weitz, D.A., 2005, Monodisperse double emulsions generated from a microcapillary devices, Science 308 537-541.

Van Leer, B, 1974, Towards the ultimate conservative difference scheme. II. Monotonicity and conservation combined in a second-order scheme, J. of Computational Physics, vol. 14, pp. 361-370.

Van Sint Annaland, M., Deen, N.G. and Kuipers, J.A.M., 2006, Direct Numerical Simulation of Complex Gas-Liquid-Solid Flows using a Combined Immersed Boundary (IB) and Volume Of Fluid (VOF) Approach, Euromech Colloquium 479 Numerical Simulation of Multiphase Flow with Deformable Interfaces, August 14-16th, 2006, The Pier, Scheveningen, The Netherlands.

Voldman, J., 2006, Electrical forces for microscale cell manipulation, Annual Review of Biomedical Engineering 8 425-454.

Wan, D. and Turek, S., 2005, Direct numerical simulation of particulate flow via multigrid FEM techniques and the fictitious boundary method, Int. J. for Numerical Methods in Fluids 51(5) 531-566.

Wan, D. and Turek, S., 2006, An efficient multigrid-FEM method for the simulation of solid–liquid two phase flows, J. of Computational and Applied Mathematics (in press).

Wang, C., Nguyen, N.T. and Wong, T. N., 2006, Optical measurement of flow field and concentration field inside a moving nanoliter droplet, Sensors and Actuators A, in press.

Wei, G., 2005a, A Fixed-Mesh Method for General Moving Objects, Technical Report FSI-05-TN73, Flow Science Inc. (http://www.flow3d.com/Bibliography/genbib.htm)

Wei, G., 2005b, An Implicit Method to Solve Problems of Rigid Body Motion Coupled with Fluid Flow, Technical Report FSI-05-TN76, Flow Science Inc. (http://www.flow3d.com/Bibliography/genbib.htm)

Welch, S.W.J., 1995, Local simulation of two-phase flows including interface tracking with mass transfer, J. of Computational Physics 121 142-154.

White, F.M., 1991, Viscous Fluid Flow, McGraw-Hill, New York.

Wu, H.-C., Hwang, W.-S. and Lin, H.-J., 2004, Development of a three-dimensional simulation system for micro-inkjet and its experimental verification, Materials Science and Engineering A 373(1-2) 268-278.

Yap Y.F., Toh K.C., Wong T.N., Chai J.C., 2004, Numerical modeling of annular flow in microchannel, IEEE EPTC 2004, Dec. 8-10, Singapore.

Yap Y.F., Chai J.C., Toh K.C., Wong T.N. and Lam Y. C., 2005, Numerical modeling of unidirectional stratified flow with and without phase change, Int. J. of Heat and Mass Transfer 48(3-4) 477-486.

Yap Y.F., Chai J.C., Toh K.C., and Wong T.N., 2006a, Modeling the flows of two immiscible fluids in a three-dimensional square channel using the level-set method, Num. Heat Transfer A: Applications 49(9) 893-904.

Yap Y.F., Chai J.C., Wong T.N. and Toh K.C., 2006b, The effects of surface tension on two-dimensional two-phase stratified flows, AIAA J. of Thermophysics and Heat Transfer 20(3) 638-640.

Yap Y.F., Chai J.C., Wong T.N., Toh K.C. and Zhang H.Y., 2006c, A global mass correction scheme for the level-set method, Num. Heat Transfer B: Fundamentals (accepted).

Yap Y.F., Chai J.C., Wong T.N., Nguyen K.C., Toh K.C. and Zhang H.Y., 2006d, Particle transport in microchannels, Num. Heat Transfer B: Fundamentals (accepted).

Yap Y.F., D. Li and J.C. Chai, Flow of Cells in Microchannels, 2006e, Journal of Physics - Conference Series 34 448–453.

Ye, C. and Li., D., 2004, 3-D transient electrophoretic motion of a spherical particle in a T-shaped rectangular microchannel, J. of Colloid and Interface Science 272 480-488.

Ye, T., Mittal, R., Udaykumar, H.S. and Shyy, W., 1999, An accurate Cartesian grid method for viscous incompressible flows with complex boundaries, J. Computational Physics 156 209-240.

Yen, T.H., Kasagi, N. and Suzuki, Y., 2003, Forced convective boiling heat transfer in microtubes at low mass and heat fluxes, Int. J. of Multiphase Flow 29 1771-1792.

Yokoi, K., 2002, Numerical method for complex moving boundary problems in a Cartesian fixed grid, Physical Review E 65(5) 055701.

Zalesak, S.T., 1979, Fully multidimensional flux-corrected transport algorithms for fluids, J. of Computational Physics 31 335-362.

Zeng, J. and Korsmeyer, T., 2004, Principles of droplet electrodynamics for lab-on-a-chip, Lab on a Chip 4 265-277.

Zheng, X., Lowengrub, J., Anderson, A. and Cristini, V., 2005, Adaptive unstructured volume remeshing-II: Application to two- and three-dimensional level-set simulations of multiphase flow, J. of Computational Physics 208 (2) 626-650.

APPENDIX: Flow of Two Stratified Fluids Driven by Marangoni Force

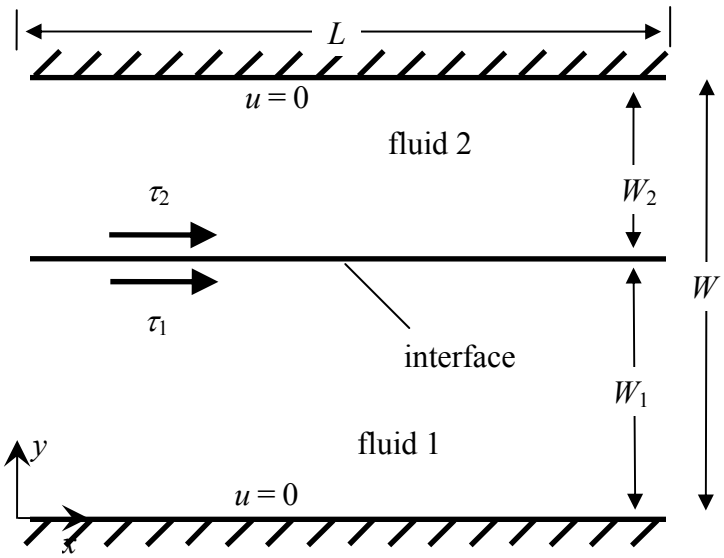

Figure A-1: Flow of two stratified fluid layers.

Figure A-1 shows a schematic of two stratified fluid layers. These fluids, i.e. fluid 1 and fluid 2, are immiscible in each other. The thickness of fluid 1 and fluid 2 are W_1 and W_2 respectively. They are separated by an interface. There exists a variation of surface tension along the interface. Such a surface tension gradient induces a net force tangential to the interface dragging both layers into motion. This force drives the fluids at the interface to flow towards region of higher surface tension. Since the fluid layers extend to infinity, the interface between the fluids remains flat. Under such a condition, the capillary force (induced by the curvature of the interface) acting normal to the interface is zero.

The stress acting on each side of the interface are τ_1 and τ_2 respectively. Surface tension varies linearly along x, i.e. $\frac{d\sigma}{dx} = const$. Due to the surface tension gradient at the interface, there is a jump in stress across the interface, i.e.

$$\tau_1 - \tau_2 = \frac{d\sigma}{dx} \tag{A-1a}$$

Then τ_1 and τ_2 can be written as

$$\tau_1 = \mu_1 \left.\frac{du}{dy}\right|_{y=W_1^-} = f\frac{d\sigma}{dx} \tag{A-1b}$$

$$\tau_2 = \mu_2 \left.\frac{du}{dy}\right|_{y=W_1^+} = (f-1)\frac{d\sigma}{dx} \tag{A-1c}$$

The motions of the fluid layers are governed by

$$\mu\frac{d^2u}{dy^2} = \frac{dp}{dx} \tag{A-2}$$

subjected to the following boundary conditions

$$y = 0,\ u = 0 \tag{A-3a}$$

$$y = W_1^-,\ u = u_m,\ \tau_1 = \mu_1 \left.\frac{du}{dy}\right|_{y=W_1^-} = f\frac{d\sigma}{dx} \tag{A-3b}$$

$$y = W_1^+,\ u = u_m,\ \tau_2 = \mu_2 \left.\frac{du}{dy}\right|_{y=W_1^+} = (f-1)\frac{d\sigma}{dx} \tag{A-3c}$$

$$y = W,\ u = 0 \tag{A-3d}$$

Integrate Eq. (A-2) gives

$$\mu\frac{du}{dy} = \frac{dp}{dx}y + A \tag{A-4a}$$

$$\mu u = \frac{dp}{dx}\frac{y^2}{2} + Ay + B \tag{A-4b}$$

For fluid 1:

$$\mu_1\frac{du}{dy} = \frac{dp}{dx}y + A_1 \tag{A-5a}$$

$$\mu_1 u = \frac{dp}{dx}\frac{y^2}{2} + A_1 y + B_1 \tag{A-5b}$$

$$y = 0,\ u = 0 \ \Rightarrow\ B_1 = 0 \tag{A-6a}$$

$$y = W_1,\ \tau_1 = \mu_1 \left.\frac{du}{dy}\right|_{y=W_1^-} = f\frac{d\sigma}{dx} \ \Rightarrow\ A_1 = f\frac{d\sigma}{dx} - W_1\frac{dp}{dx} \tag{A-6b}$$

$$y = W_1,\ u = u_m = -\frac{{W_1}^2}{2\mu_1}\frac{dp}{dx} + \frac{W_1}{\mu_1}\frac{d\sigma}{dx} f \tag{A-6c}$$

For fluid 2:

$$\mu_2 \frac{du}{dy} = \frac{dp}{dx} y + A_2 \tag{A-7a}$$

$$\mu_2 u = \frac{dp}{dx}\frac{y^2}{2} + A_2 y + B_2 \tag{A-7b}$$

$$y = W_1,\ \tau_2 = \mu_2 \left.\frac{du}{dy}\right|_{y=W_1^+} = (f-1)\frac{d\sigma}{dx} \ \Rightarrow\ A_2 = -W_1\frac{dp}{dx} - \frac{d\sigma}{dx} + \frac{d\sigma}{dx} f \tag{A-8a}$$

$$y = W,\ u = 0 \ \Rightarrow\ B_2 = \left(W_1 W - \frac{W^2}{2}\right)\frac{dp}{dx} + W\frac{d\sigma}{dx} - W\frac{d\sigma}{dx} f \tag{A-8b}$$

$$y = W_1,\ u = u_m = -\frac{{W_2}^2}{2\mu_2}\frac{dp}{dx} + \frac{W_2}{\mu_2}\frac{d\sigma}{dx} - \frac{W_2}{\mu_2}\frac{d\sigma}{dx} f \tag{A-8c}$$

Combining Eqs. (A-6c) and (A-8c) ($u_m = u_m$) gives

$$-\frac{{W_1}^2}{2\mu_1}\frac{dp}{dx} + \frac{W_1}{\mu_1}\frac{d\sigma}{dx} f = -\frac{{W_2}^2}{2\mu_2}\frac{dp}{dx} + \frac{W_2}{\mu_2}\frac{d\sigma}{dx} - \frac{W_2}{\mu_2}\frac{d\sigma}{dx} f$$

$$\left(\frac{W_1}{\mu_1} + \frac{W_2}{\mu_2}\right)\frac{d\sigma}{dx} f = \left(\frac{{W_1}^2}{2\mu_1} - \frac{{W_2}^2}{2\mu_2}\right)\frac{dp}{dx} + \frac{W_2}{\mu_2}\frac{d\sigma}{dx}$$

$$f = \frac{\left(\frac{{W_1}^2}{2\mu_1} - \frac{{W_2}^2}{2\mu_2}\right)\frac{dp}{dx} + \frac{W_2}{\mu_2}\frac{d\sigma}{dx}}{\left(\frac{W_1}{\mu_1} + \frac{W_2}{\mu_2}\right)\frac{d\sigma}{dx}} \tag{A-9}$$

Finally, the velocity can be expressed as

$$u = \frac{1}{\mu_i}\frac{dp}{dx}\frac{y^2}{2} + \frac{A_i}{\mu_i}y + \frac{B_i}{\mu_i} \tag{A-10a}$$

where

$$i = \begin{cases} 1, & \text{if } 0 \le y < W_1 \\ 2, & \text{if } W_1 \le y \le W \end{cases} \tag{A-10b}$$